
Alternative fuel effects on the lifecycle of individual contrails from formation to dissipation

Annemarie Luise Ursula Lottermoser



München 2025

Alternative fuel effects on the lifecycle of individual contrails from formation to dissipation

Annemarie Luise Ursula Lottermoser

Dissertation
an der Fakultät für Physik
der Ludwig-Maximilians-Universität
München

vorgelegt von
Annemarie Luise Ursula Lottermoser
aus Berchtesgaden

München, den 9. Dezember 2025

Erstgutachter: Prof. Dr. Markus Rapp
Zweitgutachter: Prof. Dr. George Craig
Tag der mündlichen Prüfung: 24. Februar 2026



Bayerisch Gmain, balcony, 16 July 2025

Abstract

Contrails and their evolution into contrail-cirrus clouds constitute a significant contribution to aviation's climate impact, as these anthropogenic ice clouds modify the atmospheric radiation balance. Present research investigates alternative propulsion systems, such as liquid hydrogen combustion, as potential strategies to mitigate the climate impact of contrails. These technologies can alter the physical processes involved in contrail formation and evolution. Therefore, a deep understanding of those processes is essential for assessing the potential of alternative propulsion technologies to reduce the climate impact of aviation. Recent research focuses on extending and adapting models simulating the contrail lifecycle to account for new physical processes, as well as planning and executing flight campaigns to measure emissions and contrails behind aircraft using non-conventional fuels.

This thesis presents a comprehensive model investigation of the contrail lifecycle, spanning from the initial formation to the transition of line-shaped contrails into aged contrail cirrus. The aim is to advance the understanding of how contrail properties respond to changes in the propulsion system, specifically regarding hydrogen combustion or hydrogen fuel cell systems.

The early formation phase is crucial for predicting the final number of nucleating ice crystals, which is one of the most important parameters of young contrails, determining the contrail's radiative impact. The Lagrangian Cloud Module (LCM) in a box model approach simulates contrail ice crystal formation; however, it lacks the accurate representation of plume dilution during the first seconds of plume evolution. With the shift to alternative fuels and the resulting changes in contrail formation processes, the existing model requires re-evaluation. Therefore, this thesis presents the development of the radial model (RadMod) that is used to simulate the early stage of the dynamical jet evolution. RadMod models the turbulent mixing of hot and moist engine exhaust with ambient air by solving the two-dimensional advection-diffusion equations for momentum, temperature, and water vapor. The model's validity is demonstrated through comparisons with theoretical and observational data across a range of conditions, including exhaust temperature, jet velocity, and aircraft velocity. Furthermore, RadMod is applied to simulate plume dilution; a scaling relation proposed in the literature is validated, and the simulated dilution is compared to measurements of the exhaust plume behind a fuel cell emulator. This work establishes the foundation for the intermediate-complexity model RadMod-LCM, which will be the subject of future research. Due to its lower computational cost compared to fully three-dimensional large-eddy simulations (LES), RadMod-LCM will enable extensive parameter studies across a wide range of atmospheric and engine conditions. In particular, this includes the modeling of aircraft configurations typical for alternative propulsion systems, e.g., smaller aircraft with lower flight and jet velocity.

The formation phase is followed by the vortex phase, which covers the first few minutes of the contrail's lifecycle. Previous studies investigating the contrail's evolution during the vortex phase focused on conventional aircraft propulsion systems operating under typical cruise altitude conditions. To investigate the vortex phase of individual contrails behind aircraft powered by alternative propulsion systems, the LES model EULAG coupled to LCM is employed. The input parameters are adjusted to be representative of alternative fuels or propulsion systems. These adjustments account for increased water vapor emissions, variations in the initial number of ice particles, and an extension of the atmospheric parameter space toward higher ambient temperatures. It is shown that the processes during the vortex phase, in particular the partial sublimation of ice particles in the descending wake vortex system, reduce the initial differences in the number of ice crystals. Ice crystal loss is found to increase with higher ambient temperatures and lower humidity values. A new parameterization for ice crystal loss in hydrogen contrails is provided that is incorporated

into larger-scale climate models by other research groups.

Building on this work, the subsequent transition of contrails into contrail-cirrus clouds during the dispersion phase is examined using EULAG-LCM. It is assessed how a switch to alternative propulsion systems affects the lifecycle and radiative properties of contrail cirrus. Results indicate that reducing the number of initially formed ice crystals leads to fewer but larger particles, which accelerates sedimentation and shortens contrail lifetime, highlighting the potential of emission-based mitigation strategies. In contrast, the emitted water vapor mass has a comparatively minor effect on contrail-cirrus properties relative to the initial ice crystal number, ambient temperature, and aircraft type. When averaged over all meteorological conditions, a reduction of the initial ice crystal number by a factor of 100 results in a 20-fold decrease in the lifetime-integrated total extinction, which serves as a proxy for the contrail's radiative effect. The relationship between initial ice crystal number and radiative impact is shown to be nonlinear.

Zusammenfassung

Kondensstreifen und ihre Weiterentwicklung in Kondensstreifenzirren tragen erheblich zum Klimaeinfluss der Luftfahrt bei, da diese anthropogenen Eiswolken die atmosphärische Strahlungsbilanz verändern. Aktuelle Forschungsarbeiten untersuchen alternative Antriebssysteme, wie zum Beispiel die Verbrennung von flüssigem Wasserstoff, als potenzielle Strategien zur Minderung des Klimaeinflusses von Kondensstreifen. Diese Technologien können die physikalischen Prozesse bei der Bildung und Entwicklung von Kondensstreifen verändern. Daher ist ein tiefgehendes Verständnis dieser Prozesse unerlässlich, um das Potenzial alternativer Antriebstechnologien zur Verringerung des Klimaeinflusses der Luftfahrt beurteilen zu können. Aktuelle Forschungsarbeiten konzentrieren sich darauf, Modelle zur Simulation des Kondensstreifen-Lebenszyklus zu erweitern und anzupassen, um neue physikalische Prozesse zu berücksichtigen. Darüber hinaus werden Messkampagnen durchgeführt, um Emissionen und Kondensstreifen von Flugzeugen mit nicht-konventionellen Treibstoffen zu erfassen.

Die vorliegende Arbeit präsentiert eine umfassende Modelluntersuchung des Lebenszyklus von Kondensstreifen von der initialen Bildung über die Entwicklung linienförmiger Kondensstreifen hin zu gealterten Zirren. Ziel der Arbeit ist es, das Verständnis darüber zu vertiefen, wie sich die Eigenschaften von Kondensstreifen bei veränderten Antriebssystemen von Flugzeugen, insbesondere bei Wasserstoffverbrennung oder Wasserstoff-Brennstoffzellensystemen, verändern.

Die frühe Bildungsphase ist entscheidend für die genaue Vorhersage der endgültigen Anzahl an Eispartikeln – eines der wichtigsten Parameter von jungen Kondensstreifen für deren klimawirksamen Eigenschaften. Das in einer Boxmodell-Konfiguration eingesetzte Lagrangsche Wolkenmodul (Lagrangian Cloud Module, LCM) simuliert die Bildung von Eiskristallen in Kondensstreifen; jedoch wird die Verdünnung der Abgasfahne während der ersten Sekunden nicht ausreichend abgebildet. Der Umstieg auf alternative Kraftstoffe und die damit verbundenen Änderungen in der Kondensstreifenbildung erfordern eine Neubewertung des Modells. Daher wird in dieser Arbeit das Radialmodell (RadMod) entwickelt, um die dynamische Jetentwicklung in der Frühphase zu simulieren. RadMod beschreibt die turbulente Durchmischung der heißen und feuchten Triebwerksabgase mit der Umgebungsluft durch Lösung der zweidimensionalen Advektions-Diffusions-Gleichungen für Impuls, Temperatur und Wasserdampf. Die Gültigkeit des Modells wird durch Vergleiche mit theoretischen und experimentellen Daten über eine Vielzahl von Bedingungen, wie Abgastemperatur, Jetgeschwindigkeit und Fluggeschwindigkeit, nachgewiesen. Außerdem wird RadMod zur Simulation der Plumenverdünnung angewendet; eine in der Literatur vorgeschlagene Skalierungsrelation wird validiert und die simulierte Verdünnung mit Messungen der Abgasfahne hinter einem Brennstoffzellen-Emulator verglichen. Die vorliegende Arbeit legt damit die Grundlage für das Modell RadMod-LCM mittlerer Komplexität, das in weiteren Forschungsarbeiten untersucht werden wird. Aufgrund seiner geringeren Rechenkosten im Vergleich zu dreidimensionalen Large-Eddy-Simulationen (LES) wird RadMod-LCM umfangreiche Parameterstudien über eine große Bandbreite atmosphärischer und triebwerksbezogener Bedingungen ermöglichen. Insbesondere umfasst dies die Modellierung von Flugzeugkonfigurationen, die für den Einsatz alternativer Antriebssysteme vorgesehen sind, z. B. kleinere Flugzeuge mit niedrigerer Flug- und Abgasgeschwindigkeit.

Auf die Bildungsphase folgt die Wirbelphase, die die ersten Minuten im Lebenszyklus eines Kondensstreifens umfasst. Frühere Studien zu dieser Phase konzentrierten sich auf konventionelle Antriebssysteme unter typischen Flugbedingungen in Reiseflughöhe. Zur Untersuchung der Wirbelphase von einzelnen Kondensstreifen hinter Flugzeugen mit alternativen Antriebssystemen wird in dieser Arbeit das LES-Modell EULAG gekoppelt mit dem LCM eingesetzt. Die Eingangsparameter werden so angepasst, dass sie repräsen-

tativ für alternative Treibstoffe oder Antriebssysteme sind. Diese Anpassungen berücksichtigen erhöhte Wasserdampfemissionen, Variationen in der anfänglichen Anzahl an Eispartikeln sowie eine Erweiterung des atmosphärischen Parameterraums hin zu höheren Umgebungstemperaturen. Es wird gezeigt, dass die Prozesse während der Wirbelphase, insbesondere die partielle Sublimation der Eispartikel in der absinkenden Wirbelschlepe, die anfänglichen Unterschiede in der Anzahl der Eiskristalle verringern. Zudem steigt der Eiskristallverlust mit zunehmender Umgebungstemperatur und abnehmender relativer Luftfeuchte. Es wird eine neue Parametrisierung für den Eiskristallverlust in Wasserstoff-Kondensstreifen präsentiert, die für die Integration in großskalige Klimamodelle durch andere Modellierungsgruppen Anwendung findet. Aufbauend auf diesen Ergebnissen untersucht die vorliegende Arbeit die anschließende Entwicklung von Kondensstreifen zu Kondensstreifenzirren während der Dispersionsphase, ebenfalls mit dem Modell EULAG-LCM. Es wird analysiert, wie sich alternative Antriebssysteme auf den Lebenszyklus und die Strahlungseigenschaften von Zirren auswirken. Die Ergebnisse zeigen, dass eine Reduktion der anfänglich gebildeten Eiskristallanzahl zu weniger, dafür aber größeren Partikeln führt, was die Sedimentation beschleunigt und die Lebensdauer der Kondensstreifenzirren verkürzt. Im Vergleich zur anfänglichen Anzahl an Eiskristallen, der Umgebungstemperatur und dem Flugzeugtyp hat die emittierte Wasserdampfmasse einen geringen Einfluss auf die Eigenschaften von Zirren. Gemittelt über alle meteorologischen Bedingungen führt eine Verringerung der anfänglichen Eiskristallanzahl um den Faktor 100 zu einer zwanzigfachen Abnahme der lebenszeitintegrierten Gesamttextinktion, die als Proxy für den Strahlungseffekt des Kondensstreifens dient. Die Beziehung zwischen der Anzahl anfänglicher Eiskristalle und der resultierenden Strahlungswirkung erweist sich als nichtlinear.

Contents

1	Introduction	1
1.1	Motivation: Climate impact of contrails	1
1.2	Overview of contrail lifecycle	4
1.3	Alternative aircraft propulsion systems	9
1.4	Research goal of the thesis	11
2	Extension of Contrail Formation Model	13
2.1	Introduction to the LCM box model	13
2.2	Towards intermediate complexity modeling of contrail formation: the new dynamical framework RadMod	17
2.2.1	Methods	17
2.2.2	Results	23
2.2.3	Discussion	31
2.2.4	Conclusion and outlook	34
2.3	Application of RadMod: Plume dilution study	36
2.3.1	Scaling relation for plume dilution	36
2.3.2	Comparison to measurement results	37
2.3.3	The "problem" with the plume age	38
2.4	Discussion and further steps with RadMod	41
2.4.1	Possible extensions and modifications of RadMod	41
2.4.2	RadMod-LCM coupling	42
3	Vortex Phase	47
3.1	Introduction to the EULAG-LCM model	47
3.2	High-resolution modeling of early contrail evolution from hydrogen-powered aircraft	49
3.2.1	Methods	50
3.2.2	Results	54
3.2.3	Discussion	66
3.2.4	Conclusions	67
4	Dispersion Phase	69
4.1	Method	69
4.1.1	Simulation setup	69
4.1.2	Quantities of interest	73
4.2	Results	75
4.2.1	Impact of initial ice crystal number scaling on contrail-cirrus evolution: example simulations	75
4.2.2	Parameter study of contrail-cirrus properties	79
4.3	Model intercomparison	88
4.3.1	Comparison to LES study	88
4.3.2	Comparison to CoCiP and GCM studies	89
4.4	Discussion	92
4.5	Conclusion	94

5 Summary and Concluding Remarks	95
Bibliography	99
Appendix	115

List of Figures

1.1	Best estimates of ERF terms from global aviation between 1940 and 2018	2
1.2	Overview of the contrail lifecycle	4
1.3	Schmidt-Appleman theory	6
2.1	Illustration of contrail formation as simulated with the box model	15
2.2	Comparison of RadMod velocity profiles to analytical solution	23
2.3	Self-similarity of RadMod profiles	25
2.4	RadMod thermodynamic profiles	26
2.5	Centerline velocity decay for different jet densities	27
2.6	RadMod profiles of water vapor mass mixing ratio and plume relative humidity	28
2.7	Jet spreading and centerline velocity decay in coflowing jet	30
2.8	Fitted values for coflowing-jet equations	30
2.9	Comparison of RadMod profiles with CFD data	31
2.10	Plume dilution for different jet excess temperatures and coflow velocities	37
2.11	Scaled plume dilution for different jet excess temperatures, coflow and jet excess velocities, and initial jet diameters	38
2.12	Scaled plume dilution in comparison with turbofan and measurement data	39
2.13	Conceptual scheme illustrating the differing definitions of plume age	39
2.14	Plume age and centerline plume age	40
2.15	Illustration of Eulerian and Lagrangian approach for diffusing SIPs	43
3.1	Initial mean crystal size in vortex phase simulations	52
3.2	Temporal evolution of ice crystal number concentration in (x, z) -plane during vortex phase	56
3.3	Temporal evolution of contrail properties during vortex phase	56
3.4	Impact of ambient temperature on final vertical profiles of contrail properties after vortex phase	58
3.5	Final vertical profiles of contrail properties after vortex phase: stratification analysis	58
3.6	Final vertical profiles of contrail properties after vortex phase: size-distribution width analysis	59
3.7	Impact of aircraft type on ice crystal survival fraction after vortex phase	60
3.8	Updated ice crystal loss parameterization	61
3.9	Sensitivity analysis of updated parameterization	64
3.10	Impact of ice crystal loss on subsequent contrail-cirrus evolution	65
3.11	Impact of ice crystal loss on total extinction of contrail cirrus	66
4.1	Relative humidity initialization and evolution during dispersion phase	72
4.2	Temporal evolution of ice crystal number concentration in (x, z) -plane during dispersion phase	75
4.3	Temporal evolution of effective ice crystal diameter, ice mass, and profiles of ice mass and optical width during dispersion phase	77
4.4	Contributions of in-situ sublimation and sedimentation to overall ice crystal loss during dispersion phase	78
4.5	Temporal evolution of contrail properties during dispersion phase with focus on variation of initial ice crystal number	79
4.6	Temporal evolution of contrail properties during dispersion phase: sensitivity to aircraft type and fuel-type dependent parameters	80

4.7	Temporal evolution of contrail properties during vortex phase: sensitivity to meteorological parameters	81
4.8	Temporal evolution of ice crystal size spectra during dispersion phase	82
4.9	Temporal evolution of effective ice crystal diameter at different ambient temperatures during dispersion phase	83
4.10	Normalized time-integrated total extinction of contrail cirrus	86
4.11	Normalized time-integrated total extinction of contrail cirrus: parameter study	87
4.12	Scaling relation of contrail cirrus based on Eq. 5 in Lewellen (2014)	88
4.13	Scaling relation of contrail-cirrus properties based on Eqs. 4.11a-d	90
4.14	Model intercomparison: Mean normalized net radiative forcing (ECHAM5-CCMod and CoCiP) and total extinction (EULAG-LCM)	90
A1	Time-adaptivity of radial coordinate in RadMod	117
A2	Sensitivity analysis of grid resolution	118
A3	Momentum, tracer, and energy flow rates in RadMod	119
A4	Mass flow rate in RadMod	119
A5	Temporal evolution of ice relative humidity and temperature in (x, z) -plane during vortex phase	121
A6	Comparison between z_{Δ} values and parameterized survival fractions of original and new parameterization formulations	122
A7	Reproduced Fig. 5 from Unterstrasser (2016) highlighting the updated ice crystal loss parameterization	123
A8	Reproduced Fig. 9 from Unterstrasser (2016) highlighting the updated ice crystal loss parameterization	124
A9	Reproduced Fig. 10 from Unterstrasser (2016) highlighting the updated ice crystal loss parameterization	125
A10	Temporal evolution of contrail properties during vortex phase for variations in mesh resolution, domain size, and ambient pressure	126
A11	Initial velocity magnitude of RANS-based and analytical flow field	128
A12	Evolution of ice crystal number concentration in (x, z) -plane during vortex phase: simulation with RANS-initialized flow field	129
A13	Temporal evolution of contrail properties during vortex phase: comparison between RANS-based and analytical flow field initialization	130
A14	Ice crystal survival fractions after vortex phase for RANS-based and analytical flow field initialization	131
A15	Temporal evolution of contrail properties during vortex phase for shifted initial plume position	132
A16	Temporal evolution of contrail properties during vortex phase: simulations with varied number of engines	133
A17	Simulated ice crystal survival fractions of vortex phase simulations performed during Bachelor's project and internship	133

List of Tables

2.1	Baseline parameters used in RadMod simulations	17
2.2	Measured and simulated jet properties of various studies: comparison to RadMod	25
3.1	Parameters used in vortex phase simulations	53
3.2	Fuel and exhaust properties: comparison between kerosene and hydrogen	54
4.1	Ice crystal parameters used as input for vortex phase simulations	71
4.2	Numerical and atmospheric parameters used in dispersion phase simulations	73
4.3	Comparison of dispersion phase results of EULAG-LCM with Lewellen (2014), ECHAM5-CCMod, and CoCiP	91
A1	Summary of vortex phase simulation results	134
A2	List of parameterized survival fractions: comparison between numerical and analytical formulations	135
A3	Properties of contrails used to initialize dispersion phase simulations	136

1

Introduction

1.1 Motivation: Climate impact of contrails

Widespread and rapid changes in the atmosphere, ocean, cryosphere and biosphere have occurred. Human-caused climate change is already affecting many weather and climate extremes in every region across the globe. This has led to widespread adverse impacts and related losses and damages to nature and people. [...] Every increment of global warming will intensify multiple and concurrent hazards. [...] The choices and actions implemented in this decade will have impacts now and for thousands of years.

–AR6 Synthesis Report: Climate Change 2023

This excerpt from the Intergovernmental Panel on Climate Change (IPCC) Synthesis Report (IPCC, 2023) highlights the urgent need to act on human-induced climate change. Climate change is not a distant threat, but a present crisis with accelerating impacts. Science leaves no doubt that human activity is driving these changes. Rapid and sustained mitigation is essential to limit warming, reduce risks, and preserve a livable future.

The recent IPCC report states that, across all assessed emission scenarios, the central estimate for exceeding the 1.5°C global warming threshold is in the early 2030s. In the long-term period (2081–2100), the projected 5–95% range of globally averaged surface air temperature increase is 0.2–1.5°C under a low-emission scenario and 2.7–5.7°C under a high-emission scenario (Lee et al., 2021b).

Radiative forcing of contrail cirrus

Changes in the atmospheric composition and global cloudiness affect the atmospheric energy budget by causing an imbalance between incoming solar radiation (shortwave) and outgoing terrestrial radiation (longwave). This energy imbalance is commonly quantified in terms of radiative forcing (RF) (Prather et al., 1999; Lee et al., 2009; Kärcher, 2018). The effective radiative forcing (ERF) is a metric that includes the rapid responses of the atmosphere, e.g., an adjustment in cloud cover, to a climate forcer (Myhre et al., 2013; Forster et al., 2021). It is the preferred metric that is used in global circulation models (GCMs) (Myhre et al., 2013; Smith et al., 2020; Bickel et al., 2025).

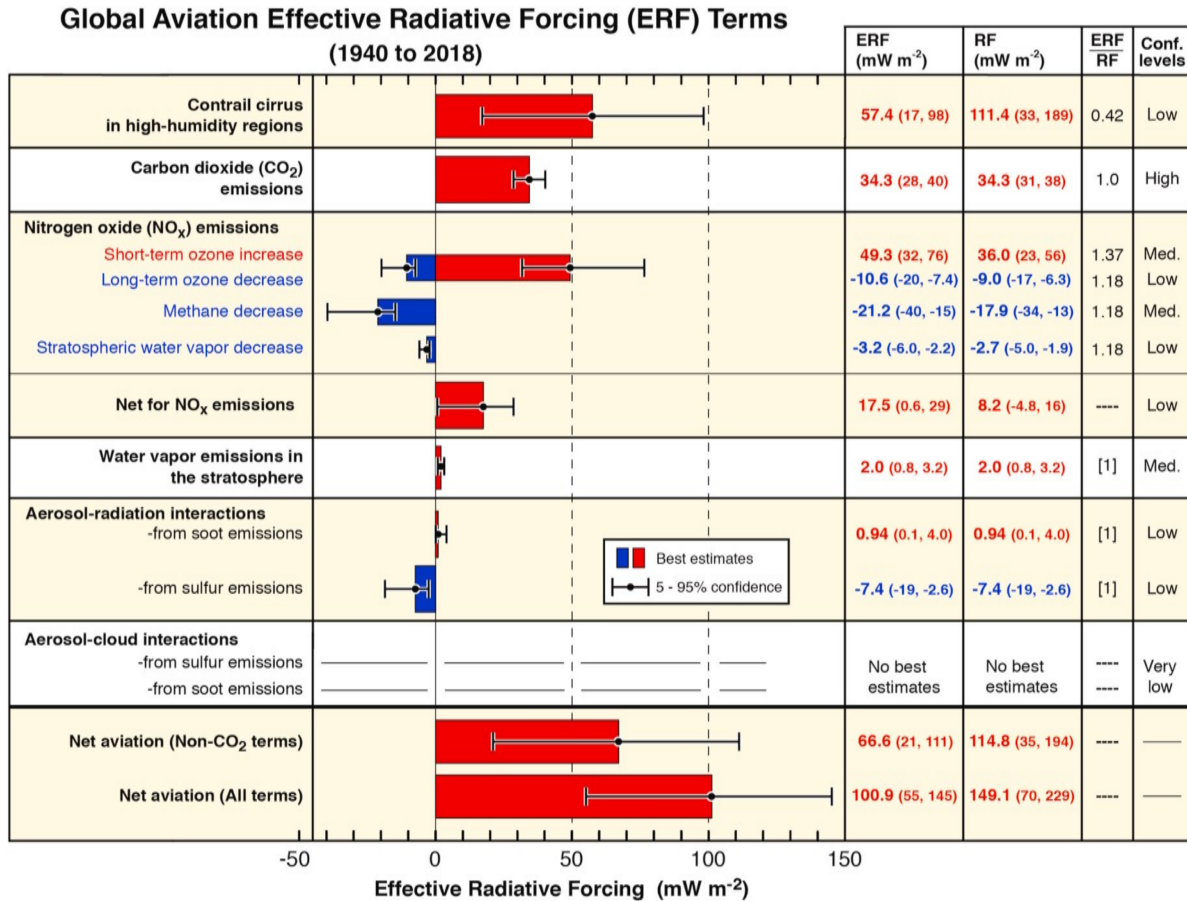


Figure 1.1: Best estimates of effective radiative forcing (ERF) components from global aviation between 1940 and 2018. Bars represent ERF best estimates, while whiskers indicate the 5–95 % confidence intervals of the RF uncertainty scaled to ERF. Red bars correspond to warming contributions, and blue bars to cooling effects. The accompanying table provides numerical values for ERF and radiative forcing (RF), including confidence intervals, ERF-to-RF ratios, and associated confidence levels. Figure taken from [Lee et al. \(2021a\)](#).

Aviation contributes approximately 3.5 % to the total present-day climate forcing through the emissions of soot, NO_x, CO₂, and water vapor, as well as through the formation of contrails and contrail-induced cirrus clouds, so-called contrail cirrus (Lee et al., 2021a, 2023). Contrails are ice clouds that originate from aircraft exhaust in the upper troposphere. Under favorable meteorological conditions, they can persist and evolve into contrail cirrus over the course of several minutes to hours (Schumann, 2005; Burkhardt and Kärcher, 2009; Lewellen et al., 2014; Unterstrasser et al., 2017a). In such cases, we refer to them as long-lived or persistent contrails. Once a contrail has transitioned into contrail cirrus, it often becomes indistinguishable from natural cirrus clouds in satellite or visual observations, as the original line-shaped structure dissipates into an irregular form (Minnis et al., 1998; Heymsfield et al., 2010; Unterstrasser et al., 2017b). This transition occurs when the ambient atmosphere is supersaturated with respect to ice along the flight track. The extent and duration of ice-supersaturated regions, determined by the prevailing synoptic conditions, govern the lifetime and spatial development of contrails (Irvine and Shine, 2015; Kärcher, 2018; Hofer and Gierens, 2025).

Contrails, whether line-shaped or evolved into irregular structures, modify atmospheric cloudiness by introducing an additional anthropogenic cloud type. Their presence may also inhibit the formation or alter the development of natural cirrus clouds, which has been studied by Burkhardt and Kärcher (2011). They showed the RF of contrail cirrus to be roughly nine times larger than that of line-shaped contrails. Earlier assessments (Penner et al., 1999; Lee et al., 2009) considered only line-shaped persistent contrails and did not account for contrail cirrus due to the limited availability of data. The updated analysis by Lee et al. (2021a), shown in Fig. 1.1, incorporates contrail-cirrus effects, using RF and ERF estimates derived from GCM studies (Burkhardt and Kärcher, 2011; Chen and Gettelman, 2013; Schumann et al., 2015; Bock and Burkhardt, 2016a; Bickel et al., 2020).

Figure 1.1 shows the best estimates of ERF from global aviation for the years between 1940 and 2018. Significant contributions stem from contrail cirrus (+57.4 mWm⁻²), CO₂ emissions (+34.3 mWm⁻²), and NO_x emissions (+17.5 mWm⁻²). Stratospheric water vapor and aerosol-radiation interactions exert smaller warming and cooling effects, respectively. The net aviation ERF, accounting for all contributing forcing terms, is estimated at +100.9 mWm⁻², indicating a net warming effect. Of this total, non-CO₂ effects, dominated by NO_x and contrail cirrus, contribute roughly two-thirds of the total aviation ERF. The best estimate for contrail-cirrus ERF is associated with substantial uncertainty, ranging from 17 to 98 mWm⁻². This wide range arises from multiple sources of uncertainty, including the frequency of ice supersaturation in the upper troposphere, the number of ice crystals (which depends on soot particle emissions, ice nucleation processes, and ice particle losses during the vortex phase), as well as uncertainties in the background cloud field, its overlap with contrail cirrus, and the microphysical properties of ice crystals, such as size and habit, which strongly influence the contrail's radiative properties (Lee et al., 2021a).

Contrail mitigation strategies

Global aviation has grown steadily over the last decades and is projected to continue increasing in the coming years. According to the International Civil Aviation Organization (ICAO), annual passenger numbers rose from 1 billion in 1985 to 4.6 billion in 2024, a trend expected to persist. Post-COVID forecast scenarios project a long-term average annual growth rate of 3.4 % in global revenue passenger kilometers through 2050 (ICAO, 2025). Compared to 2023, the International Air Transport Association (IATA) reports that international air traffic in 2024 increased by 13.7 %, reflecting continued recovery from the COVID-19 pandemic. Airlines in the Asia-Pacific region led this growth with a 26.6 % increase, accounting for nearly half of the global growth (IATA, 2025).

Given the projected growth of global aviation, not only an increase in CO₂ emissions but also an increase in contrail-cirrus coverage and occurrence frequency is expected, though assessing their radiative impact on the atmosphere remains associated with large uncertainties. These developments highlight the urgent need to evaluate effective mitigation strategies.

Mitigation options can be divided into two categories (Gierens et al., 2008): operational and technological. Operational mitigation strategies aim to prevent contrails from becoming persistent; contrails that almost immediately sublimate after formation, typically in subsaturated conditions, are insignificant from a climate

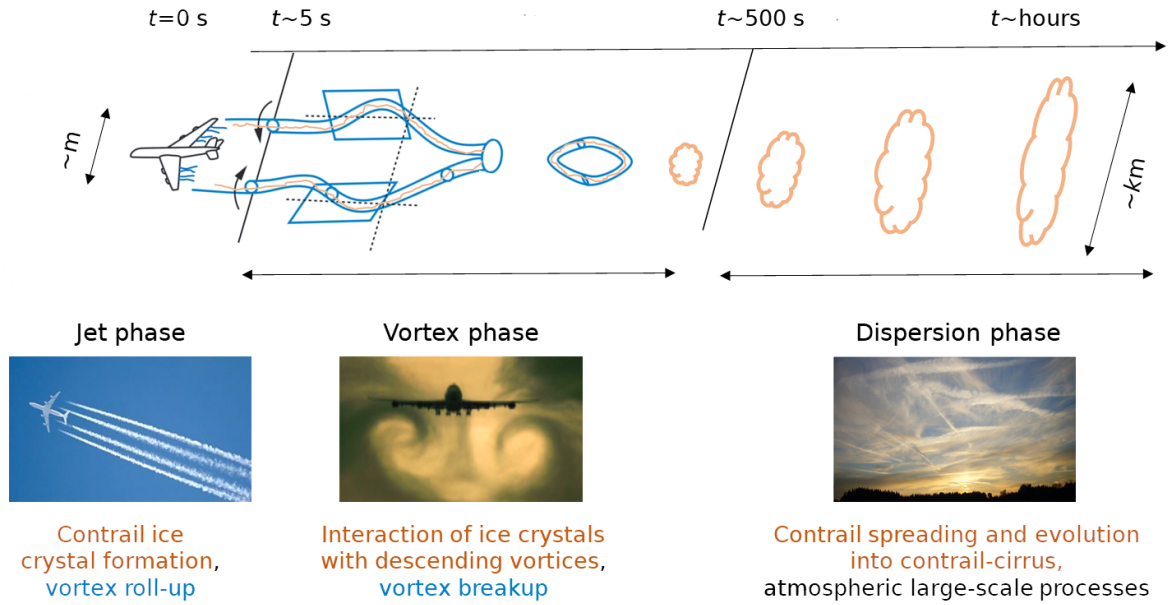


Figure 1.2: Overview of the contrail lifecycle, adapted from Paoli and Shariff (2016). Wake vortices form behind the aircraft and begin to evolve by meandering, linking, and eventually forming vortex rings (shown in blue). As the vortex structure dissipates, the initially trapped ice crystals (highlighted in orange) are released and are exposed to larger-scale atmospheric processes. Photographs by Simon Unterstrasser (MET/IPA).

perspective (Lee et al., 2023). The key criterion determining the climate impact of contrails is whether they are persistent. Therefore, contrail mitigation can be achieved by avoiding ice-supersaturated regions (ISSRs) through flight rerouting (Grewe et al., 2017; Gierens et al., 2020; Sausen et al., 2024; Frias et al., 2024) or by reducing the impact of ISSRs on contrail evolution, for example, through formation flying (Dahlmann et al., 2020; Unterstrasser, 2020; Marks et al., 2021).

Technological mitigation options involve adapting the fuel, engine design and/or propulsion system. Decreasing the water vapor emission and the overall propulsion efficiency and increasing the specific energy would decrease the duration and degree of supersaturation in the plume (Schumann, 1996). As a consequence, fewer ice crystals would form. Furthermore, modeling studies have shown that the size of the formed ice crystals has only a limited influence on the later evolution of contrail cirrus. Instead, the optical thickness of contrail cirrus is primarily governed by the number of ice crystals initially formed (Unterstrasser and Gierens, 2010b; Lewellen et al., 2014; Burkhardt et al., 2018). Reducing this number, e.g., by using alternative fuels with lower aromatic content or hydrogen as an energy carrier, appears to be an effective mitigation approach. The potential of alternative fuels and their implications on contrail evolution are discussed in Sec. 1.3.

1.2 Overview of contrail lifecycle

Contrail formation and evolution occur on a wide range of spatial and temporal scales, beginning with nanometer-sized aerosol particles on which ice crystals form within milliseconds, and developing into kilometer-scale contrail-cirrus clouds that can persist for several hours (Fig. 1.2).

In this thesis, I categorize the contrail lifecycle into three distinct phases: the formation phase, the vortex phase, and the dispersion phase. Each of these phases is described in detail below.

Contrail formation: Thermodynamic processes

The following text is taken almost verbatim from Sec. 2.1 of [Lottermoser and Unterstrasser \(2024\)](#), with only minor adaptations. Figure 1.3 is Fig. 1 from that study.

The formation of contrails depends on various parameters related to engine type and ambient conditions. The constraint that supersaturation with respect to water has to be reached in the jet exhaust plume for contrail ice particles to form was postulated by [Appleman \(1953\)](#) and has evolved into the Schmidt-Appleman-criterion (SA) ([Schmidt, 1941](#); [Schumann, 1996](#)).

After leaving the engine exit, the hot and moist exhaust gases mix with the surrounding air. As the cold ambient air is entrained into the plume, the mixture gradually dilutes and cools ([Schumann, 2005](#); [Kärcher et al., 2015](#)). The magenta lines in Fig. 1.3 depict the plume's thermodynamic evolution in (p_{wv}, T) -space. The endpoints of the lines on the right and left represent exit conditions (outside of the displayed range) and ambient conditions, respectively. In contrail science, we refer to it as "mixing line", and its slope depends on aircraft-related and atmospheric parameters:

$$G = \frac{EI_{H_2O} c_p p_{amb}}{\epsilon Q (1 - \eta)}. \quad (1.1)$$

Here, EI_{H_2O} denotes the fuel's emission index of water vapor, c_p is the specific heat capacity of dry air, p_{amb} is the ambient pressure, Q represents the fuel's specific energy, η is the overall propulsion efficiency, and $\epsilon = 0.622$ is the ratio of the molar masses of water vapor to dry air.

Although initially subsaturated because of high plume temperatures, the mixture reaches or even surpasses saturation typically within tenths of a second for suitable conditions. If the atmosphere is not cold enough, i.e., the ambient temperature is above the Schmidt-Appleman threshold temperature Θ_G , no transient liquid supersaturation (i.e., the relative humidity with respect to water RH_{wat} is larger than 100 %) emerges in the plume, and hence, no contrails form. If ambient conditions meet threshold conditions (in this example, $\Theta_G = T_{amb} = 226$ K), the plume becomes shortly water-saturated (dash-dotted line). In a colder environment ($T_{amb} = 220$ K), liquid supersaturation emerges and persists over a more extended period related to the temperature range where the solid magenta line is above the solid black line. For typical kerosene contrails, plume aerosols, mainly soot particles, are activated into water droplets and grow by condensation of water vapor. The droplets freeze to ice crystals when the plume temperature falls below the homogeneous freezing temperature ([Kärcher et al., 2015](#); [Bier et al., 2022](#)). As contrail ice crystals form via the liquid phase, transient ice supersaturation (i.e., the relative humidity with respect to ice RH_{ice} is larger than 100 %) is not a sufficient criterion for contrail formation. The SA criterion has been confirmed by multiple in-situ measurements ([Busen and Schumann, 1995](#); [Schumann et al., 1996](#); [Petzold et al., 1997](#); [Jensen et al., 1998b](#)).

In its simplest form, the mixing line concept is applied to a spatially uniform exhaust plume with mean thermodynamic properties. However, the concept can be extended, and plume heterogeneity implies that individual plume parcels can have different dilution states that relate to different points on the (same) mixing line. How this is represented in the contrail formation model is discussed in Sec. 2.1. The mixing line concept is solely based on thermodynamic considerations and helps to decide whether or not contrail formation is expected for given ambient and aircraft parameters. However, this binary information is not sufficient for understanding the contrail climate effect, as the purely thermodynamical framework of the SA criterion gives no information about the microphysical and chemical particle formation processes and resulting ice crystal properties. Contrail ice crystal formation involves complex microphysical processes occurring in the engine exhaust plume within milliseconds after emission, which is described in the following.

Contrail formation: Microphysical processes

Microphysics refers to particle physics, including the evolution of several types of aerosols, water droplets, and ice crystals.

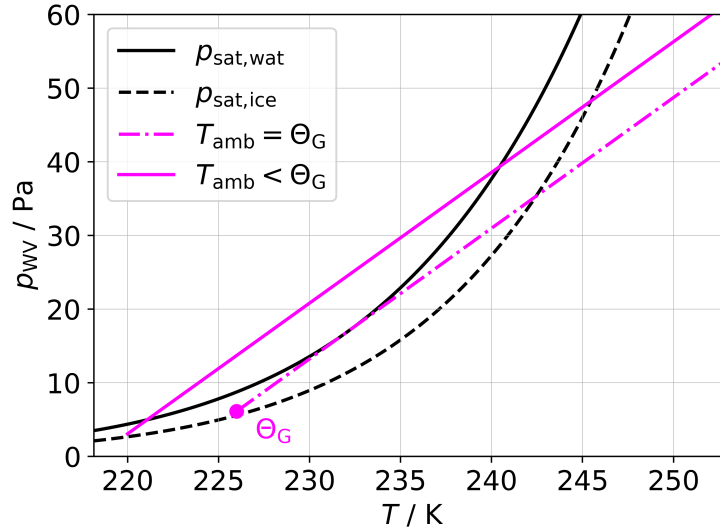


Figure 1.3: Liquid (black solid) and ice (black dashed) saturation curves in a p_{wv} - T -diagram (water vapor partial pressure versus temperature). Mixing lines (magenta curves) for two different ambient temperatures are depicted. In this example, $\Theta_G = 226$ K and $p_{amb} = 240$ hPa.

The particles that act as nuclei for water droplets and subsequent ice crystal formation are diverse. They include soot particles emitted as a direct combustion product, ultrafine volatile particles that nucleate in the exhaust plume before water saturation is reached (Kärcher, 1998), and ambient aerosols entrained from the surrounding atmosphere. These particles compete for available water vapor in the plume, and their relative importance depends on their size, solubility, and abundance. In the so-called soot-rich regime, characterized by a soot emission index exceeding $10^{14} - 10^{15}$ particles per kilogram of burnt fuel, soot particles dominate the activation process, forming the majority of the initial water droplets that can later freeze into ice crystals (Kärcher et al., 2015; Paoli and Shariff, 2016). The largest and most hygroscopic particles activate into water droplets and deplete plume supersaturation due to condensational growth. The homogeneous freezing of the droplets typically occurs between 229 and 232 K. The first droplets to freeze are those formed on large soot particles and water-soluble ambient aerosols. The freezing process marks the transition from a short-lived liquid phase to the formation of ice crystals that constitute the visible contrail (Kärcher et al., 2015). The following provides a brief overview of the particle types that may act as ice nuclei during contrail formation.

Soot particles are formed through the incomplete combustion of hydrocarbons in aviation fuel (Bockhorn, 1994). Despite their low hygroscopicity, soot particles can still activate in highly supersaturated plumes and serve as nuclei for droplet formation (Kärcher et al., 2015).

Fuel combustion also releases condensable vapors such as water vapor, sulfuric acid, nitric acid, and hydrocarbons (Kärcher, 2018). Sulfuric acid is highly water-soluble and plays a key role in the formation of ultrafine volatile particles. Increasing the sulfur content in aviation fuel does not significantly affect the number of these particles formed, but it does lead to an increase in their size (Kärcher et al., 2000; Brock et al., 2000). These particles are in the size range of less than 20 nm and nucleate in the plume on chemions (electrically charged, molecular-sized clusters), generated by chemical reactions during the combustion process. The emission index of the ultrafine volatile particles is found to be around 10^{17} per kilogram of burnt fuel (Yu and Turco, 1997). Laboratory studies have also shown that lubricant oil particles can act as a source of ultrafine volatile particles. Once formed, these particles may serve as condensation nuclei and contribute to ice crystal formation in contrails (Ungeheuer et al., 2022; Ponsonby et al., 2024; Zink et al., 2025). However, the small size of ultrafine particles means they require high supersaturation to activate due to the Kelvin curvature effect, especially in the presence of soot, which otherwise acts as a dominant sink for water vapor and suppresses the activation of smaller particles (Kärcher and Yu, 2009). Therefore, ultrafine volatile particles are expected to contribute to contrail ice crystals only in cases of low ambient temperature,

leading to a large plume supersaturation, and in the low-soot regime, which becomes especially relevant in the context of hydrogen combustion as propulsion type (Kärcher et al., 2015). Recent studies suggest that volatile particles may play a comparatively greater role compared to soot when accounting for plume heterogeneity (Lewellen, 2020) or soot morphology (Yu et al., 2024).

Ambient aerosol properties further influence contrail microphysics. Ambient aerosols in the upper troposphere typically originate from natural and anthropogenic precursor gases transported from lower altitudes (Minikin et al., 2003). In addition, aircraft act as a local source of both particles and precursor gases. According to Righi et al. (2013), aviation contributes approximately 30%–40% of the particle number concentration in the altitude region 7–12 km in the northern mid-latitudes, with increasing impact in high-density air traffic regions. Measurements from campaigns such as SCOUT-O3 and TROCCINOX have revealed substantial variability in aerosol number concentrations at cruise altitudes, ranging from 100 to over 1000 cm^{-3} (Minikin et al., 2003; Borrmann et al., 2010). Ambient aerosols are particularly relevant in soot-poor or transition regimes, where they can serve as activation nuclei for water droplets and ice crystals. In the absence of soot, e.g., in hydrogen combustion scenarios, contrail ice crystals are expected to form primarily on entrained ambient particles. A modeling study by Bier et al. (2024) assumes this, showing lower ice crystal numbers in a hydrogen-fueled case (without soot) compared to a conventional kerosene case. They prescribed aerosol number concentrations between 100 and 1200 cm^{-3} , using a log-normal size distribution with geometric mean dry radii of 3 nm (nucleation mode), 15 nm (Aitken mode), and 50 nm (accumulation mode). Final ice crystal numbers increase with ambient aerosol concentration, but smaller particles contributed less due to their higher Kelvin barrier for activation.

Vortex phase processes

The wake vortex dynamics behind the aircraft strongly affect the ice crystals' evolution after their formation. During cruise, wingtip vortices form as air moves faster over the aircraft's upper wing surface than the lower wing surface, generating a pressure differential, which induces lift. Air from the high-pressure region beneath the wing curls around the wingtips toward the low-pressure region above, creating a rotational motion. This mechanism generates a pair of counter-rotating wingtip vortices, which trail behind the aircraft. In literature, this phase is commonly referred to as the "roll-up" of wake vortices, which typically completes within a few wingspans behind the aircraft. A vortex is characterized by a vortex core, where the vorticity, the local measure of rotational motion, is maximal, and a core radius, defined as the radial distance at which tangential velocity peaks (Gerz et al., 2002). A commonly used analytical description of the tangential velocity profile is the Lamb-Oseen profile (Lamb, 1879). At the stage of finished vortex roll-up, most of the exhaust, including potentially formed contrail ice crystals, is entrained into the vortex system, forming the primary wake (Gerz and Ehret, 1997; Gerz and Holzäpfel, 1999).

The two counter-rotating vortices (in three dimensions, vortex tubes) induce a mutual downward motion, leading to a descent with a speed of typically 2 ms^{-1} . They carry an oval-shaped volume of fluid containing the exhaust gases and ice crystals downward. During the descent, the ambient pressure rises, and the enclosed air undergoes adiabatic compression. Assuming a vertical descent of 400 m, the temperature of the enclosed air rises by about 4 K (assuming an adiabatic temperature increase of 10 K km^{-1}), which leads to an increase in saturation pressure and, eventually, the partial or complete sublimation of entrained ice crystals to maintain equilibrium (Lewellen and Lewellen, 2001a; Unterstrasser and Gierens, 2010a). In-situ observations by Kleine et al. (2018) confirmed the loss of ice crystals in a contrail aged 1–2 min during the vortex phase.

The wake vortex system has a lifetime of several minutes until instabilities develop that lead to vortex decay. These instabilities arise from stratification-induced baroclinic torque, aircraft-induced shortwave, and atmospheric-induced longwave perturbations (Lewellen and Lewellen, 1996; Gerz and Holzäpfel, 1999; Holzäpfel and Gerz, 1999; Picot et al., 2015; Bouhafid et al., 2024). Perturbations across a broad range of wavelengths grow at nearly equal rates in a sinusoidal, exponentially amplifying manner. This growth continues until the vortex tubes interact and reconnect, forming vortex rings, as illustrated in Fig. 1.2. The dominant unstable mode with the largest wavelength is known as the Crow instability, with a characteristic wavelength of $8.6 b_0$, where b_0 denotes the initial vortex separation (Crow, 1970).

The magnitude of ice crystal loss in the primary wake depends strongly on ambient temperature and ambient supersaturation (Unterstrasser, 2014, 2016; Lewellen et al., 2014; Picot et al., 2015). Also, stronger stratification leads to a stronger baroclinic torque at the same height, which leads to faster detrainment and vortex breakup. In a weakly stratified atmosphere, the vortices travel further down, which leads to more substantial sublimation losses of the ice crystals compared to a stably stratified environment (Unterstrasser and Gierens, 2010b; Unterstrasser et al., 2014; Saulgeot et al., 2023).

Furthermore, the aircraft size is important when examining the crystal loss. Larger aircraft generate vortices with a larger core radius that descend further before decaying, owing to stronger vortex circulation and a higher descent speed. Consequently, the relative crystal loss is more substantial for larger aircraft than for smaller ones (Unterstrasser and Görsch, 2014).

Crystal loss is also influenced by the initial microphysical properties of the ice crystals trapped in the primary wake, such as their size and number (Unterstrasser and Gierens, 2010b; Lewellen et al., 2014).

In summary, wake vortex dynamics, influenced by turbulence and ambient- and aircraft-related parameters play a key role in the evolution of the contrail's vertical extent, ice crystal number, and ice mass.

Dispersion phase processes

Once the wake vortices and aircraft-induced turbulence have dissolved, the remaining ice crystals are exposed to atmospheric processes. During the dispersion phase, contrails evolve into contrail-cirrus clouds that may extend horizontally to several tens of kilometers. This transition is strongly impacted by the interaction with the surrounding atmosphere. Wind shear, atmospheric turbulence, and large-scale uplift or subsidence alter the evolution of the contrail's appearance and the microphysical properties of the ice crystals. Wind shear and atmospheric turbulence broaden the contrail (Jensen et al., 1998a). The resulting optical thinning is counteracted by the deposition of ambient water vapor onto the ice crystals under supersaturated conditions. Ice crystals then grow, and the contrail's optical thickness increases (Unterstrasser and Gierens, 2010a). The Kelvin effect promotes the growth of large ice crystals at the expense of smaller ones, which leads to a broadening of the ice crystal size distribution over time (Lewellen et al., 2014; Unterstrasser et al., 2017a). The small ice crystals eventually sublimate, termed as in-situ loss, regardless of ambient conditions (Lewellen et al., 2014). In contrast, large crystals, once they reach sizes of several micrometers, begin to sediment, forming fall streaks composed of relatively few but large ice particles. The sedimenting ice particles can dehydrate the contrail core region, which contains a high concentration of relatively smaller ice crystals (Chlond, 1998; Unterstrasser and Gierens, 2010a). The onset and magnitude of the sedimentation flux primarily depend on the ambient temperature (Lewellen et al., 2014): Higher temperatures, corresponding to a larger amount of ambient moisture, promote faster and more substantial ice crystal growth. In addition to in-situ sublimation and sedimentation, large-scale subsidence processes lead to subsaturated conditions, also limiting the contrail's lifetime (Bier et al., 2017; Hofer and Gierens, 2025).

Contrail internal dynamics is influenced by radiative processes, involving longwave (thermal infrared) and shortwave (solar) radiation (Unterstrasser and Gierens, 2010b; Lewellen, 2014; Paoli et al., 2017). Longwave radiation can either heat or cool the contrail, depending on the thermal regime: Net cooling causes negative buoyancy, descent, adiabatic compression, and ice sublimation; net heating leads to ascent, adiabatic expansion, and ice growth. Thus, longwave radiation can shorten or prolong the contrail lifetime. Shortwave radiation is predominantly scattered by ice crystals, producing weaker heating than longwave radiation, with a strength that varies diurnally and seasonally due to the solar zenith angle (Lewellen, 2014). Interactions between natural cirrus clouds and contrails might play an important role in affecting the evolution of both cloud types. Factors governing natural cirrus evolution include the degree of supersaturation, the concentration of heterogeneous ice nuclei, and the strength of synoptic-scale uplift. While heterogeneous nucleation requires lower supersaturation levels, homogeneous ice nucleation, i.e., the freezing of supercooled solution droplets, is considered the dominant pathway for cirrus formation in the upper troposphere due to the scarcity of heterogeneous ice nuclei (Kärcher and Ström, 2003; Möhler et al., 2006; Sölch and Kärcher, 2011). In a modeling study, Unterstrasser et al. (2017b) found that strong atmospheric uplift, which causes cirrus to form shortly after the contrail, can inhibit contrail spreading and the development of fall streaks. Conversely, under weak uplift conditions, the contrail evolves more freely, while the formation of

natural cirrus is delayed and further suppressed due to water vapor depletion by the contrail. This interaction can reduce overall natural cirrus cloud coverage (Burkhardt and Kärcher, 2011). Because contrails typically contain more and smaller ice crystals than natural cirrus, they exhibit higher optical extinction and may be distinguishable in lidar measurements when embedded within cirrus layers. However, in scenarios where natural cirrus forms near a contrail, ice crystals from one cloud type may fall into the other, making a clear distinction between the two cloud types challenging (Unterstrasser et al., 2017b).

1.3 Alternative aircraft propulsion systems

In the growing awareness of the need to decarbonize the aviation sector and to mitigate the contrail radiative effect, many projects are underway to explore the feasibility and potential of alternative propulsion systems. In this context, "alternative" refers to propulsion methods that do not rely on conventional kerosene-based jet fuel, including sustainable aviation fuels (SAFs), hydrogen, and battery-electric technologies.

SAF as aircraft fuel

SAFs are hydrocarbon fuels that can be produced from renewable sources. Unlike fossil fuels, SAFs are derived either from biogenic feedstocks, such as plants or vegetable oils, or through synthetic production, in which atmospheric carbon is captured and combined with hydrogen (produced via electrolysis) to form hydrocarbons (Schmidt et al., 2018). Over their full lifecycle, from production to combustion, SAFs generally have a lower carbon footprint than conventional jet fuel. However, biogenic SAFs face a significant drawback, as land use emissions from creating new farmland and growing feedstocks can prevent them from achieving net-zero lifecycle emissions (Searchinger et al., 2008; Prussi et al., 2021). In contrast, synthetic SAFs produced using renewable energy are essentially carbon-neutral, making them a highly promising option. Yet, their production remains both energy-intensive and costly (Clean Sky 2, 2020). One major advantage of SAFs as an alternative fuel is their compatibility with existing aircraft engines, requiring only minor or no modifications (Adler and Martins, 2023).

The current supply of SAF remains limited, and production costs are high. In 2024, global SAF output doubled compared to 2023, yet it accounted for only 0.3 % of total aviation fuel consumption. The average price per tonne was about 3.1 times higher than that of conventional jet fuel. According to IATA, SAF is expected to reach 0.7 % of airlines' total fuel use in 2025. Ongoing research and infrastructure development aim to scale up production and distribution and make SAF a commercially viable alternative (IATA, 2025).

Hydrogen as aircraft fuel

Hydrogen, on the other hand, is seen as the most climate-friendly alternative, as its use as aircraft fuel avoids in-flight CO₂ emissions completely (e.g., Verstraete, 2013; Møller et al., 2017; Timmons and Terwel, 2022). Prominent initiatives exploring hydrogen use in aviation include Airbus's ZEROe program (Airbus, 2020), as well as projects like ZeroAvia (ZeroAvia, 2017) and H2FLY (H2FLY, 2019), which focus on hydrogen fuel cells for propulsion. Additionally, several European programs, FlyZero (Debney et al., 2022), Clean Sky 2 Joint Undertaking (Clean Sky 2, 2020), and the Clean Aviation Joint Undertaking (Aviation, 2023), are advancing hydrogen aviation technologies.

Hydrogen has about three times the specific energy by mass compared to kerosene, highlighting its potential as an aircraft fuel where weight is a critical factor (Brewer, 1991). However, its energy density by volume is roughly four times lower than that of kerosene, posing significant storage challenges. To achieve practical energy densities, hydrogen must be either compressed or liquefied (Adler and Martins, 2023). Liquefaction requires cooling to around -250°C , necessitating advanced cryogenic tanks with efficient heat management systems, including insulation and materials resistant to embrittlement (Moody and Thompson, 1990; Verstraete, 2013). Additionally, the larger and differently shaped tanks mean they must be located inside the aircraft fuselage rather than in the wings, as is typical for kerosene storage (Cecere et al., 2014).

Hydrogen can be used as aircraft fuel either through combustion to power turboprops or turbofans, or in fuel cells that convert chemical energy into electrical energy. Both propulsion types are briefly outlined below. Existing kerosene-based turbomachinery can be modified to burn hydrogen, but the combustor and fuel supply systems require adaptations due to hydrogen's different combustion properties (Brand et al., 2003). Hydrogen's wider flammability limits enable leaner combustion with lower flame temperatures. Additionally, hydrogen burns faster, reducing the residence time (the time the air-fuel mixture spends in the combustor). The lower flame temperature and shorter residence time lead to reduced NO_x emissions (Khandelwal et al., 2013). Another advantage is that the gas entering the turbine is cooler, which can extend turbine lifetime and reduce maintenance frequency (Adler and Martins, 2023).

A widely studied fuel cell type is the polymer electrolyte membrane fuel cell (PEMFC), in which hydrogen molecules are electrochemically dissociated at the anode into protons and electrons. The electrons generate an external electric current that can be utilized to drive electric motors for propelling a propeller or ducted fan. Concurrently, the protons migrate through the polymer electrolyte membrane to the cathode, where they react with oxygen molecules to produce water as the only byproduct (Dicks and Rand, 2018). The efficiency of a fuel cell decreases as the current density (current per fuel cell area) increases. Fuel cells can achieve overall propulsion efficiencies of up to 60 % (Kazula et al., 2023). However, their relatively low specific power makes it challenging to scale them for the high-power demands of long-range aviation (Brelje and Martins, 2019). As a result, current assessments suggest that fuel cells are best suited for short-range aircraft, whereas hydrogen combustion remains more promising for large, long-range aircraft due to the higher specific power and lower thermal management requirements of turbomachinery (Verstraete, 2013; Adler and Martins, 2023).

SAF- and hydrogen-contrails

"SAF-contrails" or "hydrogen-contrails" are short for "contrails that form behind SAF- or hydrogen-powered aircraft" (but do not consist of SAF or hydrogen). As contrails are the most uncertain and potentially the most significant contributor to aviation's climate impact, studying the effect of alternative fuels on contrail properties is an ongoing research topic.

The fuel and combustion properties of SAF are broadly comparable to those of kerosene, though with a potentially slightly higher water vapor emission index (Teoh et al., 2022). Consequently, the SA mixing line slope is expected to be similar to that of kerosene. At the same time, recent measurement campaigns have demonstrated the potential of SAF to reduce particle emissions and contrail ice crystal numbers. In particular, during the ECLIF campaigns, the emissions and ice crystal numbers behind aircraft powered by SAF blends were measured (Bräuer et al., 2021; Voigt et al., 2021; Märkl et al., 2024; Dischl et al., 2024). Owing to their lower aromatic content compared to conventional Jet A-1, SAFs generate fewer soot particles during combustion (Moore et al., 2017). For example, Märkl et al. (2024) reported that an Airbus A350-941 operating on 100 % SAF emitted 35 % fewer soot particles, resulting in a 56 % reduction in contrail ice crystal numbers.

Based on molecular weights, the emission index of water when using hydrogen as aircraft fuel is 8.94 kg water per kg hydrogen used. For kerosene, the value is 1.26 kg water per kg kerosene used, reflecting the fact that the mass of hydrogen constitutes only 15 % of the total kerosene fuel mass (for hydrogen it is 100 %). The exact water vapor emission index for kerosene depends on the H:C ratio of the hydrocarbon chains. Thus, on a mass basis, hydrogen produces about 7.1 times more water vapor than kerosene. Hydrogen has a specific energy of 120 MJ per kilogram fuel compared to 43 MJ per kg fuel for kerosene, giving a ratio of 2.79. Consequently, the energy-specific water emission index for hydrogen is 2.57 times higher.

From a thermodynamic perspective, this results in a mixing line slope 2.57 times greater for hydrogen compared to kerosene (assuming equal overall propulsion efficiency). Supersaturation in the exhaust plume can then be reached at ambient temperatures around 10 K higher than in the kerosene case, allowing contrail formation more frequently and at lower altitudes (Schumann, 1996; Bier et al., 2024). This effect was already documented in 1957, when a NASA test aircraft with one hydrogen-burning and one kerosene-burning engine produced a contrail solely behind the hydrogen engine (Sloop, 1978). Under identical ambient conditions, the steeper mixing line for hydrogen leads to an earlier crossing of the water saturation curve, resulting in

longer durations and peak values of supersaturation in the plume. If the number of nucleation sites were the same as for kerosene, this would produce more and/or larger ice crystals. However, hydrogen combustion emits neither soot particles nor sulfate aerosols, greatly reducing the number of available ice nuclei (Kärcher et al., 2015). Fewer nucleation sites can yield fewer ice crystals, potentially lowering optical thickness and shortening contrail lifetimes, thereby reducing their warming effect (Bier et al., 2017; Bock and Burkhardt, 2019; Burkhardt et al., 2018).

For hydrogen fuel-cell propulsion, exhaust conditions may differ from hydrogen combustion. While fuel cells and combustion systems have the same specific energy and water vapor emission index, external cooling of fuel cell systems via heat exchangers can lower the exhaust temperature. Water vapor in the cathode exhaust can approach saturation (Adler and Martins, 2023), making condensation and droplet formation possible before emission. During the mixing process with the ambient air after emission, the initially cooler fuel cell plume can reach supersaturations up to 2000 %. Under such conditions, homogeneous droplet nucleation (HDN) is likely (personal communication with Dennis Hillenbrand, MET/IPA), a process where water droplets spontaneously form without the need for a nucleus. It becomes relevant for supersaturation values above 500 % (Wölk and Strey, 2001). This could potentially lead to the spontaneous formation of numerous water droplets and, subsequently, a high concentration of ice crystals (Jansen and Heymsfield, 2015). Given the lack of detailed contrail formation simulations and measurements of hydrogen fuel cell plumes, the role of HDN in fuel cell exhaust plumes is not yet understood.

1.4 Research goal of the thesis

Contrail formation is well understood for kerosene-powered aircraft with typical engine and exhaust plume characteristics. Likewise, contrail evolution during the vortex and dispersion phases has been studied in detail for the conventional kerosene case (see Sec. 1.2).

In contrast, contrail formation and evolution differ when alternative fuels or propulsion systems are used. During formation, other particle types become relevant, such as volatile particles originating from combustion products and entrained ambient aerosols. In addition, changes in aircraft and engine characteristics influence plume dynamics and thermodynamic evolution. For example, SAF or hydrogen combustion is likely to be applied in smaller, regional aircraft, which operate with reduced engine size, aircraft speed, and jet velocity. A potential fuel cell configuration would differ even more fundamentally, as it produces no exhaust jet with velocities of several hundred meters per second.

Regarding the contrail lifecycle, large-scale modeling studies (Gruber et al., 2018; Bier and Burkhardt, 2022) have shown that incorporating vortex phase ice crystal loss leads to significant changes in contrail properties at regional and global scales. To estimate the RF of contrail cirrus, GCMs with grid resolutions of several hundred kilometers rely on parameterizations derived from high-resolution, small-scale models for contrail initialization. For instance, the GCM ECHAM-CCMod incorporates parameterizations for ice nucleation from Kärcher et al. (2015) and ice crystal loss during the vortex phase from Unterstrasser (2016) (Bier and Burkhardt, 2019, 2022). Therefore, the continuous evaluation and improvement of these high-resolution, small-scale models are crucial for enhancing the accuracy and reliability of results derived from large-scale GCMs (Paoli and Shariff, 2016; Kärcher, 2018). Adapting initial ice crystal properties to account for alternative fuels and propulsion systems is therefore essential for assessing contrail properties and their radiative impact. Moreover, Sec. 1.3 outlined that hydrogen combustion may enable contrail formation at higher ambient temperatures, which must also be considered in this context.

The goal of this thesis is thus to advance the understanding of contrail formation under alternative fuels and propulsion systems and to provide detailed insight into the subsequent evolution of individual contrail(-cirrus) behind such aircraft. To structure this research goal, the thesis is organized along the three main contrail phases, formation, vortex, and dispersion, each associated with a dedicated research question:

How can the altered aircraft and engine characteristics associated with alternative fuel use be evaluated in terms of their impact on the dynamical and thermodynamic evolution of the exhaust plume?

How does the use of alternative fuels affect contrail evolution during the vortex phase, in particular the number of surviving ice crystals? Is the existing ice crystal loss parameterization, developed for kerosene scenarios, still be applicable to alternative fuel cases?

How do contrail-cirrus properties respond to the use of alternative fuels during the dispersion phase, and how does this depend on the prevailing meteorological conditions?

To address these questions, Chapters 2, 3, and 4 present results from publications produced during my PhD. Each chapter corresponds to one of the three contrail phases. At the time of writing this thesis, the publications on the formation and vortex phases are published, while the paper on the dispersion phase is under revision.

Chapter 2 focuses on the contrail formation phase. It presents the development of a new model component, RadMod, which extends the existing model used for simulating ice crystal formation. Previously, the contrail formation model relied on externally prescribed data to represent plume evolution. RadMod was developed to improve this representation by numerically solving the underlying advection-diffusion equations governing the plume's (thermo-)dynamical evolution. Section 2.3 presents a purely dynamical application of RadMod, simulating the dilution of aircraft plumes and comparing simulated with observational data. Section 2.4 outlines ongoing work, particularly the coupling of RadMod with the existing contrail formation model.

Chapter 3 addresses the vortex phase, with a particular focus on the impact of hydrogen propulsion systems on ice crystal loss during the wake vortex descent. The existing parameterization of ice crystal loss was reviewed and updated for the hydrogen scenarios.

Chapter 4 builds directly on the publication presented in the previous chapter and explores the dispersion phase, during which the contrails from hydrogen-propelled aircraft transition into contrail cirrus. A broad parameter range is explored, encompassing variations in meteorological, aircraft-related, and propulsion-related parameters.

Chapters 2 and 3 provide an introduction to the model used for the respective phase. Since the model used in Chapter 4 is already introduced in Chapter 3, no separate model introduction is provided there.

Chapter 5 addresses the research questions formulated above and outlines potential directions for future work.

Appendices A1-A4 contain the appendices and supplements of the three publications. Appendix A5 summarizes the findings of a Bachelor's thesis and an internship that I supervised during my PhD. These studies examine how different approaches to wake vortex initialization, such as varying the number of exhaust plumes or replacing the default analytical flow field with one obtained from Reynolds-Averaged Navier-Stokes (RANS) simulations, affect contrail evolution, scrutinizing the implications of some assumptions used in the contrail vortex phase simulations of Chapter 3.

2

Extension of Contrail Formation Model

Section 2.1 provides a general overview of the model, called Lagrangian Cloud Module (LCM), that is used to perform contrail formation simulations. It also discusses the main limitation of a box model approach and outlines potential avenues for improvement.

Section 2.2 is an excerpt of the publication *Lottermoser A. and Unterstrasser S. (2024). Towards intermediate complexity modelling of contrail formation: the new dynamical framework RadMod. Aeronaut. J., 129(1332):351–379. DOI: 10.1017/aer.2024.130*. Only minor formatting adjustments and rephrasings were made to ensure consistency with the thesis.

Plume dilution simulated with RadMod is examined in Sec. 2.3, and Sec. 2.4 discusses future developments of RadMod, in particular its coupling with LCM.

The studies presented in this chapter relate to Research question 1 (see Sec. 1.4), which examines how changes in aircraft and engine characteristics associated with the use of alternative fuels can be evaluated in terms of their impact on the dynamical and thermodynamic evolution of the exhaust plume.

2.1 Introduction to the LCM box model

Simulating contrail formation, i.e., the formation of ice crystals in the expanding exhaust plume behind an aircraft, requires modeling both microphysical and (thermo-)dynamical processes. These are described in the following.

LCM microphysics

The microphysical processes are simulated using the LCM, as described in [Sölch \(2008\)](#) and [Sölch and Kärcher \(2010\)](#). LCM includes routines for aerosol activation into droplets, homogeneous freezing of water droplets into ice crystals, depositional growth of ice particles, and sedimentation. In its first application, LCM was coupled to the large-eddy simulation (LES) model EULAG, forming the EULAG-LCM model version, to simulate cirrus clouds ([Sölch and Kärcher, 2010](#)). Later, LCM was also used for simulations of young and aged contrails ([Unterstrasser et al., 2014, 2017a,b; Unterstrasser, 2020](#)). For contrail formation studies, LCM was extended to also cover the formation of contrail ice crystals on emitted soot particles ([Bier et al., 2022](#)), on entrained ambient aerosols in the framework of hydrogen propulsion ([Bier et al., 2024](#)), and also on lubrication oil droplets ([Zink et al., 2025](#)). In those studies, LCM is used in a box model version.

In the particle-based approach of LCM, the particles are represented by simulation particles (SIPs). LCM distinguishes between three particle classes: aerosols, water droplets, and ice crystals. If the Schmidt-Apleman-criterion is fulfilled (see details in Sec. 1.2), water saturation in the aircraft plume is surpassed,

and ice crystal formation is possible. In LCM, aerosols are activated into water droplets if the plume water relative humidity exceeds the equilibrium saturation ratio over the droplet surface S_K , which is given by the κ -Köhler equation (Petters and Kreidenweis, 2007).

The procedure in LCM is the following. At each time step, the condensation and deposition processes are evaluated, ensuring conservation of the total water mass of all three phases (vapor, liquid, solid) in the system. The water partitioning changes during the simulation; water vapor from the environment condenses and deposits onto the SIPs based on the diffusional growth equation for liquid droplets and ice crystals, resulting in a decrease in water vapor in the ambient and an increase in water contained within the SIPs over time. The amount of water mass that has condensed or deposited, expressed as a change in specific humidity, is given by

$$R_q = \frac{-\Delta M_{\text{SIP}}}{\rho_{\text{amb}} V_{\text{box}} \Delta t}, \quad (2.1)$$

where ΔM_{SIP} is the change in total water mass contained in all SIPs, ρ_{amb} is the air density, V_{box} is the volume of the box, and Δt is the model time step. The phase changes condensation and deposition come along with the release of heat, and the phase changes evaporation and sublimation come along with the absorption of heat. The change in temperature due to these phase changes is calculated by

$$R_T = \frac{L_c \Delta M_{\text{WV,c}} + L_d \Delta M_{\text{WV,d}}}{c_p \rho_{\text{amb}} V_{\text{box}} \Delta t}. \quad (2.2)$$

c_p is the specific heat capacity of moist air, and $\Delta M_{\text{WV,c}}$ and $\Delta M_{\text{WV,d}}$ are the water vapor mass that has condensed/evaporated and deposited/sublimated, respectively. R_q and R_T serve as source terms for Eqs. 2.5 or, in the new approach, for RadMod, as further elaborated in Sec. 2.4.2.

Each SIP carries a flag that identifies whether it represents an aerosol (phase = 0), a water droplet (phase = 1), or an ice crystal (phase = 2). This allows LCM to track the number of aerosols, droplets, and ice crystals over time and to apply the correct equations. The model outputs time-resolved particle numbers, size and mass distributions, and contrail optical properties.

Plume dilution and thermodynamic evolution in a box model approach

As the aircraft exhaust mixes with the surrounding atmosphere, the plume expands and entrains ambient air. This entrainment modifies the thermodynamical properties and evolution of the plume; as the plume ages, its exhaust gas concentrations and temperature gradually approach those of the ambient air. The mixing process is referred to as dilution, which quantifies the fraction of plume air relative to ambient air at a given time. The dilution factor $\mathcal{D}(t)$ is expressed through the temporal evolution of the mixing ratio of a passive tracer χ (Kärcher, 1995)

$$\mathcal{D}(t) = \frac{\chi(t) - \chi_{\text{amb}}}{\chi_E - \chi_{\text{amb}}}. \quad (2.3)$$

A passive tracer is a quantity whose evolution is solely determined by plume dynamics; it is transported through the plume via advective and diffusive processes, but its physical properties, such as composition, remain unchanged. An example is an exhaust gas that is unaffected by microphysical and chemical processes during plume evolution. $\chi(t)$ represents the mixing ratio of a passive tracer at a specific time t , χ_E refers to the condition at engine exit, and χ_{amb} is the ambient tracer mixing ratio. By definition, the dilution factor is at maximum at the engine exit ($\mathcal{D}(t_0) = 1$) and then declines with increasing plume age ($\mathcal{D}(t) < 1$).

$\mathcal{D}(t)$ relates to the entrainment rate $\omega(t)$ via (Kärcher, 1995; Bier et al., 2022)

$$\omega(t) = -\frac{d \ln \mathcal{D}(t)}{dt}. \quad (2.4)$$

Box models are typically zero-dimensional (0D) and computationally inexpensive, which makes them advantageous compared to 3D RANS or LES plume models when exploring a multi-parameter space. In a

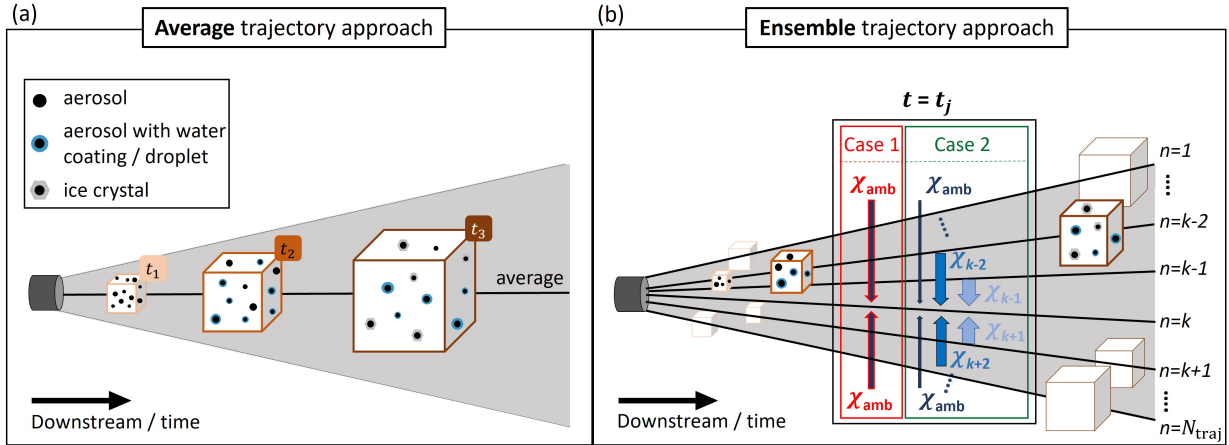


Figure 2.1: Illustration of contrail formation as simulated with the box model. (a) A particle-containing box, shown in orange, follows the plume evolution along the average trajectory representing the mean dilution state. Microphysical processes occurring inside the box are displayed. (b) Plume evolution represented by N_{traj} spreading trajectories in an ensemble trajectory approach. In "Case 1", undiluted ambient air is entrained into the plume. In "Case 2", the dilution state of the k^{th} trajectory is determined not only by the contribution from the ambient air but also, more importantly, by the dilution states of all the other trajectories in addition to the ambient air.

0D box model approach, illustrated in Fig. 2.1a, $\chi(t)$, and therefore $\omega(t)$ via Eq. 2.4, is externally prescribed from a-priori data, for example, from RANS or LES simulations of an expanding and cooling aircraft plume. This data representing the dynamical plume evolution can be averaged to obtain the plume's mean state. The mean state is then represented by a trajectory that describes the plume's mean dilution evolution (black line in Fig. 2.1a).

A box containing particles moves downstream, while the box volume increases according to \mathcal{D}^{-1} . The evolution of water vapor mass mixing ratio m_{WV} and temperature T inside the box is then given by

$$\frac{dm_{\text{WV}}(t)}{dt} = -\omega(t) (m_{\text{WV}}(t) - m_{\text{WV,amb}}) + R_{m_{\text{WV}}} \quad (2.5)$$

$$\frac{dT(t)}{dt} = -\omega(t) (T(t) - T_{\text{amb}}) + R_T. \quad (2.6)$$

Using the same $\omega(t)$ in both equations assumes that mass and heat diffuse at an equal rate, i.e., the Lewis number is 1. At each time step, the microphysical processes inside the box are simulated, including the activation of aerosols into droplets and their freezing into ice crystals (Fig. 2.1a). These processes, in turn, modify the humidity and temperature through latent heating and condensation or deposition, which enter the above equations via the source (or sink) terms $R_{m_{\text{WV}}}$ and R_T . A detailed overview of the microphysical aspects is provided in the next section. The above equations can, in principle, be applied to any species in the evolving plume (Kärcher, 1995).

Plume heterogeneity: Ensemble trajectory approach

Instead of prescribing dilution with a single average trajectory, a full set of plume-sampling trajectories can be used, as shown in Fig. 2.1b (black lines with labels n). For clarity in the illustration, the trajectories are simplified; in reality, RANS- or LES-derived trajectories are not straight and may intersect due to advective and diffusive processes. Similar to panel (a), microphysical processes are calculated in the boxes following the trajectories, illustrated in panel (b) for one example trajectory. This ensemble (multi-0D) trajectory approach captures the spatial heterogeneity in the plume: the trajectories representing the plume edge cool and dilute more quickly than those in the center. Consequently, supersaturation is reached earlier at the

edge, leading to radially distributed ice nucleation events. Effectively, this means that ice crystals form first at the plume edge and later at the plume center (in the average trajectory approach, all particles experience the same temperature and humidity at a given time). Using the ensemble approach with 25000 trajectories from 3D LES simulations, provided by [Vancassel et al. \(2014\)](#), [Bier et al. \(2022\)](#) found a more gradual increase in ice crystal number compared to the pulse-like nucleation in the average trajectory approach.

The drawback when using the ensemble trajectory approach is the following. Analogously to the 0D box model approach, but now for each trajectory individually, the dilution and the entrainment rate are calculated via Eq. 2.3 and Eq. 2.4, respectively. However, this implies that each trajectory only communicates with the ambient air, since Eq. 2.3 prescribes decreases in water vapor and temperature solely through the entrainment of undiluted ambient air. This is showcased by the red-framed "Case 1" scenario in Fig. 2.1b, which illustrates how dilution is currently represented in the box model approach.

However, the decrease in water vapor and temperature results from radial mixing across all trajectories (green-framed "Case 2" scenario). The dilution at trajectory k is determined by contributions from all trajectories (blue arrows). Since the direct neighbors of trajectory k are only weakly diluted due to their proximity to the center/large radial distance to the plume edge, their entrainment rate at k must be larger to achieve the same dilution as in the "Case 1" scenario. This is illustrated by the varying arrow thicknesses.

The simplification illustrated by "Case 1", as used in the box model approach, introduces major drawbacks on contrail formation, i.e., regarding microphysical processes of droplet activation and ice crystal nucleation. Microphysical computations are performed for each trajectory separately. As in each time step unprocessed, ambient air is entrained into the plume, the inter-trajectory communication is neglected. In this "offline approach", the feedback of microphysical processes during the radial mixing process is neglected, so particles at a given downstream position "see" microphysically unprocessed air in the radial direction. By contrast, in an "online approach", particle-induced variations in temperature and humidity influence the thermodynamical fields. For example, a box near the plume edge is cooler and reaches supersaturation earlier compared to the plume center region, leading to aerosol activation. In a box closer to the plume center, mixing would, without microphysics, bring in cold, moist air from the ambient, but because condensation in the boxes further out has already reduced water vapor and released latent heat, activation is suppressed. Hence, ice crystal formation is hampered. Moreover, the "online approach" also accounts for particle diffusion (aerosols, droplets, and ice crystals) between the boxes, which alters microphysical processes in the boxes they are transported to.

As a result of the missing communication between the trajectories in a multi-0D "offline approach", ice crystal numbers tend to be overestimated compared to 3D simulations with fully-coupled (online) microphysics ([Lewellen, 2020](#); [Bier et al., 2022](#)). This limitation is particularly relevant when considering alternative propulsion systems. As shown by [Bier et al. \(2024\)](#), in the case of hydrogen combustion, where soot and volatile particle emissions are assumed to be absent, contrail ice crystals solely form on entrained ambient aerosols. If volatile particles are emitted or form early in the plume (as may occur with hydrogen propulsion), these particles compete with ambient aerosols for the limited humidity within the plume. Unlike particle emissions, which occur once, ambient aerosols are continuously entrained into the plume. Aerosols entering at the plume edge and moving inward can deplete the water vapor before reaching the center through radial mixing processes. Consequently, emitted particles near the center may no longer find sufficient water vapor for activation and growth. On the other hand, in case of high exhaust particle concentrations, emitted particles might deplete water vapor at the center before late-time entrained ambient aerosols can be activated. The missing competition between exhaust and entrained particles in a box model is found to cause an overestimation in the final ice crystal number ([Lewellen, 2020](#)).

To address this, our future goal with the coupled model RadMod-LCM is to simulate jet dynamics explicitly instead of relying on fixed LES-based trajectories. We will dynamically simulate the effect of advection and diffusion on plume temperature and humidity, as well as on the radial re-distribution of the particles, while simultaneously calculating the microphysics with LCM. The dynamical model component RadMod is introduced in the following.

Ambient conditions	Engine properties	jet properties at engine exit
$T_{\text{amb}} = 225 \text{ K}$ $p_{\text{amb}} = 260 \text{ hPa}$ $RH_{\text{amb,ice}} = 120 \%$	$EI_{\text{H}_2\text{O}} = 1.26 \text{ kg kg}^{-1}$ $Q = 4.3 \times 10^7 \text{ J kg}^{-1}$ $\eta = 0.36$ $m_C = 0.0031 \text{ kg m}^{-1}$	$A_E = 0.25 \pi \text{ m}^2$ $C_E = 75$ $U_J = 271 \text{ m s}^{-1}$ $T_E = 549 \text{ K}$ $m_{\text{WV,exc}}(T_E) = 0.030$

Table 2.1: Baseline parameters used in our simulations

2.2 Towards intermediate complexity modeling of contrail formation: the new dynamical framework RadMod

The following Sects. 2.2.1–2.2.4 correspond to Sects. 2–5 of Lottermoser and Unterstrasser (2024). Section 2.2.1 presents the methods used to develop RadMod, Sec. 2.2.2 describes the results, Sec. 2.2.3 provides a discussion, and Sec. 2.2.4 concludes. The nomenclature for these sections is provided at the end of Sec. 2.2.4.

2.2.1 Methods

In this study, we choose the initial temperature and water vapor mixing ratio such that the total heat and water vapor content resemble that of a typical aircraft exhaust plume. We use the dilution formulae presented in Bier et al. (2024). The initial plume air-to-fuel ratio is

$$C_E = \frac{Q(1-\eta)}{\bar{c}_p(T_E - T_{\text{amb}}) + 0.5U_J^2}. \quad (2.7)$$

The values for the specific heat of combustion Q (also known as lower calorific or heating value) and the overall propulsion efficiency η are listed in Tab. 2.1.

We solve Eq. 2.7 for the jet exit temperature T_E by assuming an initial air-to-fuel ratio of $C_E = 75$ and an initial energy partitioning of 90 % (thermal) and 10 % (kinetic) energy. In the second step, we derive the initial jet excess velocity U_J . With commonly used values (see Tab. 2.1), we obtain $T_E = 549 \text{ K}$ and $U_J = 271 \text{ m s}^{-1}$. In general, a jet excess quantity is defined such that $c_{\text{excess}} = c_{\text{total}} - c_{\text{ambient}}$ for a generic variable c , i.e., "excess" means "subtraction of the background". Hence, $U_{\text{exc}} = U_{\text{tot}} - U_{\infty}$ where U_{∞} is the free-stream (or, equivalently, coflow) velocity.

The water vapor mixing ratio m_{WV} is defined as the ratio of the density of water vapor over the density of dry air. The initial excess value $m_{\text{WV,exc}}(T_E)$ is given by

$$m_{\text{WV,exc}}(T_E) = \frac{M_{\text{WV}}}{A_E \rho_{\text{dry}}} \quad (2.8)$$

$$= \frac{R EI_{\text{H}_2\text{O}} m_C}{A_E p_{\text{amb}}} T_E. \quad (2.9)$$

The total amount of water vapor M_{WV} per meter of flight path is the product of the emission index of water vapor $EI_{\text{H}_2\text{O}}$ and the fuel consumption per meter of flight path m_C , whose values are listed in Tab. 2.1. Moreover, we assume that the contribution of the water vapor partial pressure to the total ambient pressure can be neglected (i.e., $p_{\text{amb}} \approx p_{\text{dry}}$). We obtain $m_{\text{WV,exc}}(T_E) = 0.030$. The initial water vapor in the environment $m_{\text{WV,amb}}$ represents a relative humidity with respect to ice $RH_{\text{amb,ice}} = 120 \%$, which corresponds to a value of $RH_{\text{amb,wat}} < 100 \%$. Ice supersaturation (i.e., $RH_{\text{amb,ice}} > 100 \%$) is a common phenomenon in the upper troposphere (Gierens et al., 1999) and supports the formation of climate-relevant contrail cirrus (Bock and Burkhardt, 2016a; Unterstrasser et al., 2017a).

2.2.1.1 Basic knowledge on jet spreading and flow rates

In general, the evolution of a round free jet is divided into different axial regions (Lee and Chu, 2003; Ball et al., 2012). The near field represents the section of flow establishment extending from the jet nozzle to x_{pc}/d , where x_{pc} is the potential core length. The potential core is the region close to the source where the surrounding fluid has not penetrated the jet's central axis. Therefore, the jet at the centerline is not yet affected by diffusion (Lee and Chu, 2003; Ball et al., 2012). The potential core thickness decays linearly with x as the mixing zone surrounding the potential core, also termed the shear layer, spreads towards the jet center (Lee and Chu, 2003). The near and intermediate fields are characterized by the development and interaction of eddies formed in the shear layer (Ball et al., 2012; Khorsandi et al., 2013) caused by the initial strong shear between jet and environment (Or et al., 2011). The shear layer continues to grow laterally. Within the zone of established flow, i.e., in the far field, experiments revealed that the mean flow is fully developed and exhibits self-similar behavior (Wyganski and Fiedler, 1969; Panchapakesan and Lumley, 1993a; Hussein et al., 1994). Self-similarity can be understood as a state of dynamic equilibrium (Richards and Pitts, 1993) and has been observed for both constant- and variable-density jets (Djeridane et al., 1996; Charonko and Prestridge, 2017). It is characterized by a spreading of the jet while the centerline velocity $U_0(x) = U(x, r = 0)$ decreases as the axial distance from the jet nozzle increases.

In the case of a free jet, i.e., the ambient is stagnant with $U_\infty = 0 \text{ m s}^{-1}$ ($U = U_{exc} = U_{tot}$), the centerline velocity decays linearly with downstream distance and is given by (Hussein et al., 1994; Pope, 2000; Lipari and Stansby, 2011)

$$\frac{U_J}{U_0(x)} = \frac{1}{B} \frac{x - x_0}{d}, \quad (2.10)$$

where B is the decay constant and x_0 is the virtual origin. A hypothetical jet exhibiting self-similar behavior right from the beginning originates at the virtual origin. Hence, the virtual origin is the projected location of the onset of a self-similar jet with zero dimension (Or et al., 2011). Note that Eq. 2.10 is only valid for a free jet in the region of self-similarity (Ball et al., 2012).

The linear spreading behavior in a free jet is governed by (Djeridane et al., 1996; Ball et al., 2012)

$$\frac{r_{0.5}(x)}{d} = S \frac{x - x_0}{d}, \quad (2.11)$$

where S represents the spreading rate. The parameter $r_{0.5}(x)$ is defined as the radius at which the axial velocity decreases to half of its centerline value U_0 and is referred to as the velocity half-width radius. In other words, $r_{0.5}(x)$ can be understood as a proxy of the jet's width. The constants B and S are independent of the jet's Reynolds number (Pope, 2000).

The turbulent diffusion coefficient, introduced in Eq. 2.22, is connected to the centerline excess velocity and velocity half-width radius through the empirical relation

$$D_T(x) = \hat{D}_T U_{exc,0}(x) r_{0.5}(x), \quad (2.12)$$

where \hat{D}_T was observed to be within 15 % of 0.028 in $0.1 < r/r_{0.5}(x) < 1.5$, where the value of 0.028 was derived from experiments (Pope, 2000). In the case of a free jet, the product of $U_{exc,0}(x)$ and $r_{0.5}(x)$ becomes independent of x once the jet reaches its self-similar state because then, $U_{exc,0}(x)$ scales with x^{-1} , and $r_{0.5}(x)$ scales with x . Eqs. 2.10 and 2.11 hold only in the scenario without a coflow, and Sec. 2.2.2.3 reports on the axial dependencies in the case of a coflowing jet.

The mass flow rate is given by (Sforza and Mons, 1978; Khorsandi et al., 2013)

$$\dot{m}(x) = 2 \pi \int_0^\infty \rho(x, r) U_{tot}(x, r) r dr. \quad (2.13)$$

As ambient air is continuously entrained, the mass flow rate is linearly proportional to x (Ball et al., 2012). The excess momentum flow rate remains constant with axial distance (Pope, 2000; Ball et al., 2012) and is computed by

$$\dot{M}(x) = M_0 = 2 \pi \int_0^\infty \rho(x, r) U_{tot}(x, r) (U_{tot}(x, r) - U_\infty) r dr. \quad (2.14)$$

Also, the tracer mass flow rate, given by

$$\dot{\Gamma}(x) = \Gamma_0 = 2\pi \int_0^\infty \rho(x, r) U_{\text{tot}}(x, r) C_{\text{exc}}(x, r) r dr, \quad (2.15)$$

is conserved (Chu et al., 1999). $C_{\text{exc}}(x, r)$ is the tracer excess concentration. The thermal and kinetic energy flow rates are calculated via

$$\dot{E}_{\text{therm}}(x) = 2\pi \bar{c}_p \int_0^\infty \rho(x, r) T_{\text{exc}}(x, r) U_{\text{tot}}(x, r) r dr \quad (2.16)$$

$$\dot{E}_{\text{kin}}(x) = \pi \int_0^\infty \rho(x, r) (U_{\text{tot}}(x, r) - U_\infty)^2 U_{\text{tot}}(x, r) r dr. \quad (2.17)$$

The thermal energy flow rate increases and the kinetic energy flow rate decreases with increasing axial distance to the jet nozzle because momentum is continuously transferred into heat. Hence, the total energy flow rate remains constant with axial distance.

Generalizing Eq. 2.10 by accounting for density differences between jet and ambient, the centerline velocity law (Eq. 2.10) is normalized using the effective diameter in the far field instead of the initial jet diameter. This concept was originally proposed by Thring and Newby (1953) and later extended to the near field and to jets in a coflowing environment by Sautet and Stepowski (1995). Following their work, the effective diameter is given by

$$d_{\text{eff}}(x) = d \sqrt{\frac{\rho_{J,0}}{\rho_{\text{eff}}(x)}}, \quad (2.18)$$

where $\rho_{J,0}$ is the initial jet density and ρ_{eff} is the effective density that is calculated by

$$\rho_{\text{eff}}(x) = \frac{\int_0^\infty \rho(x, r) U_{\text{tot}}(x, r) (U_{\text{tot}}(x, r) - U_\infty) r dr}{\int_0^\infty U_{\text{tot}}(x, r) (U_{\text{tot}}(x, r) - U_\infty) r dr}. \quad (2.19)$$

$d_{\text{eff}}(x)$ can be understood as the diameter of a jet of ambient fluid inducing the same momentum flow rate as a variable-density jet at downstream position x . $\rho_{\text{eff}}(x)$ is the excess momentum flow rate-weighted mean density (Charonko and Prestridge, 2017).

2.2.1.2 Advection-diffusion equation (ADE) in cylindrical coordinates

We consider the turbulent flow of a round jet. The flow field is regarded as stationary and axisymmetric. The two-dimensional system is represented by an axial coordinate x and a radial coordinate r , where the use of cylindrical coordinates is appropriate given the geometry of the problem. A continuous spreading and cooling characterize the (thermo-)dynamic evolution of the hot jet. The jet is assumed to be highly turbulent with a Reynolds number $> 10^4$. The governing equations are the momentum, energy, and mass equations. Splitting the flow field quantities into a temporal mean and a fluctuating part results in the corresponding time-averaged equations.

Furthermore, the axial direction is the dominant flow direction as the mean axial velocity \bar{U} is much larger than the mean radial velocity \bar{V} . Also, axial gradients are negligible because they are significantly smaller than lateral gradients. Based on these assumptions, the axial momentum flow rate is much larger than the axial flow rate of angular momentum. Hence, the so-called swirl number is small, and we neglect the mean angular velocity.

The turbulent, time-averaged boundary-layer equations for the mean axial and radial velocity, consisting of the continuity equation and momentum equation, therefore are

$$\frac{\partial(\bar{\rho}\bar{U})}{\partial x} + \frac{1}{r} \frac{\partial(r\bar{\rho}\bar{V})}{\partial r} = 0 \quad (2.20)$$

$$\bar{\rho}\bar{U} \frac{\partial\bar{U}}{\partial x} + \bar{\rho}\bar{V} \frac{\partial\bar{U}}{\partial r} = \frac{\nu}{r} \frac{\partial}{\partial r} \left(r\bar{\rho} \frac{\partial\bar{U}}{\partial r} \right) - \frac{1}{r} \frac{\partial}{\partial r} (r\bar{\rho}u\bar{v}) \quad (2.21)$$

with ρ representing the air density and ν the molecular diffusivity (Pai, 1954; Pope, 2000). Special attention is drawn to the shear stress \overline{uv} , where u and v are the fluctuating velocity components in the axial and radial direction. The shear stress can be related to the turbulent diffusivity D_T via

$$\overline{uv} = -D_T \frac{\partial \overline{U}}{\partial r}, \quad (2.22)$$

where D_T is determined empirically as shown in Sec. 2.2.1.1. In the following, it is assumed that the turbulent diffusivity is much larger than the molecular one ($\nu + D_T \approx D_T$).

The density ρ is derived via the ideal gas law for assumed isobaric conditions

$$\rho = \frac{p_{\text{amb}}}{R T} \quad (2.23)$$

with absolute temperature T , which is the sum of the excess temperature of the hot jet $T_{\text{exc}} = \Delta T$ and the temporally and spatially constant ambient temperature T_{amb} . While the assumption of isobaricity is not applicable directly behind the engine exit, we presume the jet pressure to equate to the ambient value within a few jet diameters, as has been done in prior investigations (Kärcher and Fabian, 1994; Lewellen, 2020).

Following Kärcher and Fabian (1994), the set of equations, known as ADEs, for axial velocity \overline{U} , temperature \overline{T} , and water vapor mass mixing ratio \overline{m}_{wv} takes the form

$$\rho U \frac{\partial \overline{U}}{\partial x} + \rho V \frac{\partial \overline{U}}{\partial r} = \frac{D_T}{r} \frac{\partial}{\partial r} \left(\rho r \frac{\partial \overline{U}}{\partial r} \right) \quad (2.24)$$

$$\rho U \frac{\partial \overline{T}}{\partial x} + \rho V \frac{\partial \overline{T}}{\partial r} = \frac{D_T}{Pr} \frac{1}{r} \frac{\partial}{\partial r} \left(\rho r \frac{\partial \overline{T}}{\partial r} \right) + \frac{D_T}{\bar{c}_p} \rho \left(\frac{\partial \overline{U}}{\partial r} \right)^2 + R_T \quad (2.25)$$

$$\rho U \frac{\partial \overline{m}_{\text{wv}}}{\partial x} + \rho V \frac{\partial \overline{m}_{\text{wv}}}{\partial r} = \frac{D_T}{Pr \times Le} \frac{1}{r} \frac{\partial}{\partial r} \left(\rho r \frac{\partial \overline{m}_{\text{wv}}}{\partial r} \right) + R_{m_{\text{wv}}}. \quad (2.26)$$

For better readability, the bars indicating the averaging have been omitted. The specific heat capacity for dry air averaged over the temperature range of interest is represented by \bar{c}_p . Dividing the turbulent diffusion coefficient by the turbulent Prandtl number Pr or Lewis number Le yields thermal diffusivity or mass diffusivity, respectively. In our studies, we set $Pr = 1$, $Le = 1$, and $\bar{c}_p = 1020 \text{ J kg}^{-1} \text{ K}^{-1}$. The second term on the right-hand side of Eq. 2.25 describes the viscous heating effect, capturing the increase of internal energy (heat) because of the viscous dissipation of kinetic energy.

Eqs. 2.24–2.26 are applied for both a free jet that submerges into a stagnant surrounding and a coflowing jet where the ambient air moves with speed U_∞ . In the case of a free jet, excess axial velocity and excess thermodynamic fields are examined. In the latter case, i.e., a coflowing jet, total variables (sum of excess and ambient fields) are used.

The ADEs given above represent only incompressible flows. However, with an initial jet excess velocity of 271 m s^{-1} , the Mach number is $M = 0.90$ for our cold jet and $M = 0.58$ for our hot jet. As a rough guideline, flows with $M > 0.3$ should be treated with compressible equations (Anderson, 2017), making our approach seemingly questionable. For jet flows, however, the importance of compressibility effects is judged upon the convective Mach number M_c , which is a local metric defined in a coordinate system moving with the velocity of the turbulent structures within the shear layer (Papamoschou and Roshko, 1988; Yoder et al., 2015; Lewellen, 2020). It is defined as

$$M_c = \frac{U_1 - U_2}{c_{s,1} + c_{s,2}}, \quad (2.27)$$

where U_1 and U_2 represent the velocities of the two air streams (with $U_2 = 0 \text{ m s}^{-1}$ for a free jet) and $c_{s,1}$ and $c_{s,2}$ are the corresponding speeds of sound inside the jet and of the background, respectively. The convective Mach number is independent of the coflow velocity, as the jet velocity is the sum of excess and coflow velocity, and U_2 cancels out. With $U_1 = 271 \text{ m s}^{-1}$, the calculated M_c is approximately 0.45. When considering a hot jet with an exit temperature T_E , the speed of sound c_s increases, thereby reducing the convective Mach number. For exit temperatures around 500 K (as we assume in our model), the jet flow

can be considered low subsonic according to the definition of the convective Mach number. Hence, our incompressible approach is justified for all use cases this study presents.

For flows with $M_c > 0.5$, numerous experiments have shown that the dilution decelerates for increasing M_c (Yoder et al., 2015). In such cases, our model would overestimate the jet dilution rate.

Following Pope (2000), the momentum ADE can be solved analytically when assuming no density differences between jet and ambient air. A free jet (i.e., without a coflow) is considered.

Under these circumstances, the analytical solution for Eq. 2.24 is written as (Pope, 2000)

$$U(x, r) = U_0(x) f\left(\frac{r}{r_{0.5}}\right) \quad (2.28)$$

that consists of two terms: the axial centerline velocity $U_0(x)$ and a second term $f\left(\frac{r}{r_{0.5}}\right)$ that captures the radial dependency and reads as

$$f\left(\frac{r}{r_{0.5}}\right) = \frac{1}{(1 + cr^2)^2} \quad (2.29)$$

with $c = \frac{\sqrt{2}-1}{r_{0.5}(x)^2}$. The centerline velocity $U_0(x)$ and the velocity half-width radius are calculated using Eqs. 2.10 and 2.11.

The analytical solution for the radial velocity is (Pope, 2000)

$$V(x, r) = 4 D_T c r \frac{1 - cr^2}{(1 + cr^2)^2}. \quad (2.30)$$

In this study, we use the benchmark scenario of the dynamical evolution of a constant-density jet as verification for our numerical solution of the momentum equation.

2.2.1.3 Development of a numerical solution procedure for the ADE system

In the following, we present a numerical solution procedure that allows us to simulate the evolution of a hot jet with variable density as governed by Eqs. 2.20 and 2.24–2.26. We discretize the ADEs in a space-fixed coordinate system (with adapted spatial coordinates). In this purely dynamic framework, source terms are zero. Once the model is coupled with a microphysical model of contrail formation, the source terms R_T and $R_{m_{wv}}$ will be nonzero.

2.2.1.3.1 Coordinate-transformed ADE system

We introduce the Stokes stream function

$$U = \frac{1}{\rho r} \frac{\partial \psi}{\partial r}, \quad V = -\frac{1}{\rho r} \frac{\partial \psi}{\partial x} \quad (2.31)$$

for cylindrical coordinates. This is a valid procedure as we consider a two-dimensional and stationary flow field.

Inserting the axial and radial velocities expressed by the stream function (Eq. 2.31) into Eqs. 2.20 and 2.24, one single equation remains, since the continuity equation is by construction automatically fulfilled. The new momentum equation (not shown) is complex and unappealing to solve numerically as third derivatives in r and mixed derivatives in r and x appear. It is convenient to perform a coordinate transformation from (x, r) -space into (ϕ, ψ) -space as proposed by Kärcher and Fabian (1994).

The new radial coordinate ψ is chosen to be equivalent to the stream function. The new axial coordinate ϕ is defined such that

$$\frac{\partial \phi}{\partial x} = D_T(x). \quad (2.32)$$

This is a valid transformation as the turbulent diffusion coefficient D_T is always positive. The function that maps ϕ onto x is invertible. ϕ depends only on x because we assume that D_T is independent of r . In general, an increase or decrease in the diffusion coefficient results in a stretching or compression of the axial grid. The coordinate transformation is described by

$$\begin{aligned} \begin{pmatrix} \frac{\partial}{\partial x} \\ \frac{\partial}{\partial r} \end{pmatrix} &= \begin{pmatrix} \frac{\partial \phi}{\partial x} & \frac{\partial \psi}{\partial x} \\ \frac{\partial \phi}{\partial r} & \frac{\partial \psi}{\partial r} \end{pmatrix} \begin{pmatrix} \frac{\partial}{\partial \phi} \\ \frac{\partial}{\partial \psi} \end{pmatrix} \\ &= \begin{pmatrix} D_T & -V \rho r \\ 0 & U \rho r \end{pmatrix} \begin{pmatrix} \frac{\partial}{\partial \phi} \\ \frac{\partial}{\partial \psi} \end{pmatrix}. \end{aligned} \quad (2.33)$$

Therefore, the transformed ADEs in (ϕ, ψ) -space read as

$$\frac{\partial U}{\partial \phi} = \frac{\partial}{\partial \psi} \left(\rho^2 r^2 U \frac{\partial U}{\partial \psi} \right) \quad (2.34)$$

$$\frac{\partial T}{\partial \phi} = \frac{1}{Pr} \frac{\partial}{\partial \psi} \left(\rho^2 r^2 U \frac{\partial T}{\partial \psi} \right) + \frac{U \rho^2 r^2}{\bar{c}_p} \left(\frac{\partial U}{\partial \psi} \right)^2 + \tilde{R}_T \quad (2.35)$$

$$\frac{\partial m_{wv}}{\partial \phi} = \frac{1}{Pr \times Le} \frac{\partial}{\partial \psi} \left(\rho^2 r^2 U \frac{\partial m_{wv}}{\partial \psi} \right) + \tilde{R}_{m_{wv}}. \quad (2.36)$$

Note two significant advantages that result from that transformation: Firstly, the radial velocity disappears so that we are left with only one unknown quantity in the momentum equation (Eq. 2.34), namely the axial velocity U . Secondly, all three equations have the form of a classical diffusion equation without advection. Conveniently, all advective terms containing mixed derivative terms drop out. Nevertheless, we will still speak of an ADE to make clear that the effect of advection is implicitly accounted for. When applying the transformation formulae, the continuity equation is still implicitly fulfilled. We define a radial grid given by the coordinate ψ that follows from Eq. 2.31:

$$\psi(x, r) = \int_0^r \rho(x, r) U(x, r) r \, dr. \quad (2.37)$$

A close look at the transformed ADEs reveals that the "old" radial coordinate still appears in the equations. To solve the system of equations, we need to evaluate r^2 in (ϕ, ψ) -space, for which we use Eq. 2.31:

$$r^2 = 2 \int_0^\psi \frac{1}{\rho(\psi') U(\psi')} d\psi'. \quad (2.38)$$

A description of the implicit finite-difference discretization of Eqs. 2.34-2.36 can be found in Sec. A1. The new (ϕ, ψ) -grid is not time-constant and stretches and compresses in physical (x, r) -space. This necessitates the introduction of a time-adaptive (ϕ, ψ) -grid as described in Sec. A1.

2.2.1.3.2 Initial and boundary conditions

In the following, the generic variable c serves as a placeholder for either U , T , or m_{wv} . We prescribe a radial grid r with variable spacing. It is defined within the range of $[0, 100]$ m (for more details on the radial grid, see Sec. A1). In physical (x, r) -space, we select the initial profile $c(x_{\text{start}}, r)$. As the algorithm operates in (ϕ, ψ) -space, the initial c -profile needs to be mapped to the coordinate-transformed system.

The axial grid is specified as $x = N_x \times dx$, and N_x can be arbitrarily chosen. Throughout the study, $dx = 0.01$ m.

A step-wise function serves as the most generic shape for the initial profile:

$$c(x_{\text{start}}, r) = \begin{cases} c_0 & r \leq d/2 \\ c_\infty & r > d/2. \end{cases} \quad (2.39)$$

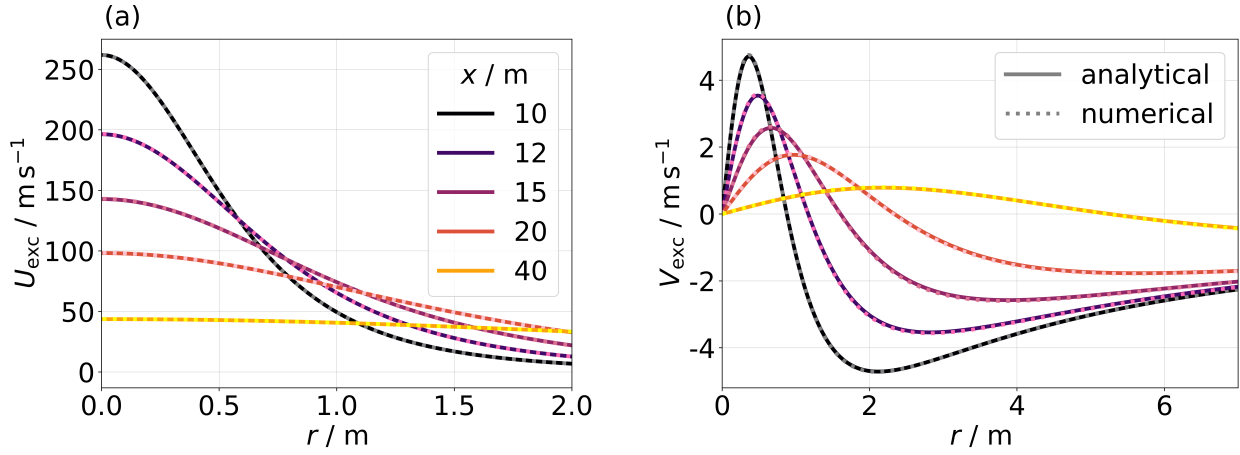


Figure 2.2: Radial profiles of (a) axial and (b) radial velocity for a constant-density jet. Solid lines depict the analytical solution from Pope (2000), and dotted lines show the numerical results. The curves are plotted at different downstream distances.

In general, when selecting a step function as initial profile for axial velocity, we define that $x_{\text{start}} = 0$ m. In the case of a free jet, c_0 is either U_J , $T_{\text{exc}} = T_E - T_{\text{amb}}$ or $m_{\text{WV,exc}}(T_E)$. Simulating a coflowing jet, we prescribe U_{tot} , T_E , and $m_{\text{WV,exc}}(T_E) + m_{\text{WV,amb}}$ (see Tab. 2.1).

Simulating a jet flowing into a stagnant ambient, we compute excess quantities, and the outer boundary of the spatial grid is chosen to be $c_{\text{exc},N_\psi} = 0$, where N_ψ is the number of grid points in ψ -space. It can be assumed that far away from the jet center, excess axial velocity, excess temperature, and excess water vapor mixing ratio are zero. In the case of a coflowing jet, we prescribe $U_{\text{tot},N_\psi} = U_\infty$, $T_{\text{tot},N_\psi} = T_{\text{amb}}$, and $m_{\text{WV,tot},N_\psi} = m_{\text{WV,amb}}$. The matrix coefficients of the inner boundary are computed differently, as shown in Sec. A1.

2.2.2 Results

The plausibility of the model outcome will be examined based on various jet configurations. We distinguish two cases:

- **Cold jet with prescribed density of air**

If we consider a cold jet ($T = T_{\text{amb}}$), solely the momentum ADE is solved. Viscous heating effects are ignored, and the density of air ρ_0 is spatially and temporally constant.

- **Hot jet with variable density of air**

Compared to the cold jet, we initialize a jet with $T_{\text{exc}} > 0$ and a suitable water vapor field. We solve all three ADEs given above. According to the ideal gas law, we account for density changes $\rho = \rho(T)$. In our implicit numerical approach, the momentum and temperature ADEs are fully (i.e., two-way) coupled and are solved simultaneously. The axial velocity can no longer be determined without knowledge of the temperature because of $U(\rho(T))$.

We first validate the numerical algorithm by comparing the numerical velocity profiles of a cold jet with the analytical solution (Sec. 2.2.2.1). We assess the jet spreading behavior for cold and hot jets and compare our model results with findings from prior studies (Sec. 2.2.2.2). Furthermore, the algorithm is employed to simulate the jet evolution in a coflowing environment (Sec. 2.2.2.3). Finally, we compare the model results with those obtained from Computational Fluid Dynamics (CFD) simulations (Sec. 2.2.2.4).

2.2.2.1 Comparison with the analytical solution

In the first development step, we investigate a cold jet, i.e., we solve for axial velocity only. In this case, an analytical solution of the momentum equation exists (see Sec. 2.2.1.2), which helps to verify the numerical

solution algorithm. We initialize $U(x_{\text{start}}, r)$ as a self-similar profile according to Eq. 2.28. As proposed in Pope (2000), we take the values from the study of Hussein et al. (1994) to calculate the axial centerline velocity and velocity half-width radius: $S = 0.094$, $B = 5.8$, and $x_0 = 4d$. These constants are specifically used to define an initial numerical profile for U , aligning with the analytical profile in this verification scenario. Alternative parameter values could be specified if they correspond to those used for the analytical U -profiles. Sec. 2.2.2.2.1 demonstrates that an arbitrary starting profile for U , such as a step function, can be chosen, allowing the parameters S , B , and x_0 to be determined from the numerical solution rather than being predefined.

The selection of a starting value x_{start} is constrained by the condition $U_J > U_0(x_{\text{start}})$. With values for S and B as described above and an initial jet diameter of 1 m, we obtain $x_{\text{start}} \approx 10$ m.

Solving the equation system presented in Sec. 2.2.1.3, the resulting radial profiles of axial and radial velocity, shown as dotted lines in Figs. 2.2a and b, agree with the analytical profiles, represented by solid lines. The radial velocity is calculated numerically by discretizing Eq. 2.31 and compared to the analytical solution (Eq. 2.30). We see an outward movement of the jet's core air ($V(r) > 0$) at small radial distances, whereas at outer regions, ambient air is entrained and moves inward ($V(r) < 0$). As the jet expands, the inward movement of ambient air shifts further outwards.

Another verification test involves the evaluation of the jet flow rates. We confirm the conservation of momentum and tracer excess concentration flow rates and the total energy flow rate. See Sec. A1 for further details.

2.2.2.2 Investigation of a turbulent jet in a stagnant environment

2.2.2.2.1 Simulations of a cold jet

After a thorough verification of the numerical results with the analytical profiles, we initialize the axial velocity as a step function as described in Sec. 2.2.1.3.2 and values listed in Tab. 2.1. In order to derive the spreading rate S , decay constant B , and virtual origin x_0 , a linear curve is fitted to our simulation data $r_{0.5}(x)/d$ and $U_J/U_0(x)$ for both a self-similar and step-wise initial profile of axial velocity. We initialize the step function at $x_{\text{start}} = 0$ m and, in a second simulation, at 10 m. Fig. 2.3a shows the centerline velocity decay for the case of an initial step function with $x_{\text{start}} = 0$ m.

The obtained fitted values of the three model setups (i.e., self-similar and step profile with two different starting values) and those from previous studies are listed in Tab. 2.2. The value of the virtual origin refers to the velocity decay fit. Not surprisingly, the fitted values in the case of a self-similar initial profile agree with the initially prescribed values. In the case of an initial step function, the spreading rate and velocity decay constant also nicely agree with prior studies. Yet, we note differences in the fitted value for the virtual origin when using different starting values of x . When also initializing the step function at $x = 10$ m downstream distance, the fitted value for the virtual origin is 5.9 m, shifting it around 10 m downstream compared to the simulation with $x = 0$ m. Initializing the axial velocity profile at $x = 10$ m as a step function results in a virtual origin located further downstream due to the time it takes for the jet to exhibit self-similar behavior. By altering the initial jet excess velocity and initial jet diameter, we find minimal variations of the fitted values S , B , and x_0 . Specifically, by halving U_J while simultaneously halving d , the jet spreading behavior in terms of S , B , and x_0 remains consistent.

The profiles in Fig. 2.3b suggest the onset of self-similarity at around 3 to 4 m downstream distance. Beyond that distance, the normalized profiles converge and collapse onto the self-similar profile. Our estimated potential core length of 3 to 4 m agrees with commonly found values of few jet diameters (Xia and Lam, 2009; Or et al., 2011; Yoder et al., 2015).

We provide a brief note on the analysis of density in the case of a cold jet: The density is radially independent so that it cancels out in Eqs. 2.24–2.26. In Eqs. 2.34–2.36, on the other hand, the density only appears in the term on the right-hand side and, at first glance, does not seem to cancel out in the equation system. Keeping in mind that $\psi \propto \rho$, the factors $\frac{r^2 \rho^2 U}{d \psi^2}$ are independent of ρ (the radial coordinate does not depend on density because it is proportional to $\rho^{-1} d\psi$). Thus, the results obtained from solving the coordinate-transformed system do not depend on the prescribed (constant) value of ρ .

	S	B	x_0/d	x/d
Panchapakesan and Lumley (1993a)	0.096	6.06	0	0–160
Hussein et al. (1994)	0.094	5.8	4	30–120
Chassaing et al. (1994)	0.09	5.15	2.8	>20
Khorsandi et al. (2013)	0.099	5.66	4	10–115
Amielh et al. (1996)	0.062	9.1	–2.6	<40
Antoine et al. (2001)	0.064	6.83	4.9	70–140
Or et al. (2011)	–	5.11	–2.4	>3
present study (self-similar profile)	0.094	5.80	4.1	10–100
present study (step profile)	0.094	5.85	5.9	10–100
present study (step profile)	0.094	5.85	–3.9	0–100

Table 2.2: Measured/simulated spreading rate S , decay constant B , virtual origin x_0/d , and axial measurement ranges x/d for turbulent axisymmetric jets in various studies

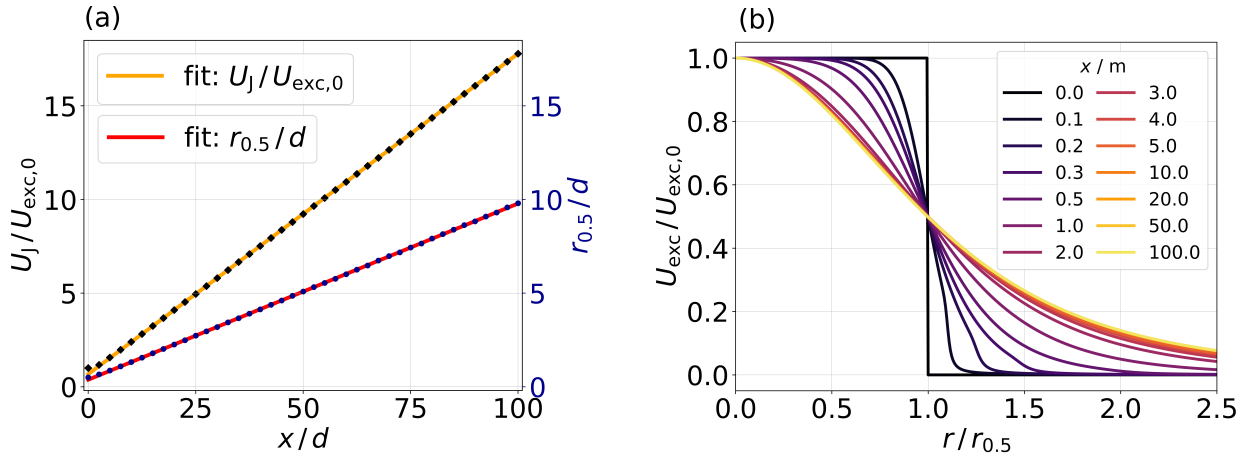


Figure 2.3: (a) Simulated centerline velocity decay (black diamonds) and radius of velocity half-width (blue dots) as functions of the normalized axial distance. Note that the axial resolution is $dx = 0.01$ m as specified in Sec. 2.2.1.3.2, but we only plotted a sample of points for illustration reasons. Linear fits are displayed in orange and red. (b) Axial velocity profiles normalized by the centerline velocity are depicted as functions of $r/r_{0.5}$ at different downstream locations. Initial values for jet diameter and excess velocity $d = 1$ m and $U_j = 271$ m s⁻¹ are used in this example.

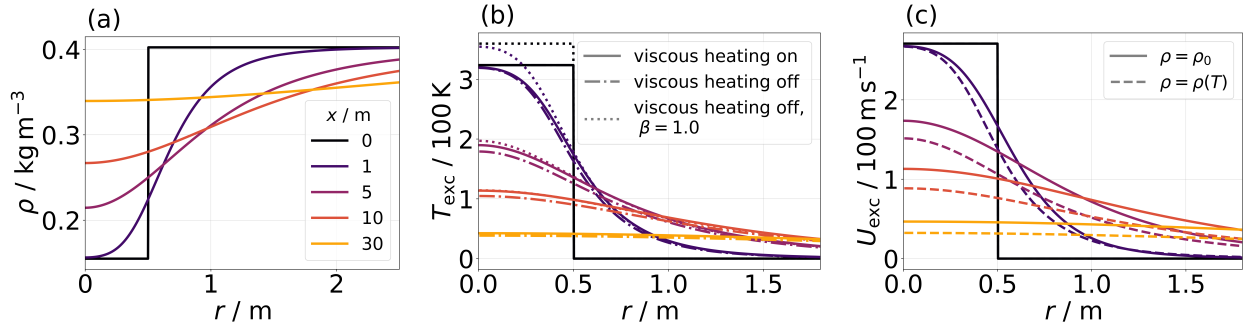


Figure 2.4: (a) Radial density profiles at different downstream distances. The initial density ratio is 0.41. (b) Radial temperature profiles with and without the viscous heating effect are displayed. (c) Radial profiles of axial velocity for a hot jet with variable density and prescribed constant density.

2.2.2.2.2 Simulations of a hot jet

In the following, we simulate the expansion of a hot jet by solving the full equation system (Eqs. 2.34-2.36). The density is allowed to vary with temperature according to Eq. 2.23. We initialize U , T , and m_{WV} as step profiles, see Sec. 2.2.1.3.2. Notably, prescribing self-similar or Gaussian initial profiles for temperature and water vapor mixing ratio is not a reasonable choice in our applications. In this case, each radial grid box corresponds to a specific point on the mixing line shown in Fig. 1.3. In a certain radius interval, the plume temperature and water vapor conditions are such that liquid saturation is surpassed (corresponding to the segment of the mixing line lying above the saturation curve). Once we couple RadMod with LCM, supersaturated conditions at initialization are not meaningful as particle nucleation and growth processes start once saturation is surpassed, and water vapor is depleted. To eliminate initial supersaturation in our profiles, we choose step functions for both T and m_{WV} independently of the shape of the initial axial velocity profile. In this case, the value pair for T and m_{WV} lies on the mixing line far to the right of the point where the mixing line crosses the saturation curve.

As it is illustrated in Figs. 2.4a and b, the plume density in the core region increases with increasing axial distance to the jet nozzle as the jet's core region ($r \leq 0.5$ m) is continuously cooled down due to the entrainment and mixing with the cold surrounding. The hot jet is expanding, so the mixture of jet and ambient air at the former jet's edge ($r \geq 0.5$ m) is heated up and becomes less dense.

Optionally, we can switch the viscous heating effect off by setting the viscous heating term to zero in Eq. 2.35. Fig. 2.4b shows results with included and excluded viscous heating terms. Not surprisingly, the inclusion of viscous heating makes the jet warmer compared to the case without the viscous heating term, where kinetic energy is lost, and the total energy flow is not conserved in the system. At maximum, the viscous heating causes a temperature difference of around 20 K. The velocity profiles, however, do not change substantially when viscous heating is switched off (not shown). In contrail formation theory (Schumann, 1996), typically, the assumption is made that the jet kinetic energy has been fully converted into thermal energy at the time contrail formation sets in. In purely thermodynamical considerations, this assumption then justifies an initial energy partitioning of 100% and 0% (instead of 90% and 10% as in our approach) and simplifies the analysis. We test the validity of this assumption by running an additional simulation that initializes the plume with 100% thermal energy. The jet kinetic energy is set to 10% of the total (reference) energy. We switch off the viscous heating effect, and after the dissipation of the jet, the total energy is identical to our default simulation with a (90%, 10%) partitioning. The dotted line in Fig. 2.4b indicates this simulation. The initial jet excess temperature is around 36 K higher in the jet center compared to the 90%-cases. While differences in the temperature profiles are apparent at $x = 1$ m, they are nearly/fully negligible after 5 and 10 m, respectively. As the excess temperature is still high and relative humidity well below saturation, the assumption of (100%, 0%)-energy partitioning in purely thermodynamical considerations is justified, also for cases with hydrogen combustion where supersaturation shapes up earlier (Bier et al., 2024).

The measurement of jets with densities differing from the density in the surrounding has been investigated in

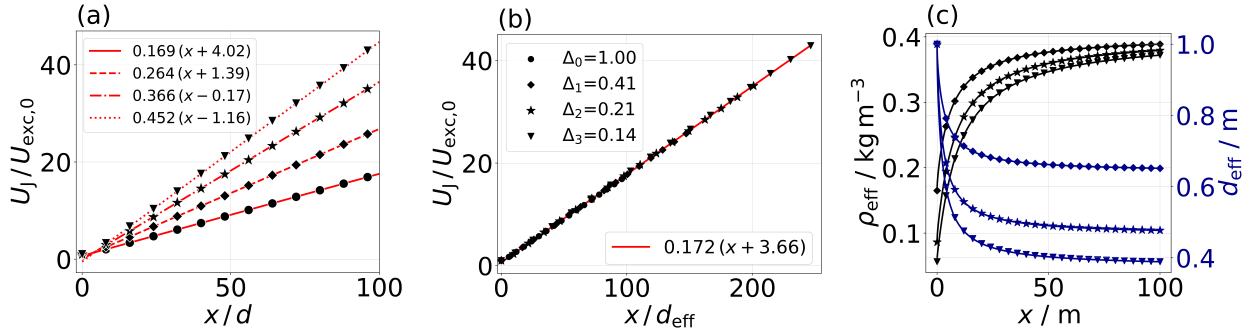


Figure 2.5: (a) Centerline velocity decay in four jets with different density ratios (see legend in panel (b)) as a function of normalized downstream distance and (b) density-scaled normalized downstream distance. (c) Effective density and diameter as functions of x . In panel (c), no curve is displayed for Δ_0 as both ρ_{eff} and d_{eff} are equal to 1.0.

several studies, e.g., [Richards and Pitts \(1993\)](#); [Djeridane et al. \(1996\)](#), or [Charonko and Prestridge \(2017\)](#). In agreement with these studies, we observe a faster mixing in such lower-density jets, see Fig. 2.4c. The jet’s initial mass, momentum, and kinetic energy fluxes are smaller, and the entrainment of ambient air leads to a faster velocity decay. The faster mixing process is also observed for the thermodynamic variables (not shown).

In order to systematically investigate jets with variable density, we initialize four jets with different density ratios $\Delta = \rho_{j,0}/\rho_\infty$, where ρ_∞ represents the density of the surrounding. For this, we increase the jet exit temperature: $\Delta_1 = 0.41$ ($T_E = 549$ K), $\Delta_2 = 0.21$ ($T_E = 1049$ K), and $\Delta_3 = 0.14$ ($T_E = 1609$ K). $\Delta_0 = 1.0$ represents a cold jet. Δ_3 is chosen to correspond to a proxy of a helium jet, for which various simulations have been performed in previous studies ([Panchapakesan and Lumley, 1993b](#); [Sautet and Stepowski, 1995](#); [Amielh et al., 1996](#)). Note that a jet having an exit temperature of >1000 K does not necessarily represent a realistic aircraft jet flow, yet, corresponds to a jet with very low density. Also, buoyancy effects are not accounted for. As has been shown experimentally in [Monkewitz et al. \(1990\)](#), a hot jet experiences a faster rate of turbulent structure growth than a cold jet. Our simulations of hot jets indicate that their spreading rates are comparable to those of cold jets. However, we observe that the velocity half-width radius is shifted closer to the centerline, a phenomenon that intensifies with increasing jet temperatures (not shown). Interpreting $r_{0.5}$ as the center of the shear layer, this shift suggests a reduction in the potential core length. Consequently, the jet reaches its self-similar state earlier ([Yoder et al., 2015](#)).

The faster decay of the axial centerline velocity with decreasing density ratio is shown in Fig. 2.5a. The virtual origin decreases for increasing density ratio, consistent with findings by [Charonko and Prestridge \(2017\)](#). For a helium-like jet (dotted line), we find a slope of 0.452 comparable to the value of 0.414 reported in [Panchapakesan and Lumley \(1993b\)](#). When normalizing with the effective diameter (Eq. 2.18), the data points lie on a unique line with $B^{-1}(\Delta_3) = 0.172$, see Fig. 2.5b.

In Fig. 2.5c, the effective diameter (blue) and effective density (black) are displayed for different density ratios (the curves for Δ_0 are not shown because $d_{eff}(\Delta_0) = \rho_{eff}(\Delta_0) = 1.0$). We see an increase in effective density and a decrease in effective diameter with downstream distance. At a fixed axial position, the effective diameter is smaller for a smaller density ratio. This outcome is expected, since $d_{eff}(\Delta_3)$ represents the diameter of a jet comprising solely ambient fluid but carrying the momentum of a helium jet, which is significantly smaller than the momentum of a cold jet. Therefore, $d_{eff}(\Delta_3)$ needs to be smaller than $d_{eff}(\Delta_2)$ (and $d_{eff}(\Delta_2)$, in turn, needs to be smaller than $d_{eff}(\Delta_1)$). For all cases, the effective density approaches ρ_∞ at larger downstream distances.

So far, we presented the evolution of U and T . We now investigate the plume water vapor mixing ratio m_{WV} , obtained by solving Eq. 2.36. Figure 2.6a shows radial profiles of excess mixing ratio at different axial positions. With temperature and total water vapor mass mixing ratio at hand, we calculate the plume relative humidity with respect to water by dividing the water vapor partial pressure $p_{WV}(m_{WV})$ by the water vapor saturation pressure $p_{sat,WV}(T)$. The relative humidity profiles are displayed in Fig. 2.6b.

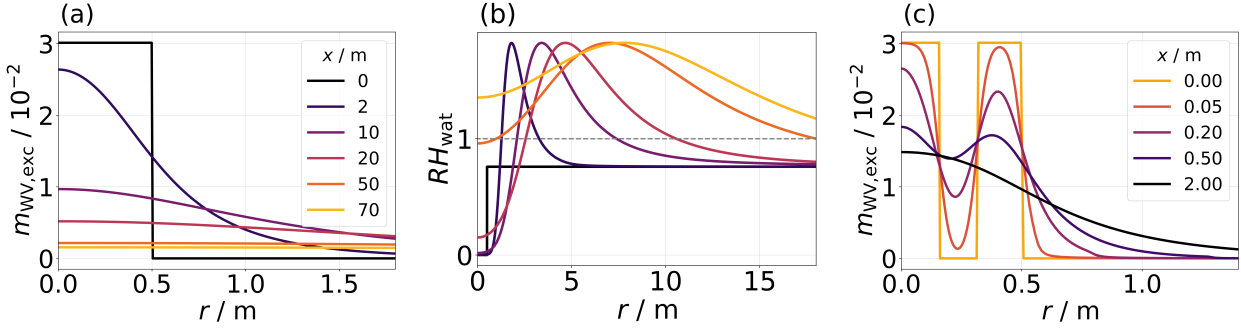


Figure 2.6: (a), (c) Radial profiles of water vapor mixing ratio and (b) plume relative humidity with respect to water. The legend in panel (a) refers to panels (a) and (b), which show the case with a classical step function. (c) Case with a water vapor deficit for medium radii of the initial jet.

Even though the initial jet features a very low value of RH_{wat} , it reaches values above 100% within the first meters behind the engine exit. Then, the supersaturation peak value decreases slightly with increasing axial distance, yet a larger area becomes supersaturated. Eventually, supersaturation is reached at all radial distances up to around 20 m. Note that in our present approach, the effect of microphysical processes on the relative humidity evolution is not considered. During contrail formation, condensation/deposition of water vapor on contrail water droplets and ice crystals would reduce the relative humidity.

Exploring the model's capabilities further, we initialize a water vapor profile with a local deficit, as seen in the orange curve in Fig. 2.6c. This serves as a simplified representation of the effect of microphysics, which reduces the water vapor via a source term in the water vapor ADE. The advective and diffusive processes then work to smooth out the deficit, gradually reducing its visibility until it is no longer discernible. The "effectiveness" of the diffusion processes is underscored by the fact that the initialized deficit region is balanced within a short distance of 1 to 2 m. The diffusion of a water vapor deficit or of a spike in ice crystal and liquid droplet mass/number is a clear advantage of the coupled dynamical-microphysical model over common trajectory-based contrail formation models (Paoli et al., 2008; Bier et al., 2022, 2024) where diffusion between neighboring trajectories is typically neglected.

2.2.2.3 Investigation of turbulent jets in a coflowing environment

In the context of contrail formation studies, our objective is to implement the concept of a moving source emitting into a stagnant atmosphere. We change the reference system by interpreting the movement of the aircraft with speed U_{AC} through the stagnant environment as a stationary aircraft surrounded by a coflowing airstream with speed $|U_{\infty}| = |U_{AC}|$. In the following, we show that our model is capable of reflecting the key features of jet expansion in a comoving environment. We examine coflowing cold and hot jets with coflow velocities 50 m s^{-1} , 150 m s^{-1} , 250 m s^{-1} , and 400 m s^{-1} .

The coflowing jet has been studied extensively, e.g., Nickels and Perry (1996); Chu et al. (1999), or Xia and Lam (2009). It has been found that the evolution of a coflowing jet differs in two main aspects compared to a free jet: The jet spreading proceeds more slowly, and the axial centerline velocity decay is slower.

Following Chu et al. (1999), we divide the jet evolution into two parts: In the strong jet regime, where the jet's excess velocity is much larger than the coflow velocity, the jet behaves as a free jet, i.e., the coflowing environment does not influence the jet's evolution. In the weak jet regime, i.e., far from the jet's origin, the jet has been decelerated and is impacted by the surrounding's movement. In this axial region, it holds $r_{0.5} \propto x^{1/3}$ and $(U_{\text{tot},0} - U_{\infty}) \propto x^{-2/3}$ as reported in several studies (Kärcher and Fabian, 1994; Chu et al., 1999; Enjalbert et al., 2009).

It is customary to define a momentum length scale $l_m^* = \frac{\sqrt{M_0}}{U_{\infty}}$ (Chu et al., 1999; Lee and Chu, 2003; Moeini et al., 2021). Note that Chu et al. (1999) and Moeini et al. (2021) use a purely kinematic momentum flow rate without the density appearing in the integral (Eq. 2.14). In our analysis, we normalize the density in M_0 by the ambient density ρ_{∞} . Hence, ρ/ρ_{∞} is approaching 1 for large axial distances where the jet density

converges to the ambient density. This density normalization ensures that the unit of the momentum length scale is meter.

Although previous studies (e.g., [Nickels and Perry \(1996\)](#) or [Davidson and Wang \(2002\)](#)) suggest power laws of the form $r_{0.5}/l_m^* = (x/l_m^*)^{1/3}$ and $U_{exc,0}/U_\infty = (x/l_m^*)^{-2/3}$, we find the need for introducing axial offsets $x_{0,w}$ and $x'_{0,w}$ in order to fit the data well:

$$\frac{r_{0.5}}{l_m^*} = a \left(\frac{x - x_{0,w}}{l_m^*} \right)^{1/3} \quad (2.40)$$

$$\frac{U_{exc,0}}{U_\infty} = a' \left(\frac{x - x'_{0,w}}{l_m^*} \right)^{-2/3}. \quad (2.41)$$

Figs. 2.7a and b show spreading and axial centerline velocity decay of a cold jet ($T_{exc} = 0$ K) for four different coflow velocities. By normalizing with the momentum length scale, the data collapse on a single curve for $x/l_m^* \gtrsim 10$. The onset of the 1/3-spreading behavior at $x'/l_m^* = 10$ was also found by [Lee and Chu \(2003\)](#). In order to assess the robustness of the normalization with the momentum length scale, we conduct simulations for a jet with $U_J = 135 \text{ m s}^{-1}$, which is about half of our default jet excess velocity. The corresponding data points, represented by the blue symbols in Fig. 2.7, align with the same curve, confirming the robustness of the scaling.

Furthermore, we simulated two coflowing hot jets with exit temperatures $T_E = 549$ K and $T_E = 1049$ K. We confirm that coflowing hot jets also exhibit spreading and velocity-decay behaviors following 1/3 and $-2/3$ power laws, respectively (not shown).

In Fig. 2.8, the fitted values for coefficients and offsets of Eqs. 2.40 and 2.41 are displayed. Fitted values for Eq. 2.40 (Eq. 2.41) are shown in blue (orange). We examine three exit temperatures (indicated by symbols) and two jet excess velocities (indicated by line styles).

We observe an increasing trend in the coefficient a and a decreasing trend in a' for an increasing coflow velocity at $U_J = 271 \text{ m s}^{-1}$ and at $U_J = 135 \text{ m s}^{-1}$. This highlights the faster spreading (represented by a) and faster centerline velocity decay (represented by a') in the presence of an increasingly strong coflow where the jet's transition from the strong into the weak's jet regime occurs earlier. These observations are independent of the exit temperature. Generally, a higher exit temperature corresponds to a larger value of a and a smaller value of a' , consistent with the findings in Sec. 2.2.2.2.2, which showed that hot jets experience faster jet spreading and centerline velocity decay due to the higher mixing rate. Similarly, the dependences of a and a' on the exit velocity follow expected trends: Faster jet spreading is observed with lower exit velocities where the jet is weaker relative to the coflow. This results in larger (smaller) values of a (a') at the same temperature.

The axial offsets $x_{0,w}$ and $x'_{0,w}$ exhibit a strong dependency on U_∞ , see Fig. 2.8b. We interpret the axial offset as the "weak jet's virtual origin", and hence, its dependence on U_∞ is not surprising. It shifts to smaller distances if the coflow is stronger and the 1/3 behavior is observed earlier. In general, we observe smaller offsets for a smaller initial excess velocity at the same temperature because, in that case, the jet enters the weak jet regime earlier.

2.2.2.4 Comparison with CFD simulations

In the current framework of the LCM box model studies ([Bier et al., 2022, 2024](#)), the dilution of the plume is not explicitly modeled but suitably prescribed. For the latter, plume dilution properties are derived from a-priori CFD simulations.

In the following, we compare the results of the dynamical jet evolution obtained by RadMod with CFD simulation data provided by AIRBUS. The jet phase behind a single turbofan engine has been modelled by AIRBUS using the Navier-Stokes solver FLUSEPA in a RANS approach. FLUSEPA is a high-order unstructured finite volume CFD solver developed by the ArianeGroup ([Brenner, 1991](#)) that is used here to simulate compressible and turbulent flows ([Pont et al., 2017](#)).

The turbofan exhaust comprises two distinct flow regions: the core flow, which extends radially up to approximately 0.3 m for the given engine, and the bypass flow extending to around 1 m. For comparing the plume

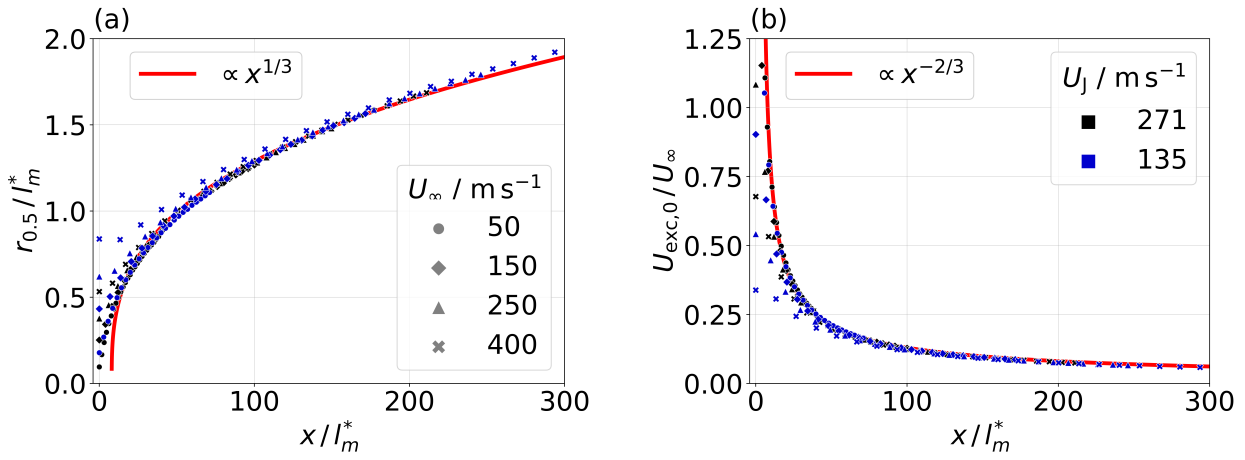


Figure 2.7: (a) Normalized jet spreading and (b) centerline velocity decay for a coflowing cold jet with different coflow velocities. Power law fits are displayed in red, and their fitted values are depicted in Fig. 2.8.

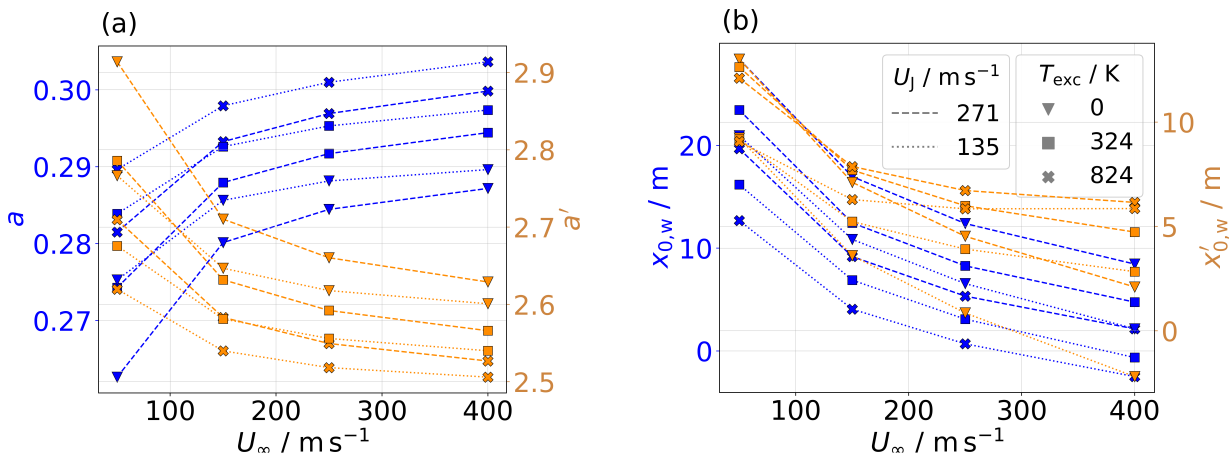


Figure 2.8: Fitted values for the coefficients a and a' and axial offsets $x_{0,w}$ and $x'_{0,w}$ as functions of the coflow velocity. Different jet configurations regarding exit temperature and initial excess velocity are analyzed.

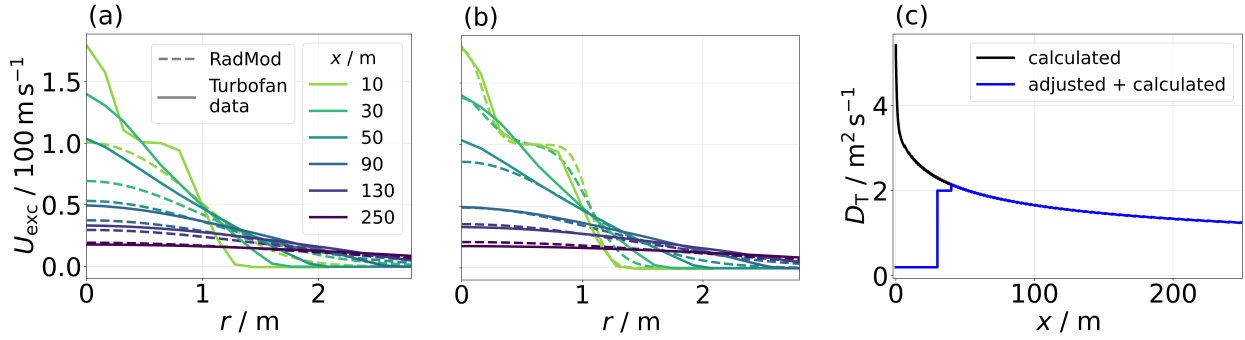


Figure 2.9: (a),(b) Axial velocity profiles of a turbofan engine at different axial distances obtained by FLUSEPA (solid) and RadMod (dashed). In (b), the diffusion coefficient in RadMod is manually adjusted within the first 40 m, see blue curve in (c). The black curve denotes D_T calculated by using Eq. 2.12.

dilution as simulated with FLUSEPA with our results of a coflowing jet obtained with RadMod, we choose ambient and exit conditions in RadMod as used in FLUSEPA ($T_{amb} = 218.8 \text{ K}$, $p_{amb} = 23842 \text{ Pa}$, $T_{E,core} = 564 \text{ K}$, $T_{E,bypass} = 224 \text{ K}$, $U_{\infty} = 231 \text{ m s}^{-1}$). We run RadMod up to an axial distance of 250 m.

Fig. 2.9a shows axial velocity profiles produced by FLUSEPA and RadMod. We observe that the profiles of RadMod evolve with different spreading rates. Initially, the diffusion appears excessively strong, whereas the profiles tend to align at larger axial distances (especially at around 250 m downstream distance). The strength of diffusion in RadMod is determined by the diffusion coefficient D_T . For a coflowing jet in RadMod, it holds $D_T \propto x^{-1/3}$. This behavior of the diffusion coefficient is expected as velocity half-width radius and centerline axial velocity evolve with $x^{1/3}$ and $x^{-2/3}$, respectively (see Sec. 2.2.2.3). We introduce a temporal adjustment to the diffusion coefficient to reach an agreement between RadMod and FLUSEPA results. Doing so, the resulting RadMod-axial velocity profiles show better alignment with the FLUSEPA data, as depicted in panel (b). The adjustment of D_T is illustrated by the blue curve in panel (c). Within the initial 40 m, D_T is a monotonically increasing, piece-wise constant function. Beyond 40 m downstream distance, there is no need to manually adjust D_T as it converges to the original D_T curve. It is then determined using Eq. 2.12 and follows a $-1/3$ behavior, depicted by the black line. For generating the black line, Eq. 2.12 is used from the beginning ($x \geq 0 \text{ m}$).

The exhaust plume behind a turbofan engine features also a rotational flow around the jet's centerline axis. Yet, the so-called swirl number is small, and the effect of the rotational flow component on the jet expansion is typically neglected: Neither the CFD data used here nor previous modeling studies (Garnier et al., 1997; Paoli et al., 2013; Cantin et al., 2022; Bouhafid et al., 2024) incorporated this aspect. This justifies our approach of neglecting the swirling component.

The pragmatic approach of adjusting the diffusion coefficient within RadMod will give us the chance to better compare contrail formation simulations with the upcoming RadMod-LCM model ("online microphysics") to those with our present multi-trajectory approach with the LCM box model ("offline microphysics"), as both model versions use a similar plume dilution based on the same a-priori CFD simulation. Previous multi-trajectory studies (Bier et al., 2022, 2024) have not used FLUSEPA, but FLUDILES data (Vancassel et al., 2014). We were also able to mimic the FLUDILES-simulated plume dilution with RadMod by adjusting D_T (not shown).

2.2.3 Discussion

2.2.3.1 Dynamical aspects

RadMod effectively models the evolution of a cold jet with a prescribed constant density, showing good alignment with theoretical and experimental studies in terms of both spreading rate and decay rate. In literature, a range of estimates exists for the location of the virtual origin x_0 . We notice a correlation between the virtual origin's location and our profiles' (prescribed) initialization point x_{start} . Shifting x_{start}

from 10 m downstream distance to 0 m introduces approximately the same shift in x_0 from ≈ 6 m to ≈ -4 m. This implies a linear relationship between x_{start} and x_0 . On the other hand, the spreading rate and decay constant exhibit only minor sensitivity to the selection of x_{start} . Therefore, the evolution of the jet appears unaffected by its initial position.

The model provides meaningful results in terms of a faster centerline velocity decay when simulating a hot jet with variable density. Simulating a proxy of a helium jet with density ratio $\Delta = 0.14$, we compare our fitted value of B^{-1} for axial centerline velocity decay, which is 0.17, with prior studies that have used the same normalization: Amielh et al. (1996) found $B^{-1}(\Delta) = 0.110$ and, according to Charonko and Prestridge (2017), Panchapakesan and Lumley (1993b) reported a value of $B^{-1}(\Delta) = 0.155$. Our finding is consistent with these values.

Also in the case of a coflowing jet, RadMod yields favorable outcomes. In the strong jet regime, the jet evolution follows the well-known linear relationships, $r_{0.5} \propto x^1$ and $U_{\text{exc},0} \propto x^{-1}$, whereas in the weak jet regime, these dependencies change to $r_{0.5} \propto x^{1/3}$ and $U_{\text{exc},0} \propto x^{-2/3}$. The initiation point of the weak jet regime is primarily determined by the velocity difference between the jet and the coflow, with the exit temperature playing a secondary role.

Radial profiles behind a turbofan engine, as obtained from a CFD model that also accounts for the complex engine mounting geometry, can be reproduced sufficiently well when we include a fine-tuning of the diffusion coefficient. Notably, the formula used to calculate the diffusion coefficient (Eq. 2.12) is valid for $x/d > 30$. This recommendation is based on empirical data from Hussein et al. (1994), which was limited to the range where the profiles exhibit self-similar behavior. Examining the onset of self-similarity in the evolution of the turbofan jet suggests that the near field extends up to around 100 m, corresponding to $x/d > 50$ (with plume diameter $d = 2$ m). Thus, the diffusion coefficient formula is strictly applicable only beyond this point. Since the initial turbofan exhaust cannot be suitably approximated by a self-similar (i.e., fully developed) jet profile, our adaptation of the diffusion coefficient in the early phase is not surprising. It does not imply that the Airbus CFD results contradict the empirical data.

In a similar exercise, we compared RadMod results with FLUDILES simulations (Vancassel et al., 2014) that simulated the jet expansion behind an A340-300 aircraft (with $d = 1$ m) and were used in our previous contrail formation simulations (Bier et al., 2022, 2024). Consistent with the preceding case study, we achieve a better model agreement when the diffusion coefficient D_T is chosen smaller than what an extrapolation of Eq. 2.12 would give for the near field. These findings suggest that the empirical formula for the diffusion coefficient should not be used in the near field when self-similarity has not yet been reached.

The stronger decline of the RadMod-profiles at larger radial distances compared to the CFD-profiles might be attributed to our assumption of a radially-constant normalized diffusivity \hat{D}_T . As illustrated in Pope (2000), $\hat{D}_T = 0.028$ decreases in $r/r_{0.5} > 1.5$ so that in RadMod the diffusion might be too weak at large radial distances. A radial adjustment of D_T could potentially address this issue and warrants further investigation in a follow-up study. Here, we calibrated the diffusion coefficient particularly at the jet edge, where supersaturation is reached first and ice crystals form.

2.2.3.2 Contrail formation modeling

Our new model describes the key features of the dynamical jet evolution that are relevant for contrail formation. Our recent contrail formation studies with the multi-0D framework and offline microphysics exploit the efficiency of the box model approach and allow us to perform extensive parameter studies (Bier et al., 2022, 2024). Despite producing more plausible results than with a box model with a single mean dilution, the "multi-0D" approach misses important phenomena as the microphysical model is run in an offline mode. As already stated in Sec. 2.1, microphysical computations are performed independently for each trajectory, neglecting any interactions among them. Yet, we have seen strong diffusive processes between nearby air parcels (or trajectories). Droplets, ice crystals, and the associated reduced water vapor amount from one air parcel can be mixed into neighboring air parcels where no droplets have yet formed. Those mixed-in droplets can then deplete water vapor and suppress further droplet activation.

While for typical soot-rich emissions contrail ice crystals form on emitted soot particles (via the liquid phase), other droplet sources like entrained ambient aerosol or ultrafine volatile plume particles contribute

to ice crystal formation in so-called soot-poor conditions (Kärcher and Yu, 2009). For contrails from hydrogen combustion, it is also unclear whether plume particles stemming from lubrication oils or chemions play a role in ice crystal formation (Ungeheuer et al., 2022; Ponsonby et al., 2024). Both scenarios have in common that competition effects between entrained and emitted droplets may occur. Those are not well-resolved in 0D-models (Kärcher and Yu, 2009) as they cannot capture the concentration gradients with opposite signs in the radial direction. Hence, the RadMod model with "online microphysics" will remedy the shortcomings mentioned in the preceding paragraphs. We will speak of an intermediate complexity model, as the level of detail of the dynamical solver is in between 3D LES (or RANS) and box model calculations.

Moreover, the RadMod model provides a framework for spatial simulations where air parcels of different ages interact. LES models are primarily run in a temporal mode, where all air parcels in the domain have the same age, as spatial LES are expensive and have been carried out only for a few cases (Lewellen, 2020). For RANS models, a spatial approach is more commonly employed (Khou et al., 2015, 2017; Cantin et al., 2022).

2.2.3.3 Limitations of the model

The newly proposed RadMod model does not capture all dynamical features of plume expansion that could be simulated with a 3D LES or RANS model. Such limitations of the intentionally simpler RadMod model are listed in the following and have to be kept in mind for our future contrail-related applications.

First of all, we assume axial symmetry in the initial jet profile, which could be an oversimplification in certain configurations. Moreover, RadMod does not incorporate turbulent fluctuations even though LES show contrail properties to be affected by them. This is a common shortcoming of contrail RANS approaches. In our approach, it could be potentially remedied by including synthetic perturbations in the data handed over from RadMod to the LCM microphysics.

The comparison with CFD data in Sec. 2.2.2.4 revealed that the formula used to calculate the diffusivity is not applicable in the initial development stage. Our typical future workflow will also use other existing CFD data or in-situ measurement data to fine-tune RadMod, in particular the diffusion coefficient, for specific configurations.

Furthermore, our approach neglects jet-vortex interactions. With increasing downstream distance, the expanding jet and exhaust plume start interacting with the wake vortices. Extending simulations with RadMod to several hundred meters downstream, RadMod results may suffer from neglecting the influence of such wake interactions. A recent study by Saulgeot et al. (2023) analyzed jet-vortex interactions. They found that the initiation of such interactions, termed the deflection phase, depends on the aircraft type and engine placement. Specifically, the onset of the deflection phase starts further downstream for engines positioned closer to the aircraft's center. Furthermore, larger aircraft tend to have jets that remain unaffected by the wake vortices over a larger axial distance. E.g., using the downstream position estimates from Tab. 2 in Saulgeot et al. (2023), the deflection phase is expected to start at $x \approx 100$ m when the engine is located at $2/3$ of the wingspan, and at $x \approx 400$ m when the engine is positioned at $1/3$ of the wingspan, for an aircraft with a wingspan of 60 m. As shown in Fig. 2.6b, water supersaturation occurs at the plume edge immediately after the emission. Consequently, the available water vapor condenses onto aerosols, followed by the subsequent freezing of the droplets into ice crystals. These processes immediately occur irrespective of the strength of the diffusivity. Even with very low diffusivity, the plume's temperature and water vapor conditions exceed the liquid saturation threshold in a certain radial interval (see Sec. 2.2.2.2). According to Garnier et al. (1997), the deflection regime starts at around 1 s after emission. Results in Bier et al. (2022) and Lewellen (2020) show that ice crystal formation is completed after around 1 s for typical cruise conditions. Based on the spatial or temporal estimates for the onset of the deflection phase, we expect that droplet activation and ice crystal nucleation for a typical aircraft will have already commenced and will be more or less completed by the time the interaction with the wake becomes significant. Despite this promising estimate, contrail formation is completed at different downstream distances for different use cases (e.g., kerosene vs. hydrogen combustion), and future RadMod applications need to scrutinize whether or not wake vortices substantially impact contrail formation.

2.2.4 Conclusion and outlook

We developed a computational model called RadMod that simulates a jet's expansion and thermodynamic evolution by solving the two-dimensional advection-diffusion equations of momentum and thermodynamic quantities. We employed a coordinate transformation originally proposed by [Kärcher and Fabian \(1994\)](#). The ADEs are two-dimensional, assuming a stationary, axially symmetric flow. Furthermore, they are Reynolds-averaged, meaning that turbulent fluctuations are not explicitly resolved. Our new model adequately captures the expansion and deceleration of a cold and a hot jet with a prescribed constant and variable density as the spreading rate and decay rate compare favorably with results from theory and previous experimental studies. Furthermore, the axial dependencies of flow rates are confirmed. The model is also able to represent the evolution of a coflowing jet.

As a first application, we carried out a comparison study with CFD data describing the exhaust plume behind a turbofan engine. The different diffusion rates underscored the significance of the diffusion coefficient. Further comparison studies will be performed to provide robust estimates of the initial strength of diffusivity. RadMod is ready to be fully coupled with a microphysical model of contrail formation. The procedure during one time step will be as follows: The thermodynamic fields generated by RadMod, such as temperature and water vapor mass mixing ratio, will serve as input for the microphysical model. These background fields are then used to simulate aerosol and cloud physical processes, including the depletion of water vapor due to condensation onto aerosols and the latent heat release from phase changes. Such changes in thermodynamic properties are subsequently passed back to RadMod and enter the ADEs via source terms. The coupling of both model codes is currently in progress.

Nomenclature

R	gas constant of dry air per molmass, $\text{J kg}^{-1} \text{K}^{-1}$
\bar{c}_p	mean specific heat capacity, $\text{J kg}^{-1} \text{K}^{-1}$
R_T	source term of temperature, $\text{kg K m}^{-3} \text{s}^{-1}$
$R_{m_{\text{WV}}}$	source term of water vapor mass mixing ratio, $\text{kg m}^{-3} \text{s}^{-1}$
Pr, Le	Prandtl number, Lewis number, 1
x, r	coordinates in axial and radial direction, m
U, V	velocities in axial and radial direction, m s^{-1}
\bar{U}, \bar{V}	mean velocities in axial and radial direction, m s^{-1}
u, v	turbulent velocity fluctuations in axial and radial direction, m s^{-1}
\overline{uv}	shear stress, $\text{m}^2 \text{s}^{-2}$
U_J	initial jet excess velocity, m s^{-1}
U_{exc}	jet excess velocity, m s^{-1}
U_{tot}	total axial velocity, m s^{-1}
U_{∞}	coflowing axial velocity / aircraft velocity, m s^{-1}
U_0	axial centerline velocity, m s^{-1}
c_s	speed of sound, m s^{-1}
M, M_c	Mach number, convective Mach number, 1
T	temperature, K
T_{amb}	ambient temperature, K
T_E	exit temperature, K
T_{exc}	excess temperature, K
C_{exc}	tracer excess concentration, m^{-3}
m_{WV}	water vapor mass mixing ratio, 1
$m_{\text{WV,exc}}$	excess water vapor mass mixing ratio, 1
$m_{\text{WV,amb}}$	ambient water vapor mass mixing ratio, 1
p_{WV}	partial pressure of water vapor, Pa
$p_{\text{sat,WV}}$	saturation pressure of water vapor, Pa
p_{amb}	ambient pressure, Pa
RH_{wat}	relative humidity with respect to water, 1
$RH_{\text{amb,wat}}$	ambient relative humidity with respect to water, 1
$RH_{\text{amb,ice}}$	ambient relative humidity with respect to ice, 1
D_T	turbulent diffusivity, $\text{m}^2 \text{s}^{-1}$
\hat{D}_T	normalized turbulent diffusivity, 1
$EI_{\text{H}_2\text{O}}$	emission index of water vapor, kg kg^{-1}
M_{WV}	total amount of water vapor per flight meter, kg m^{-1}
Q	specific combustion heat, J kg^{-1}
A_E	initial plume cross-sectional area, m^2
C_E	initial plume air-to-fuel ratio, 1
m_C	fuel combustion, kg m^{-1}
$r_{0.5}$	radius of velocity half-width, m
d, d_{eff}	jet initial diameter, effective jet diameter, m
x_0	virtual origin, m
x_{pc}	potential core length, m
x_{start}	starting value of axial grid, m
l_m^*	momentum length scale, m
S	spreading rate, 1
B	velocity decay constant, 1
\dot{m}	mass flow rate, kg s^{-1}
\dot{M}	momentum flow rate, kg m s^{-2}
$\dot{E}_{\text{therm}}, \dot{E}_{\text{kin}}$	thermal energy flow rate, kinetic energy flow rate, J s^{-1}

Greek Symbols

ρ	air density, kg m^{-3}
$\rho_{J,0}$	initial jet density, kg m^{-3}
ρ_{eff}	effective density, kg m^{-3}
Δ	ratio of initial jet density to ambient air density, 1
ν	molecular diffusivity, $\text{m}^2 \text{s}^{-1}$
ψ	stream function, radial coordinate in coordinate-transformed system, kg s^{-1}
ϕ	axial coordinate in coordinate-transformed system, $\text{m}^3 \text{s}^{-1}$
β	fraction of total energy partitioned into thermal energy, 1
η	overall propulsion efficiency, 1
$\dot{\Gamma}$	tracer concentration flow rate, $\text{kg}^2 \text{m}^{-3} \text{s}^{-1}$

2.3 Application of RadMod: Plume dilution study

The primary objective of developing RadMod was to conceptually advance the currently used box model framework for contrail formation simulations in order to better capture the interplay between jet dynamics and plume microphysics, as outlined in Sec. 2.1. Beyond this, RadMod is also a standalone (thermo-)dynamic RANS model that describes the evolution of the exhaust plume. This allows for plume studies beyond microphysical processes within the contrail formation framework.

In the purely dynamical framework of RadMod without accounting for microphysics, we assume the water vapor mass mixing ratio to be a passive tracer and adopt the definition given in Eq. 2.3, but take the inverse of it (as this is also a common measure of plume dilution): $\mathcal{D}^{-1}(t) = \frac{m_{\text{WV,exc,E}}}{m_{\text{WV,exc,0}}}$, where $m_{\text{WV,exc,E}}$ represents the plume's excess water vapor mixing ratio at the engine exit, and $m_{\text{WV,exc,0}}$ is the axial-dependent excess mixing ratio at the centerline. Using this formula, plume dilution increases with increasing time/axial distance behind the aircraft. RadMod helps to understand how plume dilution changes when jet properties, such as jet diameter and velocity, are altered, as occurs when aircraft size or propulsion type vary. Moreover, the model results can be compared to in-situ near-field measurements of aircraft emissions.

The following sections provide a summary of our results assessing the evolution of plume dilution with RadMod.

Section 2.3.1 validates a scaling relation from the literature, and Sec. 2.3.2 relates it to plume dilution measurements.

Section 2.3.3 describes differing definitions of the plume age and how they impact our understanding of plume dilution.

2.3.1 Scaling relation for plume dilution

Figure 2.10 presents the centerline dilution data obtained with RadMod as a function of downstream distance x , along with corresponding fitted curves. Results for different values of jet exit temperature T_E (panels) and coflow velocity U_∞ (symbols) are displayed. The jet excess velocity is fixed at 250 m s^{-1} . The coflow velocity cancels in the definition of the convective Mach number (see Eq. 2.27). Hence, higher values for jet and coflow velocity or lower jet temperatures can be chosen, as long as the convective Mach number remains below 0.3, and compressibility effects can be neglected. In the setup presented here, we restrict ourselves to coflow velocities ensuring that the jet is subsonic, i.e., $\text{Mach} < 1$. Supersonic jets are typically avoided in real-world (commercial) aircraft configurations, since shock waves would damage turbine components and the exhaust exit aperture. The simulations use a diffusion coefficient adjusted based on the comparison with the turbofan data (see Sec. 2.2.2.4).

In Fig. 2.10, the prefactors of the fitted curves increase with T_E but decrease with U_∞ . By contrast, the exponent is largely insensitive to jet temperature, though it tends to decrease with increasing U_∞ . As discussed in Sec. 2.2.2.2.2, higher jet temperatures enhance mixing and thus accelerate early dilution. In contrast, higher coflow velocities reduce the velocity gradient in the shear layer, leading to slower dilution than in cases where jet and coflow velocities differ strongly.

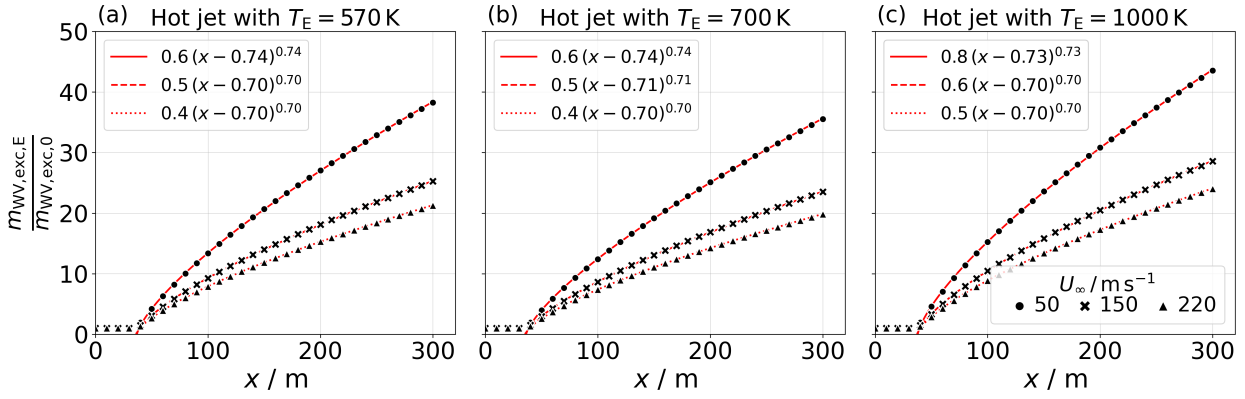


Figure 2.10: Plume dilution as a function of downstream distance for jets with increasing excess temperature. Three different coflow velocities are examined, see legend in (c). Red curves indicate fitted curves to the data points, which are shown as black symbols. Note that the axial grid resolution is 0.01 m; to improve visibility, not all data points are displayed.

Given the deviations in plume evolution between different setups, the question arises whether a single power law can describe plume dilution across a wide range of jet and engine parameters. Scaling the dilution with a function of $R_U = \frac{U_\infty}{U_J + U_\infty}$ and the downstream distance with l_m^* (l_m^* represents the momentum length scale, see Sec. 2.2.2.3) yields a data curve that is independent of coflow velocity and excess temperature. This scaling has been proposed by [Lee and Chu \(2003\)](#) using experimental data.

Figure 2.11 shows the scaled dilution versus the scaled downstream distance as simulated with RadMod. The data collapse onto a single curve. In order to test the robustness of the scaling, the set of simulations shown in Fig. 2.10 is repeated also for a jet with approximately half the jet excess velocity (orange points) and half the initial jet diameter (symbols with a magenta frame). All data points across three coflow velocities, three excess temperatures, two jet excess velocities, and two initial jet diameters align along a single curve that is described by $0.13 (x/l_m^*)^{0.78}$.

2.3.2 Comparison to measurement results

As part of the Nephel measurement campaigns, a collaboration between Airbus and DLR, the objective is to emulate a fuel cell exhaust and to characterize the resulting emissions and contrail ice crystals. An evaporation chamber designed by Airbus, serving as a fuel cell emulator, was mounted on the fuselage of a Convair C131 aircraft (emitting aircraft). During the Nephel 2 campaign, conducted in December 2023 in Minnesota, five measurement flights were performed. In these flights, an artificial tracer gas, N_2O , was released from the evaporation chamber to emulate a fuel cell exhaust plume with low jet velocity. This setup enabled the distinction between the fuel cell emulator plume and the engine exhaust plumes characterized by CO_2 emissions, subsequently detected by a following measuring aircraft, a Cheyenne Piper 400LS. In the near-field region, i.e., in the first few hundred meters behind the emitting aircraft, one of the two tracer signals was dominant, indicating that either one of the plumes was measured. In the far-field region, more than 1 km downstream, similar concentrations of CO_2 and N_2O were observed, indicating that the two plume types had become homogeneously mixed. The following analysis focuses on the evolution of N_2O dilution. The dataset comprises around 1900 measurements conducted during three flights. The excess N_2O concentration above the background as a function of downstream distance was measured. Although 3D GPS data of both the emitting and follower aircraft are available, accurately determining the precise position of each measurement within the exhaust plume remains challenging. Consequently, the fit was performed using the observed peak values, under the assumption that these correspond to measurements taken near the plume center (personal communication with Simon Braun (WOL/IPA)).

In order to compare measurement and model outcomes, input parameters for RadMod were adjusted accordingly. The following test data, provided by Simon Braun, were used: exhaust temperature $T_{exc} = 318.44$ K, jet velocity $U_J = 11.08$ m, s⁻¹, initial jet diameter $d_J = 25.4$ cm, ambient temperature $T_{amb} =$

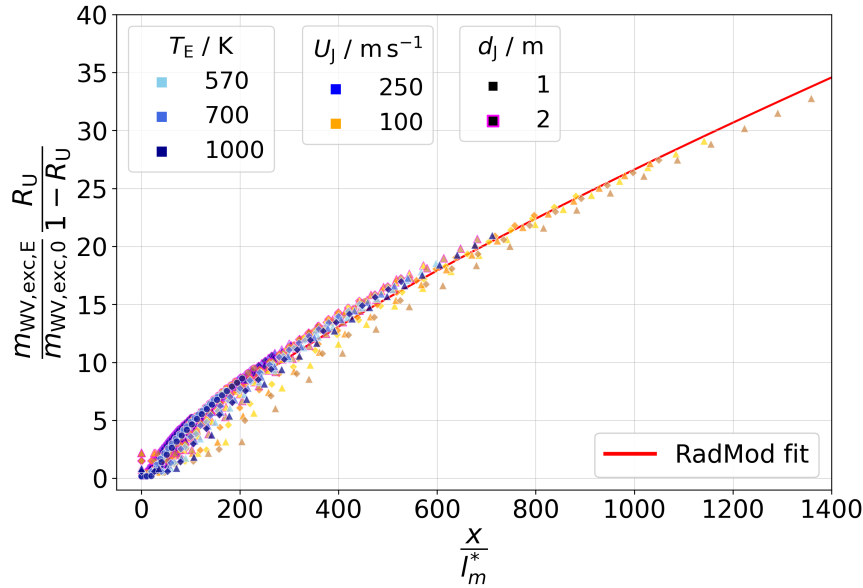


Figure 2.11: Scaled plume dilution versus scaled downstream distance. Symbols are defined as in Fig. 2.10. The color shading indicates the variation in excess temperature. Bluish tones correspond to the default jet excess velocity, while orange-like tones represent cases with decreased excess velocity. The red line shows the fitted power-law curve to all data points.

234.36 K, ambient pressure $p_{\text{amb}} = 42271$ Pa, initial N_2O molar mixing ratio in the exhaust $r_{\text{N}_2\text{O},\text{init}} = 756.6$ ppm, and aircraft velocity $U_{\text{AC}} = 92.74$ m s $^{-1}$. Assuming a molar mass for N_2O of $M_{\text{mol},\text{N}_2\text{O}} = 44.01$ g mol $^{-1}$ and dry air of $M_{\text{mol},\text{air}} = 28.96$ g mol $^{-1}$, the mass mixing ratio of N_2O calculates to $m_{\text{N}_2\text{O}} = r_{\text{N}_2\text{O}} \frac{M_{\text{mol},\text{N}_2\text{O}}}{M_{\text{mol},\text{air}}} = 0.0011$. The background molar mixing ratio of N_2O is set to 338 ppb, which corresponds to a mass mixing ratio of 5.14×10^{-7} .

To evaluate the applicability of the dilution scaling, shown in Fig. 2.11, beyond hypothetical jet and engine configurations, Fig. 2.12 presents the fitting curves of the scaled dilution from the Nephele 2 measurements and the turbofan dataset (presented in Sec. 2.2.2.4). The datasets differ in their jet diameters, exhaust temperatures, and jet and aircraft velocities, and therefore help to assess the robustness of the scaling relation. The scaled dilution curves are obtained by scaling the Nephele 2 and turbofan dilution curves as simulated with RadMod (not shown) with the respective values of $R_U/(1 - R_U)$ and l_m^* . Doing so, all three curves exhibit similar trends, with the Nephele 2 curve following $0.11 (x/l_m^*)^{0.79}$ and the turbofan curve following $0.13 (x/l_m^*)^{0.78}$ (prefactors and exponents rounded to two decimal places). The exponents are considerably closer than in the unscaled case, where values of 1.19 and 0.87 were obtained.

This constitutes a valuable tool for improving the understanding of dilution evolution and, therefore, contrail formation behind different aircraft configurations, regarding variations in propulsion systems or aircraft velocities. The demonstrated validity of the scaling relation over a wide range of parameters, including coflow velocity and excess temperature, suggests that it may help reduce the number of required contrail formation simulations in the future. However, the obtained best-fit should not be interpreted as a universal power law; further comparisons with other data sets are necessary to better constrain the diffusion coefficient used in RadMod. The analysis of the impact of further parameters on plume dilution, such as variations of the core and bypass distribution, is subject of further research. Additional datasets, simulation-based or measured, such as those from the VOLCAN campaign (VOLCAN, 2023), could help to further constrain and refine the estimated dilution exponent.

2.3.3 The "problem" with the plume age

A subtlety that has not yet been addressed concerns the treatment of the plume age. In the commonly used conceptual model of two aircraft flying in sequence at the same velocity, the plume age, i.e., the time elapsed

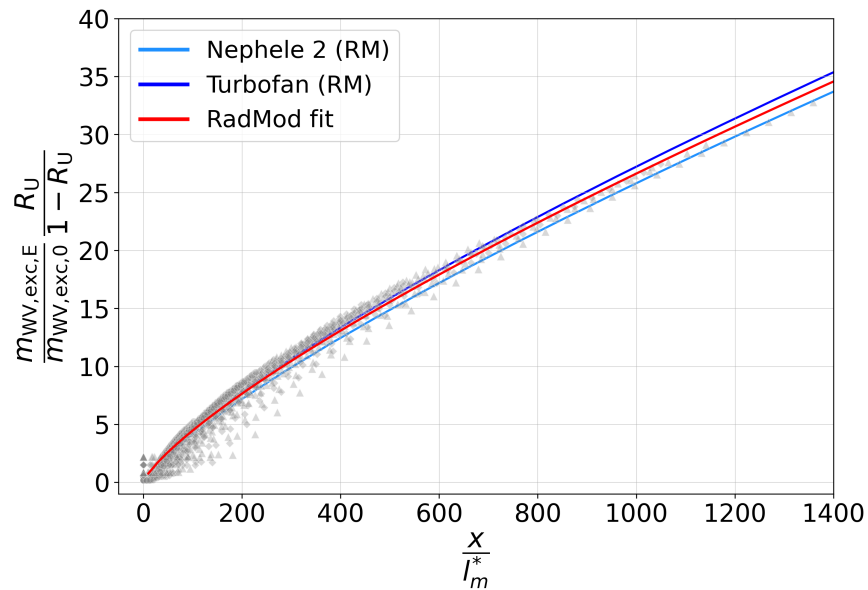


Figure 2.12: The fitted curve of Fig. 2.11 is shown in red alongside the fitted scaled dilution curves of Nephela 2 (blue) and of the turbofan data (dark blue) as simulated with RadMod (RM). The data points of Fig. 2.11 are displayed in grey.

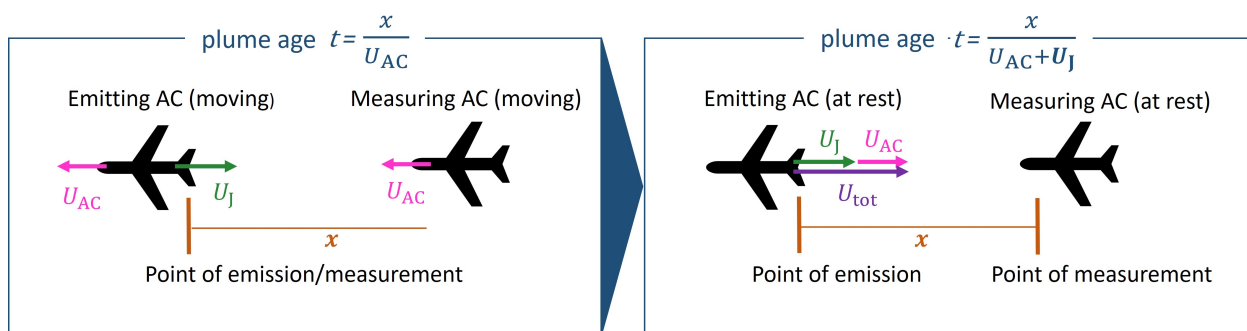


Figure 2.13: Conceptual scheme illustrating the differing definitions of plume age applied in plume dilution studies. See text for details.

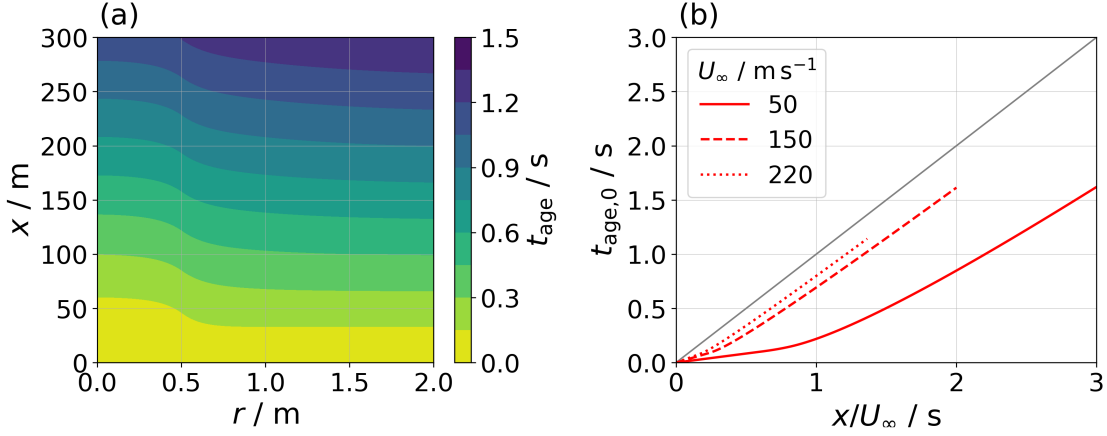


Figure 2.14: (a) Plume age as calculated via Eq. 2.42 with $U_{\infty} = 250 \text{ m s}^{-1}$ as a function of radial and axial position. (b) Plume age at the centerline versus x/U_{∞} for four different coflow velocities, differentiated by line style. The grey line indicates the one-to-one line.

since emission, is approximated as the distance between the two aircraft divided by their common velocity. This approach, illustrated in the left panel of Fig. 2.13, assumes that the emission remains stationary in the observer's frame of reference. However, this simplification neglects the fact that the exhaust jet itself leaves the emitting aircraft with a finite speed U_J , corresponding to the excess jet velocity as described in Lottermoser and Unterstrasser (2024). A more accurate interpretation, shown in the right panel of Fig. 2.13, involves a change of reference frame: Both aircraft are considered stationary, and the emission moves downstream with a total velocity U_{tot} , defined as the sum of the aircraft (or coflow) velocity and the excess jet velocity. In this frame, the plume age is given by the distance divided by U_{tot} . It is smaller than the value obtained using the first method.

An additional complication arises when considering the age of individual air parcels at different radial positions within the plume. At a fixed downstream location, air parcels closer to the plume centerline exhibit lower ages compared to those further away. This is due to the radial variation in axial velocity: Parcels near the centerline are moving faster, resulting in lower plume ages. This behavior is shown in Fig. 2.14a. The plume age is computed as

$$t_{\text{age}}(x, r) = \int_0^x \frac{1}{U_{\text{tot}}(x', r)} dx'. \quad (2.42)$$

Panel (b) shows the centerline plume age $t_{\text{age},0} = t_{\text{age}}(x, r = 0)$ simulated with RadMod. This quantity is more representative of what could be measured in practice, as it likely corresponds to the peak concentration decay. To facilitate comparison with the definition illustrated in Fig. 2.13a, it is plotted against the "classical" plume age definition, x/U_{∞} . As expected from the discussion above, $t_{\text{age},0}$ is generally smaller, since the $t_{\text{age},0}$ framework accounts for the jet's excess velocity. It is also noteworthy that both definitions converge for higher aircraft (i.e., coflow) velocities (as indicated by the dotted line approaching the one-to-one line). This behavior is consistent with physical expectations, as the relative importance of the jet velocity diminishes with increasing coflow velocity.

When plotting the scaled dilution against the scaled centerline plume age $t_{\text{age},0} \frac{U_{\infty}}{U_m^*}$, the data of the 36 parameter combinations, shown in Fig. 2.11, again collapse onto a single curve (not shown). However, the fitted exponent of 0.67 is smaller than the previously found exponent of 0.78. This supports the interpretation given above as the jet is younger in the t_{age} framework and therefore less diluted when looking at the same point on the x -axis.

2.4 Discussion and further steps with RadMod

2.4.1 Possible extensions and modifications of RadMod

2.4.1.1 Finite-volume method

RadMod solves the advection-diffusion equations for momentum, temperature, and water vapor. To simplify the numerical treatment of the system, the governing equations are transformed into a new coordinate system. The resulting form of the equation is

$$\frac{\partial c}{\partial \phi} = \frac{\partial}{\partial \psi} \left(r^2 \rho^2 U \frac{\partial c}{\partial \psi} \right), \quad (2.43)$$

where c represents either axial velocity, temperature, or water vapor mass mixing ratio. To solve this equation, a finite-difference method is applied, as described in Section A1. An alternative approach to numerically solve the equation is using finite volumes. Although the finite-difference method currently implemented in RadMod produces plausible results, this thesis includes, for the sake of completeness, a theoretical overview of how the finite-volume method can be realized within RadMod. This section is intended as a foundation for future adaptations and extensions of the numerical model. The finite-volume method offers greater flexibility in handling complex numerical meshes. For example, a cone-shaped grid that dynamically follows the expanding exhaust plume could be implemented. Such a grid configuration may improve both the numerical stability and the computational efficiency of the model compared to the existing finite-difference approach.

In the coordinate-transformed framework, two transformations have been applied: from the Cartesian to the cylindrical coordinate system $((x, y, z) \rightarrow (r, \theta, x))$ and from the cylindrical to the stream function-based coordinate system $((r, \theta, x) \rightarrow (\psi, \theta, \phi))$. As we apply RadMod for axisymmetric problems, the system reduces to two dimensions, $(r, x) \rightarrow (\psi, \phi)$.

The Jacobian for the transformation $(r, x) \rightarrow (\psi, \phi)$ reads

$$J = \begin{pmatrix} \frac{\partial r}{\partial \psi} & \frac{\partial r}{\partial \phi} \\ \frac{\partial x}{\partial \psi} & \frac{\partial x}{\partial \phi} \end{pmatrix}. \quad (2.44)$$

As we have given transformation equations of the form $\frac{\partial \psi}{\partial r}$, $\frac{\partial \psi}{\partial x}$, and $\frac{\partial \phi}{\partial x}$ (Eqs. 2.31 and 2.32), the inverse Jacobian can be written as

$$J^{-1} = \begin{pmatrix} \frac{\partial \psi}{\partial r} & \frac{\partial \psi}{\partial x} \\ \frac{\partial \phi}{\partial r} & \frac{\partial \phi}{\partial x} \end{pmatrix} \quad (2.45)$$

$$= \begin{pmatrix} U\rho r & -V\rho r \\ 0 & D_T \end{pmatrix} \quad (2.46)$$

J is then given by

$$J = \begin{pmatrix} \frac{1}{U\rho r} & \frac{V}{UD_T} \\ 0 & \frac{1}{D_T} \end{pmatrix} \quad (2.47)$$

The determinant of the Jacobian is $\det J = \frac{1}{U\rho r D_T}$.

Then, the volume element in the RadMod-transformed system is calculated from the Jacobian: $dV = \det J r d\psi d\phi = \frac{1}{U\rho D_T} d\psi d\phi$, where r is the transformation factor converting from Cartesian to cylindrical coordinates. A unit check confirms that the expression yields m^3 , as required. With the transformation vector $\vec{r} = \left(\frac{1}{U\rho r} \psi + \frac{V}{UD_T} \phi, \frac{1}{D_T} \phi \right)$, the surface elements are

$$dA_\psi = \frac{1}{D_T} \left(1 + \frac{V^2}{U^2} \right)^{1/2} r d\phi \quad \text{and} \quad (2.48)$$

$$dA_\phi = \frac{1}{U\rho} d\psi. \quad (2.49)$$

It follows that $dV = \frac{1}{\rho r (V^2 + U^2)^{1/2}} dA_\psi d\psi$ and $dV = \frac{1}{D_T} dA_\phi d\phi$.

Integrating both sides of Eq. 2.43 over a volume V and applying the divergence theorem yields

$$\oint \frac{c}{D_T} dA_\phi = \oint r \rho U \frac{\partial c}{\partial \psi} \frac{1}{(V^2 + U^2)^{1/2}} dA_\psi. \quad (2.50)$$

In a discretized form, this equation becomes

$$\left(\frac{c}{D_T U \rho} \Delta \psi \right)_{i+1/2} - \left(\frac{c}{D_T U \rho} \Delta \psi \right)_{i-1/2} = \left(\frac{r^2 \rho}{D_T} \frac{\Delta c}{\Delta \psi} \Delta \phi \right)_{j+1/2} - \left(\frac{r^2 \rho}{D_T} \frac{\Delta c}{\Delta \psi} \Delta \phi \right)_{j-1/2}, \quad (2.51)$$

where the indices i and j refer to the ϕ - and ψ -directions, respectively (equivalent to the finite-difference formulation). The half indices indicate that the fluxes across the volume boundaries are calculated. In the numerical implementation, the values given at the grid cell boundaries are used instead of the values at the grid cell centers, e.g., $c_{\text{center},j+1/2} = c_{\text{border},j+1}$. As in the finite-difference method, evaluating the $\frac{\Delta c}{\Delta \psi}$ terms at $i + 1$ yields a tridiagonal system that can be solved similarly to the procedure presented in Sec. A1.

2.4.1.2 Turbulence model

In the current formulation, the diffusivity in RadMod is described by $D_T = 0.028 r_{0.5}(x) U_0(x)$ with $r_{0.5}$ and $U_0(x)$ as half-width radius and axial centerline velocity, respectively, and the value of 0.028 empirically determined for the self-similar regime. The comparison with CFD data for a turbofan engine (Sec. 2.2.2.4) has shown a limitation of using this diffusion model, as it seems to be valid only in the region where the turbulent jet has reached its self-similar state. In the initial phase, i.e., in the first 40 m downstream, the diffusion coefficient had to be modified manually in order to match the axial velocity profiles (CFD data). This points toward the possibility of using an alternative turbulence model for turbulence closure. One of the most common models is the $k - \epsilon$ model, which includes two additional transport equations for the turbulent kinetic energy k and the turbulent dissipation ϵ to represent the evolution of the turbulent flow properties. The equations for a steady-state, axisymmetric jet read as follows (Lauder and Spalding, 1974):

$$\rho U \frac{\partial k}{\partial x} + \rho V \frac{\partial k}{\partial r} = \frac{\mu_t}{\sigma_k} \frac{1}{r} \frac{\partial}{\partial r} \left(\rho r \frac{\partial k}{\partial r} \right) + P_k + P_b - \rho \epsilon \quad (2.52)$$

$$\rho U \frac{\partial \epsilon}{\partial x} + \rho V \frac{\partial \epsilon}{\partial r} = \frac{\mu_t}{\sigma_\epsilon} \frac{1}{r} \frac{\partial}{\partial r} \left(\rho r \frac{\partial \epsilon}{\partial r} \right) + C_{1\epsilon} \frac{\epsilon}{k} (P_k + C_{3\epsilon} P_b) - C_{2\epsilon} \rho \frac{\epsilon^2}{k}. \quad (2.53)$$

Here, the turbulent viscosity is calculated as $\mu_t = \rho C_\mu \frac{k^2}{\epsilon}$. The terms P_k and P_b describe the production of k and the effect of buoyancy, respectively. σ_k , σ_ϵ , $C_{1\epsilon}$, $C_{2\epsilon}$, and $C_{3\epsilon}$ are model constants derived from experiments (Lauder and Sharma, 1974). Since the $k - \epsilon$ model involves a coupled system of equations, initial guesses for k and ϵ can be used and iteratively updated until convergence is reached.

The $k - \epsilon$ turbulence model is well established and offers several advantages, including computational efficiency and suitability for high-Reynolds-number, free-stream flows (Lauder and Spalding, 1974), such as those found in aircraft jet emissions into the atmosphere, which RadMod is designed to simulate. It may provide improved accuracy over the currently used diffusion model, particularly when compared against CFD data. Assessing its performance in this context is planned for future work.

2.4.2 RadMod-LCM coupling

The core idea behind coupling the dynamical model RadMod with the microphysics module LCM is to eliminate the need for externally prescribed fluid fields (e.g., from trajectory data) and instead simulate the evolution of momentum, temperature, and water vapor mixing ratio using the advection–diffusion equations (Eqs. 2.24–2.26) in an "online" microphysics approach. At each downstream position, these fields are passed to the LCM routines. Since LCM operates in temporal space, a corresponding time step is computed at each radial position as $\Delta t_{\text{LCM}}(r) = \Delta x_{\text{RadMod}}/U(x, r)$, where $U(x, r)$ is the local axial velocity. The microphysical processes in LCM modify the thermodynamic fields, and these changes are subsequently passed back into

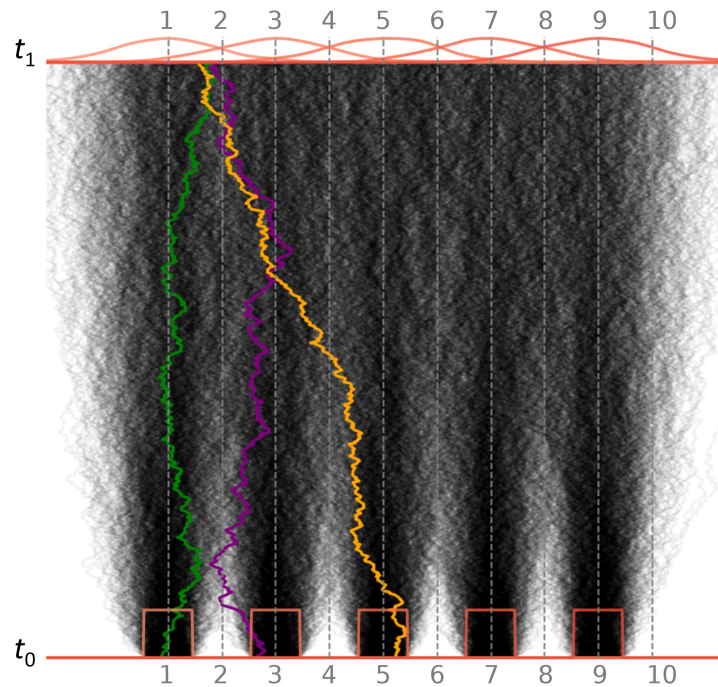


Figure 2.15: Illustration of Eulerian and Lagrangian approach for diffusing SIPs for an initial unit concentration at time step t_0 . Ten grid boxes are displayed. For better visibility, only every second grid cell contains particles. The grey lines mark the centers of the grid boxes. The particle trajectories are shown as black lines, while three representative particle trajectories are highlighted in orange, green, and purple, illustrating the potentially large radial displacement a single particle can experience. In this example, a particle from grid cells 1, 3, and 5 travels to the second grid cell. The density of particles at the next time step t_1 are presented by red curves.

RadMod as source terms. This section focuses on the treatment of SIPs in the coupled RadMod-LCM system. As in EULAG-LCM (Sec. 3.1), the RadMod-LCM system treats a two-phase flow, consisting of the fluid fields, representing the expanding and cooling jet plume, and the SIPs, representing the aerosols and ice crystals, moving in that fluid. In LCM, SIPs are treated in a Lagrangian framework, with the properties of each individual SIP tracked over time. In contrast, SIP diffusion in RadMod can be simulated using either an Eulerian or a Lagrangian approach.

In both cases, a certain number of SIPs is initialized within the grid boxes, depending on the specific simulation setup. At initialization, SIPs are assigned weights, where the weight indicates the number of real particles each SIP represents. In the standard configuration, an initial aerosol number concentration is prescribed uniformly across all grid cells, assuming that the plume is initially slightly mixed with ambient air. Alternatively, if a particle emission source is considered, SIPs are additionally initialized within the grid cells corresponding to the initial jet area. For kerosene combustion, soot particles are emitted, and the number of emitted SIPs is determined by the soot emission index and the aircraft's fuel consumption. In contrast, hydrogen combustion does not produce soot; therefore, only ambient aerosols and optionally volatile particles are initialized as SIPs. A comparison between the Eulerian and Lagrangian particle diffusion approach is shown in Fig. 2.15.

Eulerian

To illustrate particle diffusion in the Eulerian approach, consider a specific grid cell j , where a unit particle concentration is initially prescribed—that is, the concentration in cell j is set to one, while it is zero in all other cells. The concentration field then evolves according to the advection-diffusion equation. After

one time step, the initial unit concentration in cell j spreads to neighboring cells ($\dots, j - 2, j - 1, j + 1, j + 2, \dots$), which now also exhibit nonzero concentrations. To reflect the evolved concentration distribution, a loop over all SIPs in cell j is performed. Each SIP is replicated into neighboring grid cells that now have a nonzero concentration. The SIP's weight in each target cell is scaled according to the concentration value in that cell. For instance, a neighboring cell (e.g., $j + 1$) may have a concentration of 0.9, while a more distant cell may have 0.02. A SIP with a weight of 500000 would thus be replicated into grid cell $j + 1$ with a weight of 0.9×500000 and into the farther cell with 0.02×500000 . A threshold concentration can be defined to determine whether SIP replication into a given grid cell occurs, preventing unnecessary creation of low-weight SIPs. To avoid excessive computational cost due to the continuous production of SIPs, a SIP merging operation is applied. SIPs that share the same phase (i.e., dry aerosol, water droplet, or ice crystal) and type (i.e., soot, ambient aerosol, or volatile particle), and that have similar sizes, are merged into a single SIP. This merging step prevents an unmanageable increase in SIP numbers while preserving the relevant microphysical properties of the particle population. In the subsequent time step, the updated SIP population in grid cell j is again represented by a unit concentration, which is then diffused, repeating the process. This procedure is repeated for the next grid cell $j + 1$, and so on along the radial direction. An illustration of this process is shown by the red curves in Fig. 2.15. Starting from unit concentrations at the bottom row, the particle concentrations diffuse downstream (for illustration purposes, five particle concentrations evolve simultaneously, while in the model, it is one after the other). At the next time step t_1 , again a unit concentration is prescribed in each grid cell (not shown), representing the particles that remained there and/or have been diffused into that grid cell.

Lagrangian

In the Lagrangian approach, the position and velocity of each SIP are explicitly tracked and updated at every time step as they move radially and downstream. The SIPs generally follow the mean velocity field $\vec{v} = (U, V)$ calculated by RadMod, and additional turbulent velocity fluctuations \vec{v}' are superimposed. \vec{v}' causes the particles to deviate from the flow streamlines described by \vec{v} . The SIP velocity can be described by

$$\vec{v}_{\text{SIP}}(t) = \vec{v}(t) + \vec{v}', \quad (2.54)$$

where the second component accounts for the turbulent particle motion calculated by

$$\vec{v}'(t) = R(t) \vec{v}'(t - \Delta t) + \sqrt{1 - R(t)^2} \sigma_v \xi. \quad (2.55)$$

$R(t)$ is the autocorrelation function, and ξ represents a random variable drawn from a normal distribution with a mean of zero and standard deviation of one (Schilling et al., 1996; Etling, 2008). How to calculate $R(t)$ and the velocity variance σ_v is explained in the following.

The turbulent diffusion in RadMod is described via Eq. 2.12 relating the turbulent diffusion coefficient to the mean axial velocity at the centerline and the half-width radius. Alternatively, the turbulent diffusivity can be expressed via the Lagrangian timescale τ_L (Davidson and McComb, 1975; Schilling et al., 1996)

$$D_T = \overline{u^2} \tau_L, \quad (2.56)$$

where u denotes the axial velocity fluctuation, and $\overline{u^2} = \sigma_u^2$ is the variance of the axial velocity fluctuations representing the turbulence intensity. The turbulent kinetic energy TKE is proportional to σ_u^2 . Turbulence is assumed to be isotropic, i.e., the velocity variances are equal in all directions ($\sigma_u^2 = \sigma_v^2$). Therefore, turbulent diffusivity is also treated as isotropic $D_{T,x} = D_{T,y}$. The Lagrangian timescale τ_L characterizes the duration over which a fluid parcel's velocity remains correlated with its initial turbulent state. It can be obtained from the integral of the Lagrangian autocorrelation function

$$\tau_L = \int_0^\infty R(\tau) d\tau, \quad (2.57)$$

where $R(t)$ is defined as

$$R(\tau) = \frac{\overline{u(t)u(t+\tau)}}{\overline{u(t)^2}} \approx \exp\left(-\frac{\tau}{\tau_L}\right). \quad (2.58)$$

This function quantifies the degree of correlation between the current and future turbulent velocities. As $\tau \rightarrow \infty$, the correlation decays exponentially, and the fluid parcel increasingly "forgets" its initial turbulent velocity (Davidson and McComb, 1975; Etling, 2008). In case of $R = 0$, the fluctuating velocity component would be completely uncorrelated to the previous movement and would just move randomly. In case $R = 1$, the fluctuations are correlated, and the velocity fluctuation the particle experiences is the same as in the previous time step.

The velocity variance σ_u is linked to the turbulent diffusivity via a local length scale l : $\sigma_u = D_T/l$ (Pope, 2000). Consequently, the Lagrangian timescale can also be written as $\tau_L = l/\sigma_u$. Based on experimental data (Hussein et al., 1994), l is derived via

$$l(x, r) = \begin{cases} 0.12 r_{0.5}(x) & \text{for } 0.1 < r/r_{0.5} < 2.1 \\ 0 & \text{else} \end{cases}. \quad (2.59)$$

The particle response or relaxation timescale is defined as

$$\tau_p = \frac{\rho_p D_p^2}{18 \mu}, \quad (2.60)$$

which describes the duration of how long the particle needs to adjust to the fluid velocity (Davidson and McComb, 1975). ρ_p and D_p are the particle's density and diameter, respectively, and μ denotes the dynamic air viscosity.

Based on work of Tchen (1947) and Hinze (1959), the particle diffusion coefficient is defined by

$$D_{T,p} = D_T \frac{\tau_L}{\tau_L + \tau_p}. \quad (2.61)$$

This formulation reflects how the particle's inertia limits its ability to follow fluid fluctuations.

In principle, when modeling the diffusion of SIPs in RadMod-LCM, the turbulent diffusivity D_T should be replaced by the particle diffusivity $D_{T,p}$. However, for our use cases (modeling the transport of aerosols, droplets, and ice crystals) a simple calculation reveals that $\tau_p \ll \tau_L$ (on the order of $< 10^{-6}$ s compared to 10^{-4} s). Thus, particle inertia can be considered negligible, and the particles are assumed to follow the turbulent fluid motion. An adjustment of the diffusion coefficient is therefore, in a first approximation, not required.

3

Vortex Phase

Section 3.1 gives an introduction to the model EULAG-LCM that is used to simulate the evolution of young contrails during the vortex phase and their transition into aged contrail cirrus during the dispersion phase. Since the LCM has already been described in detail in Sec. 2.1, the focus is on the EULAG component. Section 3.2 is an excerpt of the publication *Lottermoser A. and Unterstrasser S. (2025). High-resolution modeling of early contrail evolution from hydrogen-powered aircraft. Atmos. Chem. Phys., 25:7903–7924. DOI: 10.5194/acp-25-7903-2025*. This study relates to Research question 2 (see Sec. 1.4), addressing how the use of alternative fuels affects the evolution of young contrails during the vortex phase.

3.1 Introduction to the EULAG-LCM model

The treatment of dynamic processes in EULAG-LCM is based on the anelastic, non-hydrostatic model EULAG (Smolarkiewicz and Margolin, 1997; Smolarkiewicz and Prusa, 2002; Grabowski and Smolarkiewicz, 2002; Prusa et al., 2008). The governing equations are

$$\frac{D\vec{v}}{Dt} = -\nabla \left(\frac{p'}{\bar{\rho}} \right) - \vec{g} \frac{\theta'}{\bar{\theta}} - \vec{f} \times \vec{v}' + D_{\vec{v}} \quad (3.1)$$

$$\frac{D\theta'}{Dt} = -\vec{v}' \cdot \nabla \theta_e + Q_R + Q_H + D_{\theta} \quad (3.2)$$

$$\frac{Dm_{WV}}{Dt} = -Q_{\text{dep}} - Q_{\text{con}} + D_{m_{WV}} \quad (3.3)$$

$$\nabla \cdot (\bar{\rho} \vec{v}) = 0, \quad (3.4)$$

where \vec{v} is the wind vector, p the pressure, ρ the air density, θ the potential temperature, and m_{WV} the mass mixing ratio of water vapor. The vector \vec{g} denotes gravitational acceleration (directed vertically), and \vec{f} is the Coriolis parameter vector. The operator D/Dt represents the material derivative. Variables with a bar correspond to anelastic, hydrostatic background profiles, while primed quantities indicate deviations from the environmental state, denoted by the subscript e , such that $\theta = \theta_e + \theta'$. The environmental state is typically a solution to the equations. The source terms Q_R , Q_H , Q_{dep} , and Q_{con} represent radiative heating/cooling, latent heat release, and water vapor deposition and condensation, respectively. The terms D_u , D_{θ} , and $D_{m_{WV}}$ denote turbulent diffusion coefficients for momentum, heat, and water vapor.

In EULAG, the governing equations can be solved using either a Lagrangian or an Eulerian framework. In this study, the Eulerian approach is employed, using the MPDATA algorithm (Smolarkiewicz and Margolin, 1998), a positive-definite advection transport scheme. Following the notation of Grabowski and

Smolarkiewicz (2002), the implicit solution for a generic prognostic variable Ψ (which may represent one of the three velocity components or potential temperature) is given by

$$\Psi_i^{n+1} = LE_i(\tilde{\Psi}) + \frac{1}{2}\Delta t F_i^{n+1}, \quad (3.5)$$

where LE denotes the MPDATA transport operator, Δt is the time step of the model, and F represents the forcing terms on the right-hand sides of Eqs. 3.1 and 3.2. The subscripts n and i indicate the temporal and spatial indices, respectively. It holds $\tilde{\Psi} = \Psi_i^n + \frac{1}{2}\Delta t F_i^n$. In order to solve Eq. 3.5, the forcings for the next time step $n + 1$ are needed. As the microphysics in EULAG-LCM requires a smaller time step than the EULAG-dynamical time step, Δt in EULAG is subdivided into several smaller time steps, $\Delta t = N \Delta t_{\text{mic}}$. During the integration from time level n to $n + 1$, the microphysical variables Ψ evolve through intermediate stages Ψ^k , each associated with a sub-step forcing term F^k . The forcing term at the next time step, F^{n+1} , is then calculated as a mean over all small time steps Δt_{mic} (Grabowski and Smolarkiewicz, 2002; Sölch, 2008).

Atmospheric diffusion in EULAG is modeled by resolving large-scale turbulent fluctuations and by using a subgrid-scale turbulence model based on the TKE approach (Unterstrasser and Gierens, 2010a). During the vortex phase (~ 1 m resolution) and dispersion phase (~ 10 m resolution), the grid spacing is smaller than the contrail dimensions, so most of the turbulent diffusion is captured by the resolved scales rather than the subgrid-scale model. In a-priori simulations, turbulent background fields are generated by superimposing uniform velocity perturbations in both the horizontal and vertical directions, denoted by u' and v' , respectively, onto the mean flow. The root-mean-square (rms) value of the perturbations, $\left(\sum_i (u'^2 + v'^2)\right)^{0.5}$, where i sums over the grid boxes, decays over time until reaching a quasi-steady state, after which it decreases only slowly. At this point, the a-priori simulation is considered complete and serves as the initialized background field for subsequent contrail simulations. Since the rms velocity remains nearly constant, no external turbulence forcing is required during the simulations. Turbulence is anisotropic in a stably stratified atmosphere, as stable stratification counteracts vertical mixing. Hence, horizontal velocity fluctuations dominate over vertical ones, leading to stronger horizontal than vertical contrail spreading. The validity of using a two-dimensional setup to generate these turbulent background fields was confirmed by comparing passive tracer diffusion results with three-dimensional data from Dürbeck and Gerz (1996).

Particles in EULAG

In EULAG-LCM, the air and particles are modeled as a two-phase flow. The Lagrangian simulation particles (see Sec. 2.1) are advected through the fluid, which is governed by Eqs. 3.1-3.4. In the Eulerian framework of EULAG, fluid properties such as wind velocity, potential temperature, and water vapor mass mixing ratio are defined in discrete grid cells. In contrast, the Lagrangian simulation particles representing ice crystals (Sec. 2.1) can occupy discrete positions within each grid cell. To compute microphysical processes such as advection, diffusional growth, sublimation, and sedimentation, volume-averaged values of the fluid properties within the respective grid cell are used. These values are assumed to remain constant over one dynamical time step Δt . To account for atmospheric turbulence, fluctuations in wind, temperature, and humidity are superimposed on the grid cell values.

Interaction between particles and the fluid occurs through the source terms Q . For instance, when water vapor from the ambient condenses onto a droplet, the droplet's mass increases according to the diffusional growth equation, while the water vapor mass mixing ratio in the fluid decreases accordingly, ensuring a closed water mass budget.

The particle trajectories are determined by the sum of the fluid velocity \vec{v} and an additional particle velocity component \vec{v}_p . This additional velocity accounts for effects from turbulent velocity fluctuations and particle inertia. The inertial component corresponds to the sedimentation velocity, while the turbulent component is modeled using a Lagrangian autocorrelation function, assuming that particle velocities remain approximately constant between time steps. Additionally, a stochastic velocity perturbation is introduced, drawn from a normally distributed random number with a standard deviation proportional to the TKE . Further details are provided in Sölch and Kärcher (2010).

Measurements of ice crystal habits and sizes in young contrails (age < 0.5 h) have shown mean particle diameters of 1 to 10 μm , with crystals predominantly exhibiting near-spherical shapes (Petzold et al., 1997; Poellot et al., 1999; Schröder et al., 2000). In aged contrails (age 15–90 min), ice crystal habits deviate from spherical, and more complex shapes have been observed (Heymsfield et al., 1998; Lawson et al., 1998). Consequently, in the contrail formation regime, only spherical particles are considered due to their small size. As ice crystals grow during the transition from contrail to contrail cirrus, this assumption becomes invalid. To account for more realistic particle shapes in this regime, EULAG-LCM employs empirical relationships derived from field observations by Mitchell (1996) and Heymsfield et al. (2002):

$$m_i = \alpha D_i^\beta \quad (3.6)$$

$$A_i = \gamma D_i^\sigma. \quad (3.7)$$

Here, m_i is the mass of an ice crystal, D_i is its maximum dimension, and A_i denotes the projected area. The coefficients α , β , γ , and σ are dependent on the crystal habit (Sölch and Kärcher, 2010).

The sedimentation velocity in EULAG-LCM is computed based on the particle's maximum dimension, mass, and projected area, which are derived from Eqs. 3.6 and 3.7. Following the approach of Heymsfield and Iaquinta (2000), Mitchell (1996), and Mitchell and Heymsfield (2005), these properties are used to determine the particle's Reynolds number. The sedimentation velocity is then calculated as

$$v_{t,i} = \frac{Re \eta_{\text{amb}}}{D_i \rho_{\text{amb}}}, \quad (3.8)$$

where η_{amb} is the dynamic viscosity, and ρ_{amb} is the ambient air density. For instance, the sedimentation velocity of a hexagonal column with a maximum dimension of 100 μm is approximately 20 cm s^{-1} (Sölch and Kärcher, 2010). In the LCM box model (Sec. 2.1), sedimentation is not accounted for, as the particles are initially too small for this effect to be significant.

Simulations with EULAG-LCM

In order to perform a LES with a large number of simulation particles, the high-performance computing cluster with parallel processing is used at Deutsches Klimarechenzentrum (DKRZ). The 3D simulation domain is subdivided into subdomains, each assigned to a single processor. The number of grid cells in the x - and y -directions is chosen to ensure that each processor handles the same number of grid cells, enabling a balanced computational load. This 2D domain decomposition decreases the simulation run times.

In the case of a 3D vortex phase simulation, the runtime can extend up to 45 h. Since the maximum wall time at DKRZ is limited to 8 h, the simulation must be split into several sub-simulations. This requires storing the thermodynamic fields and particle data at the end of each run, which are then read in by the subsequent simulation. To streamline this process, a Python module is currently being developed to manage and automate the initialization process steps and sub-simulation workflow. This tool, developed by working student Pedro Munoz Jimenez, was in the development stage at the time of writing this thesis. For dispersion phase simulations, which are performed in two dimensions in this study, the runtime is typically <2 h, so a restart process of sub-simulations is not required.

3.2 High-resolution modeling of early contrail evolution from hydrogen-powered aircraft

The following Sects. 3.2.1– 3.2.4 are the Sects. 2–5 of Lottermoser and Unterstrasser (2025). Only the section references and the formatting have been partly adapted to fit the structure of the thesis.

Section 3.2.1 describes the simulation setup and the set of simulations, Sec. 3.2.2 investigates the sensitivity of hydrogen (H_2) contrails to various parameters and presents the updated ice crystal loss parametrization. The implications of the results are discussed in Sec. 3.2.3, and Sec. 3.2.4 provides the conclusions.

3.2.1 Methods

3.2.1.1 Numerical setup and set of simulations

Generally, we assume ambient conditions such that contrails form and persist, i.e., the atmosphere is sufficiently cold and moist (Schumann, 1996; Gierens and Spichtinger, 2000).

As H₂-propulsion technology is likely to be initially employed on smaller aircraft, we conduct simulations for both an aircraft with a wingspan of $b_{\text{span}} = 60.3$ m (A350/B777-like aircraft, default) and a smaller aircraft with a wingspan of 34.4 m (A320/B737-like aircraft). Generally, the setups are consistent with previous EULAG-LCM studies, where contrails from six different aircraft types were systematically investigated (Unterstrasser and Görsch, 2014; Unterstrasser, 2016). Throughout the text, when we use "A350" ("A320") aircraft, we are generically referring to an "A350/B777-like" aircraft ("A320/B737-like" aircraft).

The number of grid points in our default model domain is $n_x = 384$, $n_y = 200$, and $n_z = 600$, where x , y , and z denote the transverse, longitudinal (along the flight direction), and vertical direction, respectively. The size of the simulation domain is adjusted based on specific conditions. For example, weaker stratification requires a larger domain, as the vortices descend further and exhibit more pronounced meandering due to the Crow instability (Crow, 1970). Additionally, for high cruise-altitude temperatures, i.e., $T_{\text{CA}} = 230, 233,$ and 235 K, the vertical domain size was increased from 600 to 800 grid points for the A350 and from 856 to 1112 grid points for the A320. The grid resolution is 1 m along the transverse and vertical and 2 m along the longitudinal direction. For simulating an A320 aircraft, the resolution is changed to $dx = dz = 0.57$ m and $dy = 1.14$ m as described in Unterstrasser and Görsch (2014). For both aircraft types, the domain size in the flight direction is chosen to allow the formation of the most unstable Crow mode. Periodic boundary conditions are applied in the horizontal and longitudinal directions. In the vertical direction, rigid boundary conditions are used, meaning that the vertical velocity component is zero at the top and bottom boundaries of the simulation domain. The total simulated time is around 6 to 7 min, where the time step increases from an initial value of 0.03 s to 0.08 s at later stages of the simulation.

The simulations start at a plume age of several seconds. At this stage, it can be assumed that the ice crystal formation is finished and the vortices have fully rolled up. We initialize the ice crystals in two disks (one per wing) with uniform ice crystal number concentrations. The flow field is a superposition of a turbulent background field and two counter-rotating Lamb-Oseen vortices. The vortex circulation, vortex core radius, and plume radius depend on the aircraft type and are given in Tab. 3.1.

We incorporate the effects of a H₂-propulsion system by varying the initial number of ice crystals (N_0) and the emitted water vapor mass (I_0). The default values of the initial ice crystal number correspond to typical values of the fuel flow rate, denoted by \dot{m}_F , and an apparent ice emission index $\text{EI}_{\text{iceno}} = 2.8 \times 10^{14} \text{ kg}^{-1}$ (Unterstrasser and Görsch, 2014), which represents a typical kerosene contrail. N_0 is then determined by

$$N_0 = m_C \times \text{EI}_{\text{iceno}}, \quad (3.9)$$

where the fuel consumption m_C is defined as $m_C := \dot{m}_F / U_\infty$. U_∞ represents the aircraft velocity. The reference values are $N_{0,\text{ref}} = 0.85 \times 10^{12} \text{ m}^{-3}$ for an A320 aircraft and $3.38 \times 10^{12} \text{ m}^{-3}$ for an A350 aircraft. To explore a broad range of scenarios, we scale N_0 up and down by factors of 10 and 100 relative to $N_{0,\text{ref}}$. The downscaling simulations are supposed to cover H₂-combustion scenarios. Conversely, the upscaling simulations could represent scenarios involving an H₂-fuel cell propulsion system with HDN occurring (see Sec. 1.3). Varying the number of ice crystals in the model is achieved by varying the weight of the SIPs, which keeps their total number roughly the same. Clearly, the assumptions on the initial ice crystal number are made for hypothetical aircraft designs, and the research on contrail formation processes in H₂ plumes started only recently (Bier et al., 2024; Ponsonby et al., 2024). A more in-depth discussion of the representativity of our N_0 choice is deferred to Sec. 3.2.3.

Analogously to N_0 , the emitted water vapor mass is calculated using

$$I_0 = m_C \times \text{EI}_{\text{H}_2\text{O}}, \quad (3.10)$$

where $\text{EI}_{\text{H}_2\text{O}}$ is the emission index of water vapor, with a value of 1.26 kg kg^{-1} for all aircraft types (Bier et al., 2024). We increase I_0 by multiplying the default values, 3.7 g m^{-1} for an A320 aircraft and 15.0 g m^{-1}

for an A350 aircraft (referred to as $I_{0,\text{kero}}$), by 2.57, resulting in 9.51 g m^{-1} and 38.55 g m^{-1} (referred to as I_{0,H_2}), respectively. The value of 2.57 corresponds to the ratio of the emission index of water vapor divided by the combustion heat (Q) of H_2 to kerosene (Bier et al., 2024). Note that N_0 and I_0 are given in units of "per meter of flight path". Table 3.2 summarizes the key differences between H_2 and kerosene fuel and exhaust properties.

We want to mention one caveat that is crucial for properly interpreting the comparison between the H_2 and kerosene scenarios. According to Tab. 3.2, switching from kerosene to H_2 , the water vapor emission index increases by a factor of 7.1, while the specific heat of combustion is a factor of 2.79 higher. The energy-specific water emission is then 2.57 times higher, which is, by the way, a crucial difference affecting the contrail formation process and potential contrail coverage (Schumann, 1996; Bier et al., 2024; Kaufmann et al., 2024). Achieving the same work rate with both fuel types, the H_2 fuel consumption is 2.79 times lower, while the water vapor emission (per flight distance) I_0 is 2.57 times larger. Moreover, it is our design choice to assume the same $N_{0,\text{ref}}$ value for both fuel scenarios. This implies that the reference apparent ice emission index ($\text{EI}_{\text{iceno,ref}}$) of the H_2 scenarios, i.e., those simulations with a higher I_0 value, is actually by a factor of 2.79 larger. Comparing a factor "100 down" simulation with a larger I_0 value, as a typical representative of a H_2 contrail, with a conventional kerosene contrail, i.e., reference N_0 and smaller I_0 value, must not be interpreted as a factor of 100 variation in $\text{EI}_{\text{iceno,ref}}$. The difference is actually smaller, with a factor of approximately 36.

Following, e.g., Unterstrasser and Sölch (2010), the initial ice crystal size distribution is represented by a lognormal distribution with a width parameter r_{SD} . We adopt a default value of $r_{\text{SD}} = 3.0$ and explore variations with a narrower ($r_{\text{SD}} = 1.0$, monodisperse) and broader ($r_{\text{SD}} = 4.0$) initial size distribution, as previous studies have identified this parameter as significant (Unterstrasser and Sölch, 2010; Unterstrasser, 2014). Note that other modeling studies that initialize the contrails at an earlier state without the specification that all emitted water vapor has already been deposited on the ice crystals show a weaker impact of the width parameter (Lewellen et al., 2014). We conducted simulations only with a 100-fold increase or decrease in N_0 when altering the width parameter to reduce the number of simulations.

Figure 3.1 shows the mean ice crystal radius versus the initial number of ice crystals for kerosene and H_2 water vapor emission. For this estimate, we use a density of ice, $\rho_i = 0.92 \text{ g cm}^{-3}$, and assume spherical particles, which is a reasonable approximation for small ice crystals with aspect ratios close to one. The radius corresponding to the mean particle mass, r_0 , is then approximated by $\sim \left(\frac{I_0}{\rho_i N_0}\right)^{1/3}$, assuming that all emitted water vapor is deposited onto the ice crystals. While the LCM represents ice crystal habits as hexagonal columns, this simplified estimate for r_0 serves as a first-order approximation to illustrate the general relationship between N_0 , I_0 , and the resulting crystal size, as shown in Fig. 3.1. A higher N_0 value generally results in a smaller mean radius, as the total amount of water is distributed among more particles. It is also evident that the initial water content I_0 directly impacts the initial particle size: The higher the I_0 , as indicated by triangles that represent the H_2 case, the larger the initial particles. The initial mean ice crystal radii remain unaffected by a variation in the initial width of the size distribution r_{SD} .

Additionally, we investigate the influence of different atmospheric conditions on the evolution of contrail ice crystals. Previous research has highlighted the importance of the ambient temperature at cruise altitude (T_{CA}), the ambient relative humidity with respect to ice ($\text{RH}_{i,\text{amb}}$), and the atmospheric stratification (N_{BV}) (described by the Brunt-Väisälä frequency) as key input parameters (Lewellen et al., 2014; Unterstrasser, 2016). We vary these parameters as outlined in Tab. 3.1. At the lower boundary of the simulation domain, we prescribe an air pressure of $p_0 = 250 \text{ hPa}$ and an air density of approximately $\rho_{\text{air},0} = 0.4 \text{ kg m}^{-3}$. For ambient temperature, we prescribe cruise-altitude values of $T_{\text{CA}} = 217, 225, 230, 233,$ and 235 K . The relative humidity with respect to ice is assumed to be constant throughout the entire simulation domain and set to either 110 or 120%. We use a background turbulence field with an eddy dissipation rate of $\epsilon = 10^{-7} \text{ m}^2 \text{ s}^{-3}$. The pressure and temperature vertical profiles are computed for an atmosphere with a vertically constant Brunt-Väisälä frequency according to Eq. 2 in Clark and Farley (1984). At cruise altitude, the resulting air pressure ranges from 231 to 235 hPa, depending on Brunt-Väisälä frequency and temperature. In Tab. 3.1, an average air pressure value is provided. It would seem appropriate to vary the ambient pressure in combination with T_{CA} to reflect a change in flight altitude. However, a variation in

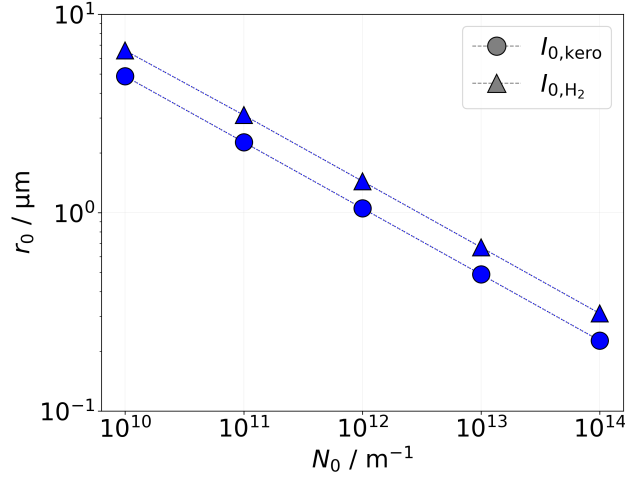


Figure 3.1: Mean initial ice crystal radius as a function of the initial number of ice crystals. Its sensitivity regarding the microphysical initialization in terms of I_0 (symbol) is depicted.

pressure has only little impact on the simulated contrail properties, as demonstrated in Sec. A3. This is because the background water vapor mass concentration is independent of ambient pressure. Hence, we do not adapt p_0 .

In Tab. 3.1, values that are marked with an asterisk refer to the default simulation of an A350 aircraft with a water vapor emission value that corresponds to a kerosene combustion system $I_0 = 15.0 \text{ g m}^{-1}$ and an initial ice crystal number $N_0 = 3.38 \times 10^{12} \text{ m}^{-1}$ at an ambient temperature of 217 K, an ambient relative humidity with respect to ice of 120 %, and a standard value for atmospheric stability of $1.15 \times 10^{-2} \text{ s}^{-1}$. Ice crystal formation is improbable for ambient temperatures exceeding 233 K, as this surpasses the homogeneous freezing temperature (Bier et al., 2024), and liquid droplets that form first in the cooling exhaust plume would not freeze. Nevertheless, we include simulations with ambient temperatures of 233 K and 235 K as limiting cases, as droplet freezing in turbulent and quickly cooling plumes is not well constrained. An overview of all performed simulations is provided in Tab. A1.

3.2.1.2 Quantities of interest

In the following, we give definitions of quantities that are used throughout the paper.

The respective total number of ice crystals per meter of flight path and the vertical ice crystal number profile are defined as follows:

$$N_{\text{tot}}(t) = \frac{1}{L_y} \iiint N(x, y, z, t) \, dx \, dy \, dz \quad \text{and} \quad (3.11)$$

$$N_v(z, t) = \frac{1}{L_y} \iint N(x, y, z, t) \, dx \, dy. \quad (3.12)$$

Here, L_y is the domain length in the longitudinal direction, and N represents the ice crystal number concentration. Both quantities, N_{tot} and N_v , are averaged along the flight direction. The total ice mass, M_{tot} , and the vertical ice mass profile, M_v , are computed analogously. The normalized ice crystal number is calculated as

$$f_N(t) = \frac{N_{\text{tot}}(t)}{N_0}. \quad (3.13)$$

In Sec. 3.2.2, we will use the term "survival fraction of ice crystals" ($f_{N,s}$), which is the normalized ice crystal number at the end of the simulation. Another pertinent quantity to examine is the number of sublimated ice crystals (N_{subl}). Vertical normalized profiles ($f_{N,v,\text{subl}}$) are computed as described in Eqs. 3.11–3.13 and track the number of ice crystals that sublimate at a specific altitude.

Aircraft and vortex parameters		
	A320/B737	A350/B777*
b_{span} (m)	34.4	60.3
Γ_0 ($\text{m}^2 \text{s}^{-1}$)	240	520
r_c (m)	3.0	4.0
r_{plume} (m)	12	20
Atmospheric conditions		
$\rho_{\text{air,CA}}$ (kg m^{-3})	0.36	
p_{CA} (10^2 Pa)	233	
T_{CA} (K)	[217*, 225, 230, 233, 235]	
$RH_{\text{i,amb}}$ (%)	[110, 120*]	
ϵ ($\text{m}^2 \text{s}^{-3}$)	10^{-7}	
N_{BV} (10^{-2} s^{-1})	[0.5, 1.15*]	
Ice crystal parameters		
	A320/B737	A350/B777
N_0 ($[10^{10}, 10^{11}, 10^{12*}, 10^{13}, 10^{14}] \text{ m}^{-1}$)	0.85	3.38
I_0 ($10^{-3} \text{ kg m}^{-1}$)	[3.7*, 9.51]	[15.0*, 38.55]
r_{SD}	[1.0, 3.0*, 4.0]	
Numerical parameters		
	A320/B737	A350/B777
dx, dy, dz (m)	0.57, 1.14, 0.57	1, 2, 1
n_x, n_y, n_z	384-768, 200, 600-1112	
t_{sim} (s)	≈ 400	
dt (s)	0.03 - 0.08	

Table 3.1: Aircraft and vortex, ice crystal, atmospheric, and numerical parameters. Multiple values in square brackets refer to sensitivity studies, and values with an asterisk refer to default values. Parameters are denoted as follows: b_{span} : wingspan; Γ_0 : circulation; r_c : vortex core radius; r_{plume} : plume radius at initialization; N_0 : initial number of ice crystals; I_0 : emitted water vapor mass; r_{SD} : width of initial ice crystal size distribution; $\rho_{\text{air,CA}}$: air density at cruise altitude; p_{CA} : air pressure at cruise altitude; T_{CA} : ambient temperature at cruise altitude; $RH_{\text{i,amb}}$: ambient relative humidity with respect to ice; ϵ : eddy dissipation rate; N_{BV} : Brunt-Väisälä frequency; dx, dy, dz : mesh sizes; n_x, n_y, n_z : number of grid points; t_{sim} : simulated time; dt : time step.

Fuel/exhaust parameters	Hydrogen	Kerosene	Ratio
$EI_{H_2O} / (\text{kg kg}^{-1})$	8.94	1.26	7.10
$Q / (10^6 \text{ J kg}^{-1})$	120	43	2.79
$EI_{H_2O} Q^{-1} / (10^{-6} \text{ kg J}^{-1})$	0.075	0.029	2.57
A320/B737			
$m_C / (10^{-3} \text{ kg m}^{-1})$	1.06	2.96	2.79^{-1}
$I_0 / (10^{-3} \text{ kg m}^{-1})$	9.51	3.7	2.57
$N_{0,\text{ref}} / (10^{12} \text{ m}^{-1})$	0.85	0.85	1
$EI_{\text{iceno,ref}} / (10^{14} \text{ kg}^{-1})$	7.81	2.8	2.79
A350/B777			
$m_C / (10^{-3} \text{ kg m}^{-1})$	4.3	12.0	2.79^{-1}
$I_0 / (10^{-3} \text{ kg m}^{-1})$	38.55	15.0	2.57
$N_{0,\text{ref}} / (10^{12} \text{ m}^{-1})$	3.38	3.38	1
$EI_{\text{iceno,ref}} / (10^{14} \text{ kg}^{-1})$	7.81	2.8	2.79

Table 3.2: Fuel, engine, and exhaust parameters for hydrogen propulsion (second column), kerosene (third column), and the ratio between them (fourth column). The water vapor mass emission index (EI_{H_2O}) and specific heat of combustion (Q) ("lower calorific value") are based on Tab. 1 of [Schumann \(1996\)](#).

3.2.2 Results

3.2.2.1 Exploring H_2 contrails

In this subsection, we examine the impact of the initial number of ice crystals and the emitted water vapor mass, corresponding to a H_2 combustion engine or a potential fuel cell setup. These two parameters are varied as described in Sec. 3.2.1.1. The simulations presented in this subsection are performed for an A350 aircraft at $T_{CA} = 217 \text{ K}$, $RH_{i,\text{amb}} = 120 \%$, and $N_{BV} = 1.15 \times 10^{-2} \text{ s}^{-1}$, which were also the baseline meteorological conditions in previous EULAG-LCM studies. Hence, this scenario has been well explored, and the new simulations build upon the existing ones. Unless stated otherwise, the presented results use the default initial values, indicated by an asterisk in Tab. 3.1.

Figure 3.2 (top row) illustrates the temporal evolution of contrail ice crystals in the (x, z) -plane over a 6 min period. The ice crystal number concentration is averaged along the flight direction. At the start of the simulation, two circular plumes are initialized at $z = 0 \text{ m}$. The centers of the plumes and of the wake vortices are co-located on each side. Within the first 2 min, a downward motion of the ice crystals is observed as the aircraft exhaust descends with the downward moving vortices, forming the primary wake. Also, we see a horizontal broadening of the contrail after few minutes due to the Crow instability ([Crow, 1970](#)). Ice crystals that are continuously detrained from the descending exhaust form a curtain between the original emission altitude and the vortex location, known as the secondary wake ([Sussmann and Gierens, 1999](#); [Unterstrasser, 2014](#)). After 6 min, ice crystals are visible close to or even above the cruise altitude as the vertically displaced air masses rise back due to buoyancy after vortex breakup. Whereas ice crystals in the secondary wake grow in size due to the deposition of the available water vapor, a significant portion of the ice crystals can sublimate in the primary wake because of adiabatic heating ([Lewellen and Lewellen, 1996](#); [Sussmann and Gierens, 1999](#); [Unterstrasser, 2016](#)).

The second row in Fig. 3.2 shows the cross-sectional ice crystal number concentrations after 6 min for the reference N_0 case ($N_0 = 3.38 \times 10^{12} \text{ m}^{-1}$) and the N_0 -upscaling and N_0 -downscaling cases. Higher final number concentrations in absolute terms are evident in the upscaling cases ($N_0 = 3.38 \times 10^{13} \text{ m}^{-1}$ and

$N_0 = 3.38 \times 10^{14} \text{ m}^{-3}$). Nonetheless, relative to the initial number, fewer ice crystals survive in these cases, as illustrated in the third row, where the final vertical profiles of normalized ice crystal numbers (green curves) are depicted. This observation is further supported by the final vertical profiles of normalized sublimated ice crystal numbers (orange curves). In the upscaling cases, ice crystals begin to sublimate at higher altitudes because they are smaller in size (see Fig. 3.1); this is a phenomenon that has already been described by Huebsch and Lewellen (2006) and Unterstrasser (2014).

Figures 3.3a and b display the temporal evolution of the normalized total ice crystal number and absolute total ice mass for different N_0 and I_0 values. The most significant reductions in f_N occur in the upscaling scenarios (red curves in Fig. 3.3a), while the N_0 -downscaling simulations (blue curves) show little to no reduction in the temporal evolution of f_N . Due to a higher absolute number of surviving ice crystals in the upscaling cases, these scenarios also exhibit a larger final total ice mass (red curves lie above the blue ones in Fig. 3.3b). The greater loss of ice crystals in the upscaling scenarios is reflected in the survival fraction depicted in Fig. 3.3c. Conversely, contrails with a lower value of N_0 (and thus larger initial crystals) are less prone to sublimation, resulting in a higher survival fraction. This implies that initial differences in ice crystal number diminish over time. In this specific scenario, initial differences spanning four orders of magnitude, with N_0 -scaling factors of 0.01 and 100, reduce to just two orders of magnitude, 0.015 and 7.5, after the vortex phase. Moreover, initializing with a greater amount of emitted water vapor (indicated by circles in Fig. 3.3c) results in larger ice crystal sizes (refer to Fig. 3.1), which in turn increases the survival fraction and ice mass. In the I_{0,H_2} simulations, the reduction in the initial differences is less pronounced, with the four-order-of-magnitude difference reducing to three orders by the end of the vortex phase.

3.2.2.2 Parameter study of H₂-contrail properties

3.2.2.2.1 Sensitivity to ambient conditions

As revealed in previous studies, the evolution of the contrail ice crystal number and ice mass is highly sensitive to ambient conditions (Lewellen and Lewellen, 2001b; Unterstrasser, 2016). This subsection investigates the impact of ambient relative humidity, temperature, and atmospheric stratification on H₂-contrail properties. Note that we performed simulations at $T_{CA} \geq 230 \text{ K}$ only for H₂ contrails with an increased I_0 value, as the formation of kerosene contrails is unlikely at these high ambient temperatures. The results presented in this subsection refer to simulations of an A350 aircraft with an initial size distribution width of $r_{SD} = 3.0$.

In Fig. 3.4, final vertical profiles of the ice crystal mass and normalized number and survival fractions after approximately 6 min are depicted. Columns represent simulations at temperatures of 217 K, 225 K, 230 K, 233 K, and 235 K, respectively. The simulations shown in the first and second rows are performed with $I_0 = I_{0,H_2}$. The ice mass (row 1 in Fig. 3.4) remains largely unaffected by variations in N_0 , except for the factor-100 downscaling simulation, which shows a significantly reduced ice mass. A notable increase in ice mass is observed with increasing temperature, attributable to a higher water vapor mass concentration in the atmosphere. This additional water vapor can be deposited onto the ice crystals, thereby increasing their size.

When examining the normalized ice crystal number (row 2 in Fig. 3.4), we observe a reduction with increasing temperature, primarily in the primary wake. Although the ice crystals grow larger during the first seconds due to the higher water vapor concentration at higher temperatures, they experience, in absolute terms, a stronger increase in the saturation pressure within the descending vortices, leading to increased sublimation (Unterstrasser, 2016; Bier and Burkhardt, 2022). This phenomenon is most pronounced in the N_0 -upscaling cases.

The sensitivity of the survival fraction to the ambient relative humidity and ambient temperature is illustrated in row 3 of Fig. 3.4. In addition to the default cases with $I_0 = I_{0,H_2}$, data points for the kerosene reference case with $I_0 = I_{0,kero}$ are displayed for $T_{CA} = 217 \text{ K}$ and 225 K (yellow symbols). Simulations with $I_0 = I_{0,H_2}$ indicate that ice crystals, which would typically sublimate under $I_{0,kero}$ conditions, are now sufficiently large to withstand adiabatic heating. This effect is most pronounced in the $RH_{i,amb} = 110 \%$, N_0 -downscaling scenarios: the differences between the yellow and the colored squares are larger than the differences between the yellow and colored circles at $N_0 \lesssim 10^{13} \text{ m}^{-3}$. Simulations at a lower ambient relative humidity (square

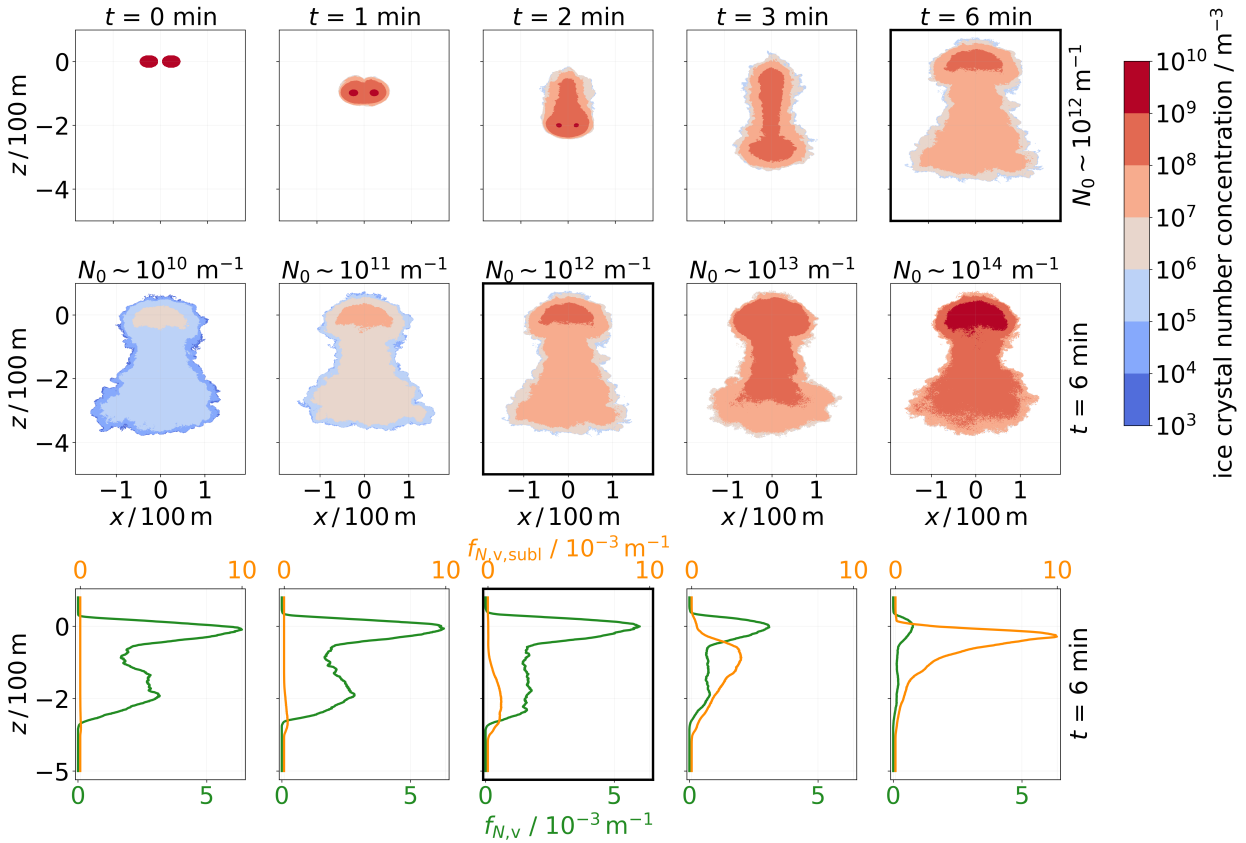


Figure 3.2: Ice crystal number concentrations, averaged along the flight direction in the (x, z) -plane, are depicted in the first and second rows. The first row illustrates the temporal evolution over 6 min. The final concentration distribution is displayed in the second row for five different N_0 values. The third row shows the normalized vertical profiles of ice crystals (green) and sublimated ice crystals (orange) (the first row depicts one simulation, whereas the second and third rows depict five different simulations). The simulation displayed in the top row refers to the simulation in the middle panels in the second and third rows, marked by the black frame. The displayed simulations are performed for an A350 aircraft at $T_{CA} = 217$ K, $RH_{i,amb} = 120$ %, and $I_0 = I_{0,H_2}$. The z coordinate is shifted such that $z = 0$ m corresponds to the cruise altitude (which is also done in Figs. 3.4, 3.5, and 3.6).

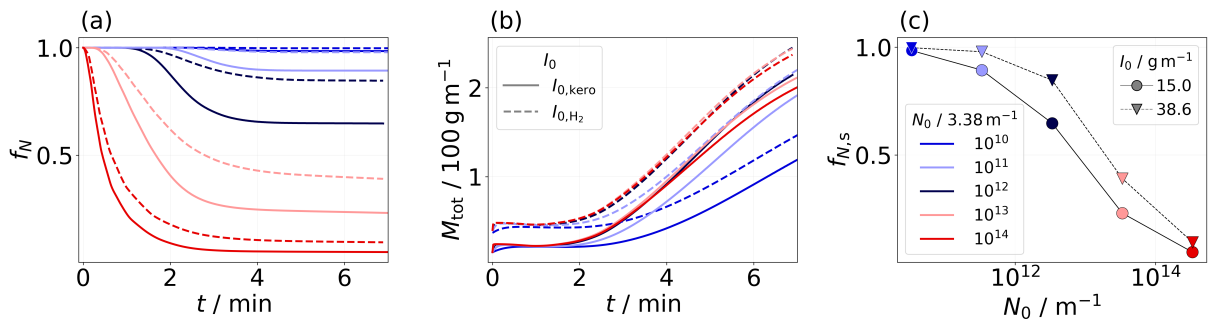


Figure 3.3: (a) and (b): Temporal evolution of the normalized total number of ice crystals and total ice mass for different values of N_0 and I_0 . (c) Survival fractions as functions of N_0 are depicted.

symbols) show a stronger loss of ice crystals, a trend consistent across the variations regarding N_0 and I_0 . This is due to the stronger sublimation effects in the primary wake in the case of a reduced relative humidity value (Unterstrasser et al., 2014; Unterstrasser, 2016). Notably, in the extreme N_0 -downscaling scenario ($N_0 \sim 10^{10} \text{ m}^{-3}$) at 120 % relative humidity, the survival fraction remains largely unaffected by the ambient temperature, with survival fractions equal or close to one at both 217 K ($f_{N,s} = 1.00$) and 235 K ($f_{N,s} = 0.95$). In contrast, for the extreme N_0 -upscaling scenario, the impact of ambient temperature is significantly more pronounced, reducing the survival fraction by a factor of 4.5, from $f_{N,s} = 0.09$ at 217 K down to $f_{N,s} = 0.02$ at 235 K. This temperature sensitivity is further amplified under drier atmospheric conditions, where the effect on the survival fraction is more substantial. For the N_0 -downscaling scenario, the survival fraction decreases by a factor of 2.24, while in the N_0 -upscaling case, the reduction even exceeds one order of magnitude. In the upscaling cases with ambient temperatures at or above 230 K, nearly all ice crystals sublimate, with $f_{N,s} < 0.15$. Initial differences in N_0 spanning four orders of magnitude are reduced to 2.98 (217 K, 120 %) and 2.85 (217 K, 110 %), and they further decrease to 2.37 (235 K, 120 %) and 2.14 (235 K, 110 %), highlighting the importance of both parameters, ambient temperature and ice relative humidity, in the context of ice crystal loss during the vortex phase.

The third ambient parameter varied in this study is stratification. Following, e.g., Unterstrasser et al. (2014), we use a Brunt-Väisälä frequency of $N_{BV} = 1.15 \times 10^{-2} \text{ s}^{-1}$ as the default and a smaller value, $N_{BV} = 0.5 \times 10^{-2} \text{ s}^{-1}$, that characterizes an atmosphere with weaker atmospheric stability. The simulation domain needs to be larger in the latter case, as the downward movement and oscillation of the vortex system are stronger. Therefore, to reduce the number of simulations and the associated computational cost, we only varied N_0 only by a factor of 100 both up and down. This simulation set is only performed for $T_{CA} = 217 \text{ K}$. Figure 3.5 displays normalized vertical profiles of the final ice crystal number (panel (a)) and the number of sublimated ice crystals (panel (b)) for both stratification scenarios (indicated by the line style). Only simulations with $I_0 = I_{0,H_2}$ are displayed here. Evidently, in a weakly stratified ambient atmosphere, the wake vortices generally descend further down. Consequently, sublimation extends to lower altitudes, especially in the default and N_0 -downscaling cases, displayed by the black and blue curves, respectively. This is mainly observed in the simulations with a default or lower N_0 value as the difference in the final contrail height is about 200 m, compared to about 50 m in the N_0 -upscaling scenario. This reduced difference in the N_0 -upscaling case arises from the fact that most ice crystals are lost at higher altitudes, independently of stratification. As anticipated, the survival fraction is reduced for contrails evolving in a weakly stratified atmosphere. Decreasing the ambient relative humidity exacerbates crystal loss further. Also, lower survival fractions are observed in scenarios with $I_0 = I_{0,kero}$, as previously noted (not shown). The original four-order-of-magnitude difference in N_0 decreases to 2.69 and 2.46 (default and weakly stratified, 120 %) and to 2.46 and 2.31 (110 %) at $I_0 = I_{0,kero}$, while it decreases to 2.98 and 2.72 (120 %), and to 2.85 and 2.66 (110 %) at $I_0 = I_{0,H_2}$.

3.2.2.2.2 Sensitivity to the microphysical initialization

We prescribe the initial ice crystal size distribution (SD) as a lognormal distribution with a specified width parameter r_{SD} ; see, e.g., Unterstrasser and Sölch (2010). A variation in r_{SD} has been shown to have a non-negligible effect on the contrail's evolution during the vortex phase (Unterstrasser, 2014). Varying the width, we adjust the geometric mean diameter such that the total initial ice mass and ice crystal number are unaffected (Unterstrasser, 2014).

In Fig. 3.6, we present simulations, in which r_{SD} is varied according to Tab. 3.1. The final contrail height for each N_0 scenario appears relatively unaffected by variations in r_{SD} , as shown in Fig. 3.6a. However, a narrower initial SD leads to a higher number of ice crystals present at lower altitudes (dashed curves). This can be explained by the delayed onset of sublimation, which occurs at lower altitudes (see panel (b)). In contrast, a broader initial SD results in a higher proportion of smaller ice crystals at the start; these smaller ice crystals which tend to sublimate at higher altitudes, leading to lower survival fractions. This pattern is observed consistently across all N_0 scenarios. To assess the robustness of these results with respect to ambient temperature, we repeated this set of simulations at $T_{CA} = 233 \text{ K}$. The general trends related to r_{SD} remain unchanged by the variation in ambient temperature. As expected based on previous findings, we

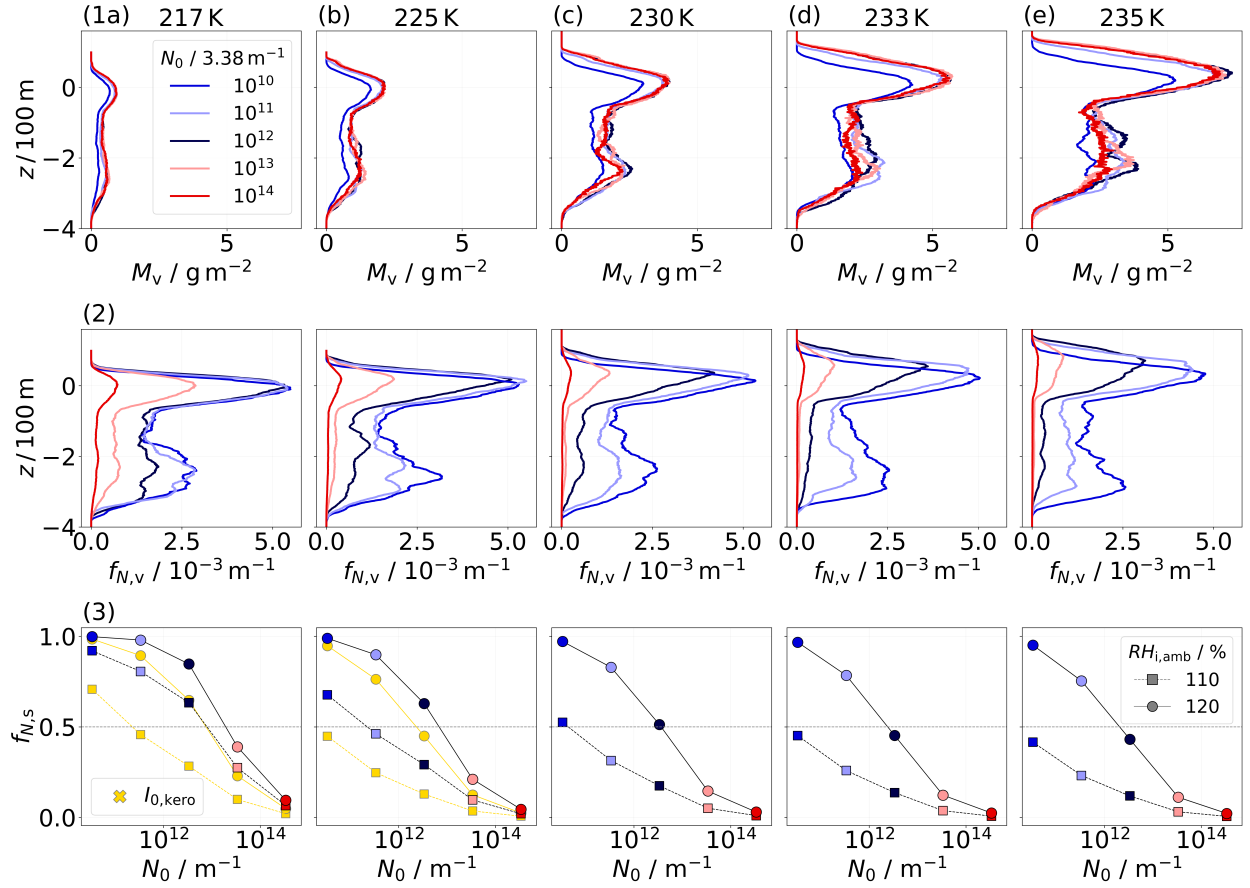


Figure 3.4: Final vertical profiles of ice mass (first row) and normalized ice crystal number (second row) for different N_0 values (as given in the legend in panel (1a)) after 6 min. Columns depict results for ambient temperatures of 217 K, 225 K, 230 K, 233 K, and 235 K (see the headings above the columns). The ambient relative humidity is 120%. The third row displays the survival fraction at the two different humidity values as indicated in panel (3e). At $T_{CA} = 217 \text{ K}$ and 225 K, yellow symbols, which refer to simulations with $I_0 = I_{0,kero}$, are plotted for comparison. A horizontal dashed line at $f_{N,S} = 0.5$ is provided as a visual guide.

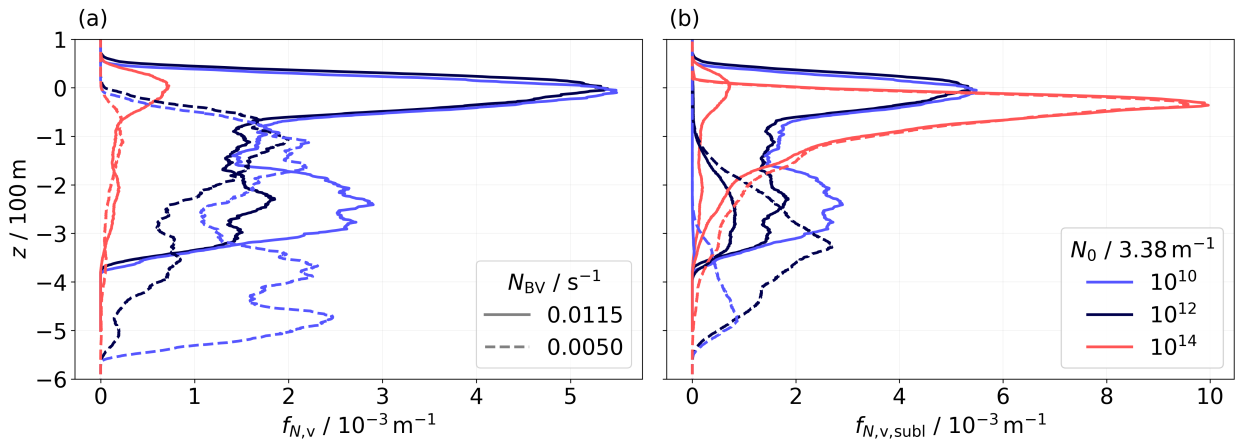


Figure 3.5: (a) Final vertical profiles of the normalized number of ice crystals and (b) the normalized number of sublimated ice crystals. Results for default (solid lines) and weaker (dashed lines) atmospheric stability are depicted. The displayed simulation results correspond to $T_{CA} = 217 \text{ K}$, $RH_{i,amb} = 120 \%$, and $I_0 = I_{0,H_2}$.

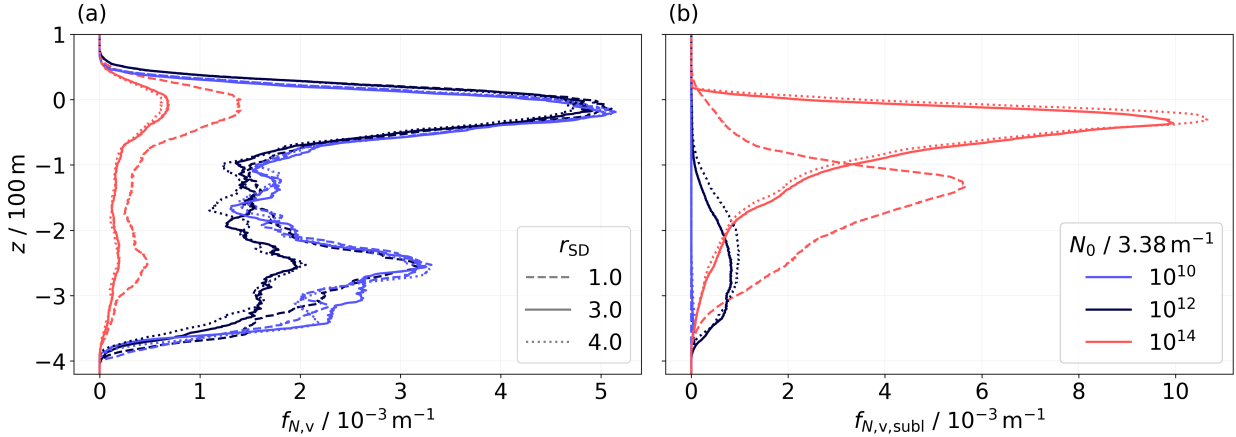


Figure 3.6: (a) Final vertical profiles of the normalized number of ice crystals and (b) the normalized number of sublimated ice crystals. Solid lines represent the reference cases with $r_{SD} = 3.0$, while initially broader and narrower ice crystal size distributions are depicted by dotted and dashed lines, respectively. The shown simulations were conducted for $T_{CA} = 217 \text{ K}$, $RH_{i,\text{amb}} = 120 \%$, and $I_0 = I_{0,\text{H}_2}$.

observe generally lower survival fractions at this temperature compared to the corresponding r_{SD} -simulation set at $T_{CA} = 217 \text{ K}$.

In aircraft plumes characterized by negligible soot emission, such as those from H_2 -powered engines, ice nucleation is assumed to predominantly occur on entrained ambient aerosol particles (Bier et al., 2024). Therefore, the dry radii of these ambient aerosols govern the size of the resulting ice crystals. Bier et al. (2024) identified several aerosol modes with sizes spanning from few nanometers to several micrometers. This broad size range is more accurately captured by an initial size distribution with larger values of r_{SD} (e.g., 3.0 and 4.0), thus considered more representative of the physical conditions.

3.2.2.2.3 Sensitivity to aircraft type

H_2 -contrail simulations for a smaller A320 aircraft with a wingspan of $b_{\text{span}} = 34.4 \text{ m}$ are performed for $T_{CA} \geq 225 \text{ K}$. The grid spacing is adapted as outlined in Tab. 3.1. We simulate this aircraft type only with an N_0 -scaling factor of 100.

Unterstrasser and Görsch (2014) have done baseline simulations for an A320 aircraft under typical kerosene conditions. As revealed in this study, the altitude at which sublimation starts is independent of the aircraft type. As described in Sec. 3.2.1.1, both N_0 and I_0 are linearly dependent on the fuel flow rate. As EI_{iceno} and $EI_{\text{H}_2\text{O}}$ are assumed to be constant across all aircraft types, the mean mass and radius of the initial ice crystals are consequently independent of the aircraft type, as both are proportional to the ratio I_0/N_0 . However, the vortex system of the A320 descends more slowly. Therefore, the sublimation threshold altitude is reached later. The vortices of the A320 dissolve before such low altitudes can be reached where strong sublimation occurs. This decreases sublimation effects in the primary wake, allowing more ice crystals to survive the vortex phase for smaller aircraft like the A320 than larger ones like the A350. This trend holds across all N_0 -scaling scenarios. Although the final A350 contrail still contains more ice crystals than the A320 contrail, the relative ice crystal loss is greater for the A350, reducing the initial large differences in ice crystal numbers.

Figure 3.7 shows how the survival fractions depend on the aircraft type. Each box, delineated by the dashed vertical lines, corresponds to a different N_0 -scaling scenario. Note that in the factor-100 upscaling scenario, where the survival fractions are less than 0.1, the y-axis is adjusted accordingly. For each scenario, simulations at $T_{CA} = 225 \text{ K}$, 230 K , 233 K , and 235 K are performed, as indicated on the x-axis. As discussed in Sec. 3.2.2.2.1, high ambient temperatures and low relative humidity values increase ice crystal loss. Overall, the A320 exhibits higher survival fractions, with the most pronounced differences at

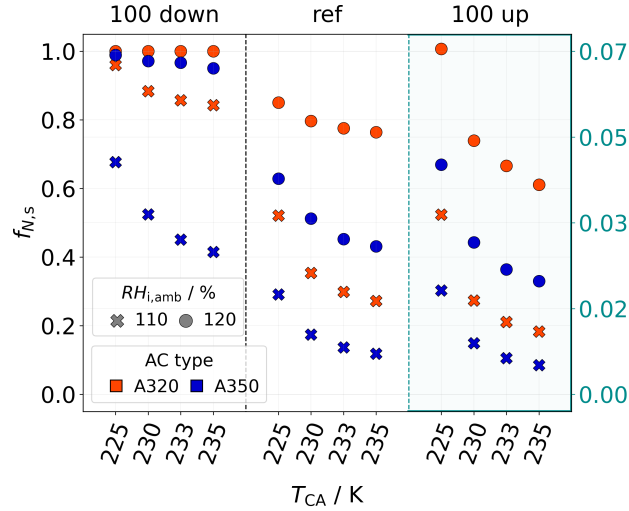


Figure 3.7: Survival fractions of an A320 (red) and an A350 (blue) aircraft. The three boxes represent the ice crystal number scaling as indicated in the heading, where, e.g., "100 down" refers to the simulation with an N_0 value equal to $3.38 \times 10^{10} \text{ m}^{-1}$ (A350) or $0.85 \times 10^{10} \text{ m}^{-1}$ (A320). In the case of a factor-100 upscaling, the survival fractions are small. Hence, we adapted the axis as indicated by the light-blue labels. Simulation results for both values of ambient relative humidity are shown (symbols).

low N_0 values and low ambient humidity (e.g., $f_{N,s} = 0.84$ for the A320 and $f_{N,s} = 0.42$ for the A350 at $T_{CA} = 235 \text{ K}$). In scenarios with a strong N_0 upscaling, nearly all ice crystals sublimate regardless of the aircraft type ($f_{N,s} \leq 0.07$).

3.2.2.3 Parameterization of ice crystal loss

Unterstrasser (2016, hereafter referred to as U2016) presents an ice crystal loss parameterization that approximates the survival fraction of ice crystals after the vortex phase, based on the ambient relative humidity, temperature at cruise altitude, thermal stratification, apparent ice crystal emission index, and aircraft parameters. Relevant aircraft parameters are the water vapor emission, the wingspan, and the wake vortices' initial circulation. A typical application of the parameterization is its implementation in larger-scale contrail models, where the contrail initialization refers to some state after vortex breakup, and effects of the wake dynamics cannot be explicitly resolved. The development of the parameterization was based on a database of more than 80 EULAG-LCM simulations, comprising sensitivity studies that varied the parameters mentioned above. Notably, the original focus was on contrails from kerosene combustion. The new set of H_2 -contrail simulations investigates the sensitivity to N_0 more systematically and over a broader range. Moreover, contrails at temperatures above 225 K have not been considered previously, and the validity of the parameterization beyond this temperature threshold is not guaranteed.

The following paragraphs will briefly repeat the parameterization formulation, describe appropriate adaptations, and analyze its applicability and performance for the new H_2 -contrail dataset.

The ice crystal loss during the vortex phase can be assessed by introducing three length scales that describe the processes relevant to downward-propagating contrail ice crystals:

- z_{desc} is the final vertical displacement of the wake vortex system, which leads to a maximum adiabatic heating experienced in the primary wake. The quantity depends most strongly on thermal stratification, aircraft mass, and wingspan.
- z_{atm} measures the effect of the ambient supersaturation on the ice crystal mass budget. z_{atm} is the distance that an air parcel has to travel down until its saturation pressure equals its vapor pressure, i.e., until its supersaturation is depleted due to adiabatic heating. The quantity depends most strongly on the ambient relative humidity.

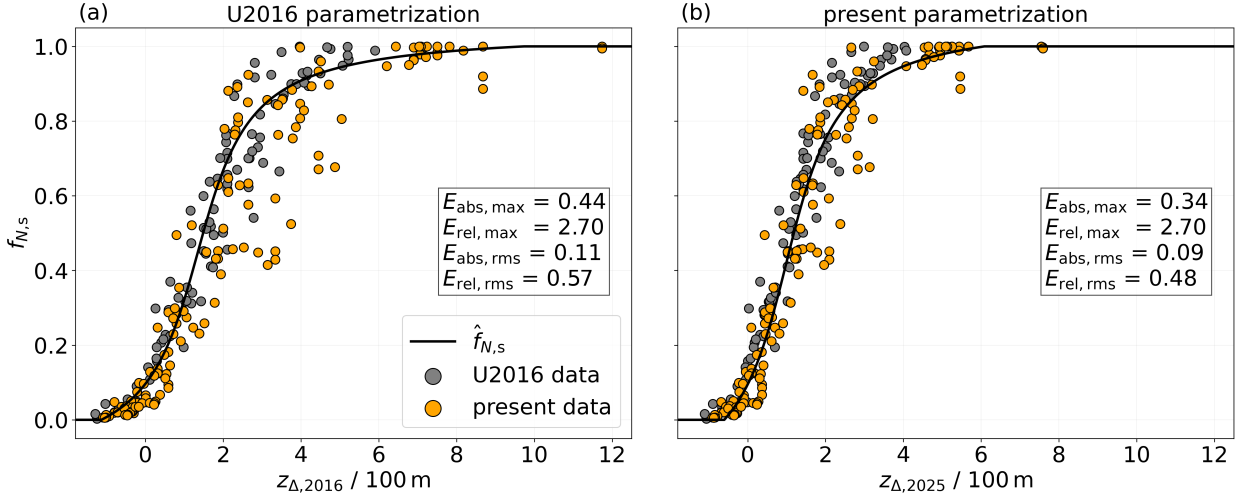


Figure 3.8: Simulated survival fraction as a function of the parameter z_{Δ} . The (a) original and (b) updated parameterizations are shown by the solid black line. Gray points represent the simulated survival fractions from the 2016 study, while orange points correspond to those from the present study. As the fit coefficients are adapted in the new formulation, the z_{Δ} parameter differs in both versions, denoted by $z_{\Delta,2016}$ and $z_{\Delta,2025}$.

- z_{emit} measures the effect of water vapor emission on the ice crystal mass budget. Analogously to z_{atm} , z_{emit} is a vertical displacement that corresponds to an adiabatic heating such that an initially saturated parcel remains at saturation when the emitted water vapor is added to the parcel. The quantity depends on the ambient temperature and the amount of emitted water vapor, which in turn depends on the fuel consumption, the emission index of water vapor, and the contrail cross-section.

The exact definitions of these length scales are given in Sec. 3.1 of U2016. We repeat the definition of z_{desc} , which is given by

$$z_{\text{desc}} = \left(\frac{8 \Gamma_0}{\pi N_{\text{BV}}} \right)^{1/2}. \quad (3.14)$$

Regarding z_{atm} and z_{emit} , we implement slightly redefined formulae. In the previous version, the definitions of z_{atm} and z_{emit} are based on the assumption of balancing water vapor concentrations. In the updated parameterization, we redefine the two length scales by requiring the conservation of water vapor mass mixing ratios, which are the quantities that are actually conserved under adiabatic changes. Hence, we introduce the adiabatic index $\kappa = 3.5$, and the modified equations read as follows:

$$(1 + s_i) \frac{e_s(T_{\text{CA}})}{T_{\text{CA}}^{\kappa}} = \frac{e_s(T_{\text{CA}} + \Gamma_d z_{\text{atm}})}{(T_{\text{CA}} + \Gamma_d z_{\text{atm}})^{\kappa}} \quad (3.15)$$

$$\frac{e_s(T_{\text{CA}})}{R_{\text{WV}} T_{\text{CA}}^{\kappa}} + \frac{\rho_{\text{emit}}}{T_{\text{CA}}^{\kappa-1}} = \frac{e_s(T_{\text{CA}} + \Gamma_d z_{\text{emit}})}{R_{\text{WV}} (T_{\text{CA}} + \Gamma_d z_{\text{emit}})^{\kappa}}. \quad (3.16)$$

Here, Γ_d denotes the dry adiabatic lapse rate, with a value of 9.8 K km^{-1} , and R_{WV} is the specific gas constant of water vapor, taken as $461.5 \text{ J kg}^{-1} \text{ K}^{-1}$. The water vapor saturation pressure is represented by e_s , and $s_i = RH_i - 1$ denotes the supersaturation. In Eq. 3.16, ρ_{emit} refers to the emitted water vapor concentration. According to U2016, we then define a linear combination of these length scales

$$z_{\Delta} = \tilde{\alpha}_{\text{atm}} z_{\text{atm}} + \tilde{\alpha}_{\text{emit}} z_{\text{emit}} - \tilde{\alpha}_{\text{desc}} \hat{z}_{\text{desc}} \quad (3.17)$$

with positive weights $\tilde{\alpha}_X$.

z_Δ is large if the buffer effect of the ambient supersaturation and the emitted water vapor outweighs the adiabatic heating due to the wake vortex descent. This means that the water vapor surplus is sufficient to keep the heated air parcel supersaturated. It should be noted that, in the simulations, the air parcel does not remain supersaturated, but RH_i quickly relaxes to 100%. Figure 3.3b reveals that the water vapor surplus deposits on the ice crystals within a few seconds (for large N_0) or within at most 30 s (for low N_0). The local maximum attained within the first half a minute clearly relates to the water vapor surplus as estimated by the two length scales z_{atm} and z_{emit} . Also note that the increase in ice mass after 2 min is due to detrained ice crystals outside of the vortex system, which grow in the supersaturated ambient air. Figure 2a in [Unterstrasser and Sölch \(2010\)](#) displays the evolution of the total ice mass in the descending wake vortex system. This nicely reveals the dependence of the peak value on the water vapor surplus and the subsequent monotonic decrease in the ice mass. Hence, the buffer effect is achieved by increasing the total mass and the mass concentrations of the ice crystals in the vortex system. The larger those quantities are after the initial growth period, the more and the longer the ice crystals can shrink until complete sublimation.

A small z_Δ (also including negative values) means that the wake vortex descent prevails for so long that a substantial fraction or even all of the entrained ice crystals are likely lost.

Following U2016, both $\tilde{\alpha}_{\text{atm}}$ and $\tilde{\alpha}_{\text{emit}}$ are modified to include the effect of a variation in N_0 , while $\tilde{\alpha}_{\text{desc}}$ can be left unchanged (i.e., $\alpha_{\text{desc}} = \tilde{\alpha}_{\text{desc}}$):

$$z_\Delta = \Psi^\gamma (\alpha_{\text{atm}} z_{\text{atm}} + \alpha_{\text{emit}} z_{\text{emit}}) - \alpha_{\text{desc}} \hat{z}_{\text{desc}}. \quad (3.18)$$

In U2016, Ψ was given by $\frac{1}{EI_{\text{iceno}}^*}$, with $EI_{\text{iceno}}^* = \frac{EI_{\text{iceno}}}{EI_{\text{iceno,ref}}}$ and a positive constant γ . In the new formulation, Ψ is defined as

$$\Psi = 1/n_0^*, \quad (3.19)$$

where n_0 is an (intermediate) ice crystal number concentration, and the "starred" quantity is the value normalized by a reference value $n_{0,\text{ref}}$. In both approaches, increasing EI_{iceno} in the original formulation or n_0 in the new formulation gives smaller weights $\tilde{\alpha}_{\text{atm}}$ and $\tilde{\alpha}_{\text{emit}}$. This reduces the buffer effect and, consequently, z_Δ . This reflects the fact that ice crystal loss becomes more substantial when the water vapor surplus is distributed over more ice crystals with smaller masses on average. With smaller mean ice crystal sizes, a specific fraction of lost ice mass translates into a larger relative fraction of lost ice crystals.

The definition of n_0 is deferred to the Appendix (Eq. A8) and the motivation for the switch from EI_{iceno}^* to n_0^* is explained in Sec. 3.2.3.

The three length scales depend only on input parameters and can be evaluated for given meteorological and aircraft properties. Notably, they are independent of N_0 , and the sensitivity of z_Δ to N_0 enters the parameterization solely by an adaptation of the weights $\tilde{\alpha}_{\text{atm}}$ and $\tilde{\alpha}_{\text{emit}}$.

Plotting the simulated $f_{N,s}$ values as functions of z_Δ with suitably chosen weights, the data points can be reasonably well approximated by an arc tangent function. Hence, the parameterized survival fraction $\hat{f}_{N,s}$ can then be defined as

$$\hat{f}_{N,s} = \hat{a}(z_\Delta), \quad (3.20)$$

with

$$\hat{a}(x) = \beta_0 + \frac{\beta_1}{\pi} \arctan(\alpha_0 + (x/100 \text{ m})). \quad (3.21)$$

In the following, we outline our procedure for determining the new set of fit coefficients. Simulations with $r_{\text{SD}} = 1.0$ and $r_{\text{SD}} = 4.0$, accounting for approximately 25% of the total dataset, were excluded from the fitting process, as they represent extreme cases of the size distribution width. However, these simulations are still shown in Fig. 3.8. We selected a representative subset of simulations using the default value of $r_{\text{SD}} = 3.0$. Additionally, some data points from simulations with weaker stability were identified as outliers and excluded. Consequently, 69% of the new simulations and the entire dataset from U2016 were used to derive the fit coefficients. A weighting was applied in the fitting procedure, with all data points at

$RH_{i,amb} = 110\%$ and $EI_{iceno}^* > 1$ being assigned higher weights (1.1 and 2.0, respectively). On the one hand, these weights were introduced to reduce the absolute errors in the $RH_{i,amb} = 110\%$ cases. This is favorable as the survival fractions are systematically smaller than for the $RH_{i,amb} = 120\%$ cases. Hence, similar absolute errors over both sets of simulations would imply larger relative errors for $RH_{i,amb} = 110\%$ cases. Furthermore, the occurrence frequency of ice supersaturation is exponentially distributed with decreasing encounter probabilities for increasing $RH_{i,amb}$ values (Petzold et al., 2017). Increasing the weights is a pragmatic solution to put more emphasis on the low- $RH_{i,amb}$ cases.

We propose the following values for the fitting coefficients:

$$\beta_0 = 0.42, \quad (3.22a)$$

$$\beta_1 = 1.31, \quad (3.22b)$$

$$\alpha_0 = -1.00, \quad (3.22c)$$

$$\alpha_{atm} = 1.27, \quad (3.22d)$$

$$\alpha_{emit} = 0.42, \quad (3.22e)$$

$$\alpha_{desc} = 0.49, \quad (3.22f)$$

$$\gamma = 0.16. \quad (3.22g)$$

Figure 3.8 presents a comparison between both versions, where the simulation data used to derive the original parameterization formulation are displayed in gray, while the present (additional) data points are shown in orange. Panel (a) depicts the 2016 parameterization curve. The new parameterization (panel (b)) reduces both the absolute maximum and root-mean-square error (see values inserted in the figure). The absolute root-mean-square is reduced by 2%, whereas the relative root-mean-square error in the U2016 data is decreased by 9%. Relative to the U2016 database, the new H_2 simulations sample particularly the space for large and very small $f_{N,s}$ values more densely. The supplement contains further plots that help to rate the changes implied by the new version.

In Fig. 3.9, we show the updated parameterization for various meteorological and aircraft scenarios. As indicated by its heading, each panel highlights specific sensitivity analyses. The dependencies of the survival fraction on the input parameters have been thoroughly explained in the preceding subsections. The following will discuss the new insights gained from the updated parameterization. It can be observed that simulations performed at temperatures above 225 K are well represented by the parameterization. This holds for both the N_0 -upscaling and N_0 -downscaling scenarios. While a critical temperature exists above which contrail formation is not possible, this temperature threshold has no direct relevance for the microphysical processes during the vortex phase. Hence, it is not surprising that the validity of the parameterization extends beyond 225 K.

The parameterization does not account for variations in r_{SD} , meaning that data points from simulations with different r_{SD} values but the same z_{Δ} value are treated identically. Notably, for N_0 -upscaling cases, simulations with $r_{SD} = 1.0$ tend to show survival fractions that are somewhat overestimated. For the time being, this is an irreducible uncertainty partly due to idealizations in our initialization.

Regarding aircraft type, the parameterization effectively represents both A350 (bluish) and A320 (reddish) cases across upscaling and downscaling scenarios, as shown in panels (f) and (g). Additionally, the parameterization is consistent with other simulation results from studies such as Lewellen et al. (2014) and Picot et al. (2015), as highlighted in panel (h). Our updated H_2 parameterization not only aligns well with these results but also particularly captures the ice crystal emission index variation study from Lewellen (2014), further demonstrating the validity of the new parameterization.

3.2.2.4 Impact of vortex phase processes on contrail-cirrus evolution

This subsection presents results of contrail-cirrus simulations and demonstrates the relevance of the ice crystal number in young contrails for the subsequent transition into contrail cirrus.

We employ the EULAG-LCM model in a setup largely based on that used in Unterstrasser et al. (2017a) and Unterstrasser et al. (2017b). The simulation domain consists of two dimensions, x (horizontal) and z

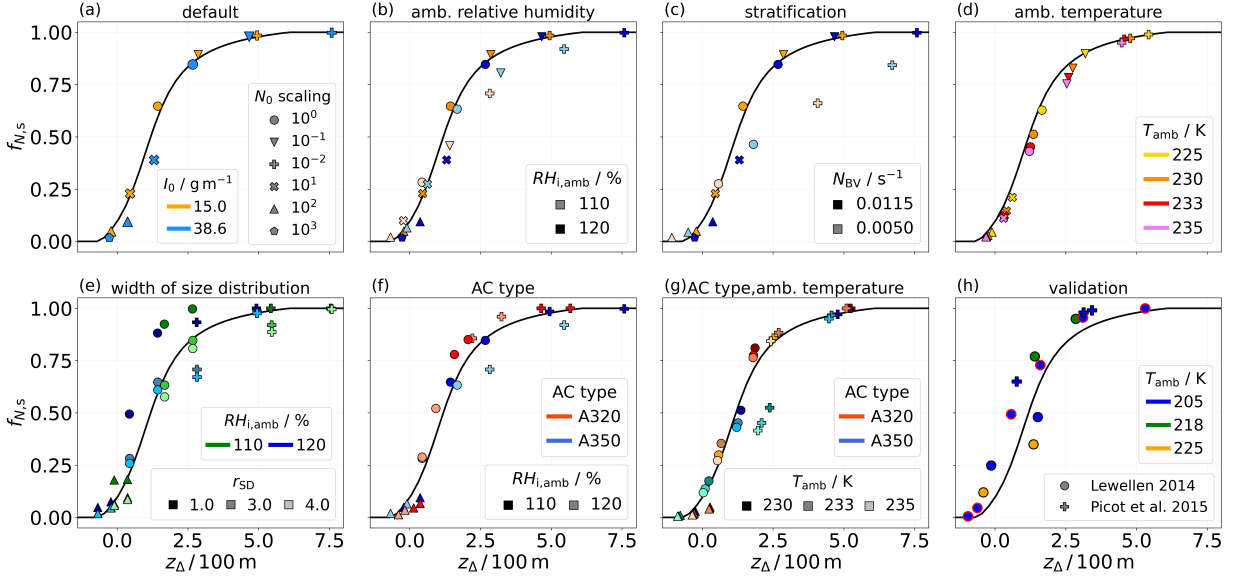


Figure 3.9: Simulated survival fractions as functions of the parameter z_{Δ} ($= z_{\Delta,2025}$), focusing exclusively on new H_2 simulations. The symbol legend in panel (a) applies to the panels (a) to (g), with symbols indicating N_0 -scaling information. In panels (a) to (c), blue symbols denote H_2 water vapor emissions, while orange symbols represent kerosene cases. Each panel highlights a different meteorological or aircraft scenario, as the headings indicate. Panel (h) displays survival fractions from other studies for comparison and validation; there, symbols with a red outline correspond to a study investigating the effects of varying the ice crystal emission index (Lewellen et al., 2014).

(vertical), which are perpendicular to the flight direction. We embed the data of the vortex phase simulation (averaged along the flight direction) in a significantly larger simulation domain spanning 40 km in the x direction and 2.5 km in the z direction, with grid resolutions of $dx = dz = 10$ m. The simulated time period is 8 h. The sedimentation velocities are determined using the Reynolds number and the maximum particle dimensions, as described in the Appendix of Sölch and Kärcher (2010). We prescribe a stepwise vertical profile of relative humidity, assuming an ambient ice supersaturated layer of 120 % between 1 and 2 km (see further details in, e.g., Unterstrasser et al. (2017a)). Additionally, a synoptic-scale updraft with a velocity of $w = 1$ cm s $^{-1}$ is imposed over a period of approximately 6 h, leading to a final adiabatic cooling of 2 K. In these exemplary simulations, we model an A350 aircraft with $T_{CA} = 225$ K, $N_{BV} = 1.0 \times 10^{-2}$ s $^{-1}$, $I_0 = I_{0,H_2}$, and $r_{SD} = 3.0$. In the first simulation series, the contrail-cirrus initialization is directly based on the results from the according vortex phase simulation (with $N_{BV} = 1.15 \times 10^{-2}$ s $^{-1}$). The initialized contrail consists of $f_{N,s} \times N_0$ ice crystals. In the second simulation series, we deliberately disregard vortex phase loss processes and initialize a contrail with N_0 ice crystals. This is accomplished using the contrail data from the first simulation series and uniformly scaling up the ice crystal number concentrations by a factor of $(f_{N,s})^{-1}$.

An important quantity for analyzing contrail evolution is the total extinction, which serves as a metric for the radiative effect of an individual contrail (Unterstrasser, 2020). It is defined as the horizontal integral of the extinction, $1 - \exp(-\tau)$, where τ represents the optical thickness along the vertical direction. Then, the total extinction is expressed as follows:

$$\begin{aligned}
 E(t) &= \int (1 - \exp(-\tau(x, t))) dx \approx \int \tau(x, t) dx \\
 &= \iint \chi(x, z, t) dz dx,
 \end{aligned} \tag{3.23}$$

where $\chi(x, z, t)$ is the extinction coefficient. It is proportional to the projected area of the ice crystals per unit volume. We assume an extinction efficiency $Q_{\text{ext}} = 2$, as described in Schumann et al. (2011). Figure 3.10

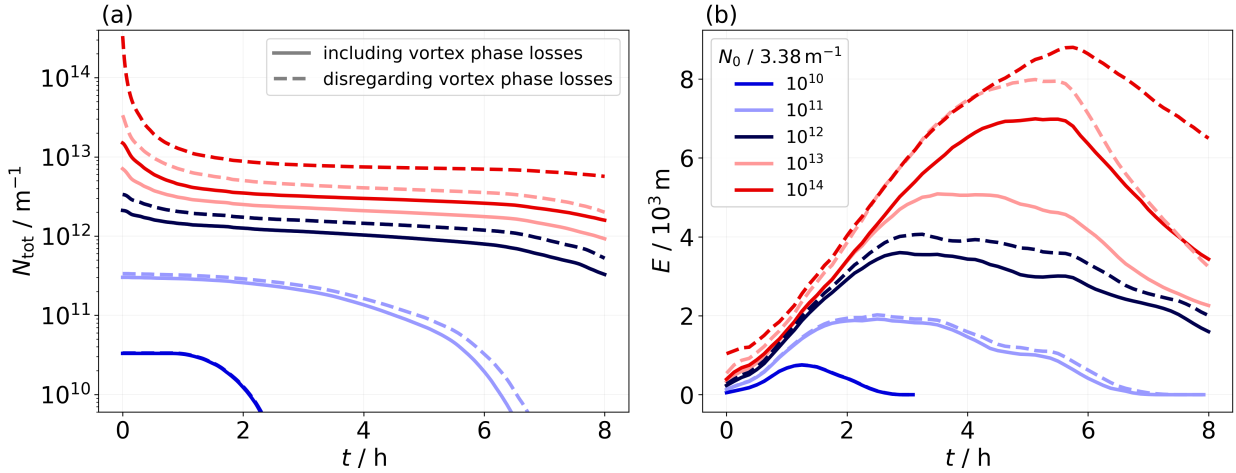


Figure 3.10: (a) Time evolution of the total number of ice crystals and (b) of the total extinction for the N_0 -upscaling and N_0 -downscaling cases. In the first simulation series, the contrails are initialized using the final state from the respective vortex phase simulations; in the second simulation series, the ice crystal numbers are upscaled by the respective survival fractions.

illustrates the temporal evolution of the total ice crystal number (panel (a)) and the total extinction (panel (b)). In both panels, the color represents the N_0 scaling, with red indicating upscaling scenarios and blue denoting downscaling scenarios. The line style differentiates between the two setups.

Based on this work, three key observations emerge. Firstly, E is significantly higher in the N_0 -upscaling scenarios. This outcome is expected, as total extinction is proportional to the effective surface area of the ice crystals; a larger number of ice crystals, as shown in panel (a), leads to a greater extinction. Secondly, the contrail (cirrus) dissipates more quickly when N_0 is smaller. In the scenario where N_0 is reduced by a factor of 100 (dark blue), the contrail disappears after only a few hours, indicating a significantly shorter lifetime. Thirdly, we observe an increase in E in the scenarios where the vortex phase losses are disregarded. In these cases, the contrail is initialized with more ice crystals compared to the first simulation series (see panel (a)).

A qualitative comparison of the two setups can be made by examining the lifetime-integrated total extinction values, $\hat{E} = \int E(t) dt$, that are displayed in Fig. 3.11a. Ignoring vortex phase losses leads, at maximum, to a difference in lifetime-integrated total extinction of 46%. This indicates that the radiative impact of an individual contrail can be significantly overestimated if vortex phase processes, such as contrail expansion and ice crystal sublimation in the primary wake, are not considered. The nonlinear increase in the \hat{E} difference between both setups in the N_0 -upscaling simulations may be attributed to saturation effects. As the number of ice crystals increases, competition for available water vapor in the spreading contrail cirrus becomes more important. Consequently, the peak ice mass does not continue to grow indefinitely with increasing N_0 values but is expected to reach a limit eventually. This explains why the simulation with a 100-fold increase in N_0 shows a smaller increase in lifetime-integrated total extinction when disregarding the vortex phase losses compared to the simulation with a 10-fold increase in N_0 . We repeated this kind of simulation series, i.e., disregarding the crystal losses from the vortex phase, for the $I_{0,\text{kero}}$ scenario. Interestingly, we observe only a small impact on the lifetime-integrated total extinction, with differences of $\leq 5\%$, when the vortex phase losses are ignored (see Fig. 3.11b). This suggests that the initial water vapor emission, compared to the ice crystal number, has only a minor impact on the radiative effect of an individual contrail-cirrus cloud.

This is just one example of a contrail-cirrus simulation set. A comprehensive analysis, examining various meteorological parameters, will follow.

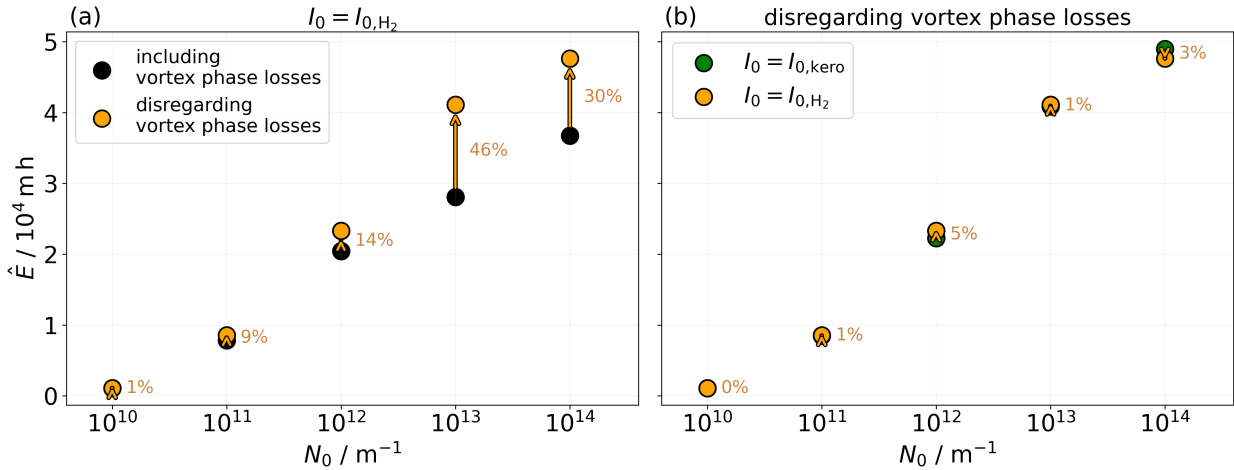


Figure 3.11: Lifetime-integrated total extinction (\hat{E}) for all five N_0 -scaling scenarios. Panel (a) highlights the increase in this quantity in the second simulation series (shown by the orange points). Panel (b) displays \hat{E} for both I_0 options. The orange points are the same in both panels.

3.2.3 Discussion

This study highlights the importance of ice crystal loss during the vortex phase depending on the propulsion system. While previous research has examined the effect of initial ice crystal numbers on crystal loss, such as [Lewellen \(2014\)](#), who varied the ice crystal emission index across six orders of magnitude, and [Unterstrasser \(2014\)](#), who explored a variation over two orders of magnitude, this work takes a systematic approach tailored explicitly to H_2 contrails. It uniquely combines variations in the initial number of ice crystals with adjustments to the emitted water vapor mass. The N_0 -upscaling scenarios may not only represent a potential H_2 -fuel cell setup but also account for the formation of contrail ice crystals on ultrafine volatile particles (UFPs). UFPs, typically nanometer-sized particles, can contribute to ice crystal formation if the plume supersaturation is high enough to overcome the Kelvin barrier for activation ([Kärcher et al., 2015](#)). This requires the reduction in the soot particle number of at least 10-fold, preventing them from acting as the primary condensation nuclei for water vapor, and an ambient temperature significantly below the formation threshold ([Kärcher, 2018](#)).

In addition to nitrogen species emissions from H_2 engines, oil vapor emissions due to engine lubrication systems are possible ([Ungeheuer et al., 2022](#); [Bier et al., 2024](#)). This can lead to the nucleation into ultrafine oil droplets, as observed in measurements ([Ungeheuer et al., 2021](#)). Experiments by [Ponsonby et al. \(2024\)](#) explored the potential of lubrication oil droplets to act as contrail ice-forming particles, revealing that these droplets are less effective as condensation nuclei than soot particles within the temperature range of 225–245 K. Nevertheless, the study showed that lubrication oil droplets can competitively deplete plume supersaturation under soot-poor conditions, as their critical supersaturation is readily achievable. In H_2 plumes, these ultrafine oil droplets might contribute to ice crystal formation alongside background aerosols. Further research on the properties of oil droplets, such as their size distribution and emission indices, is necessary to fully understand their potential role in contrail ice crystal formation processes. [Yu et al. \(2024\)](#) highlight that UFPs might significantly contribute to the total number of contrail ice particles if the sizes of the soot particles are reduced. Hence, understanding the role of UFPs in the contrail formation process requires the consideration of both soot emissions and particle sizes. The UFP number could potentially exceed that of emitted soot particles per flight distance, leading to a larger number of nucleated ice crystals in H_2 plumes compared to conventional kerosene plumes ([Kärcher et al., 2015](#); [Bier et al., 2024](#)). This justifies our approach of increasing the initial number of ice crystals to capture possible scenarios of additional ice-forming particle sources.

Furthermore, this study addresses a previously unexplored area by analyzing contrail evolution during the vortex phase at temperatures $> 225 \text{ K}$. At higher ambient temperatures, the number of nucleated ice crystals decreases, increasing the number of ice crystals that survive the vortex phase ([Bier and Burkhardt, 2022](#)).

As our study design is independent of the specific formation processes, it hypothetically determines the survival fractions for a given fixed N_0 .

We revised the original formulation of the vortex loss parameterization by incorporating the conservation of mass mixing ratios, adding a layer of complexity to the equations but ensuring that the physical assumptions are accurately represented. With appropriately chosen parameters, the arc tangent curve fits the data points well, both from U2016 and the present study. Additionally, the new formulation of the fitting function is designed to account for scenarios in which N_0 is significantly upscaled. Although the parameterization is based on the N_0 -scaling study spanning four orders of magnitude, it remains applicable even for more extreme values of N_0 . The parameterization also yields plausible results in terms of high ambient temperatures. The updated parameterization does not fully capture specific data points, particularly in cases with decreased stratification and downscaled N_0 values. As the length scale z_{desc} is the quantity that accounts for the variation in atmospheric stability, an adjustment to the formulation of z_{desc} , as initially proposed by Unterstrasser (2014), may be necessary to improve accuracy.

Next, we motivate our new choice for the adaptation factor Ψ in the updated ice crystal loss parameterization. The original version in U2016 was based on simulations that all had the same $\text{EI}_{\text{H}_2\text{O}}$ value, and the emission index EI_{iceno} was a good estimator of the representative ice crystal size in the contrail. A straightforward generalization would be to replace EI_{iceno} by the ratio $\text{EI}_{\text{H}_2\text{O}}/\text{EI}_{\text{iceno}}$ in the definition of Ψ . However, this quantity is only a proxy for the ice crystal mean mass ($:= I_0/N_0 = \text{EI}_{\text{H}_2\text{O}}/\text{EI}_{\text{iceno}}$) when all emitted water vapor deposits on the ice crystals, yet it neglects the contribution from the environment. Keeping in mind that the buffering effect of the two water vapor sources (from emission and from the environment) is already captured by z_{Δ} , we now define Ψ as a proxy for the typical ice crystal number concentration in the primary wake. The exact definition can be found in subsection A2.

One main goal of our study is to understand and systematically analyze the impact of the initial ice crystal number and of an assumed water vapor emission on the early contrail properties. We neglect any possible changes in aircraft geometry, mass, overall propulsion efficiency, etc., between current kerosene-driven aircraft and future H_2 aircraft. Clearly, such adaptations would affect the strength of the wake vortices and the fuel consumption (in addition to the factor 2.79^{-1} mentioned above). Moreover, H_2 fuel cells produce electric power that drives propellers. Design concepts with different numbers and positions of propellers and exhaust outlets exist in the literature (e.g., Marciello et al., 2023; Tiwari et al., 2024). Understanding the formation and the early evolution of contrails behind a propeller-driven aircraft deserves separate modeling studies. For the time being, we prefer to limit our study to variations in N_0 and I_0 without any other aircraft adaptation in order to avoid complicating and overloading the interpretation of our results.

Once H_2 aircraft designs are less hypothetical, one could incorporate such adaptations (like a systematically higher aircraft mass due to larger tank systems or particular aspects of H_2 fuel cell aircraft) in subsequent modeling studies.

The updated parameterization is now prepared for integration into large-scale global models, where the U2016 parameterization is already implemented (Bier and Burkhardt, 2022). Bier and Burkhardt (2022) underscore the significance of the initial number of ice crystals, highlighting the critical role of our study, which focuses on the vortex phase and ice crystal loss, in assessing the climate impact of H_2 contrails.

3.2.4 Conclusions

In this study, we simulated the evolution of contrails up to an age of approximately 6 min using the EULAG-LCM model, a fluid dynamics solver coupled with a particle-based microphysical model. The focus is on contrails produced by H_2 -powered aircraft, including both H_2 direct combustion and H_2 fuel cell systems. The simulations assume that ice crystal formation and vortex roll-up are complete at initialization. We varied the initial number of ice crystals over a wide range spanning 4 orders of magnitude, from $3.38 \times 10^{10} \text{ m}^{-3}$ ($0.85 \times 10^{10} \text{ m}^{-3}$) to $3.38 \times 10^{14} \text{ m}^{-3}$ ($0.85 \times 10^{14} \text{ m}^{-3}$) for an A350/B777-like (A320/B737-like) aircraft. Additionally, we scaled the emitted water vapor by a factor of 2.57 compared to the reference kerosene case. A parameter study was conducted, varying meteorological, microphysical, and aircraft parameters, focusing on the survival fraction / final number of ice crystals, a critical factor influencing subsequent contrail evolution.

Our simulations indicate that ice crystals tend to be larger in contrails from H₂-powered aircraft, leading to a higher likelihood of surviving the vortex phase. This effect is also observed in contrails initialized with a very small number of ice crystals, where the limited competition for available water vapor during depositional growth promotes the formation of larger ice crystals. As anticipated in previous studies, we find initial differences in the ice crystal number getting reduced after the vortex phase. The higher the initial ice crystal number, the stronger this reduction. This finding is independent of any meteorological condition. Sublimation driven by adiabatic heating in the descending vortex pair becomes more significant under drier atmospheric conditions, a trend consistent across all N_0 variations. Furthermore, a higher ambient temperature enhances ice crystal sublimation, although the surviving crystals tend to be larger. We find that the temperature sensitivity is particularly pronounced in the N_0 -upscaling scenarios. Reduced thermal stratification leads to a more significant loss of ice crystals, with this effect being more pronounced at higher initial ice crystal numbers and under drier atmospheric conditions. A shift towards a narrower initial size distribution generally produces larger ice crystal sizes, thereby reducing the extent to which initial differences are balanced, as we have consistently observed in the H₂ simulations. The weaker vortex descent associated with smaller aircraft results in a reduced sublimation of ice crystals in the primary wake, leading to higher survival fractions in the case of A320 aircraft. This trend is consistent across all N_0 values and ambient temperature scenarios.

We have refined the existing parameterization of ice crystal loss, presented by [Unterstrasser \(2016\)](#), by incorporating a new set of H₂-contrail simulations. Given that the new simulations tend to cluster at the extremes of the parameterization function, we adjusted the fitting procedure to better capture these behaviors. The updated set of fitting coefficients is provided. A comparison with simulation results from other studies demonstrates a good agreement with our updated parameterization.

It is not yet possible to make a definitive assessment of whether flying with H₂ is advantageous from a contrail perspective. Further research is needed to assess contrail formation processes for H₂ propulsion, with measurement results ([Airbus, 2023](#)) providing essential insights. As shown in Figs. 3.10 and 3.11, the initial number of ice crystals has a significant impact on the subsequent characteristics of the contrail. This study aimed to conduct a broad analysis of N_0 during the first 6 min of contrail evolution. More robustly determining the number of ice crystals formed in the H₂ case remains an active area of research.

4

Dispersion Phase

The study presented in this chapter addresses Research question 3 (see Sec. 1.4), focusing on how a switch to alternative fuels or propulsion systems affects the contrail-cirrus lifecycle during the dispersion phase. The following text is an excerpt of the manuscript draft titled *Lottermoser A. and Unterstrasser S. Modeling the impact of alternative fuels and hydrogen propulsion on contrail-cirrus: a parameter study* that has been submitted to *Journal of Geophysical Research: Atmospheres*. At the time of writing this thesis, the manuscript was in the revision process.

After introducing the method and simulation setup in Sec. 4.1, Sec. 4.2 analyzes how various ambient and aircraft-related parameters influence contrail-cirrus properties. Section 4.3.2 compares the results with other modeling approaches. The implications of the findings are discussed in Sec. 4.4, followed by the conclusions in Sec. 4.5.

4.1 Method

Section 4.1.1 describes the simulation setup. It provides a summary of the vortex phase simulations on which the present study builds (Sec. 4.1.1.1) and introduces the simulation parameters used (Sec. 4.1.1.2). Section 4.1.2 defines the quantities analyzed in this study.

4.1.1 Simulation setup

In the present study, we apply EULAG-LCM in two dimensions, with x representing the horizontal and z representing the vertical coordinate, i.e., the simulation domain is perpendicular to the flight direction. The general setup of the simulations is very similar to previous contrail-cirrus modeling studies with EULAG-LCM (e.g., Unterstrasser et al., 2017a,b; Unterstrasser, 2020). We only provide a brief summary of the basic settings, but describe in detail those aspects that have been adapted and are crucial to the present study.

The domain spans 40.96 or 81.92 km in the x -direction, depending on the strength of vertical wind shear (for higher wind shear values, the contrail spreads faster, and a larger domain is needed), and 2.5 km in the z -direction, representing a portion of the upper troposphere. Using a Cartesian grid, the mesh resolution is 10 m in both horizontal and vertical direction. The simulated time period is 8 h, with a time step ranging from 0.6 to 2 s, depending on the specific setup.

4.1.1.1 Hydrogen parameter study

Our contrail-cirrus simulations start several minutes after the contrail forms. By this point, the wake vortices have dissipated, and the contrail has a vertical extent of a few hundred meters. The final vertical

extent depends on the aircraft type, the initial microphysical properties such as the size of the formed ice crystals, and background conditions, including ambient relative humidity. The simulation results presented in [Lottermoser and Unterstrasser \(2025\)](#), from now abbreviated as LU25VP, serve as a starting point for the contrail-cirrus simulations investigated in this study. In the interest of completeness, we summarize the main findings from LU25VP.

In LU25VP, we presented and analyzed 3D simulations of young contrails, specifically focusing on contrails that form behind H_2 -powered aircraft. We modeled the initial minutes of their lifecycle, known as the vortex phase, where the interplay of ice microphysics and wake vortex descent and decay is the dominating phenomenon. We performed a total of 150 such simulations (see Tab. A1 for details), of which 100 are selected for the present study. Each defines an initial state of a contrail-cirrus simulation.

We investigated the sensitivity of H_2 -contrail properties to ambient and aircraft-dependent parameters with particular emphasis on the number of ice crystals surviving adiabatic heating during the vortex descent. By varying the initial number of ice crystals and the emitted water vapor mass, we modeled a potential H_2 -propulsion scenario. Specifically, we systematically scaled the initial ice crystal number, N_{00} , up and down by factors of 10 and 100, resulting in a range of 10^{10} to 10^{14} ice crystals per meter. The N_{00} -downscaling scenarios simulate a potential SAF- or H_2 -combustion setup, where fewer ice crystals form due to the reduction or absence of soot particle emissions, respectively ([Voigt et al., 2021](#); [Bier et al., 2024](#)). The lower bound of 10^{10} ice crystals per meter is informed by simulation results of [Bier et al. \(2024\)](#). Conversely, the N_{00} -upscaling simulations account for alternative ice crystal formation processes in soot-poor or soot-free scenarios, including the potentially significant contribution of volatile particles to the ice nucleation process. In a box model study investigating the role of lubrication oil particles in the soot-poor and H_2 -combustion scenario, [Zink et al. \(2025\)](#) showed that, at low ambient temperatures, final ice crystal number concentrations may reach up to 10^{14} m^{-1} when the oil emission index is on the order of 10^{17} kg^{-1} . Moreover, homogeneous droplet nucleation in fuel cell exhausts could similarly generate a high ice crystal number, justifying the upper limit of N_{00} in our simulations.

The increase in water vapor emission, I_{00} , when switching to H_2 results from the differing fuel properties of H_2 and kerosene and is incorporated by multiplying the default kerosene value by a factor of 2.57. I_{00} of the kerosene and hydrogen scenarios are denoted by $I_{00,\text{kero}}$ and I_{00,H_2} , respectively. The ice crystal properties used as input for the vortex phase simulations are listed in Tab. 4.1. The water vapor emission index in the SAF case can be up to 10 % higher than in the kerosene case due to the increased hydrogen content of SAF ([Teoh et al., 2022](#); [Dischl et al., 2024](#)). However, our results presented in Sec. 4.2 indicate that contrail properties are only weakly sensitive to I_{00} . Therefore, simulations using $I_{00,\text{kero}}$ and the proposed range of N_{00} values can be likewise interpreted as SAF scenarios, whereas simulations with I_{00,H_2} exclusively represent H_2 propulsion setups. Although I_{00} and N_{00} are not independent variables, as the number of initially formed ice crystals can depend on the water vapor emission, we prefer to vary I_{00} and N_{00} independently from each other within the chosen parameter range. This allows us to disentangle the effects that variations of I_{00} and N_{00} have on the subsequent contrail phases.

In LU25VP, we examined two aircraft types: an A350/B777-like aircraft with a wingspan of 60.3 m, representing a typical widebody aircraft and used as the default case, and a smaller A320/B737-like aircraft with a wingspan of 34.4 m as an example of a narrowbody aircraft. As noted in LU25VP, default values for N_{00} and I_{00} for these two aircraft were taken from [Unterstrasser and Görsch \(2014\)](#). We emphasize that some parameters, such as fuel consumption or wingspan, may not exactly reflect current aircraft specifications. Throughout this study, references to "A350" or "A320" should be understood as shorthand for "A350/B777-like aircraft" or "A320/B737-like aircraft", respectively. The inclusion of the smaller aircraft into our study accounts for the potential earlier adoption of H_2 propulsion in regional aviation. We varied the ambient temperature at cruise altitude between 217 K and 235 K, with 217 K as the default value based on cruise temperature statistics (e.g., [Kärcher et al., 2009](#)). The upper temperature limit reflects the possibility that contrails from H_2 -powered aircraft can form in warmer conditions where those from conventional kerosene combustion typically do not. The chosen temperature range corresponds to cruise-altitude pressure values between 233 and 235 hPa. Additionally, the ambient relative humidity with respect to ice was set to either 110 % or 120 %, informed by measurements ([Iwabuchi et al., 2012](#); [Petzold et al., 2020](#)). The extent of ice crystal loss may substantially differ between these two cases (see, e.g., Fig. 1 in [Unterstrasser \(2014\)](#)). We

	A320/B737	A350/B777
$N_{00} / ([10^{10}, 10^{11}, 10^{12}, 10^{13}, 10^{14}] / \text{m}^{-1})$	0.85	3.38
$I_{00} / (10^{-3} \text{ kg m}^{-1})$	[3.7, 9.5]	[15.0, 38.6]

Table 4.1: Ice crystal parameters used as input for the vortex phase simulations presented in Lottermoser and Unterstrasser (2025). N_{00} and I_{00} represent the initial ice crystal number and initial water vapor emission, respectively (prior to ice crystal loss during the vortex phase). The $N_{00} \sim 10^{12} \text{ m}^{-1}$ case is the default. High- N_{00} and low- N_{00} cases refer to the N_{00} -upscaling ($N_{00} \gtrsim 10^{13} \text{ m}^{-1}$) and N_{00} -downscaling ($N_{00} \lesssim 10^{11} \text{ m}^{-1}$) scenarios, respectively. In the second row, the numbers in brackets correspond to $I_{00,\text{kero}}$ and I_{00,H_2} , respectively.

then define the survival fraction as the final number of ice crystals surviving the vortex phase N_0 divided by the initial ice crystal number N_{00} .

The main findings in LU25VP are the following:

1. We observe survival fractions of up to 90 to 100 % if N_{00} is downscaled. This is due to the larger crystal sizes compared to the N_{00} -reference or -upscaling cases.
2. Simulations with $I_{00} = I_{00,\text{H}_2}$ show higher survival fractions compared to the default $I_{00,\text{kero}}$ cases, as the additional water vapor increases the initial average crystal sizes. This finding holds for all N_{00} variations.
3. The impact of adiabatic heating in the downward moving vortex system on the ice crystals increases with increasing ambient temperature. Therefore, survival fractions decrease with higher cruise-altitude temperatures for all N_{00} scenarios, with the strongest losses for temperatures higher than 230 K.
4. Compared to the default ambient relative humidity of 120 %, simulations with a lower value of 110 % consistently show stronger sublimation and reduced vertical extents of contrails across all N_{00} scenarios.

In summary, we find the initial differences in ice crystal number, encompassing four orders of magnitude, are reduced to three or even two orders of magnitude, depending on the initial ice crystal properties and the prescribed ambient conditions. Table A3 presents the final total number N_0 and mass I_0 of the contrails after the vortex phase that are used as input for the present contrail-cirrus study.

4.1.1.2 Contrail initialization and simulation parameters

To initialize the contrail and the background fields, the Eulerian 3D data, such as perturbations in water vapor concentration and potential temperature, are averaged along the flight direction and interpolated onto the coarser grid. The SIPs representing the ice crystals are merged to reduce their overall number. The initialized contrails are described by approximately 10^5 SIPs, which have been shown to provide robust estimates of the contrail quantities analyzed in the present study.

Figure 4.1a illustrates an example initialization setup, with the black box encompassing the region where the contrail from the 3D vortex phase simulation is embedded. In this example, the contrail is located at $x \approx 23 \text{ km}$ and has a vertical extent of around 500 m. The flight altitude in the simulation domain is at $z = 2000 \text{ m}$. This value should not be interpreted as a real flight altitude; it is only a vertical coordinate within the model domain. The prescribed temperature and pressure correspond to upper-tropospheric cruise conditions. For each contrail-cirrus simulation, we conduct four different realizations of the same setup by horizontally shifting the contrail position relative to the background, as indicated by the black box in Fig. 4.1a. With this, we ensure that we account for a potentially different contrail evolution due to small turbulence-induced perturbations in the background fields. Unless stated, we average over the four simulations and compute mean contrail quantities.

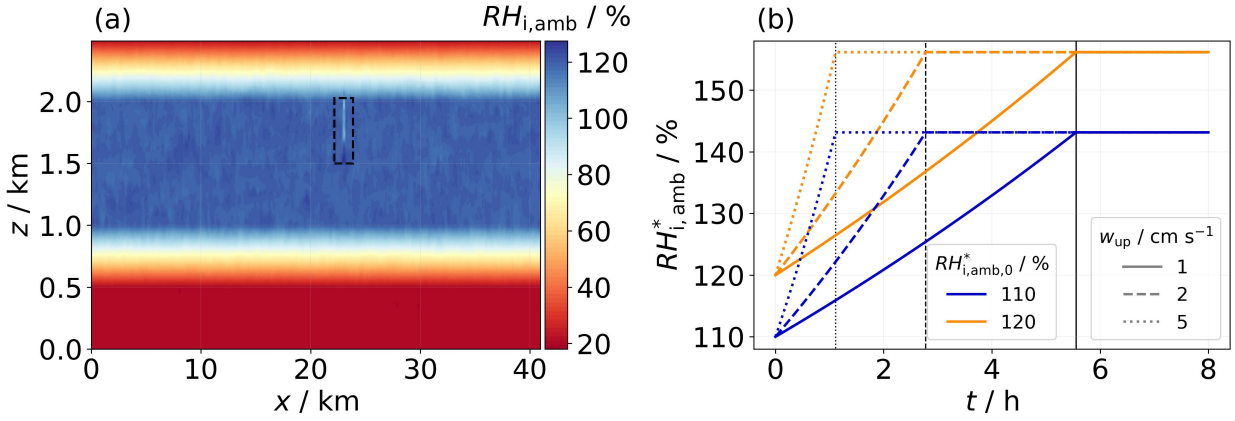


Figure 4.1: (a) Vertical profile of relative humidity with respect to ice. The black box frames the initial position of the contrail. (b) Evolution of relative humidity with respect to ice at $z = 2$ km for different updraught speeds w_{up} . The black lines mark the endpoints of the uplifting process.

Figure 4.1a also displays the initially prescribed vertical profile of ambient relative humidity with respect to ice, $RH_{i,\text{amb}}$, which we set to either 110 % or 120 % within the ice supersaturated layer (ISSL). We denote this initial value as $RH_{i,\text{amb},0}^*$. The ISSL has an initial thickness $d_{\text{ISSL},0}$ of roughly 1100 m ($RH_{i,\text{amb},0}^* = 110$ %) or 1180 m ($RH_{i,\text{amb},0}^* = 120$ %), transitioning linearly to subsaturated layers with 20 % relative humidity at the top and bottom parts of the simulation domain. In the ISSL, the local humidity values fluctuate around the prescribed $RH_{i,\text{amb}}^*$ value. Furthermore, RH_i inside the contrail is lower than the background humidity as the contrail ice crystals have already depleted water vapor in this area (LU25VP).

The background relative humidity is not static in our simulation. $RH_{i,\text{amb}}$ changes during the simulation as we prescribe a spatially homogeneous updraught of the whole domain over a certain time period. This updraught motion induces adiabatic cooling, which is represented by an external forcing term in the temperature equation in EULAG (a more technical description is given in Sec. 2 of [Unterstrasser and Gierens \(2010b\)](#)). We consider three different updraught scenarios with updraught velocities $w_{\text{up}} = 1, 2, \text{ or } 5 \text{ cm s}^{-1}$ (referred to as low, medium, high). Previous contrail-cirrus simulations have demonstrated that this parameter influences the contrail evolution ([Unterstrasser et al., 2017b](#); [Unterstrasser, 2020](#); [Lewellen, 2014](#)). To achieve a final adiabatic cooling ΔT_{cool} of 2 K (corresponding to a vertical displacement of ≈ 200 m), we terminate the uplift motion by prescribing fixed uplift durations. Faster updraughts correspond to shorter uplift times, as illustrated in Fig. 4.1b. The uplift velocities of 1, 2, and 5 cm s^{-1} yield uplift durations of 20000, 10000, and 4000 s, which are denoted by the vertical black lines. The cooling by 2 K causes $RH_{i,\text{amb}}^*$ to reach final values of 143 % in the case of $RH_{i,\text{amb},0}^* = 110$ % and 156 % for $RH_{i,\text{amb},0}^* = 120$ %. Hence, the thickness of the ISSL increases to $d_{\text{ISSL},\text{final}} = 1350$ m ($RH_{i,\text{amb},0}^* = 110$ %) or 1410 m ($RH_{i,\text{amb},0}^* = 120$ %).

For an ambient supersaturation above a critical threshold, natural cirrus can form via heterogeneous and/or homogeneous nucleation ([Koop et al., 2000](#); [Gierens, 2003](#); [Cziczko et al., 2013](#)). We deliberately deactivate both nucleation pathways and therefore suppress the formation of natural cirrus at later contrail stages. Hence, we focus on simulating contrails evolving into aircraft-induced contrail cirrus in an otherwise cloud-free atmosphere. A discussion of this assumption is deferred to Sec. 4.4.

We vary the ambient temperature at flight altitude: $T_{\text{CA}} = 217, 225, 230, 233, \text{ and } 235 \text{ K}$. Throughout the text, T_{CA} represents the initial temperature at cruise altitude. The vertical temperature profiles are characteristic of a stably stratified atmosphere, with a Brunt-Väisälä frequency N_{BV} of 0.01 s^{-1} , a typical value of the upper troposphere. Background turbulent velocity fields were derived from a-priori simulations with a root mean square value of approximately 0.12 m s^{-1} ([Unterstrasser et al., 2017a](#); [Unterstrasser, 2020](#)). Furthermore, we prescribe vertical wind shear, $s = \frac{\partial u}{\partial z}$, which is defined as the vertical gradient of the horizontal wind field. For simulations with $w_{\text{up}} = 1, 2, \text{ and } 5 \text{ cm s}^{-1}$, we apply a moderate shear value of $s = 0.002 \text{ s}^{-1}$. We additionally consider a higher shear value of 0.006 s^{-1} for simulations with $w_{\text{up}} = 1 \text{ cm s}^{-1}$.

Table 4.2 provides a summary of the setup parameters. Based on the 100 vortex phase simulations, we

Numerical parameters	
$L_x, L_z / \text{m}$	40960 (81920), 2500
$dx, dz / \text{m}$	10, 10
$t_{\text{sim}} / \text{h}$	8
dt / s	0.6, 1, 1.25, 2
Atmospheric parameters	
$N_{\text{BV}} / \text{s}^{-1}$	0.01
$RH_{i,\text{amb},0}^* / \%$	110, 120*
T_{CA} / K	217*, 225, 230, 233, 235
$\Delta T_{\text{cool}} / \text{K}$	2
$d_{\text{ISSL},0} (110 \%), d_{\text{ISSL},\text{final}} (110 \%) / \text{m}$	1100, 1350
$d_{\text{ISSL},0} (120 \%), d_{\text{ISSL},\text{final}} (120 \%) / \text{m}$	1180, 1410
$w_{\text{up}} / \text{cm s}^{-1}$	1*, 2, 5
s / s^{-1}	0.002*, 0.006

Table 4.2: Numerical and atmospheric parameters used in our simulations. L_x, L_z : domain dimension in horizontal and vertical direction (the domain size in horizontal direction is doubled in the high-shear cases); dx, dz : mesh size in horizontal and vertical direction; t_{sim} : total simulated time; dt : time step; N_{BV} : Brunt-Väisälä frequency; $RH_{i,\text{amb},0}^*$: initial ice relative humidity in the supersaturated layer; T_{CA} : initial ambient temperature at flight level; ΔT : final adiabatic cooling; $d_{\text{ISSL},0}, d_{\text{ISSL},\text{final}}$ (x %): thickness of the ice supersaturated layer at the beginning and end of the simulation (the value in brackets specifies $RH_{i,\text{amb},0}^*$); w_{up} : updraught speed; s : vertical wind shear. Values marked with an asterisk indicate the baseline values.

conducted 1600 contrail-cirrus simulations, covering four meteorological scenarios (three w_{up} values and one additional high wind shear scenario) and four initial contrail positions. Even though temperature is also a meteorological variable, our meteorological scenarios are, by definition, solely characterized by w_{up} and s . This appears reasonable as the encountered ambient temperature depends, apart from the prevailing meteorological conditions, even more strongly on the flight altitude. While the total number of simulations amounts to 1600, the variation in initial contrail position does not alter the underlying parameter configuration. Therefore, these cases are considered repetitions under identical parameter settings. As such, we effectively conducted 400 distinct parameter simulations.

4.1.2 Quantities of interest

This section introduces the key quantities used throughout the study.

The total ice crystal number N_{tot} (in units m^{-1}) is defined as the 2D spatial integral of the ice crystal concentration N (in units m^{-3})

$$N_{\text{tot}}(t) = \iint N(x, z, t) dx dz, \quad (4.1)$$

and, analogously, the total ice mass M_{tot} (in units kg m^{-1}) is the 2D spatial integral of the ice water concentration IWC (in units kg m^{-3})

$$M_{\text{tot}}(t) = \iint IWC(x, z, t) dx dz, \quad (4.2)$$

where IWC is the first moment of the lognormal mass distribution prescribed in our model (e.g., Unterstrasser, 2014). The normalized number of ice crystals $f_N(t)$ is defined as the number of ice crystals $N_{\text{tot}}(t)$ divided by the initial ice crystal number of the dispersion phase $N_0 = N_{\text{tot}}(t = 0)$. Analogously, the normalized number of sublimated ice crystals $f_{N,\text{subl}}(t)$ is the number of sublimated ice crystals divided by N_0 . This quantity can be further subdivided into $f_{N,\text{subl},\text{in situ}}(t)$, representing losses due to in-situ sublimation, and $f_{N,\text{sedi}}(t)$, representing sedimentation losses.

The vertical profiles of contrail ice crystal number N_v and ice mass M_v are

$$N_v(z, t) = \int N(x, z, t) dx \quad (4.3)$$

and

$$M_v(z, t) = \int IWC(x, z, t) dx. \quad (4.4)$$

Vertical profiles of f_N and $f_{N,\text{subl}}$ are denoted by $f_{N,v}$ and $f_{N,v,\text{subl}}$, respectively.

We further define the size D of an ice crystal, where its mass and area are derived via mass-size and area-size relationships for hexagonal columns (Sölch and Kärcher, 2010). We calculate the effective crystal diameter d_{eff} according to Yang et al. (2000), where the summed particle volume V_{tot} and summed particle projected area A_{tot} are used:

$$d_{\text{eff}} = \frac{3}{2} \frac{V_{\text{tot}}}{A_{\text{tot}}}. \quad (4.5)$$

While the size D represents the maximum dimension of a single ice crystal, and ice particle size distributions are derived in terms of D , the effective diameter d_{eff} is a measure of an ice crystal population and is employed in radiative transfer calculations or in remote sensing applications (McFarquhar and Heymsfield, 1998; Schumann et al., 2011).

An important quantity in the context of the contrail's radiative properties is the optical thickness τ , which is the vertically integrated extinction coefficient χ :

$$\tau(x, t) = \int \chi(x, z, t) dz. \quad (4.6)$$

The extinction coefficient is calculated as the projected area of all ice crystals in each grid box multiplied by the extinction efficiency, Q_{ext} . In this study, we apply a constant value of $Q_{\text{ext}} = 2$. This choice is strictly valid only in the geometric optics limit, i.e., when the size parameter is much larger than one (typically $\gtrsim 20$ to 30) (Hansen and Travis, 1974). In this regime, where ice crystal sizes are much larger than the wavelength (e.g., 2 to 4 μm for visible wavelengths), Q_{ext} approaches 2. For smaller crystals, such as in our N_{00} -upscaling case, where the size parameter is closer to unity, Mie scattering occurs and Q_{ext} oscillates around 2 (van de Hulst, 1981). We therefore acknowledge that applying a constant value represents a simplified assumption. On the other hand, using a constant Q_{ext} value in our evaluation has the advantage that χ and d_{eff} depend only on the ice crystal habit and size distribution as modeled with EULAG-LCM and not on further processes like Mie scattering. Hence, those quantities are easier to interpret.

The mean optical thickness $\tau_m(t)$ is computed as the average of $\tau(x, t)$, excluding columns where $\tau(x, t) < 0.005$. Also, we define the contrail's optical width τ_{hor} , which is written as

$$\tau_{\text{hor}}(z, t) = \int \chi(x, z, t) dx. \quad (4.7)$$

Further, the total extinction E (see Eq. 3.23) reads as

$$E(t) = \iint \chi(x, z, t) dx dz = \int \tau(x, t) dx. \quad (4.8)$$

The time-integrated total extinction \hat{E} is

$$\hat{E} = \int_0^{t_{\text{lim}}} E(t) dt, \quad (4.9)$$

which represents the cumulative effect of total extinction over the simulation period up to t_{lim} , capturing the overall radiative impact of the contrail.

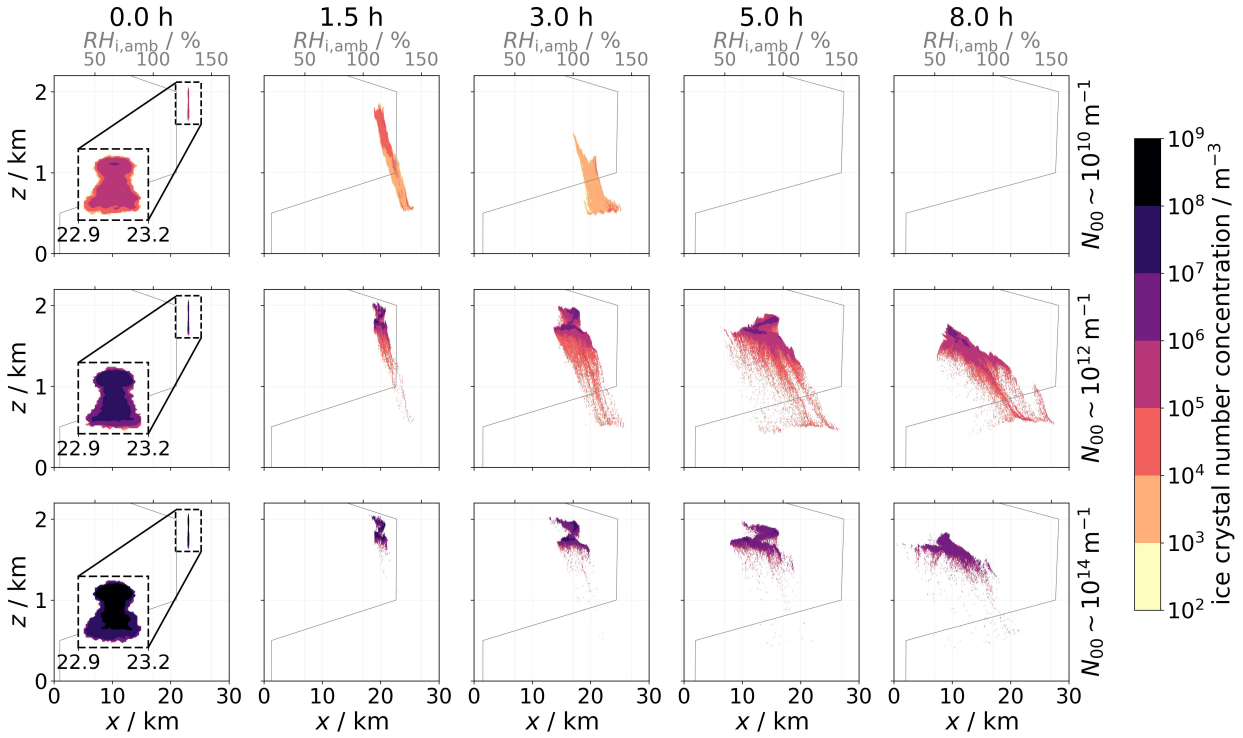


Figure 4.2: Ice crystal number concentration in the (x, z) -plane at five different time steps (columns). For better visibility, the initial contrail (first column) is magnified, enlarging the region from 22.9 to 23.2 km. The rows show results for a different initial ice crystal number N_{00} : The middle row represents the reference N_{00} case, while the upper and lower rows correspond to the factor-of-100 N_{00} -downscaling and N_{00} -upscaling simulations, respectively. The background relative humidity profile is displayed as a grey curve in each panel. Note that only a fraction of the simulation domain is depicted.

4.2 Results

This section presents example contrail-cirrus simulations as an introductory part (Sec. 4.2.1) before progressing to the parameter study of contrail-cirrus properties (Sec. 4.2.2). With a focus on the N_{00} -sensitivity, Sec. 4.2.1 illustrates the fundamental physical processes during contrail-cirrus evolution, including cross-sectional area evolution (Sec. 4.2.1.1), ice crystal loss processes (Sec. 4.2.1.2), and the temporal evolution of integrated contrail properties (Sec. 4.2.1.3). Section 4.2.2 analyzes how specific parameter variations influence the contrail-cirrus evolution (Sec. 4.2.2.1), examines a scaling relation between E and N_{00} (Sec. 4.2.2.2), investigates the response of \hat{E} to N_{00} in terms of t_{lim} and T_{CA} (Sec. 4.2.2.3), and evaluates the sensitivity of \hat{E} to N_{00} across all parameter variations (Sec. 4.2.2.4).

4.2.1 Impact of initial ice crystal number scaling on contrail-cirrus evolution: example simulations

The example simulations feature an A350/B777-like aircraft with an initial water vapor emission of 38.6 g m^{-1} , representing H_2 propulsion (see Tab. 4.1). We set the ambient conditions to the baseline values described in Tab. 4.2. Based on Figs. 4.2 to 4.5, we explain important processes involved in contrail-cirrus evolution that have been explored in previous studies (Unterstrasser and Gierens, 2010a,b; Unterstrasser et al., 2017a; Lewellen et al., 2014; Lewellen, 2014). Expanding upon these findings, our study investigates the impact of the initial ice crystal number varied over a broad range.

4.2.1.1 Low- and high- N_{00} contrails: implications on the cross-sectional areas

Figure 4.2 illustrates the temporal evolution of ice crystal number concentration. During the first hour, contrail tilting due to vertical wind shear is apparent, while entrainment of supersaturated air promotes the growth of the ice crystals. The development of fallstreaks through sedimentation (most clearly seen in the middle row of Fig. 4.2) creates two distinct regions: a compact core with high ice crystal number concentrations and an expanding area dominated by sparsely populated fallstreaks. The distribution of ice crystal sizes differs between the core and the fallstreaks: Figure 4.3 shows large ice crystals with diameters up to $100\ \mu\text{m}$ in the fallstreaks, consistent with observations by Lawson et al. (1998). In contrast, small crystals with sizes $10\text{--}20\ \mu\text{m}$ are present in the core, as reported by Voigt et al. (2017) and Wang et al. (2023).

The evolution of contrail cirrus differs significantly across the N_{00} scaling simulations. Comparing the first and third rows in Fig. 4.2, a well-developed fallstreak emerges within 1.5 h in the $N_{00} \sim 10^{10}\ \text{m}^{-1}$ scenario, whereas the $N_{00} \sim 10^{14}\ \text{m}^{-1}$ contrail retains a distinct core with relatively weak crystal settling. The low- N_{00} contrail dissipates after just 3 to 4 h. These observations are attributed to the varying crystal sizes between both scenarios, as further examined in the following section.

4.2.1.2 Low- and high- N_{00} contrails: sedimentation versus in-situ sublimation

Two primary mechanisms are responsible for the loss of ice crystals during contrail-cirrus evolution (Unterstrasser et al., 2017a): in-situ sublimation, which occurs when local humidity fluctuations induce transiently subsaturated air masses, leading to the preferential sublimation of smaller ice crystals due to the Kelvin effect (Lewellen, 2012); and sedimentation loss, where ice crystals fall into subsaturated air beneath (in our scenarios, this is the region $z \leq 700$ to $800\ \text{m}$), and sublimate. Although those ice crystals are ultimately lost due to sublimation, we refer to this as sedimentation loss.

The impact of sedimentation varies across the different N_{00} cases. Initially, ice crystals are larger in low- N_{00} contrails (10 to $20\ \mu\text{m}$) and smaller in high- N_{00} contrails (3 to $4\ \mu\text{m}$, see dotted lines in Fig. 4.3, first panel in the second row), influencing their sedimentation behavior. The fallstreaks become increasingly populated over time across all N_{00} scenarios, redistributing ice mass toward lower altitudes (Fig. 4.3, second row). However, in low- N_{00} cases, the sedimentation flux of ice crystal number and mass becomes substantial within the first 1 to 2 h, leading to a fast dehydration of the contrail core. Considering the normalized number of sublimated ice crystals, $f_{N,\text{subl}}$, in the third row, two distinct vertical sublimation peaks arise: one peak covering the contrail core and representing the in-situ losses, and one peak at lower altitudes in the subsaturated layer representing the sedimentation losses in the fallstreaks. Apparently, the order of the colors representing the N_{00} parameter is reversed in the two peaks: In low- N_{00} contrails, the ice crystals predominantly get lost by sedimentation processes, whereas the major part of ice crystals sublimate at higher altitudes in high- N_{00} contrails.

To further support this finding, Fig. 4.4 depicts the normalized number of ice crystals (solid black) and the normalized number of sublimated ice crystals (dashed black) for the different N_{00} -scaling scenarios. In the downscaling cases, sedimentation loss approaches or reaches 100%, whereas in the upscaling cases, it is nearly negligible ($\lesssim 4\%$). Instead, crystal loss in the high- N_{00} cases, where ice crystals are on average smaller (Fig. 4.8), is primarily driven by in-situ sublimation ($\gtrsim 76\%$), which is in turn absent or minimal in the low- N_{00} cases ($\lesssim 3\%$). Notably, when going from $N_{00} \sim 10^{12}\ \text{m}^{-1}$ to $N_{00} \sim 10^{14}\ \text{m}^{-1}$, the in-situ loss rate strongly increases from 41% to 87%, as the smallest ice crystals sublimate almost immediately. This is confirmed by the evolving size spectra, displayed in the first row of Fig. 4.8 ($T_{\text{CA}} = 217\ \text{K}$), showing that the size spectrum shifts toward larger crystal sizes over time across all N_{00} scalings: Small crystals sublimate in-situ, and large crystals grow at the expense of smaller ones — a process known as Ostwald ripening (Lewellen, 2012). A "fallstreak shoulder" appears earlier in the N_{00} downscaling scenarios (blue curves), while a more pronounced "sublimation tail" is observed in the upscaling cases (red curves) over the entire period.

Notably, the colored pattern of Fig. 4.4 remains largely unchanged when varying temperature or updraught speed (not shown). Thus, sedimentation emerges as the dominant factor governing the shorter lifetime of low- N_{00} contrail cirrus compared to their high- N_{00} counterparts. The initial onset of sedimentation is

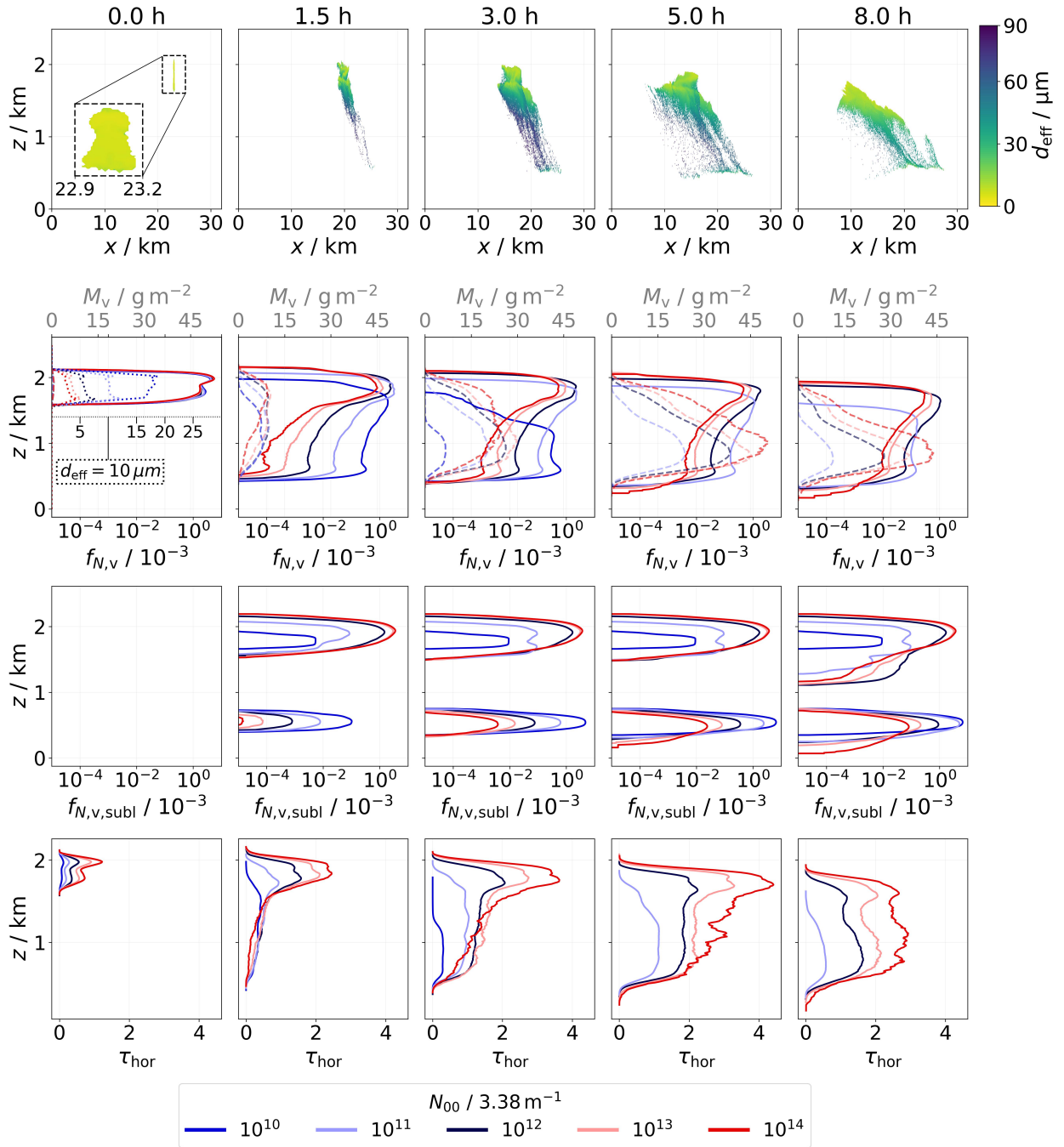


Figure 4.3: First row: temporal evolution of effective ice crystal diameter in the (x, z) -plane. Note that the d_{eff} values of the N_{00} -reference simulation are shown here. Second row: vertical profiles of ice mass (dashed) and normalized ice crystal number (solid) for the scaled initial ice crystal number (color). At $t = 0$ h, we also display the initial effective diameter (dotted). Third row: vertical profiles of normalized number of sublimated ice crystals. Fourth row: vertical profiles of optical width. The time steps are the same as for Fig. 4.2. The shown results correspond to the baseline simulation setup (see Tab. 4.2).

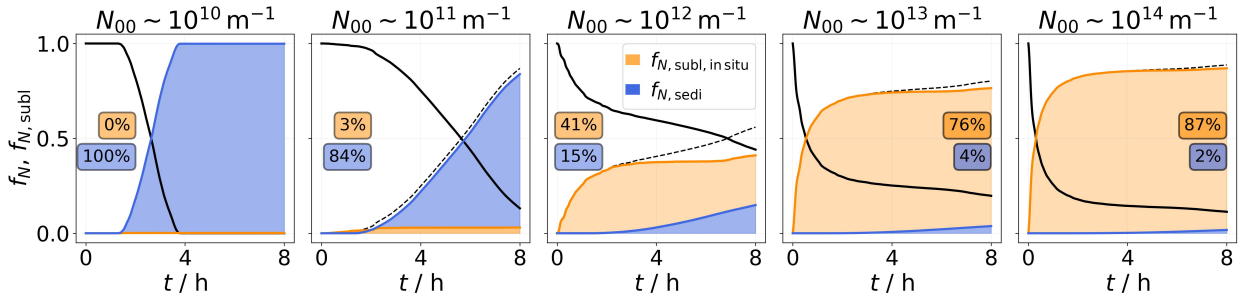


Figure 4.4: Temporal evolution of normalized number of ice crystals (solid black) and sublimated ice crystals (dashed black), where the latter is further subdivided into in-situ sublimation (orange) and sedimentation (blue). The columns represent the five N_{00} -scaling cases of the baseline simulation setup (see Tab. 4.2). The percentage values in the orange (blue) boxes indicate the final fraction of ice crystals lost due to in-situ sublimation (sedimentation).

similar across the N_{00} cases (after ≈ 70 min). It depends more strongly on ambient temperature and relative humidity. We find an earlier onset of fallstreak growth in warm cases, after ≈ 25 min for $T_{CA} = 235$ K, which was also found by Lewellen et al. (2014).

These findings have strong implications on the temporal evolution of optical width τ_{hor} , shown in the fourth row in Fig. 4.3. Evident in all scaling simulations, τ_{hor} of the fallstreaks increases over time due to the increasing number and mass of ice crystals there, whereas in the core region τ_{hor} first increases but then decreases again. Due to the steady supply of ambient water vapor in updraught scenarios and contrail spreading, ice crystals keep growing, and sedimentation losses become more substantial, eventually outweighing the deposition-induced mass increase in the core region. These processes happen earlier in the low- N_{00} contrails, which are characterized by relatively greater sedimentation fluxes. In these cases, the extinction in the fallstreaks reaches levels comparable to those in the contrail core after just 1 to 3 h. On the other hand, a high number of initial ice crystals corresponds to a large projected area density and, hence, a greater extinction of radiation. Therefore, the overall larger values of τ_{hor} observed in the high- N_{00} scenarios are expected. In these scenarios, the peak optical width continues to increase as long as the updraught motion persists.

4.2.1.3 Low- and high- N_{00} contrails: temporal evolution of contrail properties

Lastly, we examine the temporal evolution of important contrail-cirrus properties, including total ice crystal number, total ice mass, mean optical thickness, and total extinction, see Fig. 4.5. M_{tot} and E increase with the entrainment of moist air, sustaining crystal growth as long as the updraught persists. However, once the updraught ceases (in this example case, at 5.5 h), the crystal growth halts and can no longer compensate for sedimentation and in-situ losses. While the rate of change remains comparable for cases with $N_{00} \geq 10^{12} \text{ m}^{-1}$, a noticeable flattening of ice mass and total extinction occurs earlier in the $N_{00} \sim 10^{11} \text{ m}^{-1}$ and $N_{00} \sim 10^{10} \text{ m}^{-1}$ scenarios already after 2 and 1 h, respectively, due to the rapid sedimentation of ice crystals in these cases. The sensitivity of N_{tot} to N_{00} is asymmetrical, as also found by Lewellen et al. (2014): For $N_{00} \geq 10^{12} \text{ m}^{-1}$, the initial difference of a factor of 11 diminishes to a factor of 3 over time, whereas for $N_{00} < 10^{12} \text{ m}^{-1}$, the difference in N_{tot} increases. Note that the initial factor of 10^4 difference (N_{00}) diminishes to 10^2 (N_0), highlighting the importance of accounting for vortex phase losses as outlined in LU25VP. Within the first 30 min, τ_m drops due to contrail broadening (the relative change of contrail width is largest for the initially narrow contrails). After this initial drop, the ice crystal growth can overcompensate the ongoing shear-induced spreading, leading to an increase of τ_m as observed for cases with $N_{00} \geq 10^{12} \text{ m}^{-1}$. The peaks of M_{tot} and E roughly coincide in time. In contrast, τ_m stays constant or monotonically decreases for low- N_{00} contrail cirrus as the crystal growth cannot compensate for the continuous loss of sedimenting ice crystals and the shear-induced spreading.

This section has demonstrated that the N_{00} value is a key parameter with a lasting impact on the overall properties and lifetime of contrail cirrus. The example simulations presented so far showcase the relative

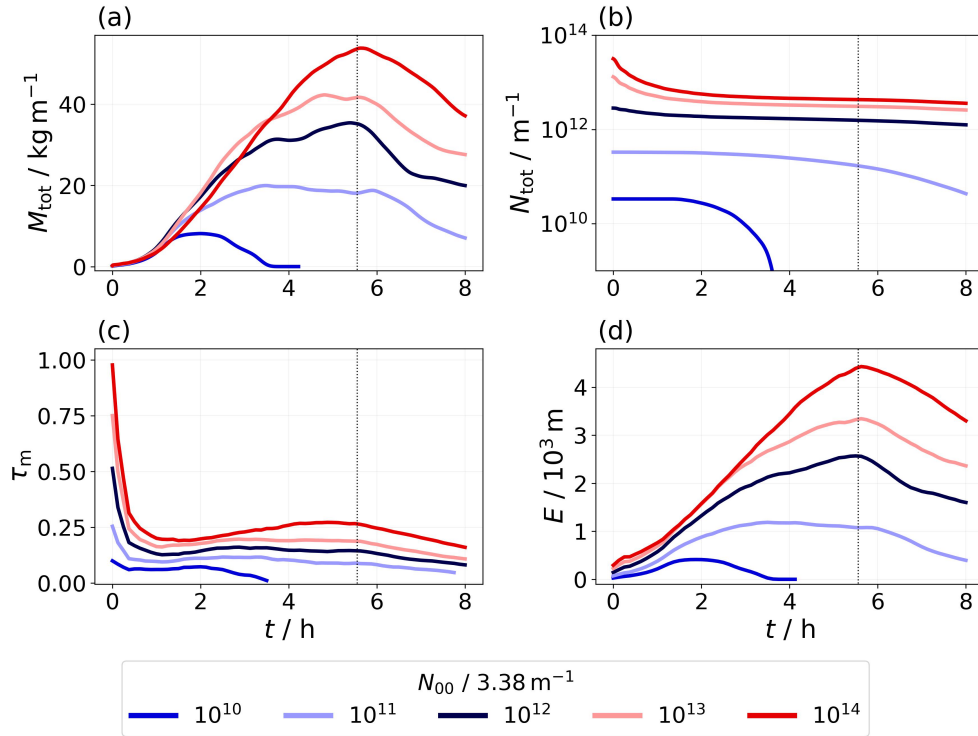


Figure 4.5: (a) Temporal evolution of the total ice mass, (b) total ice crystal number, (c) mean optical thickness, and (d) total extinction of the baseline simulation setup. The vertical black lines indicate the time point where the updraught motion stops. Colors indicate the N_{00} scaling.

contributions of in-situ sublimation and sedimentation loss across the N_{00} -scaling scenarios. For example, the rapid and intense sedimentation loss in the extreme low- N_{00} case (e.g., leftmost panel in Fig. 4.4 or dark blue curves in Fig. 4.5) leads to contrail dissipation within 3 to 4 h. This already suggests a great potential of reducing the initial ice crystal number for the purpose of reducing the contrail-cirrus radiative impact.

4.2.2 Parameter study of contrail-cirrus properties

This section aims to answer the question of how the relative differences between the N_{00} scenarios qualitatively change for variations in aircraft type and water vapor emission, as well as for variations in ambient conditions, such as ambient temperature, relative humidity, updraught speed, and vertical wind shear.

4.2.2.1 Impact of parameter variations on contrail-cirrus properties

Figures 4.6 and 4.7 show sample cross-sections, with each column representing a specific parameter variation around a baseline state as described in Sec. 4.1.1. The contrail-cirrus properties shown in Fig. 4.5, total ice mass, total ice crystal number, total extinction, and mean optical thickness, are displayed row-wise.

In general, variations in relative humidity or temperature affect the number of ice crystals surviving the vortex phase and the contrail vertical extent, which in turn influence the initialization of the dispersion phase. Updraught speed w_{up} and vertical wind shear s are only varied in the contrail-cirrus simulations. Hence, all simulations that vary only w_{up} or s are initialized with identical contrails.

Firstly, we examine variations in aircraft- and fuel-related parameters. A variation in the initial water vapor mass, shown in Fig. 4.6a, has only a minor impact on contrail-cirrus evolution: In the case of a higher water vapor emission (solid lines), the slightly larger values of total ice mass, total extinction, and optical thickness result from the higher survival fraction of ice crystals during the vortex phase, which was shown in Sec. 3.2.2.4. Thus, the slight differences in the evolution of " I_{00,H_2} "- and " $I_{00,kero}$ "-contrails stem from differences in N_0 rather than I_{00} . Switching from an A350 aircraft to a smaller A320 aircraft results in notable differences in the evolution of total contrail properties (b). The lower peak ice mass, peak total

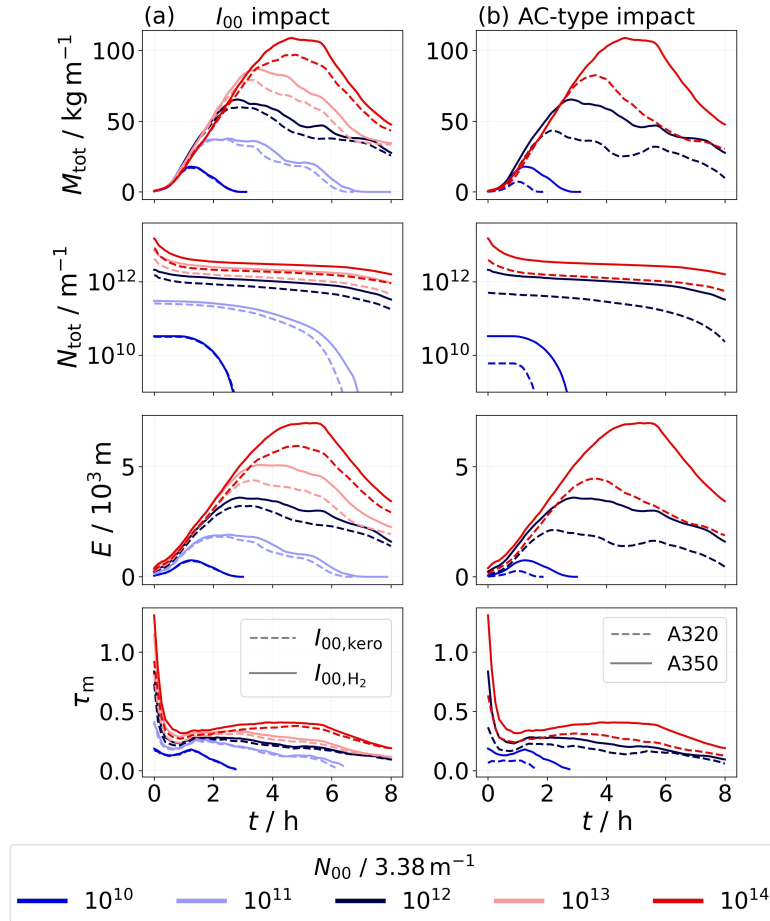


Figure 4.6: Temporal evolution of total ice mass, total ice crystal number, total extinction, and mean optical thickness depending on the N_{00} scaling, denoted by the colors. Baseline state: A350 aircraft with water vapor emissions characteristic of H_2 propulsion at $RH_{i,amb,0}^* = 120\%$ and $T_{CA} = 225\text{ K}$, with a meteorological scenario of $w_{up} = 1\text{ cm s}^{-1}$ and $s = 0.002\text{ s}^{-1}$. **Column (a):** $I_{00} = 38.6\text{ g m}^{-1}$ (solid) and 15.0 g m^{-1} (dashed); **Column (b):** A350 aircraft (solid) and A320 aircraft (dashed). In the column heading, "AC" stands for "aircraft".

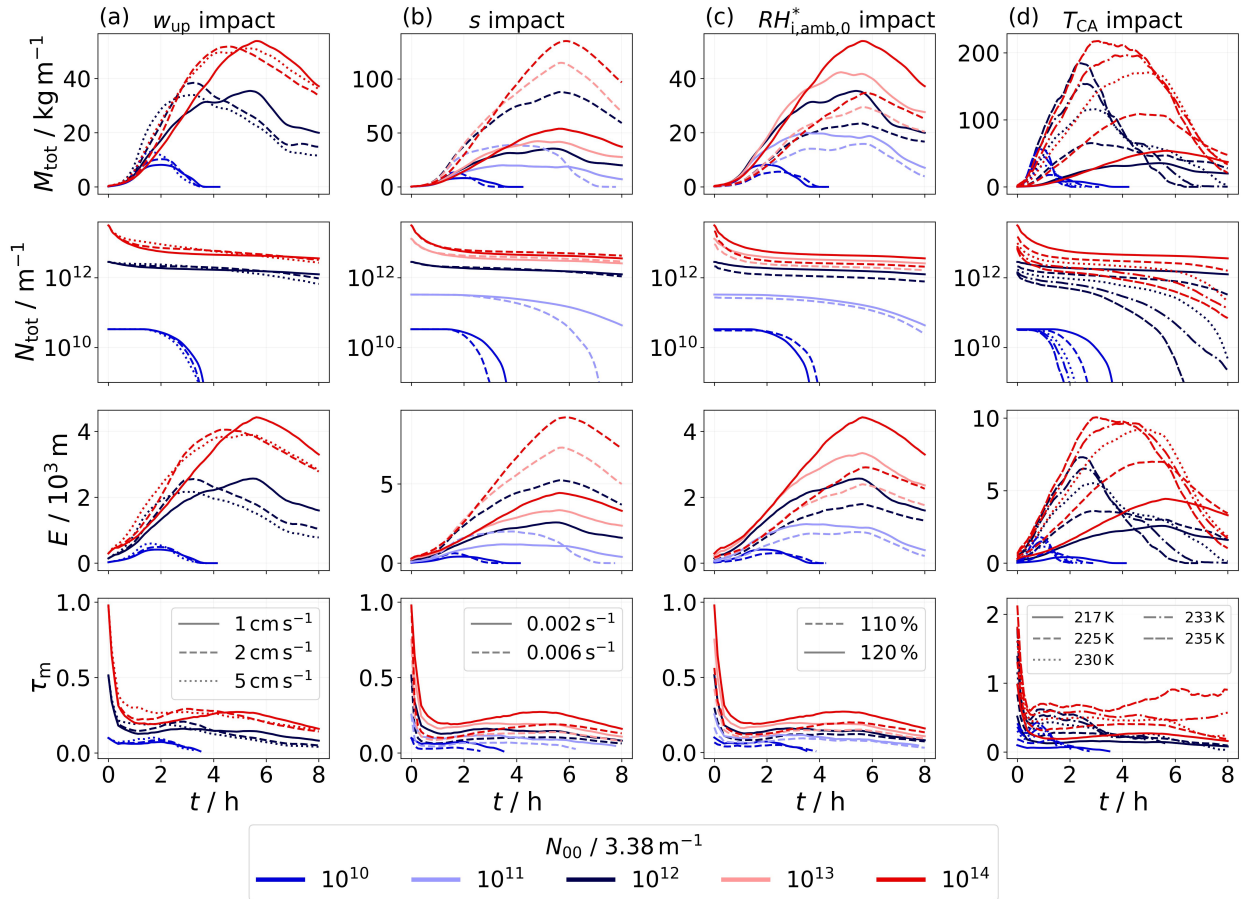


Figure 4.7: Temporal evolution of total ice mass, total ice crystal number, total extinction, and mean optical thickness depending on the N_{00} scaling, denoted by the colors. Baseline state: A350 aircraft with water vapor emissions characteristic of H_2 propulsion, under baseline ambient conditions listed in Tab. 4.2. **Column (a):** $w_{up} = 1 \text{ cm s}^{-1}$ (solid), 2 cm s^{-1} (dashed), and 5 cm s^{-1} (dotted); **Column (b):** $s = 0.002 \text{ s}^{-1}$ (solid) and 0.006 s^{-1} (dashed); **Column (c):** $RH_{i,amb,0}^* = 110 \%$ (dashed) and 120% (solid); **Column (d):** $T_{CA} = 217 \text{ K}$ (solid), 225 K (dashed), 230 K (dotted), 233 K (dash-dotted), and 235 K (densily-dashed). In columns (a) and (d), only the extreme scaling scenarios are displayed (factor 100 scaling) for better visibility. Note that the y-axis scales vary between columns.

extinction, and peak optical thickness in the A320 case compared to the A350 case can be attributed to two main factors. On the one hand, the A320 contrail is shallower after the vortex phase, leading to less spreading and reduced water vapor uptake during the contrail-cirrus evolution. On the other hand, although ice crystal number reduction during the vortex phase is less pronounced in the A320 case compared to the A350 case (LU25VP), the A320 aircraft has a smaller N_{00} value (roughly one fourth, see Tab. 4.1), which leads to a smaller N_0 value, and, therefore, to smaller peak values of ice mass, crystal number, and extinction.

Secondly, we analyze variations of ambient conditions, as shown in Fig. 4.7. A variation of updraught speed is displayed in (a). Previous studies have shown that strong but short-lasting updraughts shorten contrail lifetimes, as ice crystals grow rapidly early on but then quickly sediment (Unterstrasser and Gierens, 2010b; Unterstrasser et al., 2017b). Consistent with this, we observe a $\lesssim 10$ min earlier onset of sedimentation-induced ice crystal loss in the high-updraught cases across all parameter variations. Although initially unexpected, ice crystal loss due to in-situ sublimation ultimately dominates in high-updraught scenarios. This is explained by the short uplift period of around 1 h: Once the updraught ceases, no additional water vapor is available, leading to in-situ sublimation. In the low-updraught scenarios, by contrast, additional moisture becomes available for roughly 5.5 h, yet at a lower rate. This leads to a larger fraction of ice crystals

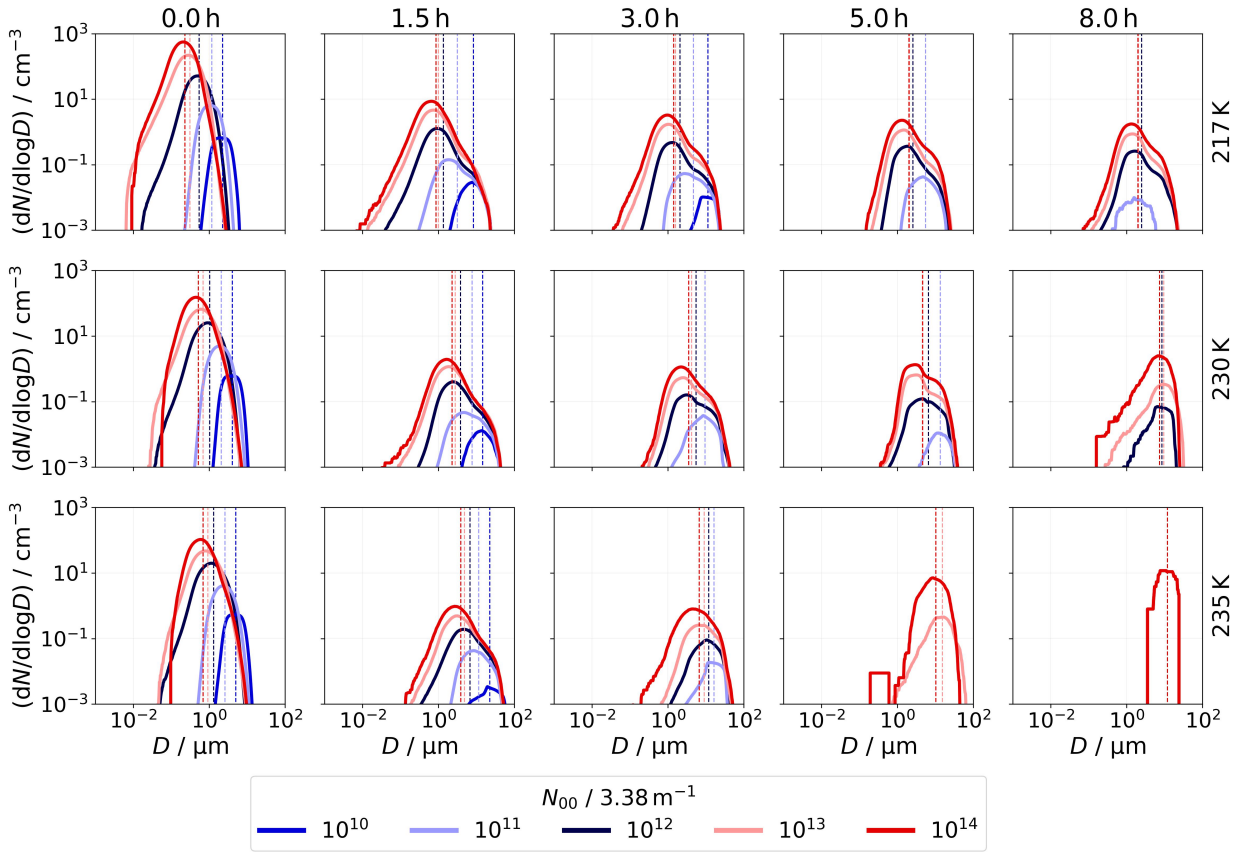


Figure 4.8: Temporal evolution of size spectra of ice crystal number for three ambient temperatures (rows). All other ambient conditions correspond to the baseline values (see Tab. 4.2). Time points are chosen as in Fig. 4.3. The vertical lines indicate the mean values of the size distributions.

that get lost by sedimentation.

The strength of vertical wind shear plays a crucial role in contrail-cirrus evolution (b). High wind shear leads to rapid contrail broadening and enhances ice crystal growth by continuously transporting them horizontally into regions with undepleted, supersaturated air. This results in a substantial increase in ice mass and extinction—exceeding 100 % in the N_{00} -upscaling scenarios and around 50 % in the downscaling cases. However, the stronger sedimentation flux under high-shear conditions also reduces contrail-cirrus lifetime. When varying the background relative humidity with respect to ice (c), we observe larger values of total ice mass, ice crystal number, extinction, and mean optical thickness for the higher $RH_{i,amb,0}^*$ value across all N_{00} scenarios. This can be attributed to three key factors: First, in the 110 % case, fewer ice crystals survive the vortex phase. Second, the updraught-induced water vapor supply during the simulation is generally lower compared to the 120 % case. Third, the initial contrail is shallower, making it less prone to horizontal spreading and subsequent ice crystal growth. In the simulation with a 100-fold reduction of N_{00} (dark blue curve), the contrail-cirrus lifetime is by around 10 min shorter in the 120 % scenario, an initially counterintuitive result. In this specific case, all ice crystals survive the adiabatic heating during the vortex phase, independent of background relative humidity. The depth of the five-minute-old contrail is hence the crucial factor determining the contrail-cirrus’ lifetime: In the 120 % case, larger ice crystals are initially present in the lower part of the contrail compared to the 110 % case, leading to a stronger sedimentation flux that ultimately reduces the lifetime. This finding, however, is specific to the low-temperature case (217 K) but applies across all meteorological scenarios considered here.

The impact of ambient temperature on contrail-cirrus evolution is substantial, shown in (d). Higher ambient temperatures correspond to higher absolute humidity levels due to the exponential increase in saturation pressure, allowing more moisture to deposit onto ice crystals and promote their growth. In Fig. 4.8,

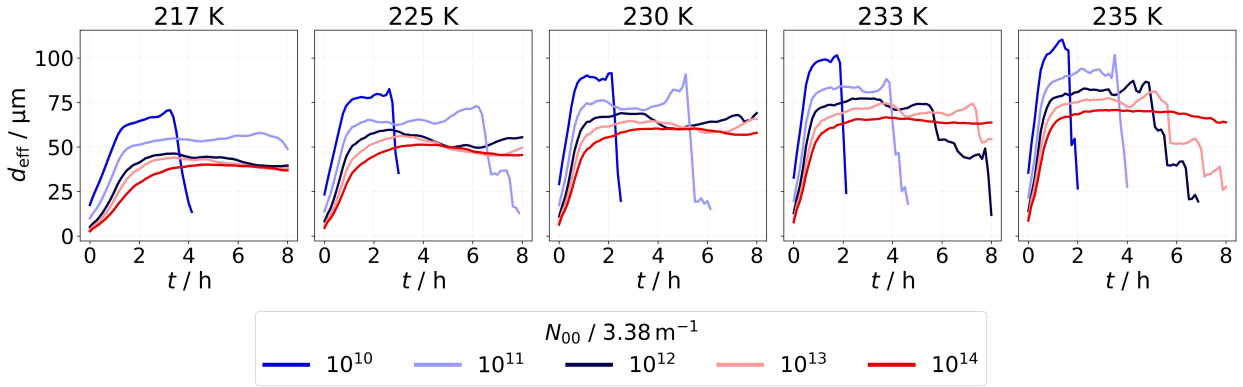


Figure 4.9: Evolution of effective diameter at five different values of ambient temperature. All other ambient conditions correspond to the baseline values (see Tab. 4.2).

each row corresponds to a different ambient temperature, revealing a clear trend of increasing crystal size with increasing temperature. Also, simulations at higher T_{CA} already start with fewer but larger crystals, resulting from the vortex phase processes (LU25VP). Consequently, peak ice mass and total extinction are approximately between 130 and 340 % ($N_{00} \sim 10^{14}$ to $N_{00} \sim 10^{10} \text{ m}^{-1}$) higher in the 235 K case compared to the 217 K scenario. The more pronounced differences in low- N_{00} contrails are further examined in Sec. 4.2.2.2. Rapid crystal growth also leads to a shorter contrail-cirrus lifetime. Ambient temperature significantly influences the evolution of the effective crystal diameter, as illustrated in Fig. 4.9. While the increase in d_{eff} remains moderate at lower temperatures, it becomes more pronounced at higher temperatures, reaching values $> 100 \mu\text{m}$ in low- N_{00} contrails.

In assessing the influence of the parameters N_{00} , I_{00} , aircraft type, $RH_{i,\text{amb},0}^*$, T_{CA} , w_{up} , and s on peak mass, extinction, and contrail-cirrus lifetime, we find that, besides N_{00} , temperature has the most significant impact on peak mass and extinction, followed by wind shear. In comparison, initial relative humidity, aircraft type, updraught speed, and initial water vapor emission are of secondary importance. However, this section offers only a partial view of the complex interdependencies involved, as the sensitivity studies presented are around a baseline state. We provide a more detailed exploration of these interdependencies in the following sections.

4.2.2.2 Scaling relation between total extinction and ice crystal number

The study of [Unterstrasser and Gierens \(2010b\)](#) has related total extinction to the initial ice crystal number via the power law

$$\frac{E(t)}{E_{\text{ref}}(t)} = \left(\frac{N_0}{N_{0,\text{ref}}} \right)^\alpha, \quad (4.10)$$

where N_0 was varied across two orders of magnitude. For the first 3 h of contrail evolution, they found α to be approximately 0.35, capturing the instantaneous sensitivity of extinction to changes in the initial number of ice crystals. [Lewellen \(2014\)](#) reported a similar value of 1/3.

Extinction is related to the projected surface area A of ice crystals, which scales with $m^{\sigma/\beta}$, where m is the ice crystal mass. The constants σ and β are the exponents of empirical power law functions for area-size and mass-size relations, namely $A \sim D^\sigma$ and $m \sim D^\beta$ ([Mitchell, 1996](#); [Heymsfield et al., 2002](#)). They depend on the ice crystal habit and size; in the simplest case, $\sigma = 2$ and $\beta = 3$ for spherical ice crystals. For crystals with non-unity aspect ratios, both σ and β are smaller (see [Sölch and Kärcher, 2010](#), and references therein). Assuming a delta-function size distribution, where all crystals have the same mass and size, the relation $\alpha = 1 - \sigma/\beta$ holds (see Sec. A4). For spherical ice crystals, this yields $\alpha \approx 0.33$, while for hexagonal columns smaller than $100 \mu\text{m}$, empirical relations by [Mitchell et al. \(1996\)](#) give $\alpha \approx 0.31$. Besides the ice crystal habit, also the shape of the size distribution affects the relation between extinction and ice crystal number. Both effects can be theoretically captured ([Schumann et al., 2011](#)). The evaluation of our model data comprises both effects. We confirm the theoretical expectations of α around 0.3 by evaluating Eq. 4.10,

which yields initial exponents $\alpha(t = t_0)$ consistently lying between 0.1 and 0.4, regardless of whether N_{00} or N_0 is used (not shown).

$\alpha(t)$ decreases across all N_{00} scaling cases during the first hour of evolution. This indicates that $E(t)$ in both upscaling and downscaling scenarios grows more slowly than in the reference case. In the upscaling cases, this can be attributed to the relatively weaker fallstreaks, the regions where most of the ice mass accumulates, thereby reducing the rate of mass growth. In the downscaling cases, the projected crystal area grows more slowly than in the reference case since the smaller ice crystal number cannot be compensated by the larger average crystal sizes. For the extreme high-temperature scenarios ($T_{CA} \geq 230$ K), $\alpha(t)$ even becomes negative in the factor-of-100 N_{00} -upscaling cases during the first 1 to 2 h, due to an initially lower number of vortex phase-surviving ice crystals. Eventually, for all cases, $\alpha(t)$ diverges at later times as either $E(t)$ or $E_{\text{ref}}(t)$ approaches zero. Comparing the use of N_{00} and N_0 in the above formula, both definitions yield qualitatively similar behavior. However, the spread in initial α values around 0.3 is reduced when N_0 is used, since the range spanned by the scaling factors (i.e., 0.01, 0.1, 10, and 100) is somewhat compressed relative to that of N_{00} . As an example, the scaling factors change to 0.015, 0.14, 3.55, and 7.5 in the case of an A350 aircraft at $T_{CA} = 217$ K, $RH_{i,\text{amb},0}^* = 120$ %, and $I_{00} = 15$ g m⁻¹.

4.2.2.3 Response of \hat{E} to N_{00} : contrail-lifetime considerations

To assess contrail significance in our study, we use the time-integrated total extinction \hat{E} , which is given in Eq. 4.9. This quantity serves as a proxy for estimating the change in the climate impact of a single contrail. In our simulations, contrail-cirrus dissipation is purely microphysically driven. However, large-scale atmospheric processes, such as subsiding air masses, may create subsaturated conditions that lead to dynamically driven contrail dissipation (Bier et al., 2017; Hofer and Gierens, 2025). To approximate scenarios where synoptic-scale processes lead to faster contrail dissipation, we integrate contrail properties up to specified time limits t_{lim} , which are smaller than the total simulated time of 8 h.

As we are interested in a relative change of contrail extinction with N_{00} , Fig. 4.10a displays $\tilde{E}_{N_{00}} = \hat{E}(N_{00})/\hat{E}(N_{00,\text{ref}})$ as a function of N_{00} , where color-coded $\tilde{E}(t_{\text{lim}})$ values connect vertical lines. As expected from Figs. 4.5-4.7, we find an increase (decrease) in $\tilde{E}_{N_{00}}$ with increasing (decreasing) N_{00} . The temporal evolutions of total extinction, exemplarily shown in these figures, demonstrate that the peak value in the extinction evolution is eventually exceeded across all N_{00} variations at some point in time, and extinction values decrease again. Hence, the vertical distances between the symbols along a vertical line get smaller for larger t_{lim} . This effect is more pronounced when the peak extinction value is reached earlier, which occurs in the low- N_{00} regime and at high ambient temperatures. When considering contrail-cirrus evolution over a two-hour period, increasing N_{00} , especially under high-temperature conditions, has only a minor effect. The orange symbols corresponding to 110 % and 120 % relative humidity remain close to one, indicating little deviation from the reference extinction. This limited impact is due to substantial in-situ sublimation in the upscaling scenarios during the early phase (see Sec. 4.2.2), where a large fraction of ice crystals is lost early. This is reflected in the strong early drop in ice crystal number (second row in Figs. 4.6 and 4.7). Additionally, the growth in ice mass is less steep due to smaller mean crystal sizes compared to the N_{00} -reference case (Fig. 4.8), resulting in a similar increase in early extinction $E(t < 2$ h) between the reference and upscaling simulations. In contrast, differences between the reference and downscaling scenarios become apparent within that period. As the contrail dissipates most quickly in the scenario with a 100-fold reduction in N_{00} , the $\tilde{E}_{N_{00}}$ value is reduced to only ≈ 10 % of the reference value. Overall, we observe a greater impact of $RH_{i,\text{amb},0}^*$ on $\tilde{E}_{N_{00}}$ in the upscaling than in the downscaling cases, particularly for long integration times.

Investigating the influence of ambient temperature on each N_{00} -scaling scenario separately, panel (b) reveals that ambient temperature plays the most significant role for short-living contrail cirrus. Under warm conditions, i.e., $T_{CA} \geq 225$ K, the ice mass gain is most pronounced in the first few hours of the contrail-cirrus lifecycle. Due to enhanced ice crystal loss because of stronger and earlier-occurring sedimentation at higher temperatures (Sec. 4.2.1), $\tilde{E}_{T_{CA}}$ gradually converges toward the 217 K reference, $\tilde{E}_{T_{CA}} = 1$, at longer integration times. In the 110 % scenarios, when T_{CA} exceeds 217 K, $\tilde{E}_{T_{CA}}$ drops below one after 6 to 8 h. Although having considerably larger peak extinction values compared to the 217 K reference (e.g., at 235 K and $N_{00} \sim 10^{11}$ m⁻¹ the peak is roughly a factor of seven higher), high- T_{CA} contrail cirrus dissipate quickly,

leading to a relatively lower lifetime-integrated total extinction. Examining the temporal evolutions of total extinction, peak total extinctions increase more strongly with higher T_{CA} values in the 120 % scenarios compared to the 110 % humidity cases (not shown). This contrast is due to the lower availability of ambient water vapor in the 110 % scenarios, limiting the growth of the ice crystals. For this reason, the temperature impact is generally more significant for 120 % than for 110 % relative humidity across all N_{00} simulations (circles deviate stronger than triangles from the reference). Additionally, the spread in high-temperature cases is particularly large in the $N_{00} \sim 10^{11} \text{ m}^{-1}$ scenario but becomes smaller in the $N_{00} \sim 10^{10} \text{ m}^{-1}$ case, where the very low number of ice crystals cannot be compensated by temperature-induced crystal growth. This finding is independent of relative humidity. Overall, the trend of the $\tilde{E}_{T_{CA}}(t_{\text{lim}} = 8 \text{ h})$ values (blue) remains approximately constant (at 120 %) or even decreases (at 110 %) with increasing temperature $T_{CA} \geq 230 \text{ K}$, except the factor-of-100 N_{00} -downscaling, 120 % humidity case. Therefore, we do not expect a substantial increase in total extinction compared to the 217 K reference when temperature is increased further within one N_{00} -scaling setup.

In summary, raising N_{00} barely changes contrail-cirrus extinction during the first 2 h because the majority of the ice crystals sublime in that period (see Fig. 4.4). By contrast, reducing N_{00} leads to a significant effect already within that phase, as the low- N_{00} contrails dissipate before the 4 h mark under conditions of low humidity and high temperature. At high temperatures ($T_{CA} \geq 225 \text{ K}$), contrail cirrus initially gain ice mass rapidly, leading to large peak extinction values early (i.e., within 2 h). However, strong sedimentation causes them to dissipate quickly, so their integrated extinction approaches or even falls below the 217 K reference after 6–8 h. We provide implications of these findings in Sec. 4.4.

4.2.2.4 Impact of N_{00} scaling on mean normalized \hat{E} across parameter variations

In the following, we show the average of \hat{E} across all ambient and meteorological conditions, aircraft type, and water vapor emission values considered in this study. The resulting normalized values are shown in Fig. 4.11a. The fitting curves exhibit nonlinear behavior: While upscaling N_{00} by a factor of 100 leads only to a factor of 1.2 in $\hat{E}/\hat{E}_{\text{ref}}$ for $t_{\text{lim}} = 2 \text{ h}$, downscaling by a factor of 100 results in a fivefold difference. Increasing the integration time generally leads to a steepening of the curves, particularly in the low- N_{00} regime, where the contrail cirrus dissipates within a few hours (see Sec. 4.2.2). As a result, the reduction in \hat{E} relative to the reference becomes more pronounced for longer-living contrail cirrus, increasing from a factor of 5 to a factor of 20. At the high- N_{00} end, however, the increase in \hat{E} compared to the reference is much smaller than in the low- N_{00} regime, with $\hat{E}/\hat{E}_{\text{ref}}$ increasing only from a factor of 1.2 to a factor of 2.1. Further, we show $\hat{E}/\hat{E}_{\text{ref}}$ as a function of $N_0/N_{0,\text{ref}}$ (accounting for ice crystal number reduction during vortex phase), displayed as dashed line. This curve is closer to the one-to-one line as relatively more ice crystals are present in the N_{00} -downscaling cases compared to the upscaling cases.

Panels (b) to (f) display the average curves for integration times of 2 and 8 h (i.e., short- and long-living contrail cirrus), with each panel illustrating the effect of a specific parameter variation around the mean state. Focusing on a reduction in the initial ice crystal number, $N_{00}/N_{00,\text{ref}} < 1$, contrail extinction decreases relative to \hat{E}_{ref} in scenarios involving a smaller aircraft with increased water vapor emission, higher ambient temperatures, and under conditions of high supersaturation. This indicates that, when few but large ice crystals are present after the vortex phase, a humid environment with ample available water vapor promotes rapid sedimentation. The opposite, i.e., higher $\hat{E}/\hat{E}_{\text{ref}}$ values, is observed for the N_{00} -upscaling, yet the effect is less pronounced. Overall, we find the largest deviations from the mean state for variations in aircraft type and ambient temperature, particularly for short integration times, as anticipated in Sec. 4.2.2. Overall, a reduction in the initial ice crystal number by factors of 100 and 10 decreases mean total extinction by factors of approximately 20 and 2, respectively. Conversely, increasing N_{00} by factors of 10 and 100 leads to an increase in total extinction by factors of approximately 1 and 2, respectively. The most significant reduction is observed for an A320 aircraft, where a factor 100 decrease in N_{00} results in a factor 33 reduction in mean total extinction.

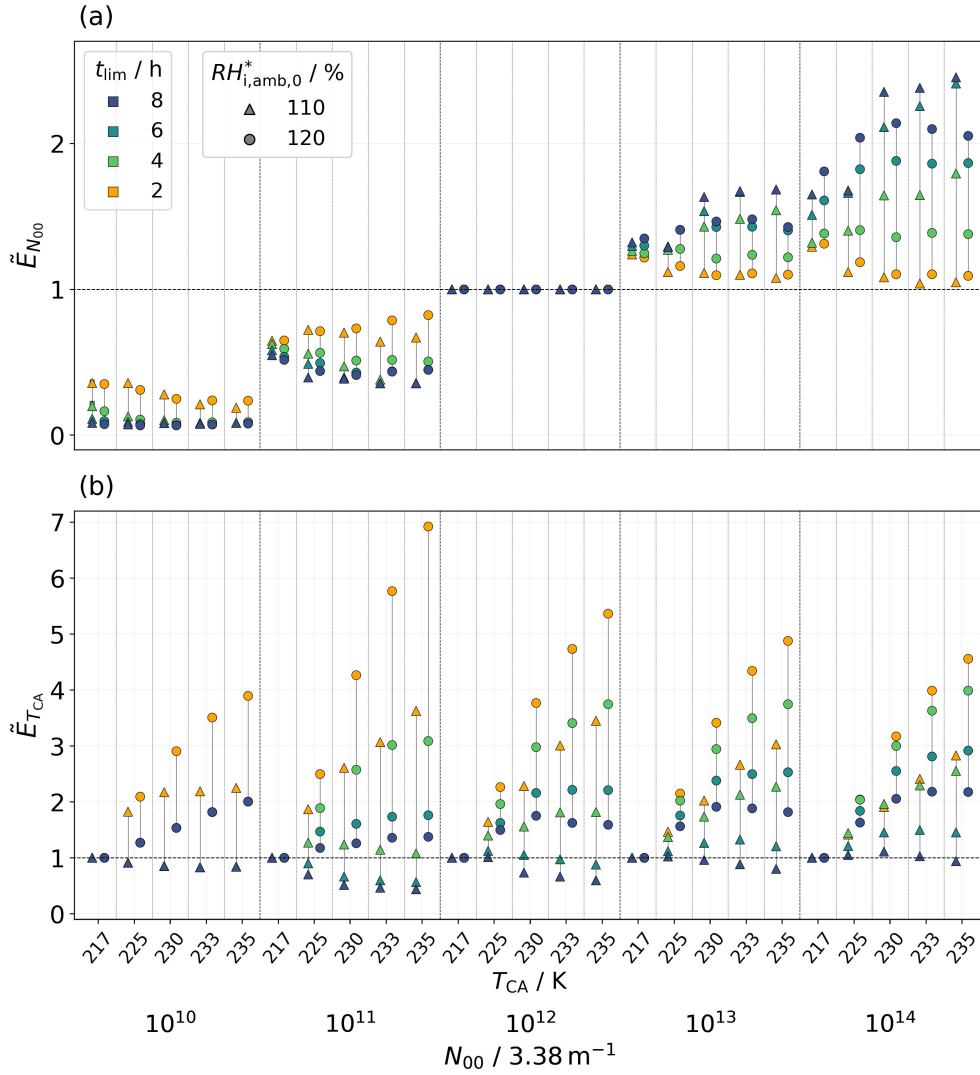


Figure 4.10: (a) Normalized time-integrated total extinction $\tilde{E}_{N_{00}}$ and (b) $\tilde{E}_{T_{CA}}$, i.e., \hat{E} normalized either by $\hat{E}(N_{00}=N_{00,\text{ref}})$ or $\hat{E}(T_{CA}=217 \text{ K})$. The data points represent averages over the updraught scenarios. The displayed simulations are for an A350 aircraft with $I_{00} = I_{00,\text{H}_2}$ and $s = 0.002 \text{ s}^{-1}$.

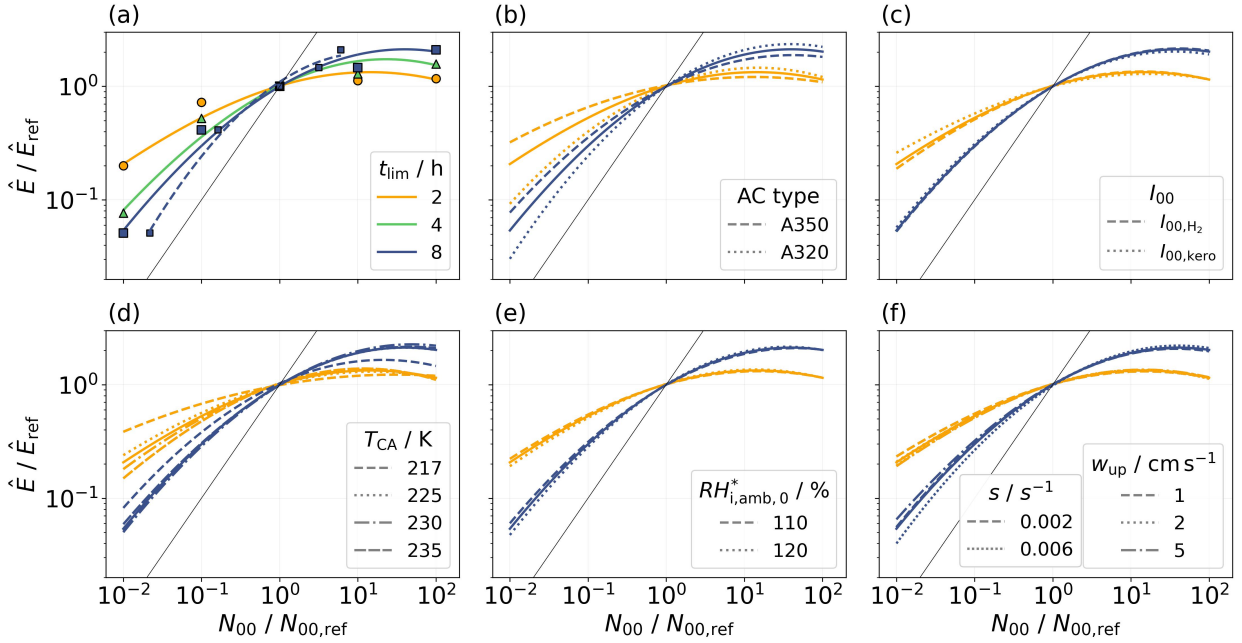


Figure 4.11: Normalized time-integrated total extinction as a function of the normalized initial number of ice crystals. Grey lines depict one-to-one lines. (a) Average values over aircraft type, I_{00} , T_{CA} , $RH_{i,amb,0}^*$, w_{up} , and s for time integration limits of 2, 4, and 8 h. For $t_{lim} = 8$ h, the dashed line connecting smaller symbols indicates that $N_0/N_{0,ref}$ is used as x-axis. The orange and blue solid lines displayed in panel (a) are also shown in panels (b) to (f). (b) Sensitivity to aircraft type. (c) Sensitivity to I_{00} . (d) Sensitivity to T_{CA} . (e) Sensitivity to $RH_{i,amb,0}^*$. (f) Sensitivity to w_{up} and s (the dashed lines of $w_{up} = 1 \text{ cm s}^{-1}$ and $s = 0.002 \text{ s}^{-1}$ are identical). Note that only $t_{lim} = 2$ h and $t_{lim} = 8$ h curves are displayed in panels (b) to (f) to better differentiate between curves with different line styles. Data points are shown in panel (a), while panels (b) to (f) present fitting curves only. In panel (f), the dashed and dotted lines that can be differentiated from the mean state refer to the s -variation, as the w_{up} -lines closely align with the solid lines.

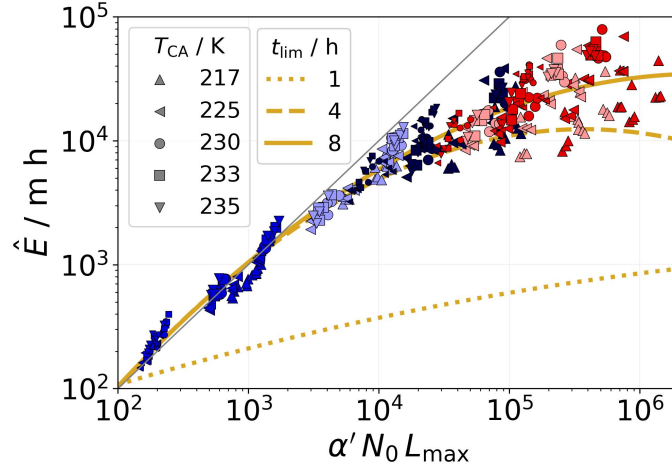


Figure 4.12: Extinction scaling based on Eq. 5 in Lewellen (2014). Colors as in Fig. 4.3 and Figs. 4.5-4.9. Symbols indicate ambient temperature, whereas symbol size represents the aircraft type (small symbols for A320 aircraft). No differentiation is made between different values of I_{00} , $RH_{i,amb,0}^*$, w_{up} , and s . The grey line represents the one-to-one relationship, and the orange solid line shows the best-fit curve to the data points. The dotted and dashed orange lines correspond to fits of data points when integrating only up to 1 and 4 h, respectively (these data points are not shown in the plot). α' is defined analogously to its definition in L2014, $\alpha' = 18\pi \frac{\mu}{g\rho_i}$ with μ as air viscosity, g as gravitational constant, and ρ_i as ice density.

4.3 Model intercomparison

In the following, we compare our EULAG-LCM results with those of a LES study (Sec. 4.3.1) and with results of the Contrail Cirrus Prediction model (CoCiP) and the Global Circulation Model (GCM) ECHAM5-CCMod (Sec. 4.3.2).

4.3.1 Comparison to LES study

One of the most comprehensive studies on contrail-cirrus simulations has been performed by Lewellen (2014), which comprises more than 200 large-eddy simulations using a binned microphysics scheme over a broad range of parameter variations. Lewellen (2014), hereafter L2014, derived simplified formulations that relate the contrail's maximum and lifetime-integrated properties to simulation input parameters and contrail properties determined from the simulation data. The scaling properties derived from L2014's simulation data can serve as a means to compare the simulation results of different contrail-cirrus models. A direct comparison of simulation results is often hampered by the fact that different modeling studies use different baseline conditions, and comparisons of results with slightly differing setup parameters remain inconclusive. Applying the relations proposed in L2014 to our dataset allows us to evaluate whether EULAG-LCM and the model used in L2014 predict consistent trends for key contrail properties, such as maximum total ice mass, contrail width, and total extinction. The latter is half the projected ice crystal surface area as used in L2014. These quantities depend not only on prescribed parameters (e.g., cruise-altitude temperature, ambient humidity, wind shear) but also on simulation-derived variables, such as maximum contrail depth and lifetime. Hence, the simplified model cannot be used to predict contrail-cirrus properties simply from given environmental and initial contrail properties. The strength of the simplified model is to relate various properties of the simulated contrail using simple relationships.

We first consider the relation between the lifetime-integrated surface area of the ice crystals to the number of ice crystals surviving the vortex phase and the maximum contrail depth during contrail-cirrus evolution: $\hat{S} \sim \alpha' N_0 L_{max}$ (Eq. 5 in L2014). Replacing \hat{S} with \hat{E} , Fig. 4.12 illustrates whether our simulation data support this scaling relation. Our results exhibit the same linear trend predicted by the model, with a strong clustering of data points regarding N_{00} sensitivity, represented by color. Slight deviations from this

linear relationship occur only in high- N_{00} and low-temperature simulations. Section 4.4 provides a detailed discussion of this finding. Fitting curves to the data are displayed by the orange lines, where the data points only of the $t_{\text{lim}} = 8$ h scenario are shown.

Furthermore, L2014 provides scaling relations for maximum ice mass M_{max} , maximum surface area (in our case maximum total extinction E_{max}), time-integrated surface area (in our case time-integrated total extinction \hat{E}), and maximum contrail width x_{max} :

$$M_{\text{max}} \sim c_a \rho_c x_{\text{max}} L_{\text{max}} \quad (4.11a)$$

$$E_{\text{max}} \sim c_b \beta_b (N_0 M_{\text{max}}^2)^{1/3} \quad (4.11b)$$

$$\hat{E} \sim c_c E_{\text{max}} t_{\text{life}} \quad (4.11c)$$

$$x_{\text{max}} \sim c_d s L_{\text{max}} t_{\text{life}} \quad (4.11d)$$

We apply these to our results for cross-validation, as shown in Fig. 4.13. As noted by L2014, the maximum ice mass is related to the available water vapor in the atmosphere ρ_c , calculated by $\rho q_{\text{sat}}(RH_{i,\text{amb},0}^* - 1)$, initially and at cruise altitude, multiplied by the contrail-cirrus cross-sectional area $x_{\text{max}} L_{\text{max}}$ (panel (a)). The maximum ice crystal surface area or extinction can be estimated using $(N_0 M_{\text{max}}^2)^{1/3}$ (panel (b)). The integrated total extinction is simply the product of the maximum total extinction and the contrail lifetime t_{life} (panel (c)). Additionally, the maximum contrail width is related to shear, multiplied by the maximum contrail depth and lifetime (panel (d)). By fitting lines to our data points, we obtain slopes of $c_a = 0.14$, $c_b = 0.29$, $c_c = 0.52$, and $c_d = 0.15$, which we compare to the values reported in L2014: $c_{a,\text{L2014}} = 0.08$, $c_{b,\text{L2014}} = 0.7$, $c_{c,\text{L2014}} = 0.56$, and $c_{d,\text{L2014}} = 0.25$. The difference in c_b can be attributed to our use of total extinction, which is approximately half of the total surface area used in L2014. Consistent with the findings in L2014, we observe a steeper slope in panel (b) for low- N_{00} scenarios. Differences in c_a and c_d between L2014 and our study may arise from differing definitions of contrail width. As the contrail-cirrus evolves, no distinct spatial boundaries can be defined. Hence, thresholds based on individual judgment must be applied, which may explain variations in the derived x_{max} values. In our approach, we determine the contrail width by including all columns containing a nonzero number of ice crystals. These are first stored in binary format and then smoothed. By applying a threshold to the smoothed data of 0.05, we identify which columns are included in the width calculation. This allows us to account for diffused regions of the contrail cirrus that are loosely connected to the bulk, while excluding isolated patches that are completely detached.

4.3.2 Comparison to CoCiP and GCM studies

Section 4.3.1 dealt with the comparison of high-resolution contrail-cirrus simulations from two different LES codes. In a next step, we compare our results with two further contrail models that operate on different spatial and temporal scales, namely CoCiP (Schumann, 2012) and the GCM ECHAM5-CCMod (Burkhardt and Kärcher, 2011; Bock and Burkhardt, 2016b). Both models have been used in the past to examine the sensitivity of contrail-cirrus properties to a variation of ice crystal number (Burkhardt et al., 2018; Bier and Burkhardt, 2022; Teoh et al., 2022; Rubin-Zuzic et al., 2025). While it is tempting to compare the outcomes of the three modeling approaches, such comparisons must be made with caution due to significant differences in spatial scales and mesh resolutions, which in turn influence the relevance, selection, and implementation of physical processes. These include, for example, saturation effects in contrail clusters, cloud overlap, interactions with natural clouds, and the representation of early contrail formation processes during initialization. Furthermore, the studies differ in their choice of reference ice crystal numbers and base years. In the case of EULAG-LCM, no specific base year is defined as we provide an unweighted mean over all considered simulation setups (see Tab. A3). Bier and Burkhardt (2022) (hereafter, BB2022), Märkl et al. (2024) (hereafter, M2024), Teoh et al. (2022) (hereafter, T2022), and Rubin-Zuzic et al. (2025) (hereafter, RZ2025) evaluate the impact of contrail ice crystal number on the net radiative forcing (RF), whereas the present study evaluates the time-integrated total extinction. Radiative transfer calculations as in Forster et al. (2012) suggest a linear relationship between \hat{E} and instantaneous RF for fixed irradiances, i.e., contrail properties change while the radiative scenario is unchanged, such that the radiative fluxes impinging the contrail layer remain the same (not shown).

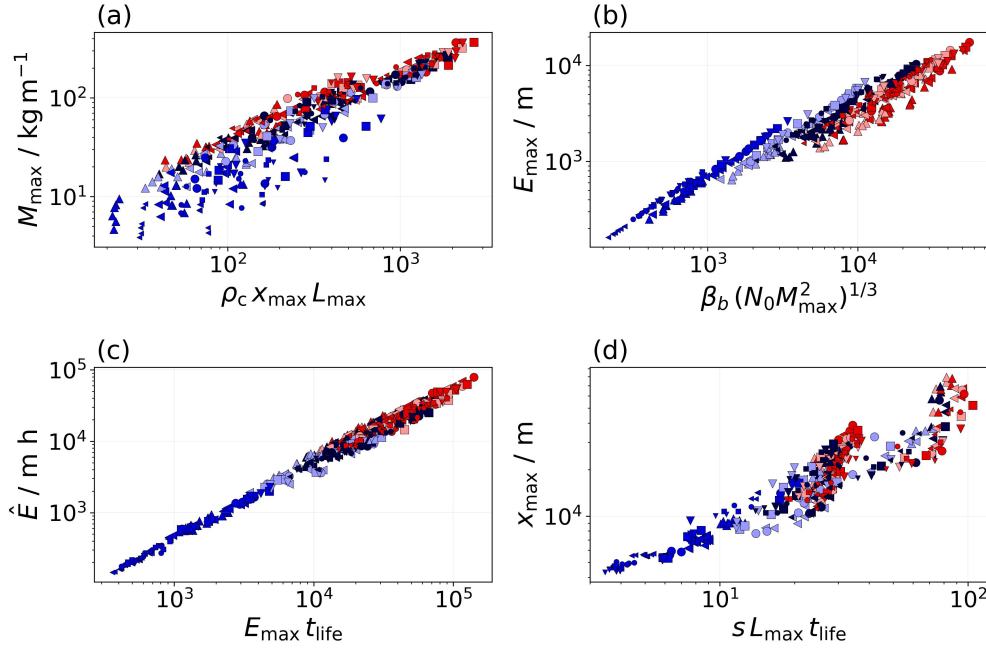


Figure 4.13: Scaling relations as given in Eqs. 4.11a-d. According to L2014, $\beta_b = (36\pi/\rho_i^2)^{1/3}$. Colors, symbols, and symbol sizes as in Fig. 4.12.

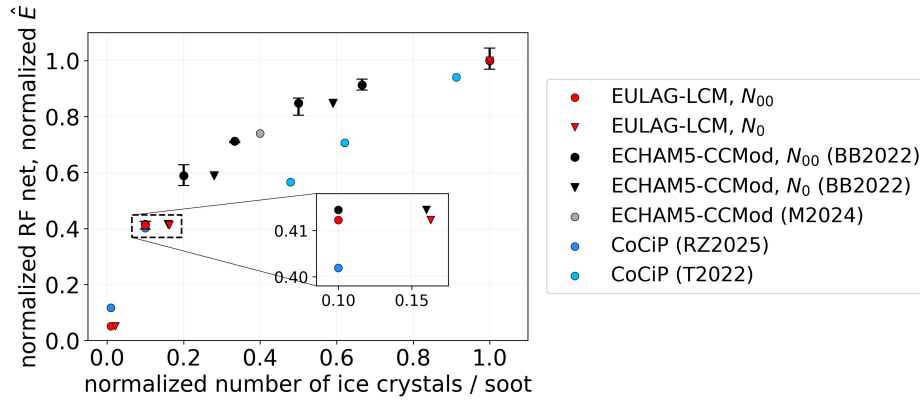


Figure 4.14: Mean normalized net radiative forcing, computed using ECHAM5-CCMod (Bier and Burkhardt (2022) (black), Märkl et al. (2024) (grey)), and CoCiP (Rubin-Zuzic et al. (2025) (blue), Teoh et al. (2022) (light blue)), presented alongside the mean normalized time-integrated total extinction values from our study (red). Data points from ECHAM5-CCMod and CoCiP are plotted against the normalized soot emission (circles), while data points from Bier and Burkhardt (2022) and our study are additionally plotted against the normalized number of ice crystals surviving the vortex phase (triangles).

	c_a	c_b	c_c	c_d	norm. \hat{E} or RF net for 90 % red. in soot or N_{00}	norm. \hat{E} or RF net for 99 % red. in soot or N_{00}
EULAG-LCM	0.14	0.29	0.52	0.15	0.41	0.05
Comparison studies	0.08 ⁽¹⁾	0.7 ⁽¹⁾	0.56 ⁽¹⁾	0.25 ⁽¹⁾	0.41 ⁽²⁾ , 0.40 ⁽³⁾	0.12 ⁽³⁾

Table 4.3: Comparison of modeling approaches regarding contrail properties⁽¹⁾ and effect of soot or N_{00} reduction on contrail-cirrus radiative properties^(2,3). ⁽¹⁾Lewellen (2014): Fitting coefficients for scaling relations of contrail properties, given in Eqs. 4.11a-d. ⁽²⁾Bier and Burkhardt (2022): global average of RF net over five years. ⁽³⁾Rubin-Zuzic et al. (2025): average of RF net across the European region for the year 2019.

Using the ECHAM5-CCMod model over five simulated years, BB2022 estimate the change in global mean net RF due to contrail cirrus resulting from a reduction in soot number emissions. Their study reduces the reference soot number emissions by 90 %, 80 %, 67 %, 50 %, and 33 %, as represented by the black circles in Fig. 4.14. For the 90 % reduction case, this leads to a 59 % decrease in mean RF compared to the reference scenario. The study of M2024 applies ECHAM5-CCMod to estimate the reduction of contrail-cirrus RF for a 60 % reduction in soot number concentration. They found a reduction of 26 % in RF for a global fleet using 100 % SAF in the year 2018. The corresponding data point agrees with previous ECHAM5-CCMod studies and is shown in grey in Fig. 4.14.

Similarly, using CoCiP for the European region in the year 2019, RZ2025 reports a 60 % and 88 % reduction in mean normalized net RF when soot emissions are decreased by 90 % and 99 %, respectively. These data points are shown in blue in Fig. 4.14. For the 90 % reduction case, our work aligns with both studies, BB2022 and RZ2025, as we find a 59 % reduction in mean \hat{E} . For the 99 % reduction case, we find the larger reduction in mean \hat{E} of 95 % compared to the value of 88 % suggested by CoCiP. Also using CoCiP, T2022 investigated the use of SAF blends on the contrail climate impact in the North Atlantic for 2019. Data points corresponding to 10 %, 50 %, and 100 % SAF blending ratios are shown in light blue. Generally, their mean net RF appears lower than with the GCM, indicating a stronger impact of reducing the initial particle number on the contrail-cirrus radiative effect. The deviation from GCM results, as well as potential discrepancies with the CoCiP study by RZ2025 when extrapolating to lower initial particle numbers, indicates that the RF sensitivity to ice crystal number in CoCiP (or possibly also in other models) depends also on the specific model application.

BB2022 accounts for ice crystal loss during the vortex phase by implementing the vortex phase parameterization of Unterstrasser (2016). Consequently, Fig. 4.14 also presents results as a function of the normalized number of ice crystals surviving the vortex phase, represented by triangles for both ECHAM5-CCMod and our study. In both cases, a 84 % reduction in ice crystal number is observed when the nucleated number of ice crystals is reduced by 90 %. This agreement is expected, as both models account for vortex phase losses similarly, ECHAM5-CCMod through the parametrization and our study via the prescribed initial conditions.

Overall, the three models find fairly similar reduction rates for the 90 % and 99 % cases. Given that contrail cirrus are simulated on different spatial scales, true reduction rates can differ and may, in reality, depend on the considered spatial scales. Hence, the partly excellent agreement should not obscure the fact that we cannot expect the true outcomes for the considered scenarios with the various models to match. Nevertheless, the consistency in the trends strengthens confidence in the robustness and plausibility of the simulation results. Table 4.3 provides a summary of our comparison study.

In our results sections, we describe changes relative to the reference in terms of multiplicative factors, whereas the above comparison uses additive (percentage) changes. Both approaches have their justifications, but the additive one can obscure the strong non-linearity between ice crystal number and \hat{E} or RF. For instance, reducing the ice crystal number by 99 % lowers \hat{E} by 95 %. At first glance, this might suggest changes of similar magnitude. However, a 100-fold decrease in ice crystal number reduces \hat{E} by only a factor of 20.

4.4 Discussion

This study aims to provide an overview of the potential implications of alternative aircraft propulsion on the contrail radiative effect. A hypothetical SAF- or H₂-propulsion setup is represented by systematically increasing and decreasing the number of initially nucleated contrail ice crystals in the model. Also, the initially emitted water vapor by the aircraft engines is adapted, although we find its influence on the later contrail-cirrus properties to be minor.

We want to emphasize the importance of differentiating between synoptically controlled versus sedimentation-dominated regimes: The influence of alternative fuels is weaker on short-living contrail cirrus in a synoptically controlled regime than on long-living contrail cirrus in sedimentation-dominated regimes, as already found in a global modeling study (Bier et al., 2017). The effect of SAF or H₂ as a combustion fuel becomes exceptionally significant after few hours when the low- N_{00} contrail cirrus has dissipated compared to a long-living kerosene contrail. While H₂ contrails form more frequently than kerosene contrails (Hofer et al., 2024), their comparatively short lifetimes tend to counteract this effect. Also, the impact of ambient temperature on contrail-cirrus evolution is more pronounced in synoptically controlled regimes characterized by subsidence, where rapid ice mass growth leads to considerably higher extinction values (Fig. 4.10b). Under warm conditions, contrail cirrus typically consists of fewer but larger ice crystals, whereas colder conditions favor smaller crystals. In regimes characterized by subsidence, both contrail types dissipate more quickly compared to sedimentation-dominated scenarios. However, due to faster ice crystal growth and higher extinction values, contrails formed in a warm atmosphere can contribute more strongly to radiative forcing before dissipating. In contrast, in sedimentation-driven regimes, the radiative impact differs. While warm-case contrail cirrus experience rapid growth, they also exhibit shorter lifetimes due to the efficient sedimentation of large ice crystals. Conversely, cold-case contrail cirrus develop more slowly but persist significantly longer, as smaller ice crystals sediment more slowly. As a result, despite lower peak extinction, contrails in cold conditions can exert a larger radiative impact over time. This finding is particularly relevant for H₂ combustion, which is expected to produce contrail cirrus with fewer but larger ice crystals.

In our simulations, we neglect several physical processes, such as the formation of natural cirrus by homogeneous or heterogeneous nucleation, the radiative heating of the contrail, and ice crystal aggregation. The evolution of an individual contrail can be perturbed by surrounding natural cirrus, as the study by Unterstrasser et al. (2017b) has shown. The presence of natural cirrus below the contrail hampers the development of fallstreaks, potentially prolonging contrail lifetimes, which could be especially relevant in the N_{00} -downscaling simulations. Additionally, in order to maintain clarity and isolate the effects of H₂ propulsion on contrail properties, we chose to simulate individual contrails rather than contrail clusters, thereby avoiding added complexity in interpreting our results.

Furthermore, radiation alters the contrail-cirrus evolution as shown by past studies (Unterstrasser and Gierens, 2010b; Lewellen et al., 2014). Solar and thermal radiation entering the contrail layer interact with the ice crystals, changing the internal contrail dynamics. During a cloudless summer day, this leads to an updraft motion, and the temperature within the contrail decreases adiabatically, thereby increasing the relative humidity in the contrail (Unterstrasser and Gierens, 2010b). The increasing ice mass then leads to a higher total extinction. We suspect that in case of a high- N_{00} contrail, radiation and an imposed updraft motion could prevent some of the small ice crystals from sublimating in-situ as the radiation impact becomes considerable already within the first 3 h, where most of the sublimation in the N_{00} -upscaling scenarios happen (Fig. 4.4). In contrast, the low- N_{00} contrails might experience even stronger sedimentation in radiation-driven updraft situations. The already large ice crystals would grow even larger and fall out more rapidly, lowering the contrail-cirrus lifetime. This implies that the differences between high- and low- N_{00} contrails could be amplified once radiative effects are considered, with higher extinction values and longer-living contrails in the former and shorter-living contrails in the latter case. Then, the curves in Fig. 4.11 potentially exhibit larger slopes. Despite these expectations, we have chosen to model contrail cirrus in a setup without radiation to avoid introducing additional complexity that would make it difficult to disentangle the underlying processes.

The study of Gierens (2012) showed that aggregation plays a role in contrail cirrus embedded in naturally formed cirrus clouds. In such cases, sedimenting ice crystals from the natural cirrus layer may interact

with the contrail below, depleting contrail ice mass through aggregation. However, as our setup does not include natural cirrus formation or interactions, this process is not considered here. Nevertheless, since sedimentation velocities in low- N_{00} contrails can be comparable to those in natural cirrus, neglecting aggregation between contrail ice crystals might introduce a bias in these cases. This is particularly important for the fallstreak regions, where sedimentation is strongest and large crystals dominate (see Fig. 4.3). However, as aggregation effects scale with the square of ice crystal number concentration (Gierens, 2012; Unterstrasser et al., 2017c), the low number concentrations in the fallstreaks are expected to compensate for the high sedimentation velocities there, potentially limiting the significance of aggregation in low- N_{00} contrails. Additionally, the narrow size distribution of ice crystals in the fallstreaks (Fig. 11 in Unterstrasser et al. (2017a)) suggests only minor differences in sedimentation velocities, further reducing the expected influence of aggregation.

Lastly, we discuss the implications of our chosen vertical relative humidity profile. Initially, the thickness of the ISSL is either 1100 or 1180 m depending on the prescribed humidity value at flight altitude. The flight level, set at $z = 2000$ m in the simulation domain, is located at the top of the ISSL (Fig. 4.1a). Altering the setup by lowering the flight altitude to $z = 1500$ m or by reducing the ISSL's thickness to 500 to 600 m would likely lead to a different evolution of contrail total extinction. The relative contribution of fallstreak ice crystals to total extinction increases over time (Fig. 4.3). A thinner ISSL reduces the vertical extent of fallstreaks, which in turn lowers extinction values and accelerates contrail dissipation. While high- N_{00} contrails would be largely unaffected, since core ice crystals dominate their extinction, this sensitivity is particularly relevant for low- N_{00} contrails, where nearly all ice mass resides in the fallstreaks. Hence, the extinction and lifetime estimates for low- N_{00} contrails in our current configuration may represent upper bounds, assuming the ISSL is on average thinner.

The comparison with the study by L2014 shows good agreement, with our results confirming the proposed scaling relations based on the slopes obtained from linear fits. One notable discrepancy between L2014 and our study appears in Fig. 4.12, which shows the relationship between \hat{E} and $N_0 L_{\max}$. While L2014 reports an excellent linear relationship, our data exhibit a deviation from linearity in the high- \hat{E} regime. One may argue that extending the simulation period would improve the alignment of our data points with the one-to-one line in that regime. This interpretation is supported by our observation that the fitted curves converge toward the one-to-one line as the time-integration limit increases, as illustrated by the orange fitting lines in Fig. 4.12. For a small time limit of 1 h, the slope of $\hat{E}(\alpha' N_0 L_{\max})$ is much smaller than one. We repeated a set of 32 simulations, where we extended the simulation period from 8 h to 20 h. As expected, the resulting data points move closer to the one-to-one line, but a noticeable gap remains (not shown). This occurs because the total extinction often starts to decline once the updraught ceases (Fig. 4.5). Hence, extending the integration limit does increase \hat{E} , but the data points are still far from the one-to-one line. We consider this deviation reasonable, as in real-world conditions, the lifetime of ice supersaturated regions in the atmosphere typically does not exceed a few hours (Irvine et al., 2014), and large-scale subsidence often leads to subsaturation and contrail dissipation. Therefore, updraughts lasting up to 12 h and producing ice supersaturations as high as 1800 %, as in the simulations of L2014 (where natural cirrus formation in the contrail vicinity was not accounted for), should be considered highly idealized. Hence, we deem a less-than-linear relationship between the time-integrated total extinction and the initial ice crystal number more reasonable.

In Fig. 4.11, we expect that further increasing N_{00} would not significantly increase the normalized time-integrated total extinction, even for long integration times. This is due to three reasons. First, higher N_{00} values result in lower ice crystal survival fractions during the vortex phase, yielding N_0 values comparable or even smaller to those already considered. Second, the resulting smaller core ice crystals would be even more prone to in-situ sublimation than in the cases studied so far. Third, peak extinction, which is roughly timed with the termination of updraught motion, occurs within 8 h in our simulations, and this point in time is independent of N_{00} if $N_{00} \geq 10^{12} \text{ m}^{-3}$ (Fig. 4.5d). As a result, further increases in N_{00} would likely yield similar total extinction evolutions. At the low- N_{00} end, further reducing N_{00} is unlikely to affect vortex phase survival fractions, at least in high-humidity cases, since the number of surviving ice crystals there is already one or close to one. However, these very few but large ice crystals would sediment more rapidly during the dispersion phase, leading to a shorter contrail-cirrus lifetime. Overall, we expect that the general nonlinear shape of the curves in Fig. 4.11 would remain largely unchanged, even with more extreme variations in N_{00} .

4.5 Conclusion

Using the LES code EULAG coupled to the particle-based cloud module LCM, we simulated contrail cirrus behind SAF- or H₂-powered aircraft. Building on a previous study that examined H₂ contrails in the first few minutes after formation, we use those simulations as initial conditions. These contrails are characterized by a broad range of nucleated ice crystal numbers N_{00} , spanning from 10^{10} up to 10^{14} ice crystals per flight meter, and larger ice crystal sizes due to the increased water vapor emission. We conducted 400 contrail-cirrus simulations, accounting for variations in ambient relative humidity with respect to ice, ambient temperature, updraught-induced adiabatic cooling, and vertical wind shear. Simulations for an A350/B777-like aircraft and a smaller A320/B737-like aircraft have been performed. While we have chosen the larger aircraft for compatibility with previous studies (Unterstrasser et al., 2017a,b), the smaller aircraft better mimics the design concepts of future hydrogen aircraft. Our results indicate that in-situ sublimation is the main driver for ice crystal loss in high- N_{00} contrails, whereas low- N_{00} contrail cirrus exhibit stronger sedimentation fluxes, leading to faster dissipation. In general, we find a nonlinear dependency of time-integrated total extinction \hat{E} to N_{00} . The impact of ambient temperature, especially in cases where ambient temperature exceeds 230 K, is most pronounced for short-lived contrail cirrus. We find a stronger overall reduction in \hat{E} for the smaller of the two studied aircraft types. Averaging across all ambient conditions, we find that a 100-fold reduction in N_{00} leads to a 20-fold reduction in \hat{E} . In percentage terms, this is equivalent to a 95 % reduction in \hat{E} for a 99 % reduction in N_{00} . Similarly, a 10-fold reduction in N_{00} results in a 2-fold decrease in \hat{E} , corresponding to a 59 % reduction in \hat{E} for a 90 % reduction in N_{00} . Our study is consistent with previously established scaling relations for contrail ice mass, width, and total extinction. Furthermore, comparisons with results from ECHAM5-CCMod and CoCiP show good agreement, demonstrating a similar contrail response to a soot/ice crystal number variation despite analyzing the effect on different spatial scales and considered time periods. The interaction of H₂ contrail cirrus with natural cirrus and the roles of radiation and aggregation in the H₂ contrail-cirrus evolution are the foci of future work.

5

Summary and Concluding Remarks

This thesis has presented studies on all main stages of the contrail lifecycle, i.e., formation, vortex, and dispersion phase, focusing on alternative fuels and propulsion systems. This section revisits the research questions introduced in Sec. 1.4 and answers them by summarizing the findings of Chapters 2–4. Potential avenues for future research beyond the scope of this work are also outlined.

How can the altered aircraft and engine characteristics associated with alternative fuel use be evaluated in terms of their impact on the dynamical and thermodynamic evolution of the exhaust plume?

- To address this, I developed a new dynamical plume model, RadMod, designed to evaluate how variations in aircraft and engine characteristics affect plume dilution and thermodynamic evolution.
- RadMod successfully reproduces scaling relations derived from both experiments and theory, demonstrating its ability to capture different jet-spreading behaviors under varying exhaust temperatures and coflowing conditions. Its flexibility with respect to input parameters, such as jet diameter, jet velocity, aircraft velocity, jet/ambient temperature, tracer concentration, and ambient pressure, makes it applicable to a wide range of propulsion setups. These include turbofan engines, small engines of regional aircraft (on which hydrogen propulsion is likely to be implemented first), demonstrator aircraft used in measurement campaigns, and the cold, low-velocity jets typical of fuel cells.
- RadMod validated a scaling relation for centerline plume dilution, which helps to provide a unified framework for describing plume dilution across a range of jet and engine configurations. The scaling was tested against CFD data as well as measurement data from the Nephele 2 campaign, showing good agreement.
- With this development, we have taken a step toward an intermediate-complexity contrail formation model, bridging the gap between a fully coupled three-dimensional LES with ice microphysics (computationally expensive) and a trajectory-based approach with offline microphysics (computationally cheap). The coupled RadMod-LCM framework will enable a systematic exploration of contrail formation across a broad parameter space in the context of alternative propulsion systems.

The comparison with CFD-based turbofan profiles of axial velocity drew attention to the treatment of turbulent diffusivity within RadMod. The relation used for the turbulent diffusion coefficient is valid for

a fully developed turbulent jet, but it might not necessarily give an accurate representation of turbulence in the jet's near field. Hence, the diffusion coefficient in the near field was adjusted, and an agreement of RadMod with the CFD data was achieved. Using a more sophisticated, though computationally more expensive, approach, such as the $k - \epsilon$ turbulence model, could probably improve accuracy across the entire axial distance. However, given that RadMod's strength lies in its computational efficiency, an alternative path forward is to use additional LES-generated or measurement data to validate and fine-tune the diffusion coefficient in the near field empirically.

Coupling the dynamical model part RadMod with the microphysical model part LCM requires the simulation of the particles' turbulent transport in the thermodynamic fields generated by RadMod. This can be accomplished by either diffusing the particle concentration or tracking individual particles using their mean velocity plus a turbulent velocity component. Ongoing research will show the feasibility and computational efficiency of both approaches.

How does the use of alternative fuels affect contrail evolution during the vortex phase, in particular the number of surviving ice crystals? Is the existing ice crystal loss parameterization, developed for kerosene scenarios, still be applicable to alternative fuel cases?

- Ice crystal loss during the vortex phase is highly sensitive to the initial number of ice crystals, which can vary considerably when switching to alternative fuels and propulsion systems.
- The initial difference of four orders of magnitude in ice crystal number reduces to a difference of two orders of magnitude after the vortex phase. This trend is consistent for the range of ambient temperatures (217 K–235 K) and relative humidity values (110 % and 120 %), considered in this study.
- Compared to conventional kerosene combustion, the on average larger initial ice crystal size, resulting from the higher water vapor emission when using hydrogen as fuel (whether through combustion or in a fuel cell), generally leads to a higher fraction of surviving ice crystals.
- The crystal loss parameterization for conventional aircraft developed in [Unterstrasser \(2016\)](#) is expanded in the recent study to include hydrogen-powered aircraft. The updated parameterization has been implemented in the GCM ECHAM-CCMod and is also part of the open-source library *pycontrails*, a contrail and contrail climate impact modeling tool used in, e.g., [Frias et al. \(2024\)](#) and [Teoh et al. \(2024\)](#).

How do contrail properties respond to the use of alternative fuels during the dispersion phase, and how does this depend on the prevailing meteorological conditions?

- The crucial factor determining the contrail-cirrus radiative effect is the initial number of ice crystals, rather than the initial ice mass.
- In contrail cirrus formed behind H₂- or SAF-powered aircraft, ice crystal loss is dominated by sedimentation when the initial crystal number is low, and by in-situ sublimation when it is high.
- A high ambient temperature, which can be encountered in H₂-propulsion scenarios, reduces the contrail-cirrus lifetime due to strong sedimentation.
- Meteorological scenarios with strong but short-lasting updraughts of the simulation domain increase ice mass and total extinction more rapidly than long-lasting updraughts. On the other hand, strong updraughts accelerate contrail-cirrus dissipation. Increased wind shear broadens the contrail, resulting in a substantial increase in ice mass and total extinction. These findings, previously observed for conventional kerosene cases, similarly apply to the alternative-fuel scenarios considered here.

- We find the general trend of short-lived, optically thin contrail cirrus when the initial ice crystal number is significantly reduced. A factor of 100 reduction in the initial ice crystal number results in a factor of 20 reduction in total extinction, a quantity that is used here as a measure of the climate impact. This suggests great contrail mitigation potential of low-emission engines. Because the relationship between total extinction and initial ice crystal number is nonlinear, we expect only a weak increase in climate impact when the number of nucleated ice crystals increases, but a further, potentially strong, decrease when it drops below the factor-100 reduction considered here.

The significant sensitivity of total extinction on the ice crystal number necessitates a further refinement of determining the latter quantity. Upcoming data from recent flight campaigns probing plumes of hydrogen combustion aircraft (DLR, 2025) and from laboratory studies of hydrogen propulsion emissions will provide information on ice crystal properties, such as total number and size distribution. The role of volatile particles formed from the emission of lubrication oil vapor or nitric acid remains uncertain, and future measurements will be required to better constrain their contribution to the ice crystal formation process. Furthermore, assuming that ambient aerosol particles are the major or only source of ice nuclei in future hydrogen propulsion systems, in-situ measurements of ambient aerosols in the upper troposphere will be important. Such data help define the upper and lower bounds of aerosol concentrations, which strongly influence the number of ice crystals formed (Bier et al., 2024). The measurement data can be used as input for future EULAG-LCM studies investigating the lifecycle of hydrogen contrails.

In the studies presented in this thesis, individual contrails are modeled, and potential interactions with other contrails or natural cirrus clouds are neglected. Such interactions could especially be relevant in regions of high supersaturation and strong uplift, where natural cirrus forms rapidly. For example, cirrus clouds scavenging moisture from a contrail could slow crystal growth when the contrail initially contains few ice crystals. The resulting weaker sedimentation could prolong the contrail's lifetime, leading to a less pronounced impact of hydrogen combustion. Exploring these processes will be an interesting focus for future studies.

Bibliography

- Adler, E. J. and Martins, J. R. (2023). Hydrogen-powered aircraft: Fundamental concepts, key technologies, and environmental impacts. *Progress in Aerospace Sciences*, 141:100922. DOI: [10.1016/j.paerosci.2023.100922](https://doi.org/10.1016/j.paerosci.2023.100922).
- Airbus (2020). Towards the world's first hydrogen-powered commercial aircraft. <https://www.airbus.com/en/innovation/energy-transition/hydrogen/zeroe#concepts>. Accessed: 2024-03-13.
- Airbus (2023). Contrail-chasing Blue Condor makes Airbus' first full hydrogen-powered flight. <https://www.airbus.com/en/newsroom/stories/2023-11-contrail-chasing-blue-condor-makes-airbus-first-full-hydrogen-powered#>. Accessed: 2022-12-13.
- Airbus (2024). A320 characteristics. https://aircraft.airbus.com/sites/g/files/jlcbta126/files/2024-06/AC_A320_0624.pdf. Accessed: 2025-05-30.
- Amielh, M., Djeridane, T., Anselmet, F., and Fulachier, L. (1996). Velocity near-field of variable density turbulent jets. *Int. J. Heat Mass Transf.*, 39:2149–2164. DOI: [10.1016/0017-9310\(95\)00294-4](https://doi.org/10.1016/0017-9310(95)00294-4).
- Anderson, J. D. (2017). *Fundamentals of Aerodynamics*. McGraw-Hill series in aeronautical and aerospace engineering. McGraw-Hill Education. ISBN: [9781259251344](https://www.isbn-international.org/product/9781259251344).
- Antoine, Y., Lemoine, F., and Lebouché, M. (2001). Turbulent transport of a passive scalar in a round jet discharging into a co-flowing stream. *Eur. J. Mech. B Fluids*, 20(2):275–301. DOI: [10.1016/S0997-7546\(00\)01120-1](https://doi.org/10.1016/S0997-7546(00)01120-1).
- Appleman, H. (1953). The formation of exhaust condensation trails by jet aircraft. *Bull. Am. Meteorol. Soc.*, 34(1):14–20. DOI: [10.1175/1520-0477-34.1.14](https://doi.org/10.1175/1520-0477-34.1.14).
- Aviation, C. (2023). Clean Aviation. <https://www.clean-aviation.eu/>. Accessed: 2025-08-11.
- Ball, C. G., Fellouah, H., and Pollard, A. (2012). The flow field in turbulent round free jets. *Prog. Aerosp. Sci.*, 50:1–26. DOI: [10.1016/j.paerosci.2011.10.002](https://doi.org/10.1016/j.paerosci.2011.10.002).
- Bickel, M., Ponater, M., Bock, L., Burkhardt, U., and Reineke, S. (2020). Estimating the Effective Radiative Forcing of Contrail Cirrus. *J. Clim.*, 33(5):1991–2005. DOI: [10.1175/JCLI-D-19-0467.1](https://doi.org/10.1175/JCLI-D-19-0467.1).
- Bickel, M., Ponater, M., Burkhardt, U., Righi, M., Hendricks, J., and Jöckel, P. (2025). Contrail Cirrus Climate Impact: From Radiative Forcing to Surface Temperature Change. *J. Clim.*, 38(8):1895–1912. URL: [10.1175/JCLI-D-24-0245.1](https://doi.org/10.1175/JCLI-D-24-0245.1).
- Bier, A. and Burkhardt, U. (2019). Variability in Contrail Ice Nucleation and Its Dependence on Soot Number Emissions. *J. Geophys. Res.*, 124:3384–3400. DOI: [10.1029/2018JD029155](https://doi.org/10.1029/2018JD029155).
- Bier, A. and Burkhardt, U. (2022). Impact of Parametrizing Microphysical Processes in the Jet and Vortex Phase on Contrail Cirrus Properties and Radiative Forcing. *J. Geophys. Res.*, 127(23):e2022JD036677. DOI: [10.1029/2022JD036677](https://doi.org/10.1029/2022JD036677).
- Bier, A., Burkhardt, U., and Bock, L. (2017). Synoptic Control of Contrail Cirrus Life Cycles and Their Modification Due to Reduced Soot Number Emissions. *J. Geophys. Res.*, pages 11584–11603. DOI: [10.1002/2017JD027011](https://doi.org/10.1002/2017JD027011).

- Bier, A., Unterstrasser, S., and Vancassel, X. (2022). Box model trajectory studies of contrail formation using a particle-based cloud microphysics scheme. *Atmos. Chem. Phys.*, 22(2):823–845. DOI: [10.5194/acp-22-823-2022](https://doi.org/10.5194/acp-22-823-2022).
- Bier, A., Unterstrasser, S., Zink, J., Hillenbrand, D., Jurkat-Witschas, T., and Lottermoser, A. (2024). Contrail formation on ambient aerosol particles for aircraft with hydrogen combustion: a box model trajectory study. *Atmos. Chem. Phys.*, 24(4):2319–2344. DOI: [10.5194/acp-24-2319-2024](https://doi.org/10.5194/acp-24-2319-2024).
- Bock, L. and Burkhardt, U. (2016a). Reassessing properties and radiative forcing of contrail cirrus using a climate model. *J. Geophys. Res.*, 121(16):9717–9736. DOI: [10.1002/2016JD025112](https://doi.org/10.1002/2016JD025112).
- Bock, L. and Burkhardt, U. (2016b). The temporal evolution of a long-lived contrail cirrus cluster: Simulations with a global climate model. *J. Geophys. Res.*, 121(7):3548–3565. DOI: [10.1002/2015JD024475](https://doi.org/10.1002/2015JD024475).
- Bock, L. and Burkhardt, U. (2019). Contrail cirrus radiative forcing for future air traffic. *Atmos. Chem. Phys.*, 19(12):8163–8174. DOI: [10.5194/acp-19-8163-2019](https://doi.org/10.5194/acp-19-8163-2019).
- Bockhorn, H. (1994). *Soot formation in Combustion - Mechanisms and Models*. Springer Berlin, Heidelberg. DOI: [10.1007/978-3-642-85167-4](https://doi.org/10.1007/978-3-642-85167-4).
- Borrmann, S., Kunkel, D., Weigel, R., Minikin, A., Deshler, T., Wilson, J. C., Curtius, J., Volk, C. M., Homan, C. D., Ulanovsky, A., Ravegnani, F., Viciani, S., Shur, G. N., Belyaev, G. V., Law, K. S., and Cairo, F. (2010). Aerosols in the tropical and subtropical UT/LS: in-situ measurements of submicron particle abundance and volatility. *Atmos. Chem. Phys.*, 10(12):5573–5592. DOI: [10.5194/acp-10-5573-2010](https://doi.org/10.5194/acp-10-5573-2010).
- Bouhafid, Y., Bonne, N., and Jacquin, L. (2024). Combined Reynolds-averaged Navier-Stokes/Large-Eddy Simulations for an aircraft wake until dissipation regime. *Aerosp. Sci. Technol.*, 154:109512. DOI: [10.1016/j.ast.2024.109512](https://doi.org/10.1016/j.ast.2024.109512).
- Brand, J., Sampath, S., Shum, F., Bayt, R., and Cohen, J. (2003). *Potential Use of Hydrogen In Air Propulsion*. DOI: [10.2514/6.2003-2879](https://doi.org/10.2514/6.2003-2879).
- Bräuer, T., Voigt, C., Sauer, D., Kaufmann, S., Hahn, V., Scheibe, M., Schlager, H., Huber, F., Le Clerq, P., Moore, R. H., and Anderson, B. E. (2021). Reduced ice number concentrations in contrails from low-aromatic biofuel blends. *Atmos. Chem. Phys.*, 21:16817–16826. DOI: [10.5194/acp-21-16817-2021](https://doi.org/10.5194/acp-21-16817-2021).
- Brelje, B. J. and Martins, J. R. R. A. (2019). Electric, hybrid, and turboelectric fixed-wing aircraft: A review of concepts, models, and design approaches. *Progress in Aerospace Sciences*, 104:1–19. DOI: [10.1016/j.paerosci.2018.06.004](https://doi.org/10.1016/j.paerosci.2018.06.004).
- Brenner, P. (1991). *Three-dimensional aerodynamics with moving bodies applied to solid propellant*. DOI: [10.2514/6.1991-2304](https://doi.org/10.2514/6.1991-2304).
- Brewer, G. (1991). *Hydrogen Aircraft Technology*. Routledge, 1st edition. DOI: [10.1201/9780203751480](https://doi.org/10.1201/9780203751480).
- Brock, C. A., Schröder, F., Kärcher, B., Petzold, A., Busen, R., and Fiebig, M. (2000). Ultrafine particle size distributions measured in aircraft exhaust plumes. *J. Geophys. Res.*, 105(D21):26555–26567. DOI: [10.1029/2000JD900360](https://doi.org/10.1029/2000JD900360).
- Burkhardt, U., Bock, L., and Bier, A. (2018). Mitigating the contrail cirrus climate impact by reducing aircraft soot number emissions. *Climate and Atmospheric Science*, 1(1):37. DOI: [10.1038/s41612-018-0046-4](https://doi.org/10.1038/s41612-018-0046-4).
- Burkhardt, U. and Kärcher, B. (2009). Process-based simulation of contrail cirrus in a global climate model. *J. Geophys. Res.*, 114:D16201. DOI: [10.1029/2008JD011491](https://doi.org/10.1029/2008JD011491).
- Burkhardt, U. and Kärcher, B. (2011). Global radiative forcing from contrail cirrus. *Nature Clim. Ch.*, 1(1):54–58. DOI: [10.1038/nclimate1068](https://doi.org/10.1038/nclimate1068).

- Busen, R. and Schumann, U. (1995). Visible contrail formation from fuels with different sulfur contents. *Geophys. Res. Lett.*, 22:1357–1360. DOI: [10.1029/95GL01312](https://doi.org/10.1029/95GL01312).
- Cantin, S., Chouak, M., Morency, F., and Garnier, F. (2022). Eulerian–Lagrangian CFD-microphysics modeling of a near-field contrail from a realistic turbofan. *International Journal of Engine Research*, 23(4):661–677. DOI: [10.1177/1468087421993961](https://doi.org/10.1177/1468087421993961).
- Cecere, D., Giacomazzi, E., and Ingenito, A. (2014). A review on hydrogen industrial aerospace applications. *International Journal of Hydrogen Energy*, 39(20):10731–10747. DOI: [10.1016/j.ijhydene.2014.04.126](https://doi.org/10.1016/j.ijhydene.2014.04.126).
- Charonko, J. J. and Prestridge, K. (2017). Variable-density mixing in turbulent jets with coflow. *J. Fluid Mech.*, 825:887–921. DOI: [10.1017/jfm.2017.379](https://doi.org/10.1017/jfm.2017.379).
- Chassaing, P., Harran, G., and Joly, L. (1994). Density fluctuation correlations in free turbulent binary mixing. *J. Fluid Mech.*, 279:239–278. DOI: [10.1017/S0022112094003903](https://doi.org/10.1017/S0022112094003903).
- Chen, C.-C. and Gettelman, A. (2013). Simulated radiative forcing from contrails and contrail cirrus. *Atmos. Chem. Phys.*, 13(24):12525–12536. DOI: [10.5194/acp-13-12525-2013](https://doi.org/10.5194/acp-13-12525-2013).
- Chlond, A. (1998). Large-Eddy Simulation of Contrails. *J. Atmos. Sci.*, 55(5):796–819. DOI: [10.1175/1520-0469\(1998\)055<0796:LESOC>2.0.CO;2](https://doi.org/10.1175/1520-0469(1998)055<0796:LESOC>2.0.CO;2).
- Chu, P. C. K., Lee, J. H., and Chu, V. H. (1999). Spreading of Turbulent Round Jet in Coflow. *J. Hydraul. Eng.*, 125(2):193–204. DOI: [10.1061/\(ASCE\)0733-9429\(1999\)125:2\(193\)](https://doi.org/10.1061/(ASCE)0733-9429(1999)125:2(193)).
- Clark, T. L. and Farley, R. D. (1984). Severe downslope windstorm calculations in two and three spatial dimensions using anelastic interactive grid nesting: a possible mechanism for gustiness. *J. Atmos. Sci.*, 41:329–350. DOI: [10.1175/1520-0469\(1984\)041<0329:SDWCIT>2.0.CO;2](https://doi.org/10.1175/1520-0469(1984)041<0329:SDWCIT>2.0.CO;2).
- Clean Sky 2 (2020). Hydrogen-powered aviation – A fact-based study of hydrogen technology, economics, and climate impact by 2050. DOI: [10.2843/471510](https://doi.org/10.2843/471510).
- Crow, S. (1970). Stability theory for a pair of trailing vortices. *AIAA Journal*, 8:2172–2179. DOI: [10.2514/3.6083](https://doi.org/10.2514/3.6083).
- Cziczo, D. J., Froyd, K. D., Hoose, C., Jensen, E. J., Diao, M., Zondlo, M. A., Smith, J. B., Twohy, C. H., and Murphy, D. M. (2013). Clarifying the Dominant Sources and Mechanisms of Cirrus Cloud Formation. *Science*, 340:1320–1324. DOI: [10.1126/science.1234145](https://doi.org/10.1126/science.1234145).
- Dahlmann, K., Matthes, S., Yamashita, H., Unterstrasser, S., Grewe, V., and Marks, T. (2020). Assessing the Climate Impact of Formation Flights. *Aerospace*, 7(12):172. DOI: [10.3390/aerospace7120172](https://doi.org/10.3390/aerospace7120172).
- Davidson, G. and McComb, W. (1975). Turbulent diffusion in an aerosol jet. *Journal of Aerosol Science*, 6(3):227–247. DOI: [10.1016/0021-8502\(75\)90092-0](https://doi.org/10.1016/0021-8502(75)90092-0).
- Davidson, M. J. and Wang, H. J. (2002). Strongly Advected Jet in a Coflow. *J. Hydraul. Eng.*, 128(8):742–752. DOI: [10.1061/\(ASCE\)0733-9429\(2002\)128:8\(742\)](https://doi.org/10.1061/(ASCE)0733-9429(2002)128:8(742)).
- Debney, D., Beddoes, S., Foster, M., James, D., Kay, E., Kay, O., Shawki, K., Stubbs, E., Thomas, D., Weider, K., and Wilson, R. (2022). Zero-Carbon Emission Aircraft Concepts, Fly-Zero Report FZO-AIN-REP-0007. <https://www.ati.org.uk/wp-content/uploads/2022/03/FZO-AIN-REP-0007-FlyZero-Zero-Carbon-Emission-Aircraft-Concepts.pdf>. Accessed: 2025-08-08.
- Dicks, A. L. and Rand, D. A. J. (2018). *Fuel Cell Systems Explained*. John Wiley & Sons Ltd. DOI: [10.1002/9781118706992](https://doi.org/10.1002/9781118706992).

- Dischl, R., Sauer, D., Voigt, C., Harlaß, T., Sakellariou, F., Märkl, R., Schumann, U., Scheibe, M., Kaufmann, S., Roiger, A., Dörnbrack, A., Renard, C., Gauthier, M., Swann, P., Madden, P., Luff, D., Johnson, M., Ahrens, D., Sallinen, R., Schripp, T., Eckel, G., Bauder, U., and Le Clercq, P. (2024). Measurements of particle emissions of an A350-941 burning 100% sustainable aviation fuels in cruise. *Atmos. Chem. Phys.*, 24(19):11255–11273. DOI: [10.5194/acp-24-11255-2024](https://doi.org/10.5194/acp-24-11255-2024).
- Djeridane, T., Amielh, M., Anselmet, F., and Fulachier, L. (1996). Velocity turbulence properties in the near-field region of axisymmetric variable density jets. *Phys. Fluids*, 8(6):1614–1630. DOI: [10.1063/1.868935](https://doi.org/10.1063/1.868935).
- DLR (2025). DLR press release for Blue Condor Campaign. <https://www.dlr.de/en/latest/news/2025/world-first-in-flight-measurements-of-contrails-from-hydrogen-propulsion>. accessed: 2025-06-25.
- Dürbeck, T. and Gerz, T. (1996). Dispersion of aircraft exhausts in the free atmosphere. *J. Geophys. Res.*, 101(D20):26007–26016. DOI: [10.1029/96JD02217](https://doi.org/10.1029/96JD02217).
- Enjalbert, N., Galley, D., and , L. (2009). An entrainment model for the turbulent jet in a coflow. *Comptes Rendus Mécanique*, 337(9):639–644. DOI: [10.1016/j.crme.2009.09.005](https://doi.org/10.1016/j.crme.2009.09.005).
- Etling, D. (2008). *Theoretische Meteorologie: Eine Einführung*. Springer Berlin, Heidelberg. DOI: [10.1007/978-3-540-75979-9](https://doi.org/10.1007/978-3-540-75979-9).
- Forster, L., Emde, C., Unterstrasser, S., and Mayer, B. (2012). Effects of three-dimensional photon transport on the radiative forcing of realistic contrails. *J. Atmos. Sci.*, 69:2243–2255. DOI: [10.1175/JAS-D-11-0206.1](https://doi.org/10.1175/JAS-D-11-0206.1).
- Forster, P., Storelvmo, T., Armour, K., Collins, W., Dufresne, J.-L., Frame, D., Lunt, D. J., Mauritsen, T., Palmer, M. D., Watanabe, M., Wild, M., and Zhang, H. (2021). *The Earth's Energy Budget, Climate Feedbacks, and Climate Sensitivity*, pages 923–1054. Cambridge University Press. DOI: [10.1017/9781009157896.009](https://doi.org/10.1017/9781009157896.009).
- Frias, A. M., Shapiro, M. L., Engberg, Z., Zopp, R., Soler, M., and Stettler, M. (2024). Feasibility of contrail avoidance in a commercial flight planning system: an operational analysis. *Environmental Research: Infrastructure and Sustainability*, 4(1). DOI: [10.1088/2634-4505/ad310c](https://doi.org/10.1088/2634-4505/ad310c).
- Garnier, F., Brunet, S., and Jacquin, L. (1997). Modelling exhaust plume mixing in the near field of an aircraft. *Ann. Geophys.*, 15(11):1468–1477. DOI: [10.1007/s00585-997-1468-1](https://doi.org/10.1007/s00585-997-1468-1).
- Gerz, T. and Ehret, T. (1997). Wingtip vortices and exhaust jets during the jet regime of aircraft wakes. *Aerosp. Sci. Technol.*, 1(7):463–474. DOI: [10.1016/S1270-9638\(97\)90008-0](https://doi.org/10.1016/S1270-9638(97)90008-0).
- Gerz, T. and Holzäpfel, F. (1999). Wing-tip vortices, turbulence, and the distribution of emissions. *AIAA Journal*, 37(10):1270–1276. DOI: [10.2514/2.595](https://doi.org/10.2514/2.595).
- Gerz, T., Holzäpfel, F., and Darracq, D. (2002). Commercial aircraft wake vortices. *Prog. Aerosp. Sci.*, 38(3):181–208. DOI: [10.1016/S0376-0421\(02\)00004-0](https://doi.org/10.1016/S0376-0421(02)00004-0).
- Gierens, K. (2003). On the transition between heterogeneous and homogeneous freezing. *Atmos. Chem. Phys.*, 3:437–446. DOI: [10.5194/acp-3-437-2003](https://doi.org/10.5194/acp-3-437-2003).
- Gierens, K. (2012). Selected topics on the interaction between cirrus clouds and embedded contrails. *Atmos. Chem. Phys.*, 12:11943–11949. DOI: [10.5194/acp-12-11943-2012](https://doi.org/10.5194/acp-12-11943-2012).
- Gierens, K., Lim, L., and Eleftheratos, K. (2008). A review of various strategies for contrail avoidance. *The Open Atmospheric Science Journal*, 2:1–7. DOI: [10.2174/1874282300802010001](https://doi.org/10.2174/1874282300802010001).
- Gierens, K., Matthes, S., and Rohs, S. (2020). How Well Can Persistent Contrails Be Predicted? *Aerospace*, 7(12). DOI: [10.3390/aerospace7120169](https://doi.org/10.3390/aerospace7120169).

- Gierens, K., Schumann, U., Helten, M., Smit, H., and Marenco, A. (1999). A distribution law for relative humidity in the upper troposphere and lower stratosphere derived from three years of MOZAIC measurements. *Ann. Geophys.*, 17(9):1218–1226. DOI: [10.1007/s00585-999-1218-7](https://doi.org/10.1007/s00585-999-1218-7).
- Gierens, K. and Spichtinger, P. (2000). On the size distribution of ice-supersaturated regions in the upper troposphere and lowermost stratosphere. *Ann. Geophys.*, 18(4):499–504. DOI: [10.1007/s00585-000-0499-7](https://doi.org/10.1007/s00585-000-0499-7).
- Grabowski, W. and Smolarkiewicz, P. (2002). A Multiscale Anelastic Model for Meteorological Research. *Mon. Weather Rev.*, 130(4):939–956. DOI: [10.1175/1520-0493\(2002\)130<0939:AMAMFM>2.0.CO;2](https://doi.org/10.1175/1520-0493(2002)130<0939:AMAMFM>2.0.CO;2).
- Grewe, V., Matthes, S., Frömming, C., Brinkop, S., Jöckel, P., Gierens, K., Champougny, T., Fuglestedt, J., Haslerud, A., Irvine, E., and Shine, K. (2017). Feasibility of climate-optimized air traffic routing for trans-Atlantic flights. *Environmental Research Letters*, 12(3):034003. DOI: [10.1088/1748-9326/aa5ba0](https://doi.org/10.1088/1748-9326/aa5ba0).
- Gruber, S., Unterstrasser, S., Bechtold, J., Vogel, H., Jung, M., Pak, H., and Vogel, B. (2018). Contrails and their impact on shortwave radiation and photovoltaic power production – a regional model study. *Atmos. Chem. Phys.*, 18(9):6393–6411. DOI: [10.5194/acp-18-6393-2018](https://doi.org/10.5194/acp-18-6393-2018).
- H2FLY (2019). H2FLY. Accessed: 2025-08-11.
- Hansen, J. E. and Travis, L. D. (1974). Light scattering in planetary atmospheres. *Space Sci. Rev.*, 16:527–610. DOI: [10.1007/BF00168069](https://doi.org/10.1007/BF00168069).
- Heymsfield, A., Baumgardner, D., DeMott, P., Forster, P., Gierens, K., and Kärcher, B. (2010). Contrail microphysics. *Bulletin of the American Meteorological Society*, 91(4):465–472. DOI: [10.1175/2009BAMS2839.1](https://doi.org/10.1175/2009BAMS2839.1).
- Heymsfield, A., Lawson, R., and Sachse, G. (1998). Growth of ice crystals in a precipitating contrail. *Geophys. Res. Lett.*, 25(9):1335–1338. DOI: [10.1029/98GL00189](https://doi.org/10.1029/98GL00189).
- Heymsfield, A. J. and Iaquinta, J. (2000). Cirrus crystal terminal velocities. *J. Atmos. Sci.*, 57(7):916–938. DOI: [10.1175/1520-0469\(2000\)057<0916:CCTV>2.0.CO;2](https://doi.org/10.1175/1520-0469(2000)057<0916:CCTV>2.0.CO;2).
- Heymsfield, A. J., Lewis, S., Bansemmer, A., Iaquinta, J., Miloshevich, L. M., Kajikawa, M., Twohy, C., and Poellot, M. R. (2002). A general approach for deriving the properties of cirrus and stratiform ice cloud particles. *J. Atmos. Sci.*, 59:3–29. DOI: [10.1175/1520-0469\(2002\)059<0003:AGAFDT>2.0.CO;2](https://doi.org/10.1175/1520-0469(2002)059<0003:AGAFDT>2.0.CO;2).
- Hinze, J. (1959). *Turbulence: An Introduction to Its Mechanism and Theory*. McGraw-Hill series in mechanical engineering. McGraw-Hill. LCCN: [58009860](https://lccn.loc.gov/58009860).
- Hofer, S., Gierens, K., and Rohs, S. (2024). Contrail formation and persistence conditions for alternative fuels. *Meteorol. Z.* DOI: [10.1127/metz/2024/1178](https://doi.org/10.1127/metz/2024/1178).
- Hofer, S. M. and Gierens, K. M. (2025). Synoptic and microphysical lifetime constraints for contrails. *Atmos. Chem. Phys.*, 25(16):9235–9247. DOI: [10.5194/acp-25-9235-2025](https://doi.org/10.5194/acp-25-9235-2025).
- Holzäpfel, F., Gerz, T., and Baumann, R. (2001). The turbulent decay of trailing vortex pairs in stably stratified environments. *Aerosp. Sci. Technol.*, 5(2):95–108. DOI: [10.1016/S1270-9638\(00\)01090-7](https://doi.org/10.1016/S1270-9638(00)01090-7).
- Holzäpfel, F. and Gerz, T. (1999). Two-dimensional wake vortex physics in the stably stratified atmosphere. *Aerosp. Sci. Technol.*, 3(5):261–270. DOI: [10.1016/S1270-9638\(00\)86962-X](https://doi.org/10.1016/S1270-9638(00)86962-X).
- Huesch, W. and Lewellen, D. (2006). Sensitivity Study on Contrail Evolution. *36th AIAA Fluid Dynamics Conference and Exhibit*, AIAA 2006-3749:1–14. DOI: [10.2514/6.2006-3749](https://doi.org/10.2514/6.2006-3749).
- Hussein, H. J., Capp, S. P., and George, W. K. (1994). Velocity measurements in a high-Reynolds-number, momentum-conserving, axisymmetric, turbulent jet. *J. Fluid Mech.*, 258:31–75. DOI: [10.1017/S002211209400323X](https://doi.org/10.1017/S002211209400323X).

- IATA (2025). Annual Review 2025. <https://www.iata.org/contentassets/c81222d96c9a4e0bb4ff6ced0126f0bb/iata-annual-review-2025.pdf>. Accessed: 2025-07-23.
- ICAO (2025). Post-COVID-19 Forecasts Scenarios. <https://www.icao.int/post-covid-19-forecasts-scenarios>. Accessed: 2025-07-24.
- IPCC (2023). *Climate Change 2023: Synthesis Report. Contribution of Working Groups I, II and III to the Sixth Assessment Report of the Intergovernmental Panel on Climate Change*. IPCC. DOI: [10.59327/IPCC/AR6-9789291691647](https://doi.org/10.59327/IPCC/AR6-9789291691647).
- Irvine, E. A., Hoskins, B. J., and Shine, K. P. (2014). A Lagrangian analysis of ice-supersaturated air over the North Atlantic. *J. Geophys. Res.*, 119(1):90–100. DOI: [10.1002/2013JD020251](https://doi.org/10.1002/2013JD020251).
- Irvine, E. A. and Shine, K. P. (2015). Ice supersaturation and the potential for contrail formation in a changing climate. *Earth System Dynamics*, 6(2):555–568. DOI: [10.5194/esd-6-555-2015](https://doi.org/10.5194/esd-6-555-2015).
- Iwabuchi, H., Yang, P., Liou, K., and Minnis, P. (2012). Physical and optical properties of persistent contrails: Climatology and interpretation. *J. Geophys. Res.*, 117(D6):D06215. DOI: [10.1029/2011JD017020](https://doi.org/10.1029/2011JD017020).
- Jansen, J. and Heymsfield, A. J. (2015). Microphysics of Aerodynamic Contrail Formation Processes. *J. Atmos. Sci.*, 72(9):3293–3308. DOI: [10.1175/JAS-D-14-0362.1](https://doi.org/10.1175/JAS-D-14-0362.1).
- Jensen, E., Ackerman, A., Stevens, D., Toon, O., and Minnis, P. (1998a). Spreading and growth of contrails in a sheared environment. *J. Geophys. Res.*, 103(D24):31557–31568. DOI: [10.1029/98JD02594](https://doi.org/10.1029/98JD02594).
- Jensen, E., Toon, O., Kinne, S., Sachse, G., Anderson, B., Chan, K., Twohy, C., Gandrud, B., Heymsfield, A., and Miale-Lye, R. (1998b). Environmental conditions required for contrail formation and persistence. *J. Geophys. Res.*, 103:3929–3936. DOI: [10.1029/97JD02808](https://doi.org/10.1029/97JD02808).
- Kärcher, B. (1995). A trajectory box model for aircraft exhaust plumes. *J. Geophys. Res.*, 100:18835–18844. DOI: [10.1029/95JD01638](https://doi.org/10.1029/95JD01638).
- Kärcher, B. (2018). Formation and radiative forcing of contrail cirrus. *Nature Communications*, 9(1):1824. DOI: [10.1038/s41467-018-04068-0](https://doi.org/10.1038/s41467-018-04068-0).
- Kärcher, B., Burkhardt, U., Bier, A., Bock, L., and Ford, I. J. (2015). The microphysical pathway to contrail formation. *J. Geophys. Res.*, 120(15):7893–7927. DOI: [10.1002/2015JD023491](https://doi.org/10.1002/2015JD023491).
- Kärcher, B. and Fabian, P. (1994). Dynamics of aircraft exhaust plumes in the jet-regime. *Ann. Geophys.*, 12(10):911–919. DOI: [10.1007/s00585-994-0911-9](https://doi.org/10.1007/s00585-994-0911-9).
- Kärcher, B., Mayer, B., Gierens, K., Burkhardt, U., Mannstein, H., and Chatterjee, R. (2009). Aerodynamic contrails: Microphysics and optical properties. *J. Atmos. Sci.*, 66:227–243. DOI: [10.1175/2008JAS2768.1](https://doi.org/10.1175/2008JAS2768.1).
- Kärcher, B. and Ström, J. (2003). The roles of dynamical variability and aerosols in cirrus cloud formation. *Atmos. Chem. Phys.*, 3(3):823–838. DOI: [10.5194/acp-3-823-2003](https://doi.org/10.5194/acp-3-823-2003).
- Kärcher, B. and Yu, F. (2009). Role of aircraft soot emissions in contrail formation. *Geophys. Res. Lett.*, 36:L01804. DOI: [10.1029/2008GL036649](https://doi.org/10.1029/2008GL036649).
- Kaufmann, S., Dischl, R., and Voigt, C. (2024). Regional and seasonal impact of hydrogen propulsion systems on potential contrail cirrus cover. *Atmos. Environ.*, 24:100298. DOI: [10.1016/j.aeoa.2024.100298](https://doi.org/10.1016/j.aeoa.2024.100298).
- Kazula, S., de Graaf, S., and Enghardt, L. (2023). Review of fuel cell technologies and evaluation of their potential and challenges for electrified propulsion systems in commercial aviation. *Journal of the Global Power and Propulsion Society*, 7:43–57. DOI: [10.33737/jgpps/158036](https://doi.org/10.33737/jgpps/158036).

- Khandelwal, B., Karakurt, A., Sekaran, P. R., Sethi, V., and Singh, R. (2013). Hydrogen powered aircraft : The future of air transport. *Progress in Aerospace Sciences*, 60:45–59. DOI: [10.1016/j.paerosci.2012.12.002](https://doi.org/10.1016/j.paerosci.2012.12.002).
- Khorsandi, B., Gaskin, S., and Mydlarski, L. (2013). Effect of background turbulence on an axisymmetric turbulent jet. *J. Fluid Mech.*, 736. DOI: [10.1017/jfm.2013.465](https://doi.org/10.1017/jfm.2013.465).
- Khou, J., Ghedhaïfi, W., Vancassel, X., Montreuil, E., and Garnier, F. (2017). CFD simulation of contrail formation in the near field of a commercial aircraft: Effect of fuel sulfur content. *Meteorol. Z.*, 26(6):585–596. DOI: [10.1127/metz/2016/0761](https://doi.org/10.1127/metz/2016/0761).
- Khou, J.-C., Ghedhaïfi, W., Vancassel, X., and Garnier, F. (2015). Spatial Simulation of Contrail Formation in Near-Field of Commercial Aircraft. *J. Aircraft*, 52(6):1927–1938. DOI: [10.2514/1.C033101](https://doi.org/10.2514/1.C033101).
- Kleine, J., Voigt, C., Sauer, D., Schlager, H., Scheibe, M., Jurkat-Witschas, T., Kaufmann, S., Karcher, B., and Anderson, B. E. (2018). In Situ Observations of Ice Particle Losses in a Young Persistent Contrail. *Geophys. Res. Lett.*, 45(24):13553–13561. DOI: [10.1029/2018GL079390](https://doi.org/10.1029/2018GL079390).
- Koop, T., Luo, B., Tsias, A., and Peter, T. (2000). Water activity as the determinant for homogeneous ice nucleation in aqueous solutions. *Nature*, 406(6796):611–4. DOI: [10.1038/35020537](https://doi.org/10.1038/35020537).
- Kärcher, B. (1998). On the potential importance of sulfur-induced activation of soot particles in nascent jet aircraft exhaust plumes. *Atmos. Res.*, 46(3):293–305. DOI: [10.1016/S0169-8095\(97\)00070-7](https://doi.org/10.1016/S0169-8095(97)00070-7).
- Kärcher, B., Turco, R. P., Yu, F., Danilin, M. Y., Weisenstein, D. K., Miake-Lye, R. C., and Busen, R. (2000). A unified model for ultrafine aircraft particle emissions. *J. Geophys. Res.*, 105(D24):29379–29386. DOI: [10.1029/2000JD900531](https://doi.org/10.1029/2000JD900531).
- Lamb, S. H. (1879). *Hydrodynamics*. Republished in Dover Publications, New York 1945.
- Launder, B. E. and Sharma, B. I. (1974). Application of the energy-dissipation model of turbulence to the calculation of flow near a spinning disc. *Letters in Heat and Mass Transfer*, 1(2):131–137. DOI: [10.1016/0094-4548\(74\)90150-7](https://doi.org/10.1016/0094-4548(74)90150-7).
- Launder, B. E. and Spalding, D. B. (1974). The numerical computation of turbulent flows. *Computer Methods in Applied Mechanics and Engineering*, 3(2):269–289. DOI: [10.1016/0045-7825\(74\)90029-2](https://doi.org/10.1016/0045-7825(74)90029-2).
- Lawson, R., Heymsfield, A., Aulenbach, S., and Jensen, T. (1998). Shapes, sizes and light scattering properties of ice crystals in cirrus and a persistent contrail during SUCCESS. *Geophys. Res. Lett.*, 25(9):1331–1334. DOI: [10.1029/98GL00241](https://doi.org/10.1029/98GL00241).
- Lee, D. S., Allen, M. R., Cumpsty, N., Owen, B., Shine, K. P., and Skowron, A. (2023). Uncertainties in mitigating aviation non-co2 emissions for climate and air quality using hydrocarbon fuels. *Environ. Sci.: Atmos.*, 3:1693–1740. DOI: [10.1039/D3EA00091E](https://doi.org/10.1039/D3EA00091E).
- Lee, D. S., Fahey, D. W., Forster, P. M., Newton, P. J., Wit, R. C., Lim, L. L., Owen, B., and Sausen, R. (2009). Aviation and global climate change in the 21st century. *Atmos. Environ.*, 43(22):3520–3537. DOI: [10.1016/j.atmosenv.2009.04.024](https://doi.org/10.1016/j.atmosenv.2009.04.024).
- Lee, D. S., Fahey, D. W., Skowron, A., Allen, M. R., Burkhardt, U., Chen, Q., Doherty, S. J., Freeman, S., Forster, P. M., Fuglestedt, J., Gettelman, A., De León, R. R., Lim, L. L., Lund, M. T., Millar, R. J., Owen, B., Penner, J. E., Pitari, G., Prather, M. J., Sausen, R., and Wilcox, L. J. (2021a). The contribution of global aviation to anthropogenic climate forcing for 2000 to 2018. *Atmos. Environ.*, 244:117834. DOI: [10.1016/j.atmosenv.2020.117834](https://doi.org/10.1016/j.atmosenv.2020.117834).
- Lee, J. H. W. and Chu, V. H. (2003). *Turbulent Jets and Plumes*. Springer New York, NY. DOI: [10.1007/978-1-4615-0407-8](https://doi.org/10.1007/978-1-4615-0407-8).

- Lee, J.-Y., Marotzke, J., Bala, G., Cao, L., Corti, S., Dunne, J. P., Engelbrecht, F., Fischer, E., Fyfe, J., Jones, C., Maycock, A., Mutemi, J., Ndiaye, O., Panickal, S., and Zhou, T. (2021b). Future Global Climate: Scenario-Based Projections and Near-Term Information. In Masson-Delmotte, V., Zhai, P., Pirani, A., Connors, S., Péan, C., Berger, S., Caud, N., Chen, Y., Goldfarb, L., Gomis, M., Huang, M., Leitzell, K., Lonnoy, E., Matthews, J., Maycock, T., Waterfield, T., Yelekçi, O., Yu, R., and Zhou, B., editors, *Climate Change 2021: The Physical Science Basis. Contribution of Working Group I to the Sixth Assessment Report of the Intergovernmental Panel on Climate Change*, pages 553–672. Cambridge University Press. DOI: [10.1017/9781009157896.006](https://doi.org/10.1017/9781009157896.006).
- Lewellen, D. and Lewellen, W. (1996). Large-eddy simulations of the vortex-pair breakup in aircraft wakes. *AIAA Journal*, 34(11):2337–2345. DOI: [10.2514/3.13399](https://doi.org/10.2514/3.13399).
- Lewellen, D. and Lewellen, W. (2001a). The effects of aircraft wake dynamics on contrail development. *J. Atmos. Sci.*, 58(4):390–406. DOI: [10.1175/1520-0469\(2001\)058<0390:TEOAWD>2.0.CO;2](https://doi.org/10.1175/1520-0469(2001)058<0390:TEOAWD>2.0.CO;2).
- Lewellen, D. C. (2012). Analytic solutions for evolving size distributions of spherical crystals or droplets undergoing diffusional growth in different regimes. *J. Atmos. Sci.*, 69:417–434. DOI: [10.1175/JAS-D-11-029.1](https://doi.org/10.1175/JAS-D-11-029.1).
- Lewellen, D. C. (2014). Persistent contrails and contrail cirrus. Part 2: Full Lifetime Behavior. *J. Atmos. Sci.*, pages 4420–4438. DOI: [10.1175/JAS-D-13-0317.1](https://doi.org/10.1175/JAS-D-13-0317.1).
- Lewellen, D. C. (2020). A Large-Eddy Simulation Study of Contrail Ice Number Formation. *J. Atmos. Sci.*, 77(7):2585–2604. DOI: [10.1175/JAS-D-19-0322.1](https://doi.org/10.1175/JAS-D-19-0322.1).
- Lewellen, D. C. and Lewellen, W. S. (2001b). Effects of aircraft wake dynamics on measured and simulated NO_x and HO_x wake chemistry. *J. Geophys. Res.*, 106(D21):27661–27672. DOI: [10.1029/2001JD000531](https://doi.org/10.1029/2001JD000531).
- Lewellen, D. C., Meza, O., and Huebsch, W. W. (2014). Persistent contrails and contrail cirrus. Part 1: Large-eddy simulations from inception to demise. *J. Atmos. Sci.*, 71(12):4399–4419. DOI: [10.1175/JAS-D-13-0316.1](https://doi.org/10.1175/JAS-D-13-0316.1).
- Lipari, G. and Stansby, P. K. (2011). Review of Experimental Data on Incompressible Turbulent Round Jets. *Flow Turbul. Combust.*, 87:79–114. DOI: [10.1007/s10494-011-9330-7](https://doi.org/10.1007/s10494-011-9330-7).
- Lottermoser, A. and Unterstrasser, S. (2024). Towards intermediate complexity modelling of contrail formation: the new dynamical framework RadMod. *Aeronaut. J.*, 129(1332):351–379. DOI: [10.1017/aer.2024.130](https://doi.org/10.1017/aer.2024.130).
- Lottermoser, A. and Unterstrasser, S. (2025). High-resolution modeling of early contrail evolution from hydrogen-powered aircraft. *Atmos. Chem. Phys.*, 25:7903–7924. DOI: [10.5194/acp-25-7903-2025](https://doi.org/10.5194/acp-25-7903-2025).
- Manhart, M. (2004). A Zonal Grid Algorithm for DNS of Turbulent Boundary Layers. *Comput. Fluids*, 33(3):435–461. DOI: [10.1016/S0045-7930\(03\)00061-6](https://doi.org/10.1016/S0045-7930(03)00061-6).
- Marciello, V., Di Stasio, M., Ruocco, M., Trifari, V., Nicolosi, F., Meindl, M., Lemoine, B., and Caliendo, P. (2023). Design Exploration for Sustainable Regional Hybrid-Electric Aircraft: A Study Based on Technology Forecasts. *Aerospace*, 10(2). DOI: [10.3390/aerospace10020165](https://doi.org/10.3390/aerospace10020165).
- Märkl, R. S., Voigt, C., Sauer, D., Dischl, R. K., Kaufmann, S., Harlaß, T., Hahn, V., Roiger, A., Weiß-Rehm, C., Burkhardt, U., Schumann, U., Marsing, A., Scheibe, M., Dörnbrack, A., Renard, C., Gauthier, M., Swann, P., Madden, P., Luff, D., Sallinen, R., Schripp, T., and Le Clercq, P. (2024). Powering aircraft with 100 % sustainable aviation fuel reduces ice crystals in contrails. *Atmos. Chem. Phys.*, 24(6):3813–3837. DOI: [10.5194/acp-24-3813-2024](https://doi.org/10.5194/acp-24-3813-2024).
- Marks, T., Dahlmann, K., Grewe, V., Gollnick, V., Linke, F., Matthes, S., Stumpf, E., Swaid, M., Unterstrasser, S., Yamashita, H., and Zumegen, C. (2021). Climate Impact Mitigation Potential of Formation Flight. *Aerospace*, 8(1):14. DOI: [10.3390/aerospace8010014](https://doi.org/10.3390/aerospace8010014).

- McFarquhar, G. M. and Heymsfield, A. J. (1998). The definition and significance of an effective radius for ice clouds. *J. Atmos. Sci.*, 55(11):2039–2052. DOI: [10.1175/1520-0469\(1998\)055<2039:TDASOA>2.0.CO;2](https://doi.org/10.1175/1520-0469(1998)055<2039:TDASOA>2.0.CO;2).
- Minikin, A., Petzold, A., Ström, J., Krejci, R., Seifert, M., van Velthoven, P., Schlager, H., and Schumann, U. (2003). Aircraft observations of the upper tropospheric fine particle aerosol in the Northern and Southern Hemispheres at midlatitudes. *Geophys. Res. Lett.*, 30(10):1503. DOI: [10.1029/2002GL016458](https://doi.org/10.1029/2002GL016458).
- Minnis, P., Young, D., Garber, D., Nguyen, L., Smith Jr, W., and Palikonda, R. (1998). Transformation of contrails into cirrus during SUCCESS. *Geophys. Res. Lett.*, 25(8):1157–1160. DOI: [10.1029/97GL03314](https://doi.org/10.1029/97GL03314).
- Mitchell, D. and Heymsfield, A. (2005). Refinements in the treatment of ice particle terminal velocities, highlighting aggregates. *J. Atmos. Sci.*, 62:1637–1644. DOI: [10.1175/JAS3413.1](https://doi.org/10.1175/JAS3413.1).
- Mitchell, D. L. (1996). Use of mass- and area-dimensional power laws for determining precipitation particle terminal velocities. *J. Atmos. Sci.*, 53, 12:1710–1723. DOI: [10.1175/1520-0469\(1996\)053<1710:UOMAAD>2.0.CO;2](https://doi.org/10.1175/1520-0469(1996)053<1710:UOMAAD>2.0.CO;2).
- Mitchell, D. L., Chai, S. K., Liu, Y., Heymsfield, A. J., and Dong, Y. (1996). Modeling Cirrus Clouds. Part I: Treatment of Bimodal Size Spectra and Case Study Analysis. *J. Atmos. Sci.*, 53(20):2952–2966. DOI: [10.1175/1520-0469\(1996\)053<2952:MCCPIT>2.0.CO;2](https://doi.org/10.1175/1520-0469(1996)053<2952:MCCPIT>2.0.CO;2).
- Moeini, M., Khorsandi, B., and Mydlarski, L. (2021). Effect of coflow turbulence on the dynamics and mixing of a nonbuoyant turbulent jet. *J. Hydraul. Eng.*, 147(1):04020088. DOI: [10.1061/\(ASCE\)HY.1943-7900.0001830](https://doi.org/10.1061/(ASCE)HY.1943-7900.0001830).
- Möhler, O., Field, P. R., Connolly, P., Benz, S., Saathoff, H., Schnaiter, M., Wagner, R., Cotton, R., Krämer, M., Mangold, A., and Heymsfield, A. J. (2006). Efficiency of the deposition mode ice nucleation on mineral dust particles. *Atmos. Chem. Phys.*, 6(10):3007–3021. DOI: [10.5194/acp-6-3007-2006](https://doi.org/10.5194/acp-6-3007-2006).
- Monkewitz, P. A., Bechert, D. W., Barsikow, B., and Lehmann, B. (1990). Self-excited oscillations and mixing in a heated round jet. *J. Fluid Mech.*, 213:611–639. DOI: [10.1017/S0022112090002476](https://doi.org/10.1017/S0022112090002476).
- Moody, N. R. and Thompson, A. W. (1990). Hydrogen effects on material behavior. In *The Fourth International Conference on Hydrogen Effects on Material Behavior*. DOI: [10.1007/BF03221074](https://doi.org/10.1007/BF03221074).
- Moore, R. H., Thornhill, K. L., Weinzierl, B., Sauer, D., D’Ascoli, E., Kim, J., Lichtenstern, M., Scheibe, M., Beaton, B., Beyersdorf, A. J., Barrick, J., Bulzan, D., Corr, C. A., Crosbie, E., Jurkat, T., Martin, R., Riddick, D., Shook, M., Slover, G., Voigt, C., White, R., Winstead, E., Yasky, R., Ziemba, L. D., Brown, A., Schlager, H., and Anderson, B. E. (2017). Biofuel blending reduces particle emissions from aircraft engines at cruise conditions. *Nature*, 543(7645):411–415. DOI: [10.1038/nature21420](https://doi.org/10.1038/nature21420).
- Myhre, G., Shindell, D., Bréon, F.-M., Collins, W., Fuglestedt, J., Huang, J., Koch, D., Lamarque, J.-F., Lee, D., Mendoza, B., Nakajima, T., Robock, A., Stephens, G., Takemura, T., and Zhang, H. (2013). *Anthropogenic and Natural Radiative Forcing*, pages 659–740. Cambridge University Press. DOI: [10.1017/CBO9781107415324.018](https://doi.org/10.1017/CBO9781107415324.018).
- Møller, K. T., Jensen, T. R., Akiba, E., and Li, H. (2017). Hydrogen - A sustainable energy carrier. *Progress in Natural Science: Materials International*, 27(1):34–40. DOI: [10.1016/j.pnsc.2016.12.014](https://doi.org/10.1016/j.pnsc.2016.12.014).
- Nickels, T. B. and Perry, A. E. (1996). An experimental and theoretical study of the turbulent coflowing jet. *J. Fluid Mech.*, 309:157–182. DOI: [10.1017/S0022112096001590](https://doi.org/10.1017/S0022112096001590).
- Or, C., Lam, K., and Liu, P. (2011). Potential core lengths of round jets in stagnant and moving environments. *Journal of Hydro-environment Research*, 5:81–91. DOI: [10.1016/j.jher.2011.01.002](https://doi.org/10.1016/j.jher.2011.01.002).
- Pai, S.-I. (1954). *Fluid Dynamics of Jets*. D. Van Nostrand Co. Inc. DOI: [10.1017/S0368393100120474](https://doi.org/10.1017/S0368393100120474).

- Paige, C. C. and Saunders, M. A. (1982a). Algorithm 583: LSQR: Sparse Linear Equations and Least Squares Problems. *ACM Trans. Math. Softw.*, 8(2):195–209. DOI: [10.1145/355993.356000](https://doi.org/10.1145/355993.356000).
- Paige, C. C. and Saunders, M. A. (1982b). LSQR: An Algorithm for Sparse Linear Equations and Sparse Least Squares. *ACM Trans. Math. Softw.*, 8(1):43–71. DOI: [10.1145/355984.355989](https://doi.org/10.1145/355984.355989).
- Panchapakesan, N. R. and Lumley, J. L. (1993a). Turbulence measurements in axisymmetric jets of air and helium. Part 1. Air jet. *J. Fluid Mech.*, 246:197–223. DOI: [10.1017/S0022112093000096](https://doi.org/10.1017/S0022112093000096).
- Panchapakesan, N. R. and Lumley, J. L. (1993b). Turbulence measurements in axisymmetric jets of air and helium. Part 2. Helium jet. *J. Fluid Mech.*, 246:225–247. DOI: [10.1017/S0022112093000102](https://doi.org/10.1017/S0022112093000102).
- Paoli, R., Nybelen, L., Picot, J., and Cariolle, D. (2013). Effects of jet/vortex interaction on contrail formation in supersaturated conditions. *Phys. Fluids*, 25(053305):1–28. DOI: [10.1063/1.4807063](https://doi.org/10.1063/1.4807063).
- Paoli, R. and Shariff, K. (2016). Contrail Modeling and Simulation. *Annu. Rev. Fluid Mech.*, 48(1):393–427. DOI: [10.1146/annurev-fluid-010814-013619](https://doi.org/10.1146/annurev-fluid-010814-013619).
- Paoli, R., Thouron, O., Cariolle, D., García, M., and Escobar, J. (2017). Three-dimensional large-eddy simulations of the early phase of contrail-to-cirrus transition: effects of atmospheric turbulence and radiative transfer. *Meteorol. Z.*, 26(6):597–620. DOI: [10.1127/metz/2017/0764](https://doi.org/10.1127/metz/2017/0764).
- Paoli, R., Vancassel, X., Garnier, F., and Mirabel, P. (2008). Large-eddy simulation of a turbulent jet and a vortex sheet interaction: particle formation and evolution in the near field of an aircraft wake. *Meteorol. Z.*, 17(2):131–144. DOI: [10.1127/0941-2948/2008/0278](https://doi.org/10.1127/0941-2948/2008/0278).
- Papamoschou, D. and Roshko, A. (1988). The compressible turbulent shear layer: an experimental study. *J. Fluid Mech.*, 197:453–477. DOI: [10.1017/S0022112088003325](https://doi.org/10.1017/S0022112088003325).
- Pauen, J., Unterstrasser, S., and Stephan, A. (2024). Towards Refined Contrail Simulations Of Formation Flight Scenarios. https://www.icas.org/icas_archive/icas2024/data/papers/icas2024_0502_paper.pdf. accessed: 2025-03-02.
- Penner, J. E., Lister, D. H., Griggs, D. J., Dokken, D. J., and McFarland, M. (1999). Aviation and the Global Atmosphere. Technical report, Intergovernmental Panel on Climate Change (IPCC), IPCC Secretariat, c/o World Meteorological Organization, Geneva, Switzerland.
- Petters, M. D. and Kreidenweis, S. M. (2007). A single parameter representation of hygroscopic growth and cloud condensation nucleus activity. *Atmos. Chem. Phys.*, 7(8):1961–1971. DOI: [10.5194/acp-7-1961-2007](https://doi.org/10.5194/acp-7-1961-2007).
- Petzold, A., Busen, R., Schröder, F. P., Baumann, R., Kuhn, M., Ström, J., Hagen, D., Whitefield, P., Baumgardner, D., Arnold, F., Borrmann, S., and Schumann, U. (1997). Near-field measurements on contrail properties from fuels with different sulfur content. *J. Geophys. Res.*, 102:29867–29880. DOI: [10.1029/97JD02209](https://doi.org/10.1029/97JD02209).
- Petzold, A., Kramer, M., Neis, P., Rolf, C., Rohs, S., Berkes, F., Smit, H. G. J., Gallagher, M., Beswick, K., Lloyd, G., Baumgardner, D., Spichtinger, P., Nédélec, P., Ebert, V., Buchholz, B., Riese, M., and Wahner, A. (2017). Upper tropospheric water vapour and its interaction with cirrus clouds as seen from IAGOS long-term routine in situ observations. *Faraday Discuss.*, 200:229–249. DOI: [10.1039/C7FD00006E](https://doi.org/10.1039/C7FD00006E).
- Petzold, A., Neis, P., Rütimann, M., Rohs, S., Berkes, F., Smit, H. G. J., Krämer, M., Spelten, N., Spichtinger, P., Nédélec, P., and Wahner, A. (2020). Ice-supersaturated air masses in the northern mid-latitudes from regular in situ observations by passenger aircraft: vertical distribution, seasonality and tropospheric fingerprint. *Atmos. Chem. Phys.*, 20(13):8157–8179. DOI: [10.5194/acp-20-8157-2020](https://doi.org/10.5194/acp-20-8157-2020).

- Picot, J., Paoli, R., Thouron, O., and Cariolle, D. (2015). Large-eddy simulation of contrail evolution in the vortex phase and its interaction with atmospheric turbulence. *Atmos. Chem. Phys.*, 15(13):7369–7389. DOI: [10.5194/acp-15-7369-2015](https://doi.org/10.5194/acp-15-7369-2015).
- Poellot, M. R., Arnott, W. P., and Hallett, J. (1999). In situ observations of contrail microphysics and implications for their radiative impact. *J. Geophys. Res.*, 104(D10):12077–12084. DOI: [10.1029/1999JD900109](https://doi.org/10.1029/1999JD900109).
- Ponsonby, J., King, L., Murray, B. J., and Stettler, M. E. J. (2024). Jet aircraft lubrication oil droplets as contrail ice-forming particles. *Atmos. Chem. Phys.*, 24(3):2045–2058. DOI: [10.5194/acp-24-2045-2024](https://doi.org/10.5194/acp-24-2045-2024).
- Pont, G., Brenner, P., Cinnella, P., Maugars, B., and Robinet, J.-C. (2017). Multiple-correction hybrid k-exact schemes for high-order compressible RANS-LES simulations on fully unstructured grids. *Journal of Computational Physics*, 350:45–83. DOI: [10.1016/j.jcp.2017.08.036](https://doi.org/10.1016/j.jcp.2017.08.036).
- Pope, S. B. (2000). *Turbulent Flows*. Cambridge University Press. DOI: [10.1017/CBO9780511840531](https://doi.org/10.1017/CBO9780511840531).
- Prather, M., Sausen, R., Grossman, A., Haywood, J., Rind, D., and Subbaraya, B. (1999). *Potential Climate Change from Aviation*. Cambridge University Press.
- Prusa, J., Smolarkiewicz, P., and Wyszogrodzki, A. (2008). EULAG, a computational model for multiscale flows. *Comput. Fluids*, 37(9):1193–1207. DOI: [10.1016/j.compfluid.2007.12.001](https://doi.org/10.1016/j.compfluid.2007.12.001).
- Prussi, M., Lee, U., Wang, M., Malina, R., Valin, H., Taheripour, F., Velarde, C., Staples, M. D., Lonza, L., and Hileman, J. I. (2021). CORSIA: The first internationally adopted approach to calculate life-cycle GHG emissions for aviation fuels. *Renewable and Sustainable Energy Reviews*, 150:111398. DOI: [10.1016/j.rser.2021.111398](https://doi.org/10.1016/j.rser.2021.111398).
- Rabe, B. L. (2024). Parametric Study of High-Resolution Simulations of Contrails During the Vortex Phase with Emphasis on Initial Conditions. <https://elib.dlr.de/209715/>. accessed: 2025-05-04.
- Richards, C. D. and Pitts, W. M. (1993). Global density effects on the self-preservation behaviour of turbulent free jets. *J. Fluid Mech.*, 254:417–435. DOI: [10.1017/S0022112093002204](https://doi.org/10.1017/S0022112093002204).
- Ricou, F. P. and Spalding, D. B. (1961). Measurements of entrainment by axisymmetrical turbulent jets. *J. Fluid Mech.*, 11(1):21–32. DOI: [10.1017/S0022112061000834](https://doi.org/10.1017/S0022112061000834).
- Righi, M., Hendricks, J., and Sausen, R. (2013). The global impact of the transport sectors on atmospheric aerosol: simulations for year 2000 emissions. *Atmos. Chem. Phys.*, 13(19):9939–9970. DOI: [10.5194/acp-13-9939-2013](https://doi.org/10.5194/acp-13-9939-2013).
- Rubin-Zuzic, M., Bugliaro, L. G., Marsing, A., Voigt, C., Simson, C., Kaiser, S., and Ziegler, P. (2025). Reduced Contrail Radiative Effect for Future Fleets with Low Soot and Water Vapour Emissions. *Atmospheric Environment: X*. DOI: [10.1016/j.aeaoa.2025.100353](https://doi.org/10.1016/j.aeaoa.2025.100353).
- Saffman, P. (1993). *Vortex dynamics*. Cambridge University Press. DOI: [10.1017/CBO9780511624063](https://doi.org/10.1017/CBO9780511624063).
- Saulgeot, P., Brion, V., Bonne, N., Dormy, E., and Jacquin, L. (2023). Effects of atmospheric stratification and jet position on the properties of early aircraft contrails. *Phys. Rev. Fluids*, 8:114702. DOI: [10.1103/PhysRevFluids.8.114702](https://doi.org/10.1103/PhysRevFluids.8.114702).
- Sausen, R., Hofer, S., Gierens, K., Bugliaro, L., Ehrmantraut, R., Sitova, I., Walczak, K., BurrIDGE-Diesing, A., Bowman, M., and Miller, N. (2024). Can we successfully avoid persistent contrails by small altitude adjustments of flights in the real world? *Meteorol. Z.*, 33(1):83–98. DOI: [10.1127/metz/2023/1157](https://doi.org/10.1127/metz/2023/1157).
- Sautet, J. C. and Stepowski, D. (1995). Dynamic behavior of variable-density, turbulent jets in their near development fields. *Phys. Fluids*, 7(11):2796–2806. DOI: [10.1063/1.868658](https://doi.org/10.1063/1.868658).

- Schilling, V., Siano, S., and Etling, D. (1996). Dispersion of aircraft emissions due to wake vortices in stratified shear flows: a two-dimensional numerical study. *J. Geophys. Res.*, 101(D15):20965–20974. DOI: [10.1029/96JD02013](https://doi.org/10.1029/96JD02013).
- Schmidt, E. (1941). Die Entstehung von Eisnebel aus den Auspuffgasen von Flugmotoren. *Schriften der Deutschen Akademie der Luftfahrtforschung*, 44:1–15. accessed: 2022-11-19.
- Schmidt, P., Batteiger, V., Roth, A., Weindorf, W., and Raksha, T. (2018). Power-to-Liquids as Renewable Fuel Option for Aviation: A Review. *Chemie Ingenieur Technik*, 90(1-2):127–140. DOI: [10.1002/cite.201700129](https://doi.org/10.1002/cite.201700129).
- Schröder, F., Kärcher, B., Duroure, C., Ström, J., Petzold, A., Gayet, J., and ... Borrmann, S. (2000). On the transition of contrails into cirrus clouds. *J. Atmos. Sci.*, 57(4):464–480. DOI: [10.1175/1520-0469\(2000\)057<0464:OTTOCI>2.0.CO;2](https://doi.org/10.1175/1520-0469(2000)057<0464:OTTOCI>2.0.CO;2).
- Schumann, U. (1996). On conditions for contrail formation from aircraft exhausts. *Meteorol. Z.*, 5:4–23. DOI: [10.1127/metz/5/1996/4](https://doi.org/10.1127/metz/5/1996/4).
- Schumann, U. (2005). Formation, properties and climatic effects of contrails. *C. R. Phys.*, 6(4-5):549–565. DOI: [10.1016/j.crhy.2005.05.002](https://doi.org/10.1016/j.crhy.2005.05.002).
- Schumann, U. (2012). A contrail cirrus prediction model. *Geosci. Model Dev.*, 5(3):543–580. DOI: [10.5194/gmd-5-543-2012](https://doi.org/10.5194/gmd-5-543-2012).
- Schumann, U., Mayer, B., Gierens, K., Unterstrasser, S., Jessberger, P., Petzold, A., Voigt, C., and Gayet, J.-F. (2011). Effective Radius of Ice Particles in Cirrus and Contrails. *J. Atmos. Sci.*, 68(2):300–321. DOI: [10.1175/2010JAS3562.1](https://doi.org/10.1175/2010JAS3562.1).
- Schumann, U., Penner, J. E., Chen, Y., Zhou, C., and Graf, K. (2015). Dehydration effects from contrails in a coupled contrail-climate model. *Atmos. Chem. Phys.*, 15(19):11179–11199. DOI: [10.5194/acp-15-11179-2015](https://doi.org/10.5194/acp-15-11179-2015).
- Schumann, U., Ström, J., Busen, R., Baumann, R., Gierens, K., Krautstrunk, M., Schröder, F., and Stingl, J. (1996). In situ observations of particles in jet aircraft exhausts and contrails for different sulfur-containing fuels. *J. Geophys. Res.*, 101(D3):6853–6870. DOI: [10.1029/95JD03405](https://doi.org/10.1029/95JD03405).
- Schwaborn, D., Gerhold, T., and Heinrich, R. (2006). The DLR TAU-Code: Recent Applications in Research and Industry. In *ECCOMAS CFD 2006 CONFERENCE*. accessed: 2025-06-30.
- Searchinger, T., Heimlich, R., Houghton, R. A., Dong, F., Elobeid, A., Fabiosa, J., Tokgoz, S., Hayes, D., and Yu, T.-H. (2008). Use of U.S. Croplands for Biofuels Increases Greenhouse Gases Through Emissions from Land-Use Change. *Science*, 319(5867):1238–1240. DOI: [10.1126/science.1151861](https://doi.org/10.1126/science.1151861).
- Sforza, P. M. and Mons, R. F. (1978). Mass, momentum, and energy transport in turbulent free jets. *Int. J. Heat Mass Trans.*, 21:371–384. DOI: [10.1016/0017-9310\(78\)90070-4](https://doi.org/10.1016/0017-9310(78)90070-4).
- Sloop, J. L. (1978). Liquid Hydrogen As a Propulsion Fuel, 1945-1959, Scientific and Technical Information Office at the National Aeronautics and Space Administration. <https://core.ac.uk/download/pdf/10339184.pdf>. accessed: 2025-06-12.
- Smith, C. J., Kramer, R. J., Myhre, G., Alterskjær, K., Collins, W., Sima, A., Boucher, O., Dufresne, J.-L., Nabat, P., Michou, M., Yukimoto, S., Cole, J., Paynter, D., Shiogama, H., O'Connor, F. M., Robertson, E., Wiltshire, A., Andrews, T., Hannay, C., Miller, R., Nazarenko, L., Kirkevåg, A., Olivié, D., Fiedler, S., Lewinschal, A., Mackallah, C., Dix, M., Pincus, R., and Forster, P. M. (2020). Effective radiative forcing and adjustments in CMIP6 models. *Atmos. Chem. Phys.*, 20(16):9591–9618. DOI: [10.5194/acp-20-9591-2020](https://doi.org/10.5194/acp-20-9591-2020).

- Smolarkiewicz, P. and Margolin, L. (1997). On forward-in-time differencing for fluids: an Eulerian/semi-Lagrangian non-hydrostatic model for stratified flows. *Atmosphere-Ocean Special*, 35:127–152. DOI: [10.1080/07055900.1997.9687345](https://doi.org/10.1080/07055900.1997.9687345).
- Smolarkiewicz, P. and Margolin, L. (1998). MPDATA: A Finite-Difference Solver for Geophysical Flows. *J. Comput. Phys.*, 140(2):459–480. DOI: [10.1006/jcph.1998.5901](https://doi.org/10.1006/jcph.1998.5901).
- Smolarkiewicz, P. and Prusa, J. (2002). Forward-in-time differencing for fluids: simulation of geophysical turbulence. *D. Drikakis, B.J. Geurts Eds., Turbulent Flow Computation, Kluwer Academic Publishers, Dordrecht*, 1:207–240. DOI: [10.1007/0-306-48421-8_8](https://doi.org/10.1007/0-306-48421-8_8).
- Sölch, I. (2008). *Ein Euler-Lagrange'sches Zirruswolken Modell mit expliziter Aerosol- und Eismikrophysik. Studien zur Aggregation von Eispartikeln*. PhD thesis, LMU München. DOI: [10.5282/edoc.9827](https://doi.org/10.5282/edoc.9827).
- Sölch, I. and Kärcher, B. (2010). A large-eddy model for cirrus clouds with explicit aerosol and ice microphysics and Lagrangian ice particle tracking. *Q. J. R. Meteorol. Soc.*, 136:2074–2093. DOI: [10.1002/qj.689](https://doi.org/10.1002/qj.689).
- Sölch, I. and Kärcher, B. (2011). Process-oriented large-eddy simulations of a midlatitude cirrus cloud system based on observations. *Q. J. R. Meteorol. Soc.*, 137(655):374–393. DOI: [10.1002/qj.764](https://doi.org/10.1002/qj.764).
- Sussmann, R. and Gierens, K. (1999). Lidar and numerical studies on the different evolution of vortex pair and secondary wake in young contrails. *J. Geophys. Res.*, 104:2131–2142. DOI: [10.1029/1998JD200034](https://doi.org/10.1029/1998JD200034).
- Tchen, C. (1947). *Mean value and correlation problems connected with the motion of small particles suspended in a turbulent fluid*. PhD thesis, TU Delft. DOI: [10.1007/978-94-017-6101-7](https://doi.org/10.1007/978-94-017-6101-7).
- Teoh, R., Engberg, Z., Schumann, U., Voigt, C., Shapiro, M., Rohs, S., and Stettler, M. E. J. (2024). Global aviation contrail climate effects from 2019 to 2021. *Atmos. Chem. Phys.*, 24(10):6071–6093. DOI: [10.5194/acp-24-6071-2024](https://doi.org/10.5194/acp-24-6071-2024).
- Teoh, R., Schumann, U., Voigt, C., Schripp, T., Shapiro, M., Engberg, Z., Molloy, J., Koudis, G., and Stettler, M. E. J. (2022). Targeted Use of Sustainable Aviation Fuel to Maximize Climate Benefits. *Environ. Sci. Technol.*, 56(23):17246–17255. DOI: [10.1021/acs.est.2c05781](https://doi.org/10.1021/acs.est.2c05781).
- Thring, M. W. and Newby, M. P. (1953). Combustion length of enclosed turbulent jet flames. *Symp. Combust.*, 4(1):789–796. DOI: [10.1016/S0082-0784\(53\)80103-7](https://doi.org/10.1016/S0082-0784(53)80103-7).
- Timmons, D. and Terwel, R. (2022). Economics of aviation fuel decarbonization: A preliminary assessment. *Journal of Cleaner Production*, 369:133097. DOI: [10.1016/j.jclepro.2022.133097](https://doi.org/10.1016/j.jclepro.2022.133097).
- Tiwari, S., Pekris, M. J., and Doherty, J. J. (2024). A review of liquid hydrogen aircraft and propulsion technologies. *International Journal of Hydrogen Energy*, 57:1174–1196. DOI: [10.1016/j.ijhydene.2023.12.263](https://doi.org/10.1016/j.ijhydene.2023.12.263).
- Ungeheuer, F., Caudillo, L., Ditas, F., Simon, M., van Pinxteren, D., Kilic, D., Rose, D., Jacobi, S., Kürten, A., Curtius, J., and Vogel, A. L. (2022). Nucleation of jet engine oil vapours is a large source of aviation-related ultrafine particles. *Commun. Earth Environ.*, 3(319):1–8. DOI: [10.1038/s43247-022-006](https://doi.org/10.1038/s43247-022-006).
- Ungeheuer, F., van Pinxteren, D., and Vogel, A. L. (2021). Identification and source attribution of organic compounds in ultrafine particles near Frankfurt International Airport. *Atmos. Chem. Phys.*, 21:3763–3775. DOI: [10.5194/acp-21-3763-2021](https://doi.org/10.5194/acp-21-3763-2021).
- Unterstrasser, S. (2014). Large eddy simulation study of contrail microphysics and geometry during the vortex phase and consequences on contrail-to-cirrus transition. *J. Geophys. Res.*, 119(12):7537–7555. DOI: [10.1002/2013JD021418](https://doi.org/10.1002/2013JD021418).

- Unterstrasser, S. (2016). Properties of young contrails - a parametrisation based on large-eddy simulations. *Atmos. Chem. Phys.*, 16(4):2059–2082. DOI: [10.5194/acp-16-2059-2016](https://doi.org/10.5194/acp-16-2059-2016).
- Unterstrasser, S. (2020). The Contrail Mitigation Potential of Aircraft Formation Flight Derived from High-Resolution Simulations. *Aerospace*, 7(12):170. DOI: [10.3390/aerospace7120170](https://doi.org/10.3390/aerospace7120170).
- Unterstrasser, S. and Gierens, K. (2010a). Numerical simulations of contrail-to-cirrus transition - Part 1: An extensive parametric study. *Atmos. Chem. Phys.*, 10(4):2017–2036. DOI: [10.5194/acp-10-2017-2010](https://doi.org/10.5194/acp-10-2017-2010).
- Unterstrasser, S. and Gierens, K. (2010b). Numerical simulations of contrail-to-cirrus transition - Part 2: Impact of initial ice crystal number, radiation, stratification, secondary nucleation and layer depth. *Atmos. Chem. Phys.*, 10(4):2037–2051. DOI: [10.5194/acp-10-2037-2010](https://doi.org/10.5194/acp-10-2037-2010).
- Unterstrasser, S., Gierens, K., Sölch, I., and Lainer, M. (2017a). Numerical simulations of homogeneously nucleated natural cirrus and contrail-cirrus. Part 1: How different are they? *Meteorol. Z.*, 26(6):621–642. DOI: [10.1127/metz/2016/0777](https://doi.org/10.1127/metz/2016/0777).
- Unterstrasser, S., Gierens, K., Sölch, I., and Wirth, M. (2017b). Numerical simulations of homogeneously nucleated natural cirrus and contrail-cirrus. Part 2: Interaction on local scale. *Meteorol. Z.*, 26(6):643–661. DOI: [10.1127/metz/2016/0780](https://doi.org/10.1127/metz/2016/0780).
- Unterstrasser, S. and Görsch, N. (2014). Aircraft-type dependency of contrail evolution. *J. Geophys. Res.*, 119(24):14,015–14,027. DOI: [10.1002/2014JD022642](https://doi.org/10.1002/2014JD022642).
- Unterstrasser, S., Hoffmann, F., and Lerch, M. (2017c). Collection/aggregation algorithms in Lagrangian cloud microphysical models: rigorous evaluation in box model simulations. *Geosci. Model Dev.*, 10(4):1521–1548. DOI: [10.5194/gmd-10-1521-2017](https://doi.org/10.5194/gmd-10-1521-2017).
- Unterstrasser, S., Paoli, R., Sölch, I., Kühnlein, C., and Gerz, T. (2014). Dimension of aircraft exhaust plumes at cruise conditions: effect of wake vortices. *Atmos. Chem. Phys.*, 14(5):2713–2733. DOI: [10.5194/acp-14-2713-2014](https://doi.org/10.5194/acp-14-2713-2014).
- Unterstrasser, S. and Sölch, I. (2010). Study of contrail microphysics in the vortex phase with a Lagrangian particle tracking model. *Atmos. Chem. Phys.*, 10(20):10003–10015. DOI: [10.5194/acp-10-10003-2010](https://doi.org/10.5194/acp-10-10003-2010).
- van de Hulst, H. C. (1981). *Light scattering by small particles*. Dover. DOI: [10.1002/qj.49708436025](https://doi.org/10.1002/qj.49708436025).
- Vancassel, X., Mirabel, P., and Garnier, F. (2014). Numerical simulation of aerosols in an aircraft wake using a 3D LES solver and a detailed microphysical model. *Int. J. Sustainable Aviation*, 1(2):139–159. DOI: [10.1504/IJSA.2014.065480](https://doi.org/10.1504/IJSA.2014.065480).
- Verstraete, D. (2013). Long range transport aircraft using hydrogen fuel. *International Journal of Hydrogen Energy*, 38(34):14824–14831. DOI: [10.1016/j.ijhydene.2013.09.021](https://doi.org/10.1016/j.ijhydene.2013.09.021).
- Voigt, C., Kleine, J., Sauer, D., Moore, R. H., Bräuer, T., Le Clercq, P., Kaufmann, S., Scheibe, M., Jurkat-Witschas, T., Aigner, M., Bauder, U., Boose, Y., Borrmann, S., Crosbie, E., Diskin, G. S., DiGangi, J., Hahn, V., Heckl, C., Huber, F., Nowak, J. B., Rapp, M., Rauch, B., Robinson, C., Schripp, T., Shook, M., Winstead, E., Ziemba, L., Schlager, H., and Anderson, B. E. (2021). Cleaner burning aviation fuels can reduce contrail cloudiness. *Commun. Earth Environ.*, 2(1):114. DOI: [10.1038/s43247-021-00174-y](https://doi.org/10.1038/s43247-021-00174-y).
- Voigt, C., Schumann, U., Minikin, A., Abdelmonem, A., Afchine, A., Borrmann, S., Boettcher, M., Buchholz, B., Bugliaro, L., Costa, A., Curtius, J., Dollner, M., Dörnbrack, A., Dreiling, V., Ebert, V., Ehrlich, A., Fix, A., Forster, L., Frank, F., Fütterer, D., Giez, A., Graf, K., Grooß, J.-U., Groß, S., Heimerl, K., Heinold, B., Hüneke, T., Järvinen, E., Jurkat, T., Kaufmann, S., Kenntner, M., Klingebiel, M., Klimach, T., Kohl, R., Krämer, M., Krisna, T. C., Luebke, A., Mayer, B., Mertes, S., Molleker, S., Petzold, A., Pfeilsticker, K., Port, M., Rapp, M., Reutter, P., Rolf, C., Rose, D., Sauer, D., Schäfler, A., Schlage, R., Schnaiter, M., Schneider, J., Spelten, N., Spichtinger, P., Stock, P., Walser, A., Weigel,

- R., Weinzierl, B., Wendisch, M., Werner, F., Wernli, H., Wirth, M., Zahn, A., Ziereis, H., and Zöger, M. (2017). ML-CIRRUS: The Airborne Experiment on Natural Cirrus and Contrail Cirrus with the High-Altitude Long-Range Research Aircraft HALO. *Bull. Am. Meteorol. Soc.*, 98(2):271–288. DOI: [10.1175/BAMS-D-15-00213.1](https://doi.org/10.1175/BAMS-D-15-00213.1).
- VOLCAN (2023). 100 Prozent nachhaltiges Kerosin im Emissions-Check. <https://www.dlr.de/de/aktuelles/nachrichten/2023/01/100-prozent-nachhaltiges-kerosin-im-emissions-check>. accessed: 2024-07-25.
- Wang, Z., Bugliaro, L., Jurkat-Witschas, T., Heller, R., Burkhardt, U., Ziereis, H., Dekoutsidis, G., Wirth, M., Groß, S., Kirschler, S., Kaufmann, S., and Voigt, C. (2023). Observations of microphysical properties and radiative effects of a contrail cirrus outbreak over the North Atlantic. *Atmos. Chem. Phys.*, 23(3):1941–1961. DOI: [10.5194/acp-23-1941-2023](https://doi.org/10.5194/acp-23-1941-2023).
- Williams, J. (2008). A Fortran 2008 edition of LSQR, a conjugate-gradient type method for solving sparse linear equations and sparse least-squares problems. <https://github.com/jacobwilliams/LSQR/>. accessed: 2024-03-07.
- Wölk, J. and Strey, R. (2001). Homogeneous nucleation of h₂o and d₂o in comparison: The isotope effect. *The Journal of Physical Chemistry B*, 105(47):11683–11701. DOI: [10.1021/jp0115805](https://doi.org/10.1021/jp0115805).
- Wynanski, I. and Fiedler, H. (1969). Some measurements in the self-preserving jet. *J. Fluid Mech.*, 38(3):577–612. DOI: [10.1017/S0022112069000358](https://doi.org/10.1017/S0022112069000358).
- Xia, L. and Lam, K. (2009). Velocity and concentration measurements in initial region of submerged round jets in stagnant environment and in coflow. *J. Hydro-Environ. Res.*, 3(1):21–34. DOI: [10.1016/j.jher.2009.03.002](https://doi.org/10.1016/j.jher.2009.03.002).
- Yang, P., Liou, K., Wyser, K., and Mitchell, D. (2000). Parameterization of the scattering and absorption properties of individual ice crystals. *J. Geophys. Res.*, 105:4699–4718. DOI: [10.1029/1999JD900755](https://doi.org/10.1029/1999JD900755).
- Yoder, D., DeBonis, J., and Georgiadis, N. (2015). Modeling of turbulent free shear flows. *Computers and Fluids*, 117:212–232. DOI: [10.1016/j.compfluid.2015.05.009](https://doi.org/10.1016/j.compfluid.2015.05.009).
- Yu, F., Kärcher, B., and Anderson, B. E. (2024). Revisiting Contrail Ice Formation: Impact of Primary Soot Particle Sizes and Contribution of Volatile Particles. *Environ. Sci. Technol.*, 58(40):17650–17660. DOI: [10.1021/acs.est.4c04340](https://doi.org/10.1021/acs.est.4c04340).
- Yu, F. and Turco, R. P. (1997). The role of ions in the formation and evolution of particles in aircraft plumes. *Geophys. Res. Lett.*, 24(15):1927–1930. DOI: [10.1029/97GL01822](https://doi.org/10.1029/97GL01822).
- ZeroAvia (2017). The Clean Future of Flight. <https://zeroavia.com/>. accessed: 2022-06-20.
- Zink, J., Unterstrasser, S., and Jurkat-Witschas, T. (2025). On the Potential Role of Lubrication Oil Particles in Contrail Formation for Kerosene and Hydrogen Combustion. *J. Geophys. Res.*, 130(12). DOI: [10.1029/2025jd043487](https://doi.org/10.1029/2025jd043487).

Appendix

A1 Appendix of publication “Towards intermediate complexity modelling of contrail formation: the new dynamical framework RadMod”

The following text is published as the appendix of Lottermoser A. and Unterstrasser S. (2024). *Towards intermediate complexity modelling of contrail formation: the new dynamical framework RadMod*. *Aeronaut. J.*, 129(1332):351–379. DOI: [10.1017/aer.2024.130](https://doi.org/10.1017/aer.2024.130). Only small formatting changes were made to ensure consistency with the thesis.

Numerical Descriptions

Implicit finite-difference discretization and solution of linear system

We numerically solve the coordinate-transformed ADE of a general quantity c by applying a finite difference scheme. We specify our numerical grid in ψ and ϕ , where the ψ -values are calculated as described in Eq. 2.37, whereas the ϕ -values are determined via Eq. 2.32 using the diffusion coefficient (Eq. 2.12). We define $c_{i,j} := c(\phi_i, \psi_j)$, where the subscripts refer to the i 'th and j 'th element of the ϕ and ψ -grid, respectively. The initial conditions are given for $\phi = 0$, and the boundary conditions are prescribed at $\psi = 0$ and $\psi = \psi_{\max}$. The spatial grid has N_ψ grid cells, and the time integration is carried out up to a suitable end point $N_\phi \times \Delta\phi$.

All three ADEs are solved similarly. Even though ϕ (and x in the original formulation) should not be confused with physical time, the evolution progresses along the ϕ -axis. Therefore, we refer to the time index as i and the time step as $\Delta\phi$, following the convention in conventional finite difference approaches.

Applying a forward scheme for the inner and a backward scheme for the outer derivative results in

$$\frac{\partial c}{\partial \phi} = \frac{\partial}{\partial \psi} \left(\rho^2 r^2 U \frac{\partial c}{\partial \psi} \right) + f(\phi, \psi) \quad (\text{A1})$$

$$\frac{c_{i+1,j} - c_{i,j}}{\Delta\phi} = \frac{1}{\Delta\psi_{j-1}} \left(\rho_{i,j}^2 r_{i,j}^2 U_{i,j} \frac{c_{i+1,j+1} - c_{i+1,j}}{\Delta\psi_j} - \rho_{i,j-1}^2 r_{i,j-1}^2 U_{i,j-1} \frac{c_{i+1,j} - c_{i+1,j-1}}{\Delta\psi_{j-1}} \right) + f_{i,j}. \quad (\text{A2})$$

$f(\phi, \psi)$ represents the viscous heating term in the temperature ADE. In case $c = U$ or $c = m_{\text{WV}}$, $f(\phi, \psi) = 0$. Note that the momentum ADE is nonlinear in U , and a backward Euler would lead to a nonlinear set of equations. To overcome this, we use a mixed approach in Eq. A1, where U in the "prefactor" U is evaluated at the current time step i and c in the derivative term is evaluated at the next step $i + 1$. The index j in the grid increment $\Delta\psi_j$ signifies the usage of a non-equidistant numerical grid in the radial direction. The axial increment $\Delta\phi_i$ varies with the time step, and the turbulent diffusion coefficient is recalculated using Eq. 2.12.

Grouping the terms for i and $i + 1$ leads to a tridiagonal linear system of equations of the form $A \vec{c}_{i+1} = \vec{c}_i$. The quadratic matrix A has dimensions (N_ψ, N_ψ) .

To calculate $r_{i,j}$ in Eq. A1, the grid points in (ϕ, ψ) -space can be translated into positions in real radius space via Eq. 2.38:

$$r_{i,j}^2 = 2 \int_0^{\psi_j} \frac{1}{\rho(\phi, \psi') U(\phi, \psi')} d\psi' \quad (\text{A3})$$

$$= 2 \left(\sum_{j'=0}^{j-1} \int_{\psi_{j'}}^{\psi_{j'+1}} \frac{1}{\rho(\phi, \psi') U(\phi, \psi')} d\psi' \right). \quad (\text{A4})$$

The integral is numerically solved by a second-order quadrature scheme.

Based on our discretization, the main diagonal and the first off-diagonals in A are occupied. However, twice-forward or twice-backward schemes must be applied to the boundaries.

For the inner boundary $j = 0$, twice forward, and for the outer boundary $j = N_\psi - 1$, twice backward must be applied:

$$\begin{aligned} \frac{c_{i+1,0} - c_{i,0}}{\Delta\phi} &= \frac{1}{\Delta\psi_0} \left(\rho_{i,1}^2 r_{i,1}^2 U_{i,1} \frac{c_{i+1,2} - c_{i+1,1}}{\Delta\psi_1} - \rho_{i,0}^2 r_{i,0}^2 U_{i,0} \frac{c_{i+1,1} - c_{i+1,0}}{\Delta\psi_0} \right) \\ \frac{c_{i+1,N_\psi-1} - c_{i,N_\psi-1}}{\Delta\phi} &= \frac{1}{\Delta\psi_{N_\psi-2}} \left(\rho_{i,N_\psi-1}^2 r_{i,N_\psi-1}^2 U_{i,N_\psi-1} \frac{c_{i+1,N_\psi-1} - c_{i+1,N_\psi-2}}{\Delta\psi_{N_\psi-2}} - \right. \\ &\quad \left. \rho_{i,N_\psi-2}^2 r_{i,N_\psi-2}^2 U_{i,N_\psi-2} \frac{c_{i+1,N_\psi-2} - c_{i+1,N_\psi-3}}{\Delta\psi_{N_\psi-3}} \right). \end{aligned} \quad (\text{A5})$$

We start the grid indices with 0 and end with $N_\psi - 1$ in order to transfer it to Python code more easily.

Grouping all c_{i+1} -terms on one side and all c_i -terms on the other side of the equation results in a tridiagonal matrix system, where the diagonal and the off-diagonals are occupied.

The inner boundary condition is derived as follows. Since we calculate all quantities at the grid cell centers (and not at the boundaries), we have to define an inner fictitious point $\tilde{c}_0 = c_{-0.5}$. Thus, the system has temporarily $N_\psi + 1$ dimensions:

$$\begin{aligned} \frac{\partial c}{\partial\phi} &= \frac{\partial}{\partial\psi} \left(\rho^2 r^2 U \right) \frac{\partial c}{\partial\psi} + \rho^2 r^2 U \frac{\partial^2 c}{\partial\psi^2} \\ \frac{c_{i+1,0} - c_{i,0}}{\Delta\phi} &= \frac{1}{\Delta\psi_0^2} \left(\rho_{i,1}^2 r_{i,1}^2 U_{i,1} - \rho_{i,0}^2 r_{i,0}^2 U_{i,0} \right) (c_{i+1,1} - c_{i+1,0}) + \\ &\quad \frac{1}{\Delta\psi_{-0.5} \Delta\psi_0} \rho_{i,0}^2 r_{i,0}^2 U_{i,0} \left(\frac{8}{3} c_{i+1,-0.5} - 4 c_{i+1,0} + \frac{4}{3} c_{i+1,1} \right). \end{aligned} \quad (\text{A6})$$

The coefficients of the discretization of the second partial derivative were derived by developing the derivative around $j = 0$, where the distance to the inner grid edge ($r = 0$) $\Delta\psi_{-0.5}$ is equal to $\Delta\psi_0/2$.

As an inner boundary condition, we set $c_{i,-0.5}$ equal to $c_{i,0}$ to avoid a discontinuity at the center. As an outer boundary condition, it holds $c_{i,N_\psi-1} = 0$. That means, the last row and column in the matrix system vanish, and the system dimension reduces from $N_\psi + 1$ down to $N_\psi - 1$. Thus, the final matrix system is

$$\begin{pmatrix} \tilde{C}_0 & \tilde{D}_0 & 0 & 0 & 0 & 0 & 0 & 0 & 0 \\ B_1 & C_1 & D_1 & 0 & 0 & 0 & 0 & 0 & 0 \\ 0 & B_2 & C_2 & D_2 & 0 & 0 & 0 & 0 & 0 \\ \vdots & & & & & & & & \\ 0 & 0 & 0 & 0 & 0 & 0 & B_{N_\psi-3} & C_{N_\psi-3} & D_{N_\psi-3} \\ 0 & 0 & 0 & 0 & 0 & 0 & B_{N_\psi-2} & C_{N_\psi-2} & 0 \end{pmatrix} \begin{pmatrix} c_{i+1,0} \\ c_{i+1,1} \\ c_{i+1,2} \\ \vdots \\ c_{i+1,N_\psi-3} \\ c_{i+1,N_\psi-2} \end{pmatrix} = \begin{pmatrix} c_{i,0} \\ c_{i,1} \\ c_{i,2} \\ \vdots \\ c_{i,N_\psi-3} \\ c_{i,N_\psi-2} \end{pmatrix} \quad (\text{A7})$$

where the matrix coefficients \tilde{C}_0 and \tilde{D}_0 deserve special attention as they are calculated using Eq. A6, whereas the other coefficients are computed via Eq. A1. The matrix coefficients are dependent on x .

We maintain two different code versions. One code is written in Python, from which all plots in this study have been generated. On the other hand, the Fortran code will eventually be coupled to our microphysical code. In Python, the linear system is solved by a standard algorithm from the numpy library. In the Fortran version, we apply a simple preconditioner and use the LSQR algorithm, which is well-suited for large, sparse matrices (Paige and Saunders, 1982a,b; Williams, 2008).

Time-adaptivity of radial grid

The radial coordinate $r(\psi_j)$ appears in Eq. A1 and needs to be computed in each time step according to Eq. 2.38. It is inversely proportional to the axial velocity. As the centerline velocity decays with x ,

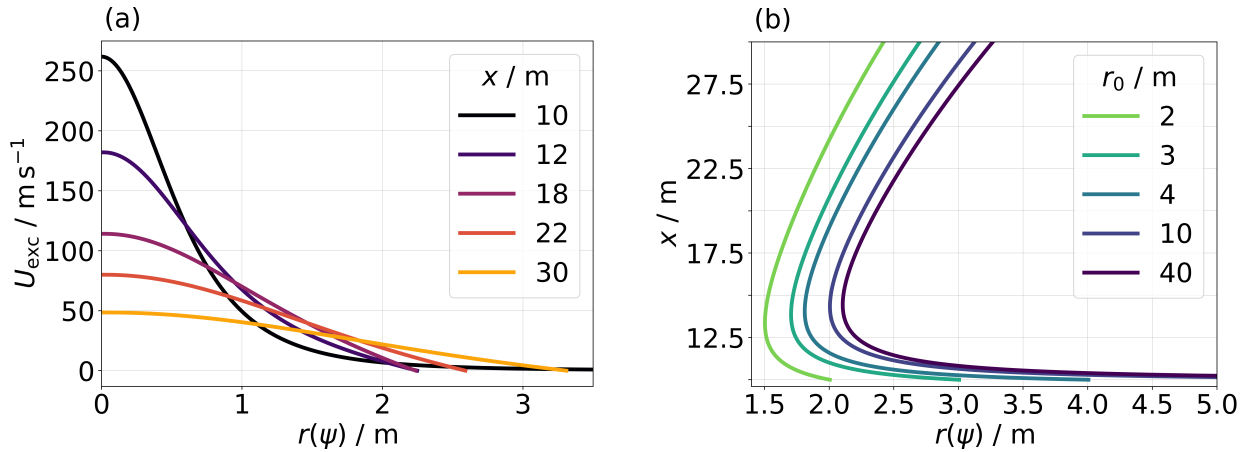


Figure A1: (a) Radial profiles of excess axial velocity at different downstream distances x as given in the legend. (b) Location of different grid boxes with fixed ψ values in (x, r) -space. The selected ψ -values correspond to specific radii at $x = 0$, as listed in the legend.

$r(\psi = \psi_{\text{const}})$ increases in the jet's core region. On the other hand, the axial velocity increases at the outer parts of the jet, i.e., $r(\psi = \psi_{\text{const}})$ decreases for large ψ_{const} values. Consequently, the radial grid ψ_j features an "inward movement" in terms of the real radius r . Fig. A1b shows the location of different grid boxes in (x, r) -space. The selected (time-constant) ψ -values corresponding to real radii r at $x = 0$ range from 2 m to 40 m. The grid box initialized at $r_0 = 40$ m (dark purple curve), e.g., moves inward and is located at $r \approx 2$ m at $\Delta x = 5$ m. Hence, the equidistant grid in ψ covers only a limited fraction of the real radius space shortly after initialization. This shortcoming becomes apparent in Fig. A1a, where the profiles break off at certain radial locations. To counteract this undesired numerical behavior, we introduce a re-mapping of the radial grid: At each time step, the deformed radial coordinate grid is reset to the original radial grid, and the radial profiles (i.e., axial velocity, temperature, and water vapor mixing ratio) are interpolated back onto the initial grid. By doing so, we keep $r(\psi)$ constant with respect to x .

Grid resolution analysis

Throughout the study, we use a logarithmic radial grid (in r -space) due to its computational efficiency, which provides accuracy comparable to that of a linear radial grid. We define fixed inner and outer boundaries, r_{min} and r_{max} , respectively, and specify the grid resolution using $1/n_{r,\text{dec}}$.

Fig. A2 shows radial profiles of axial velocity and water relative humidity for different values of $n_{r,\text{dec}}$. The analytical axial velocity profiles are included as a benchmark. For the smallest value $n_{r,\text{dec}} = 10$, the analytical and numerical profiles for U_{exc} disagree. Moreover, the relative humidity profile is not sufficiently smooth. Whereas the RH_{wat} -profiles appear to be smooth enough for $n_{r,\text{dec}} = 50$, the U_{exc} -profiles still show slight discrepancies. We observe a perfect agreement for $n_{r,\text{dec}} = 200$. Therefore, all our simulations presented in the main body of the paper have been conducted with a default value of $n_{r,\text{dec}} \geq 200$.

Examination of flow rates

As part of our model validation, we evaluate the axial dependency of the various flow rates of a cold and hot jet as described in Sec. 2.2.1.1. This analysis encompasses free and coflowing jets with varying coflow velocities. We demonstrate that our model conserves, as desired, the flow rates of both momentum and tracer excess concentration along the axial direction.

As an example, the flow rates of a coflowing jet with $U_{\infty} = 250 \text{ m s}^{-1}$ are shown in Fig. A3. In Fig. A3a, the conservation of both quantities is confirmed for both a cold and a hot jet.

Fig. A3b shows the thermal, kinetic, and total energy flow rates of a hot jet with variable density (hot jet with $T_E = 549 \text{ K}$). At the jet's origin, the energy partitioning is 90%/10% (thermal/kinetic) as prescribed. With increasing axial distance, kinetic energy is continuously converted into thermal energy via viscous

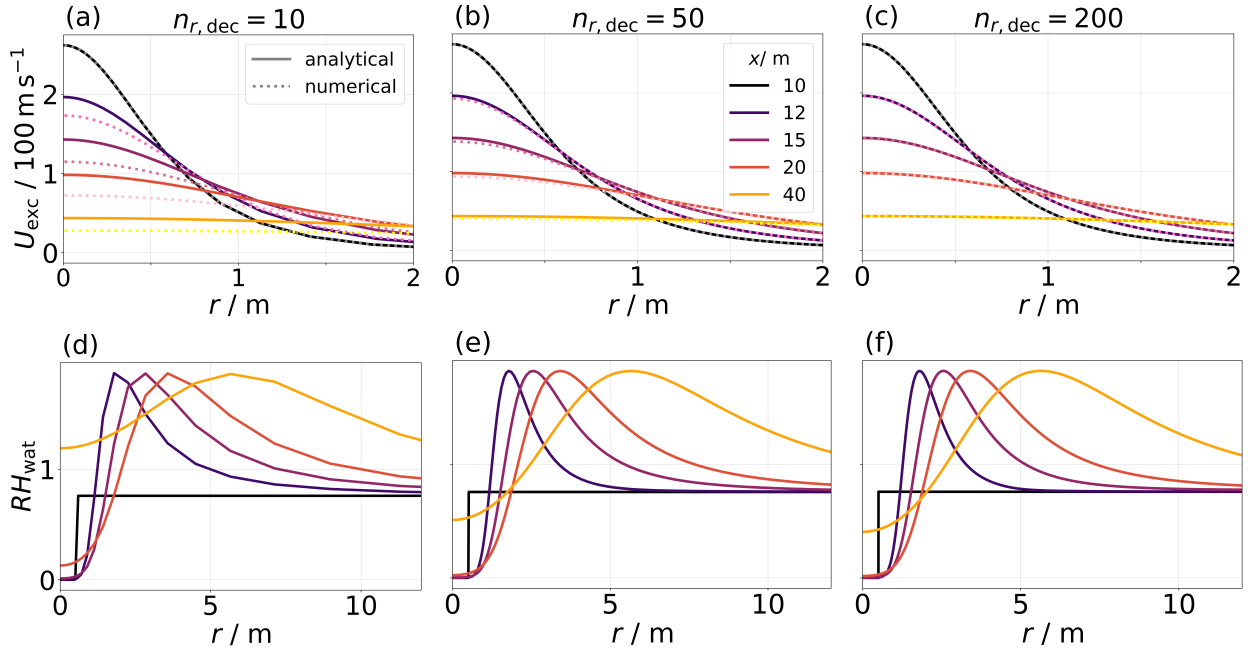


Figure A2: Radial profiles of axial velocity (panels (a) to (c)) and plume relative humidity with respect to water (panels (d) to (f)) at different axial distances to the jet nozzle (see legend in panel (b)). Results with three different grid resolutions are shown.

heating. The result is a decay of the kinetic energy towards zero at the desired rate ($\dot{E}_{\text{kin}}(x) \propto x^{-1}$), while the thermal energy increases. The conservation of the total energy flow rate is correctly represented in our model despite the complex coordinate transformation and time-adaptivity of the numerical grid.

The continuous entrainment of ambient air into the plume causes the mass flow rate to grow with increasing distance from the jet origin (Pope, 2000; Ball et al., 2012). The data of Ricou and Spalding (1961) is linearly fitted by $\dot{m}/m_0 = 0.32 \frac{x-x_0}{d}$ with an entrainment rate of 0.32. This value was confirmed by Panchapakesan and Lumley (1993a). Measurements by Sforza and Mons (1978) yielded a value of 0.28, whereas Khorsandi et al. (2013) reported a value slightly higher (0.36). We simulated a hot, free jet with density ratios as described in Sec. 2.2.2.2.2. By applying the density scaling $\rho_\infty/\rho_{J,0}$, as also done in the previously mentioned studies, our data lie on a single line as shown in Fig. A4. When considering the region $10 < x/d < 100$, we find an entrainment rate of 0.38 and a normalized virtual origin of -19.74 . When forcing the virtual origin to zero, we obtain an entrainment rate of 0.44. Our model confirms the linear increase with x and yields a plausible value for the entrainment rate.

A2 Appendix of publication “High-resolution modeling of early contrail evolution from hydrogen-powered aircraft”

The following text is published as the appendix of Lottermoser A. and Unterstrasser S. (2025). *High-resolution modeling of early contrail evolution from hydrogen-powered aircraft*. *Atmos. Chem. Phys.*, 25:7903–7924. DOI: [10.5194/acp-25-7903-2025](https://doi.org/10.5194/acp-25-7903-2025). Only minor formatting adjustments were made.

Definition of the ice crystal concentration n_0 in the new parameterization

As described in Sec. 3.2.2.3, the adaptation factor Ψ accounting for the mean ice crystal size (in the original formulation given by $1/EI_{\text{iceno}}^*$) is now defined differently. In the new formulation, Ψ is expressed as $\Psi = 1/n_0^*$, where n_0 represents an (intermediate) ice crystal number concentration:

$$n_0 = N_0/A_p, \quad (\text{A8})$$

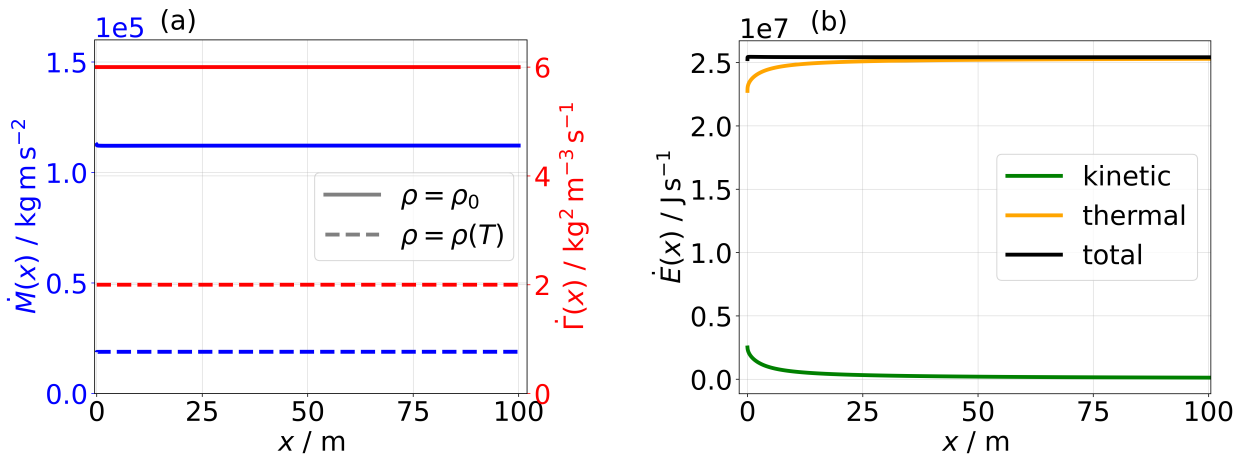


Figure A3: (a) Momentum and tracer excess concentration flow rates, which are constant over the entire axial range within 0.6 % (momentum flow rate) and 1.0 % (tracer concentration flow rate). This holds for both a constant and a variable density jet. (b) Thermal, kinetic, and total energy flow rates.

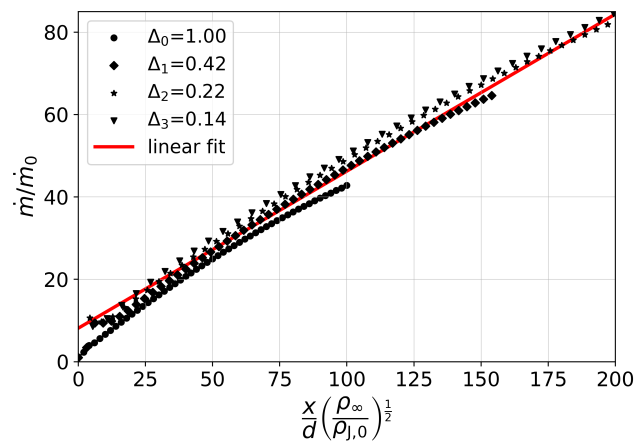


Figure A4: Mass flow rate of hot jets with different density ratios Δ normalized by the initial mass flow rate as a function of density-scaled downstream distance. The red fitted line has a slope of 0.38 with a normalized virtual origin of -19.74 .

where N_0 is the initial ice crystal number (per meter of flight path), and A_p is the intermediate plume cross-sectional area. Hence, n_0 represents an average concentration in the primary wake. We recall $N_0 = m_C \times EI_{\text{iceno}}$ (see Eq. 3.9) and the empirical relationships for conventional aircraft designs of different sizes as studied in [Unterstrasser and Görsch \(2014\)](#) and derived in [Unterstrasser \(2016, hereafter U2016\)](#): $m_C \sim b_{\text{span}}^2$ (Eq. A9 in U2016) and $A_p \sim b_{\text{span}}^2$ (Eqs. A6 and A7 in U2016), where b_{span} is the wingspan of the aircraft. Hence, n_0 is roughly independent of aircraft type, but it depends linearly on EI_{iceno} . Note that the empirical relation for A_p is derived from the simulation results and is not supposed to be adapted. The actual fuel consumption m_C may, however, deviate from the empirical relationship representing typical kerosene fuels and should serve as input to the parameterization.

The parameterization was trained such that the kerosene A350 simulations serve as reference cases for determining $n_{0,\text{ref}}$ and $n_0^* = n_0/n_{0,\text{ref}}$ (with $N_{0,\text{ref}} = 3.38 \times 10^{12} \text{ m}^{-1}$ and $b_{\text{span},\text{ref}} = 60.3 \text{ m}$). Note that, in particular, the m_C values of our A350 setups deviate from the empirical relationship (see Fig. A1c in U2016); hence, switching to a smaller A320 aircraft gives a smaller n_0 value ($1.29 \times 10^9 \text{ m}^{-3}$ (A350) versus $8.93 \times 10^8 \text{ m}^{-3}$ (A320)), leading to $n_0^* = 0.69$.

Differences between the original and new parameterization implementation

This section summarizes the differences between the original parameterization provided in [Unterstrasser \(2016\)](#) and the new one presented in Sec. 3.2.2.3. The overall design of the parameterization has not changed, and the cookbook of individual computations, as listed in Sec. A6 of U2016, received only minor changes, which are as follows:

- In step 2, the formula for computing the plume area is now $A_p = 2 \times \pi r_p^2$; this replaces Eq. A7 of U2016, which was given by $A_p = 4 \times \pi r_p^2$.
- In step 3, z_{atm} and z_{emit} are redefined using the adiabatic index κ (as given in Eqs. 3.15 and 3.16). Moreover, the bisection method for solving the nonlinear equation can be replaced by analytically defined fit functions provided in the subsequent subsection.
- In steps 3 and 4, new values for the fitting coefficients are used as given in Eqs. 3.22a–3.22g. Moreover, the adaptation factor Ψ uses a new definition, as given in the previous subsection.

The supplement contains Fortran and Python implementations of the new and the original parameterization.

Analytical fit functions of z_{atm} and z_{emit}

To compute the length scales z_{atm} and z_{emit} (Eqs. 3.15 and 3.16), we have, thus far, employed the numerical bisection method. Here, we present an alternative approach that directly calculates these length scales based on input data for temperature, ambient supersaturation, and water vapor concentration. The corresponding formulae are as follows:

$$\tilde{z}_{\text{atm}} = 607.46 \text{ m} \times s_i^{0.897} \times \left(\frac{T_{\text{CA}}}{205 \text{ K}} \right)^{2.225} \quad (\text{A9})$$

and

$$\begin{aligned} \tilde{z}_{\text{emit}} = & 1106.6 \text{ m} \times \left(\frac{\rho_{\text{emit}}}{10 \text{ mg/m}^3} \right)^{0.678+0.0116 T_{205}} \\ & \times \exp((-0.0807 + 0.000428 T_{205}) T_{205}) \end{aligned} \quad (\text{A10})$$

with $T_{205} = T_{\text{CA}}/\text{K} - 205$.

The resulting length scales show only slight deviations from those derived using the bisection method, with a maximum deviation of 3 m for z_{atm} and 7 m for z_{emit} . Applying the analytical relations to calculate the parameterized survival fraction, we observe no change in 44 % of the data (when rounded to two digits, as done in Tab. A1) and a maximum deviation of 2 %. A detailed comparison is provided in Tab. A2. Section A3 contains further plots that demonstrate the suitability of the fit functions.

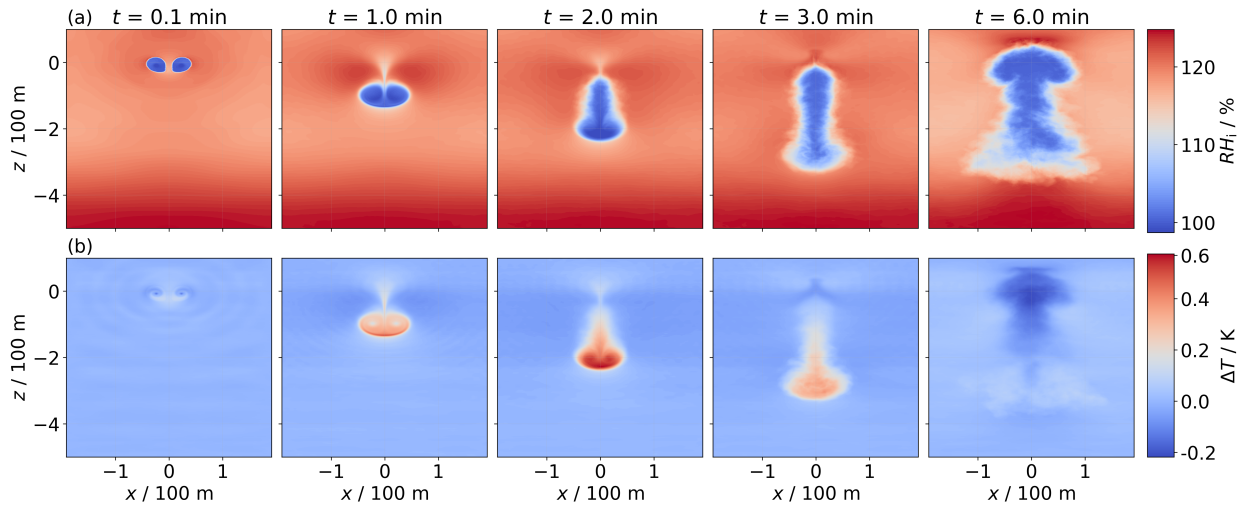


Figure A5: (a) Temporal evolution of relative humidity with respect to ice and (b) temperature difference in the (x, z) -plane (averaged along flight direction). In (b), the vertical background temperature profile is subtracted to highlight the temperature evolution, particularly within the primary wake. Note that the first column corresponds to 0.1 min, whereas the zeroth time step is shown in the main body of the manuscript. This distinction is made because the thermodynamic fields exhibit almost no visible features at the initial time step. The depicted exemplary simulation is performed for an A350/B777-like aircraft at $T_{CA} = 217$ K, $RH_{i,amb} = 120\%$, $N_{BV} = 1.15 \times 10^{-2} \text{ s}^{-1}$, $N_0 = 3.38 \times 10^{12} \text{ m}^{-1}$, $I_0 = 15.0 \text{ g m}^{-1}$, and $r_{SD} = 3.0$.

A3 Supplement of publication “High-resolution modeling of early contrail evolution from hydrogen-powered aircraft”

The following text is published as the supplement of Lottermoser A. and Unterstrasser S. (2025). *High-resolution modeling of early contrail evolution from hydrogen-powered aircraft. Atmos. Chem. Phys.*, 25:7903–7924. DOI: [10.5194/acp-25-7903-2025](https://doi.org/10.5194/acp-25-7903-2025). Only small modifications regarding the formatting were made.

Temporal and spatial evolution of temperature and humidity during the vortex phase

Figure A5 illustrates the evolution of ice relative humidity (a) and temperature difference (b), where the background temperature profile has been subtracted. Within the wake vortices, the ice relative humidity remains close to saturation until the vortices dissipate. This phenomenon results from the sublimation of ice crystals trapped in the primary wake. The sublimation increases the local water vapor concentration, balancing the decrease in RH_i caused by adiabatic heating. Note that humidity values below 100% may occur as the sublimation does not instantaneously relax the humidity field to saturation. In the secondary wake, RH_i also remains near saturation as detrained ice crystals deplete ambient moisture, reducing the environmental supersaturation toward saturation. The presented humidity fields are quite smooth, as they are averages along the flight direction.

Initially, the temperature perturbation is nearly everywhere close to zero. The centers of the wake vortices feature a pressure drop to compensate for centrifugal forces and can lead to a very localized temperature drop. Due to the prescribed stable stratification, air masses at the original flight altitude have a higher potential temperature than air masses beneath. Hence, the descending primary wake is identified by positive ΔT values. A similar consideration explains the negative ΔT values after 6 min around $z = 0$ m. Air masses from the primary wake rise back to the initial altitude and push or contain also air masses from lower altitudes (with lower potential temperature) to $z = 0$ m leading to $\Delta T < 0$ K.

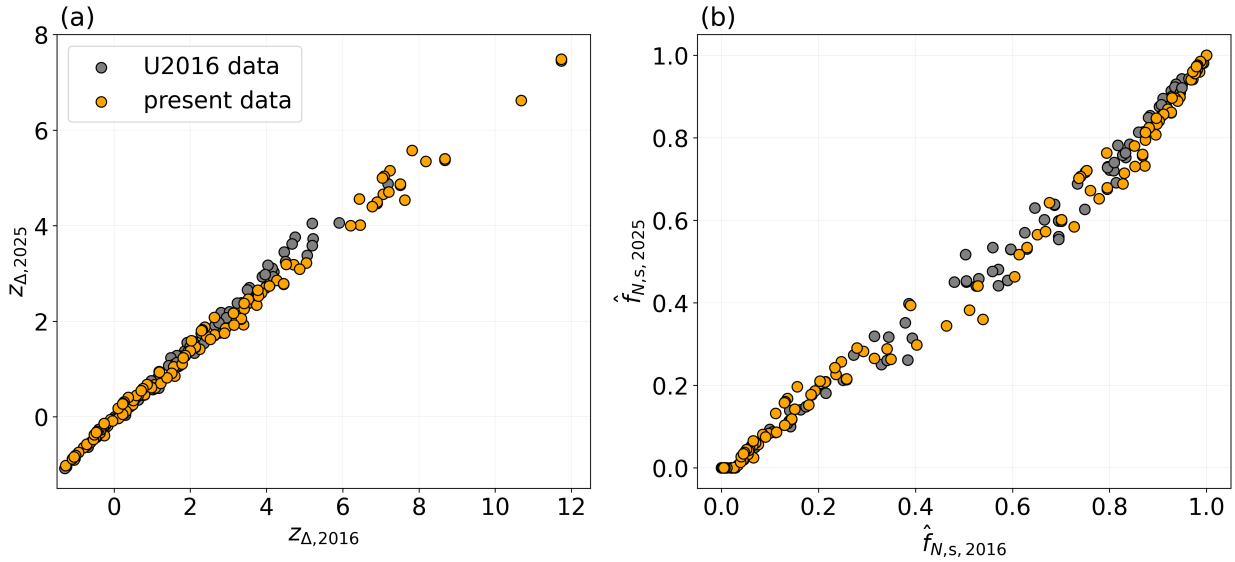


Figure A6: (a) Scatter plot comparing the 2016 z_{Δ} values with the z_{Δ} values from the present study, and (b) a similar comparison for the parameterized survival fractions.

Further information on ice crystal loss parameterization

Evaluation of z_{atm} and z_{emit}

In the ice crystal loss parameterization, the two length scales z_{atm} and z_{emit} are implicitly defined. In the original version in U2016, the nonlinear equations were solved using a numerical method (classical bisection method). To speed up evaluations and to provide explicit formulations, fit formulae for the two length scales z_{atm} and z_{emit} were derived as outlined in Sec. A3 of this study. In order to compare both versions simulation-wise, the length scale values determined with the bisection method and the fit formulae are compared. Moreover, the corresponding survival fractions based on either evaluation method are calculated. The outcomes are provided in Tab. A2. As noted in the main text, applying the analytical relations to compute the parameterized survival fraction yields no change for 44% of the data points (rounded to two decimal places, as in Tab. A1), and the maximum deviation observed is 2%.

Comparison of the original and new ice crystal loss parameterization

The original ice crystal loss parameterization proposed in U2016 has been implemented in several larger-scale contrail models to refine the contrail initialization in those models (Gruber et al., 2018; Bier and Burkhardt, 2022), and applications were restricted to conventional kerosene contrails.

This section presents comparison plots between the original and updated versions of the ice crystal loss parameterization. Figure A6 shows scatter plots of z_{Δ} (panel (a)) and the parameterized survival fraction $\hat{f}_{N,s}$ (panel (b)), with the x-axis representing the original (2016) values and the y-axis showing the updated (2025) data. The values of z_{Δ} are similar across both formulations, although $z_{\Delta, 2025}$ is generally slightly lower. However, differences in z_{Δ} should not be over-interpreted as this quantity serves as argument in an arctan-type function (see Eq. 3.21) to retrieve the survival fraction. The arctan-type function formulation includes three fit coefficients that change from one version to the other version. Hence, panel (b) shows the eventual differences in the parameterized survival fraction from the two versions. Likewise, $\hat{f}_{N,s}$ exhibits only minor scatter between the two versions.

Furthermore, we reproduce plots that were shown in U2016 (Figs. 5, 9, and 10 in that publication). In the new versions of those plots (Figs. A7–A9 in this document), we juxtapose the outcome of the original and the new parameterization. This should demonstrate that the switch to the new formulation has only marginal implications on applications focusing on conventional kerosene contrails.

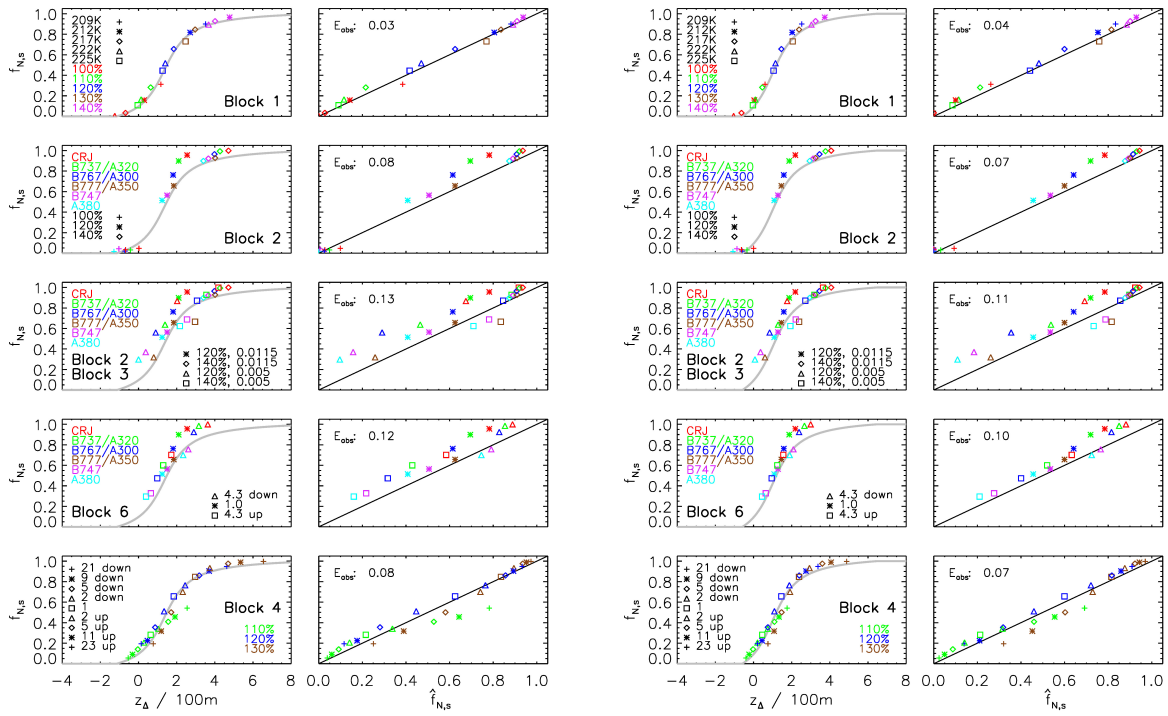


Figure A7: Reproduced version of Fig. 5 in U2016. The first two columns show the original plot from U2016. The third and fourth columns use the parameterized survival fractions as obtained from the new parameterization version described in the present study.

Adapted figure caption of U2016:

Columns 1 and 3: Relationship between simulated survival fraction $f_{N,s}$ and z_{Δ} . The grey curve shows the fit function $\hat{a}(z_{\Delta})$ as defined in Eq. 3.21 in the present study.

Columns 2 and 4: Relationship between simulated survival fraction $f_{N,s}$ and approximated survival fraction $\hat{f}_{N,s}$. The black line shows the one-to-one line. Each row shows a subset of simulations taken from various simulation blocks defined in Table A2 of U2016. For example, the first row shows simulations of block 1, where RH_i and T_{CA} are varied. The legend in the plot provides a list of the symbols and colors, which uniquely define the simulation parameters of each plotted data point. The root mean square of the absolute error $\hat{f}_{N,s} - f_{N,s}$ is denoted as E_{abs} and given for each subset.

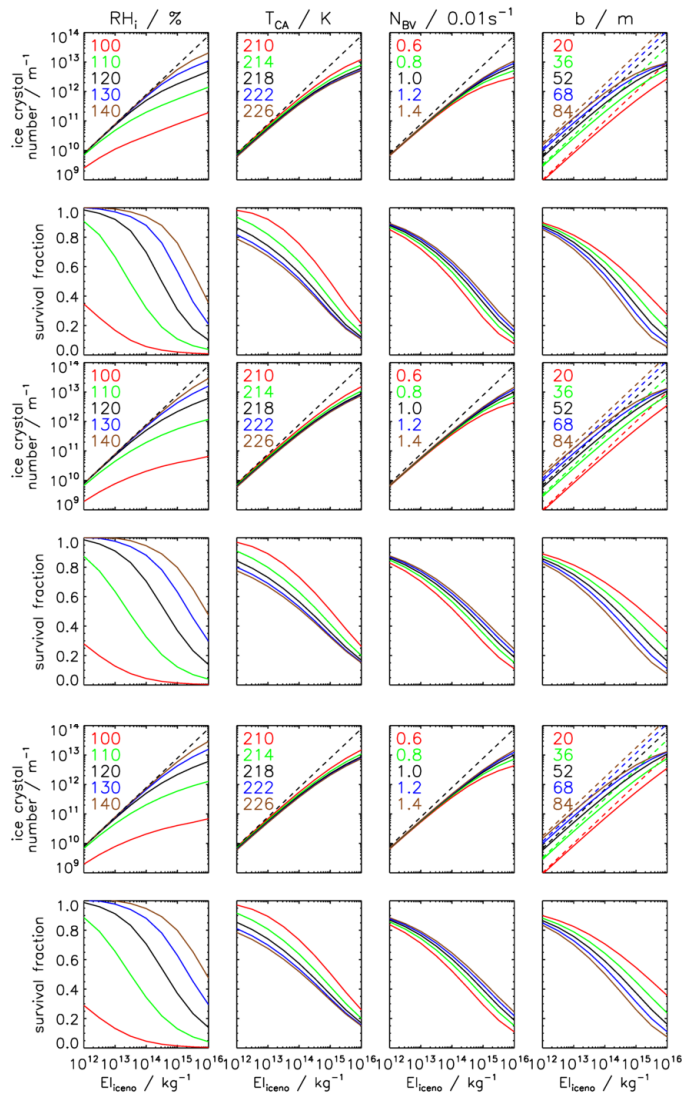


Figure A8: Reproduced version of Fig. 9 in U2016. The first two rows show the original plot from U2016. The other rows use the parameterized survival fractions as obtained from the new parameterization version described in the present study, evaluating z_{atm} and z_{emit} either via bisection (rows 3 and 4) or by employing the fit functions (rows 5 and 6).

Adapted figure caption of U2016:

Sensitivity of ice crystal loss to EI_{icenso} for various values of RH_i , T , N_{BV} , and b (from left to right). b is the aircraft's wingspan (denoted by b_{span} in Sec. 3.2). See legend for the color coding. Rows 1, 3, and 5: Ice crystal number per meter of flight path before and after the vortex phase (dashed and solid curves). Note that the initial ice crystal number depends only on b and EI_{icenso} (following Eq. A10 in U2016, which assumes a water vapor emission index of 1.25 kg kg^{-1}). Hence, only one dashed curve is shown in the columns for RH_i , T , and N_{BV} , respectively. Rows 2, 4, and 6: survival fraction.

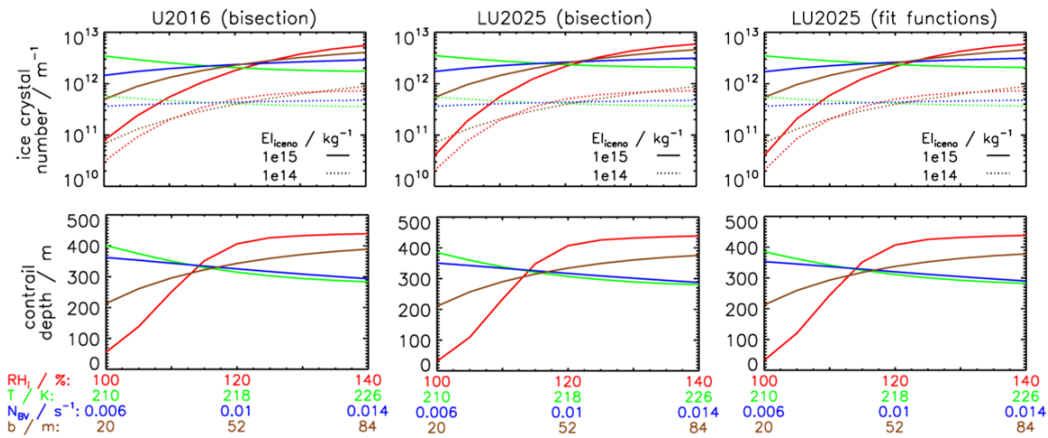


Figure A9: Reproduced version of Fig. 10 in U2016. The first column shows the original plot from U2016. The two other columns use the new parameterization version (for both types of z_{atm} and z_{emit}).

Adapted figure caption of U2016:

Ice crystal number per meter of flight path (top) and contrail depth (bottom) after the vortex phase as a function of RH_i , T , N_{BV} , or b . EI_{iceno} is 10^{15} or 10^{14} kg^{-1} . The contrail depth parameterization does not depend on EI_{iceno} . Note that the parameterization of the contrail depth H was not updated in the present study. The slightly different results come from the fact that the parameterization of H uses the parameterized $f_{N,s}$ value as input. Note that the original plot in U2016 showed an additional panel with ice crystal number concentrations, which is left out here.

Sensitivity analyses: Numerical and physical aspects

In the following, three sensitivity studies are presented. We compare the results of a reference simulation, performed for an A350/B777-like aircraft at $T_{CA} = 217 \text{ K}$, $RH_{i,amb} = 120 \%$, $N_{BV} = 1.15 \times 10^{-2} \text{ s}^{-1}$, $N_0 = 3.38 \times 10^{12} \text{ m}^{-1}$, $I_0 = 15.0 \text{ g m}^{-1}$, and $r_{SD} = 3.0$ (solid black lines in Fig. A10). These are compared to simulations in which the grid resolution, domain size, and ambient pressure are varied individually.

Impact of grid resolution

In the reference setup, we employ a horizontal and vertical grid spacing of 1 m. To assess the sensitivity of contrail evolution to mesh resolution, we conduct an additional simulation using a finer resolution of 0.5 m. As shown by the magenta curves in Fig. A10, the higher-resolution simulation results in a relative increase of 7.7 % in total ice mass and a reduction in ice crystal survival fraction from 64.7 % to 62.1 %. Vertical profiles of ice crystal number and mass (not shown) indicate that, in the high-resolution setup, fewer ice crystals are detrained from the vortex system. Instead, a larger fraction remains trapped within the primary wake, where they are more prone to sublimation due to adiabatic heating. The reduced detrainment can be attributed to the way secondary vorticity, generated by baroclinic torque arising from density and pressure gradients between the wake and the ambient air (Holzäpfel et al., 2001), develops in the simulation. Although the underlying physical conditions, such as pressure and density gradients, remain unchanged, the finer grid spacing enables a more accurate resolution of these instabilities, potentially altering the dynamics of vortex destabilization. We hypothesize that the improved representation of secondary vorticity results in less disruption of the vortex cores, thereby reducing ice crystal detrainment and increasing sublimation within the primary wake. Alongside this physical explanation of the observed results, we note that background turbulence could likewise influence the detrainment process and contribute to the observed behavior. While the resulting discrepancies in ice crystal number and mass are moderate compared to those induced by variations in the initial ice crystal number, they underscore the relevance of mesh resolution and its potential impact on

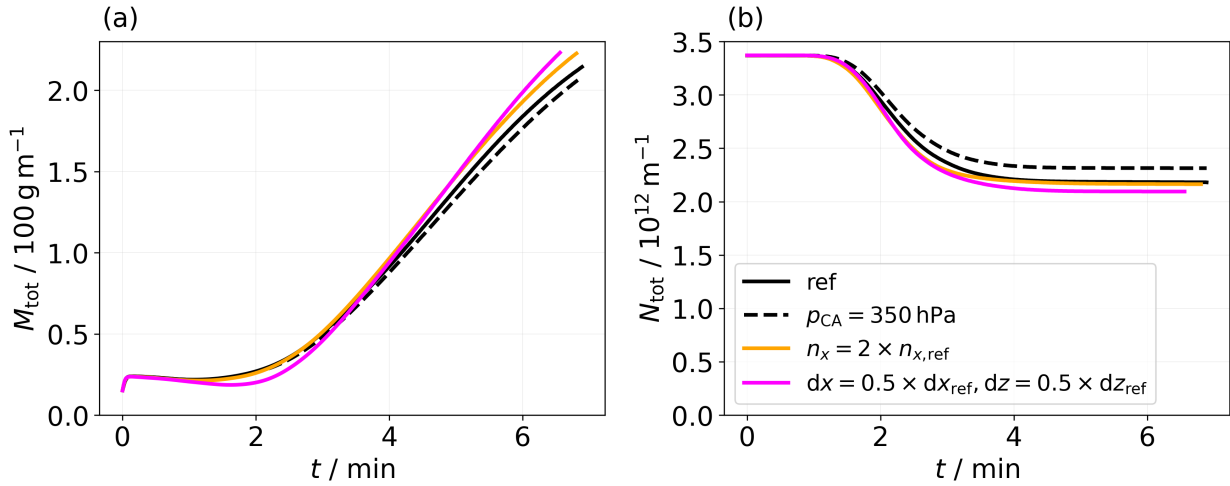


Figure A10: (a) Evolution of total ice crystal number and (b) total ice mass for the reference case and three sensitivity simulations, differentiated by color and line style. The dashed black curves represent a simulation conducted at a higher ambient pressure value. The orange curves correspond to a simulation with doubled domain width. The magenta curves show the results from a simulation with a higher mesh resolution in transverse and vertical direction.

simulation outcomes. However, in the context of a sensitivity study focused on variations in initial ice crystal number, where ice crystal survival fractions span the full range from 0 to 100%, we consider deviations in ice crystal survival fraction below 3% to be minor. Given the substantial computational demands of finer mesh resolutions (roughly eight times higher CPU time) and considering the comparatively minor differences in simulation outcomes, we consider the baseline resolution appropriate for the objectives of this study.

Impact of domain size

The default domain size in the transverse direction is 384 grid boxes, corresponding to 384 m in our reference A350/B777 simulation with a grid spacing of $dx = 1 \text{ m}$. In a sensitivity simulation, we increase the domain width from 384 m to 768 m; the results are shown as orange curves in Fig. A10. This modification yields a slight reduction in final ice crystal survival fraction from 64.7% to 64.2% and a relative increase of 4.6% in final ice mass. A plausible explanation is that, in the narrower domain, the descending vortex pairs might interact across the transverse boundaries, damping their descent and thereby enhancing ice crystal survival. Horizontal profiles reveal that, from about 2 min onward, the wider-domain simulation exhibits slightly lower ice crystal number and mass near the outer edges of the vortices, while more ice crystals and ice mass are found in the vortex centers. This supports the hypothesis that transverse interactions across the boundaries in the narrow domain might influence vortex dynamics and particle motion. However, it is equally plausible that the minor deviations in the evolution of ice crystal number and mass reflect variability introduced by background turbulence, as discussed in the previous section. As the wider domain has a negligible effect on the contrail properties, most notably the ice crystal survival fraction, yet significantly increases computational expense, a transverse width of 384 grid boxes is deemed sufficient for our simulations.

Impact of pressure variation

A variation of the ambient pressure value has only minor impact on the evolution of ice crystal mass and number, see black dashed curves in Fig. A10. The pressure at flight altitude of the reference simulation is 231 hPa. We increase the pressure to 350 hPa, keeping all other setup parameters (specifically ambient temperature) unchanged. We observe a slightly reduced final ice mass and a slightly increased number of surviving ice crystals in the higher-pressure case. These differences can be primarily attributed to the pressure dependence of water vapor diffusivity, which appears in the governing equation for ice mass

growth (Sölch and Kärcher, 2010). Since diffusivity is inversely proportional to pressure, higher ambient pressure leads to lower diffusivity, thereby reducing the rate of ice crystal growth. Conversely, sublimation is also reduced under higher pressure for the same reason, leading to a slightly higher survival fraction. An additional, though secondary, factor is the pressure dependence of sedimentation velocity. Increased pressure results in a small reduction in sedimentation velocity. However, for a pressure increase of 120 hPa, the resulting change in sedimentation velocity is on the order of 0.5 %, and is thus considered negligible in this context. Overall, the sensitivity of contrail evolution to ambient pressure variations is weak. The final ice crystal survival fraction changes from 64.7 % to 68.7 %, and the total ice mass differs relatively by 4.0 %. This limited sensitivity is expected: The amount of available atmospheric water vapor, expressed in terms of water vapor concentration $\rho_{\text{WV,avail}} = (RH_{i,\text{amb}} - 1) \times \rho_{\text{WV,sat,ice}} = (RH_{i,\text{amb}} - 1) \times \frac{e_s(T)}{R_{\text{WV}} T}$, is primarily temperature-dependent and independent of ambient pressure. Moreover, the adiabatic heating in the descending vortex pair does not depend on ambient pressure.

A4 Appendix of manuscript “Modeling the impact of alternative fuels and hydrogen propulsion on contrail-cirrus: a parameter study”

The following text is the appendix of the manuscript *Lottermoser A. and Unterstrasser S. Modeling the impact of alternative fuels and hydrogen propulsion on contrail-cirrus: a parameter study*, which is under revision for *Journal of Geophysical Research: Atmospheres*.

Initial contrail-cirrus properties

Table A3 provides an overview of the vortex phase simulations presented in Lottermoser and Unterstrasser (2025), which serve as initial conditions for the contrail-cirrus simulations of the present study.

Derivation of α in extinction scaling

We consider two ice crystal populations: one with $N_{p,1}$ identical ice crystals of mass m_1 and size D_1 , and the other with $N_{p,2}$ identical ice crystals of mass m_2 and size D_2 . Assuming a fixed total ice mass, i.e., $M_{\text{tot},1} = M_{\text{tot},2}$, it follows that $N_{p,1} m_1 = N_{p,2} m_2$. From this, we obtain

$$\gamma = \frac{N_{p,2}}{N_{p,1}} = \frac{m_1}{m_2}. \quad (\text{A11})$$

Given the area-size and mass-size relationships in Sec. 4.2.2.2, it holds

$$A_2 = N_{p,2} D_2^\sigma \quad (\text{A12})$$

$$= N_{p,2} \left(\left(\frac{1}{\gamma} m_1 \right)^{1/\beta} \right)^\sigma \quad (\text{A13})$$

$$= \gamma N_{p,1} \gamma^{-\sigma/\beta} m_1^{\sigma/\beta} \quad (\text{A14})$$

$$= \left(\frac{N_{p,2}}{N_{p,1}} \right)^{1-\sigma/\beta} A_1, \quad (\text{A15})$$

which is equivalent to Eq. 4.10. It follows that $\alpha = 1 - \frac{\sigma}{\beta}$.

A5 Impact of wake vortex and plume initialization on contrail evolution

During my PhD, I supervised the Bachelor’s thesis of Benedikt Rabe and the DAAD internship of Adam Schroeder. Both projects involved vortex phase simulations of young contrails, focusing on the impact of the wake vortex initialization method and the initial spatial distribution of the plumes. The first subsection

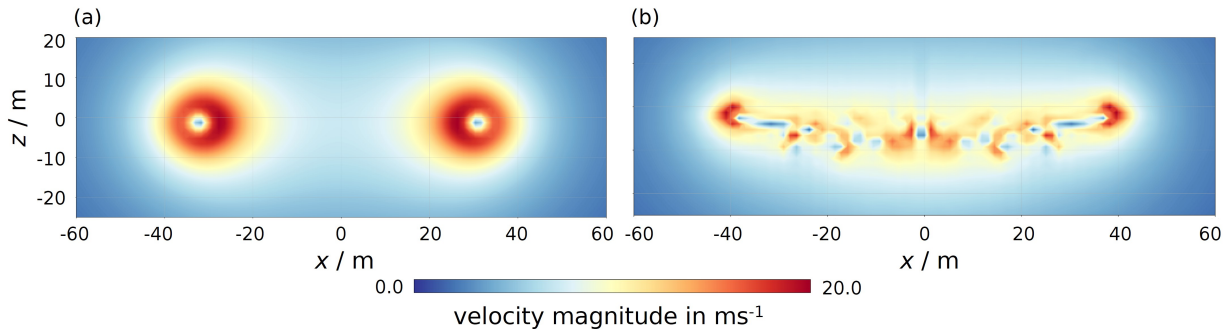


Figure A11: (a) Initial velocity magnitude as 2D data slice for an analytical Lamb-Oseen vortex representation and (b) for a RANS-based initialization for an A380 at downstream position $X = 10$ m. Figure adapted from Rabe (2024).

provides a brief summary of the key findings from Benedikt's study, titled "Parametric study of high-resolution simulations of contrails during the vortex phase with emphasis on initial conditions" (Rabe, 2024). After receiving the necessary tools and computational resources, Benedikt conducted the simulations, and the analysis was carried out in collaboration.

The second subsection presents part of Adam's work, which investigates the influence of a plume number variation.

RANS-based versus analytical wake vortex initialization

The analyses presented in this subsection are included in Benedikt's Bachelor's thesis Rabe (2024), and parts of this work have been published in Pauen et al. (2024). Up to the time when this project was conducted, the initialization of the wake vortex flow field behind an aircraft was done by using the analytical model of two counter-rotating Lamb-Oseen vortices (Saffman, 1993). As part of the DLR-Airbus collaboration, we received flow fields downstream of an A380 aircraft from a-priori CFD simulations based on the RANS equations. For an A320 aircraft, flow field data from the model TAU-MGLET, which comprises the RANS code TAU (Schwamborn et al., 2006) coupled to the LES model MGLET (Manhart, 2004), are available. By accounting for the actual aircraft geometry, these RANS-based flow fields provide a more sophisticated and realistic initialization of the wake vortex field. The input fields to EULAG-LCM are 2D slices perpendicular to the flight direction. In both the A320 and A380 case, two different downstream positions behind the aircraft's tail are provided, which are denoted by X , following the notation in Rabe (2024). In addition to the vortex initialization variation, Benedikt performed simulations with a 100-fold increase in the number of initial ice crystals and increased water vapor emission, corresponding to the values used in Lottermoser and Unterstrasser (2025), to study the impact of a potential hydrogen fuel cell system as propulsion technology. He also examined a variation of the plume position and conducted simulations with an inward-shifted initial position of the engines. As not otherwise stated, the simulations presented in this section were performed at $T_{\text{amb}} = 217$ K and $N_{\text{BV}} = 1.15 \times 10^{-2} \text{ s}^{-1}$.

Figure A11 illustrates the two different initialization methods, in the following simply called "analytical" and "RANS", referring to the velocity field initialization in EULAG. The RANS-based approach (panel (b)) resolves the full aircraft geometry.

As shown in detail by Rabe (2024), the method used to initialize the flow field has a lasting impact on the ice crystal evolution. Figure A12 displays the first minute of ice crystal number evolution in the RANS case for the A320, $X = 90$ m scenario. In addition to the development of the well-known primary and secondary wake structures in the analytical case, new features emerge. Ice crystals are entrained into a turbulent structure related to a secondary vortex pair near the aircraft center, in addition to the wingtip vortices. This structure transports the ice crystals vertically upward as early as 20 s after emission. In contrast, the secondary wake in the analytical case becomes apparent only after 1 to 2 min, as shown in the first row of Fig. 3.2.

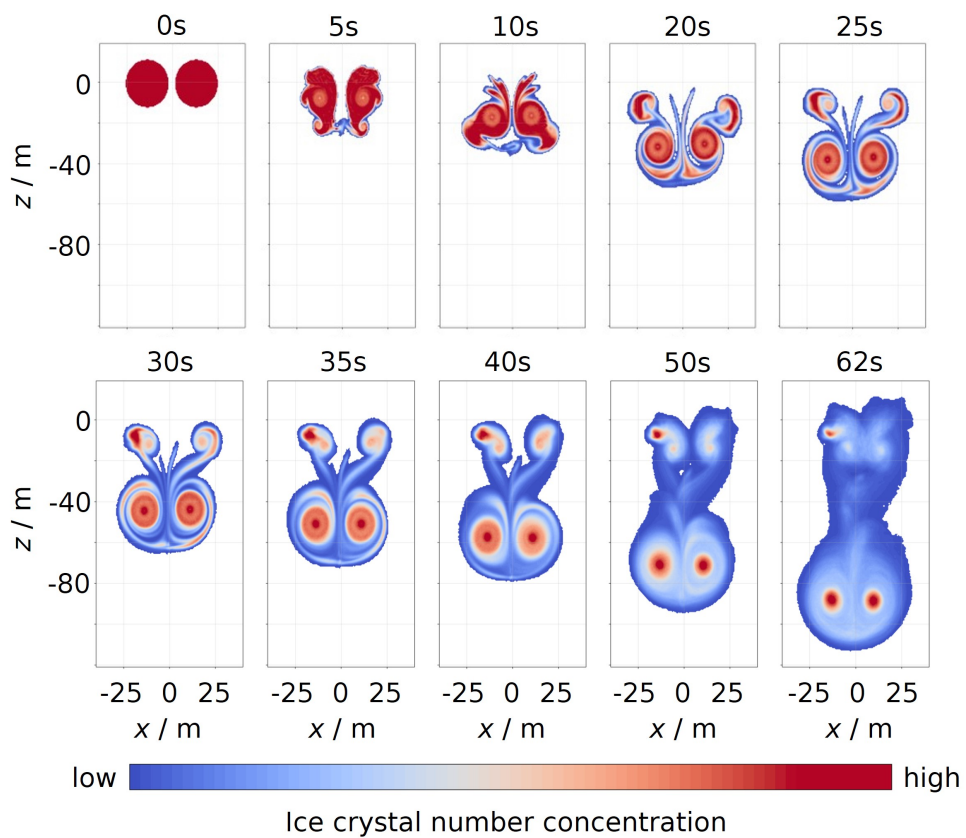


Figure A12: Temporal evolution of ice crystal number concentration in (x, z) -plane averaged along flight direction for RANS simulation A320, $X = 90$ m. Figure adapted from Rabe (2024).

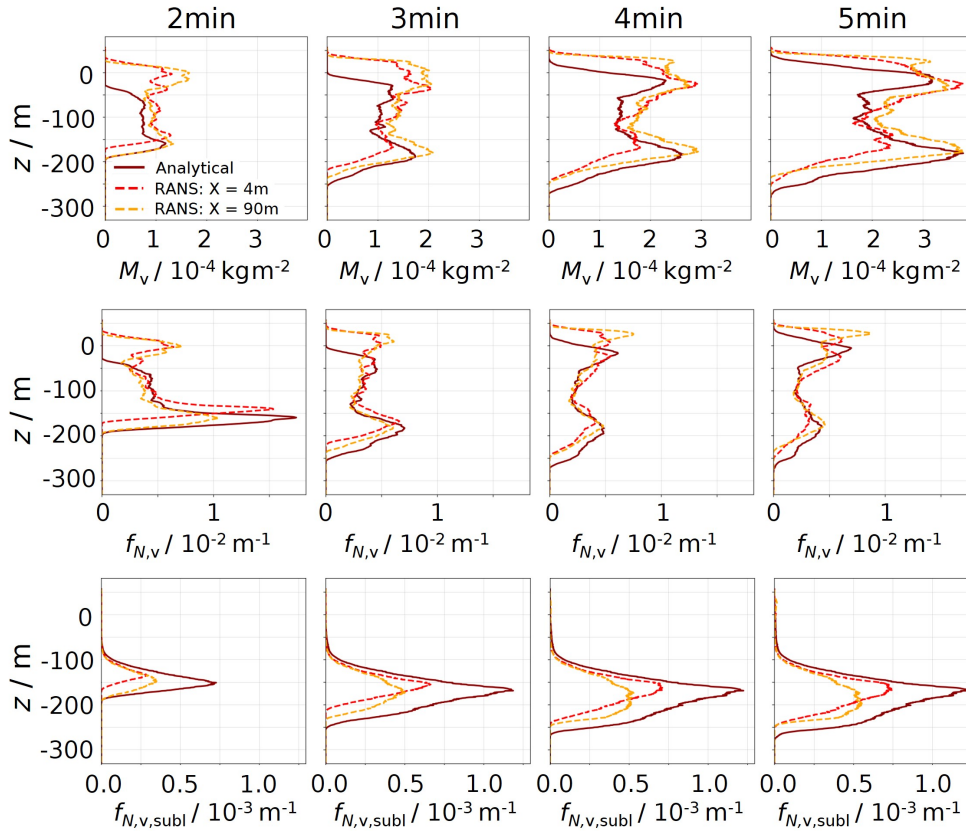


Figure A13: Temporal evolution of vertical profiles of ice mass (first row), normalized ice crystal number (second row), and normalized number of sublimated ice crystals (third row). A comparison between the RANS-based and the analytical flow field initialization is shown. Figure adapted from [Rabe \(2024\)](#).

All RANS simulations, encompassing different aircraft types and downstream positions, consistently show that a larger fraction of ice crystals remains close to the flight level compared to their analytical counterparts. In the latter, all ice crystals are entrained in the primary wake and transported downward by the descending vortex pair, where they are prone to sublimation. This behavior can be seen in Fig. A13, which presents vertical profiles of ice mass (top row), ice crystal number concentration (middle row), and number of sublimated ice crystals (bottom row). In the analytical case, a pronounced peak in sublimated ice crystals appears at lower altitudes, reflecting adiabatic heating within the primary wake. In contrast, the RANS simulations show more ice crystals retained at higher altitudes, attributed to early-developing turbulent structures that keep them near the flight level.

These differences in the sublimation behavior between the analytical and RANS simulations result in slightly higher survival fractions in the RANS cases in most of the $RH_{i,amb}$ conditions, as shown in Fig. A14.

Consistent with the results presented in [Lottermoser and Unterstrasser \(2025\)](#), Benedikt finds lower survival fractions in the case of an initial higher number of ice crystals (not shown here). This finding is independent of whether a RANS or an analytical initialization for the wake vortex field is used. Still, the survival fraction is larger in the RANS-based approach.

As previously noted, Benedikt conducted a sensitivity study on the engine position by placing the initial plumes closer to the aircraft fuselage. In the default setup, commonly used in earlier studies (e.g., [Unterstrasser, 2014](#); [Lottermoser and Unterstrasser, 2025](#)), the plume centers are co-located with the wingtip vortex centers. The lateral distance between the vortex pair is defined as $b_0 = \pi/4 \times b_{span}$, where b_{span} is the aircraft's wingspan. Accordingly, the default plume position (i.e., the distance from the plume center to the aircraft's centerline) is $b_0/2$, which equals 13.5 m for an A320 aircraft with a wingspan of 34.4 m, as defined in [Unterstrasser and Görsch \(2014\)](#). However, this symmetry does not necessarily reflect real

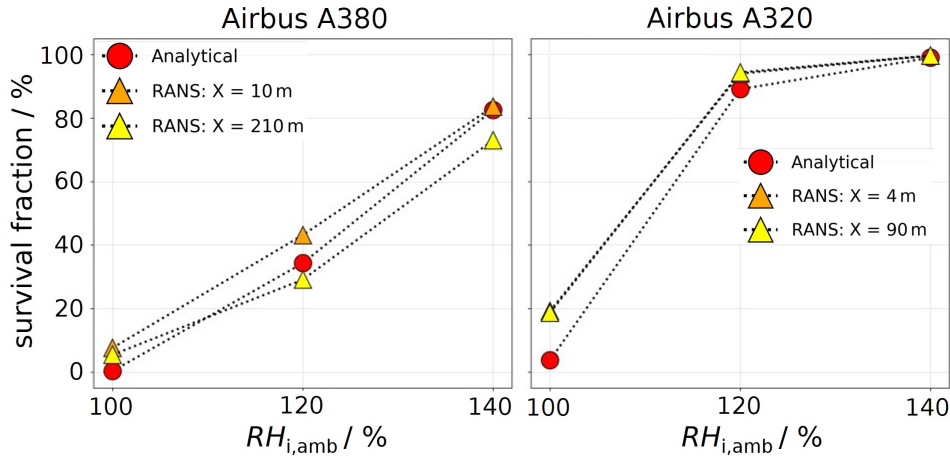


Figure A14: Ice crystal survival fraction for the analytical and the RANS simulations as indicated in the legend. Three different ambient relative humidity values are considered. The left and the right panel correspond to the A380 and A320 case, respectively. Figure adapted from Rabe (2024).

aircraft engine placements. To account for this, Benedikt investigated an alternative plume location based on data from Airbus (2024), placing the plume center 5.75 m from the aircraft's centerline. Horizontal profiles of ice crystal number and mass (not shown) reveal that, within the initial minute of downward propagation, a larger fraction of ice crystals sublimates when the plumes are positioned closer to the aircraft's centerline. This is due to the increased overlap of the initial plumes, leading to higher local number concentrations. In the overlapping region, ice crystal growth is hampered in the early seconds, as more crystals compete for the available water vapor. Figure A15, left panel, shows the corresponding evolution of total ice mass, with less increase during the first seconds in the "real" case. Overall, 61 % of ice crystals sublimates compared to 73 % in the default setup, as shown in the right panel.

The simulations presented in this section explore more realistic, less idealized initialization conditions. Future work will include simulations that combine RANS-based flow field initialization with variations in the initial plume position to investigate whether the individual effects counteract each other.

Impact of varying plume number on contrail evolution

As part of a DAAD ("Deutscher Akademischer Austauschdienst") internship, Adam joined our group in 2024 for a three-month period. During this time, he conducted vortex phase simulations with a focus on plume initialization. In particular, we accounted for different engine-wing configurations by investigating the impact of varying the number of initial plumes/engines on the contrail evolution. Adam performed simulations for an A320-like aircraft with a wingspan of $b_{\text{span}} = 34.4$ m, using an analytical Lamb-Oseen profile to initialize the wake vortex flow field, at an ambient temperature of $T_{\text{amb}} = 230$ K and an ambient relative humidity with respect to ice of $RH_{i,\text{amb}} = 120$ %. To study the impact of plume number variation on the contrail evolution, we extended the default setup, two plumes with a radius of 12 m (Unterstrasser and Görsch, 2014), by introducing two alternative configurations: one with six plumes (each 2 m in radius) and another with ten plumes (1 m in radius). In all cases, we initialized the same total number of ice crystals, $N_0 = 3.38 \times 10^{12} \text{ m}^{-3}$. As the total plume area decreases with an increasing number of initial plumes, the resulting ice crystal number concentration becomes higher. We would have expected higher ice crystal survival fractions with a higher plume number, as ice crystals closer to the aircraft fuselage would not be entrained into the vortex system and remain close to the flight altitude. However, similar to the results in the preceding section, the higher number concentration in the plumes leads to reduced ice mass growth during the initial seconds of evolution (see left panel of Fig A16), which decreases the average ice crystal size. Consequently, sublimation in the descending primary wake is more pronounced than in the default setup. This effect is evident in the right panel of Fig. A16, which shows the temporal evolution of the normalized

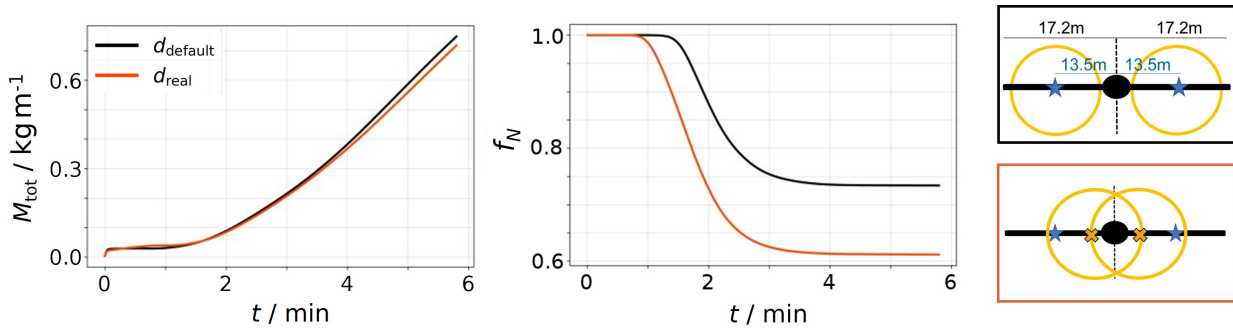


Figure A15: Temporal evolution of total ice mass (left panel) and normalized number of ice crystals (right panel) for the default initial plume position (black curves) compared to a configuration with plume positions placed closer to the aircraft fuselage (red curves). Simulations were performed at $T_{\text{amb}} = 235 \text{ K}$ and $RH_{i,\text{amb}} = 120 \%$. The sketches on the right illustrate the engine position shift, where the blue stars and yellow crosses denote the centers of the wake vortices and the initial plume positions, respectively. The plume radius is set to 12 m in both cases. Figure adapted from Rabe (2024).

ice crystal number. Using six initial plumes reduces the ice crystal survival fraction from the default case of 79 % down to 71 %, and even further to 67 % when distributing the initial ice crystals to ten plumes. In summary, both projects demonstrated how variations in the initial setup of vortex phase simulations can influence contrail evolution. Our default, idealized approach assumes one plume per wing, a Lamb-Oseen vortex profile, and co-located plume and vortex centers. Modifying any of these assumptions, such as changing the plume number or position, affects the simulation outcomes, particularly the ice crystal survival fraction. Although differences in survival fraction of ≈ 10 to 20 % seem minor compared to the full range of 0–100 % when varying the initial ice crystal number (Lottermoser and Unterstrasser, 2025), these findings are important to consider in future studies.

Figure A17 summarizes this section by showing the simulated survival fractions as a function of the parameterization parameter z_{Δ} (introduced in Sec. 3.2.2.3). The results of the present simulations are shown as colored symbols, previous simulations as grey circles, together with the parameterization curve. Simulations of the A320 and A380 with an analytical initialization of the vortex pair are shown as red circles, while those with a RANS initialization appear as orange and yellow triangles (as in Fig. A14). To aid differentiation, A320 symbols are outlined in blue. For both aircraft types, Benedikt performed simulations at ambient relative humidities over ice of 100 %, 120 %, and 140 %. The simulations with the shifted initial plume positions and increased number of initial plumes are shown as magenta diamonds and blue crosses/hexagons. With the exception of a few outliers (the 6 and 10 engine variation for one setup and the RANS values for the A320 case at $RH_{i,\text{amb}} = 100 \%$) the data points scatter closely around the parameterization curve.

Further refinement of the initialization procedure could include implementing a more realistic initial ice crystal size distribution based on LCM box model simulations. Additionally, the current assumption that all emitted water vapor condenses onto ice crystals could be adapted. For example, scenarios with 80 % of the water mass on ice crystals and 20 % remaining as vapor in the environment could be explored. These refinements represent promising directions for future vortex phase research.

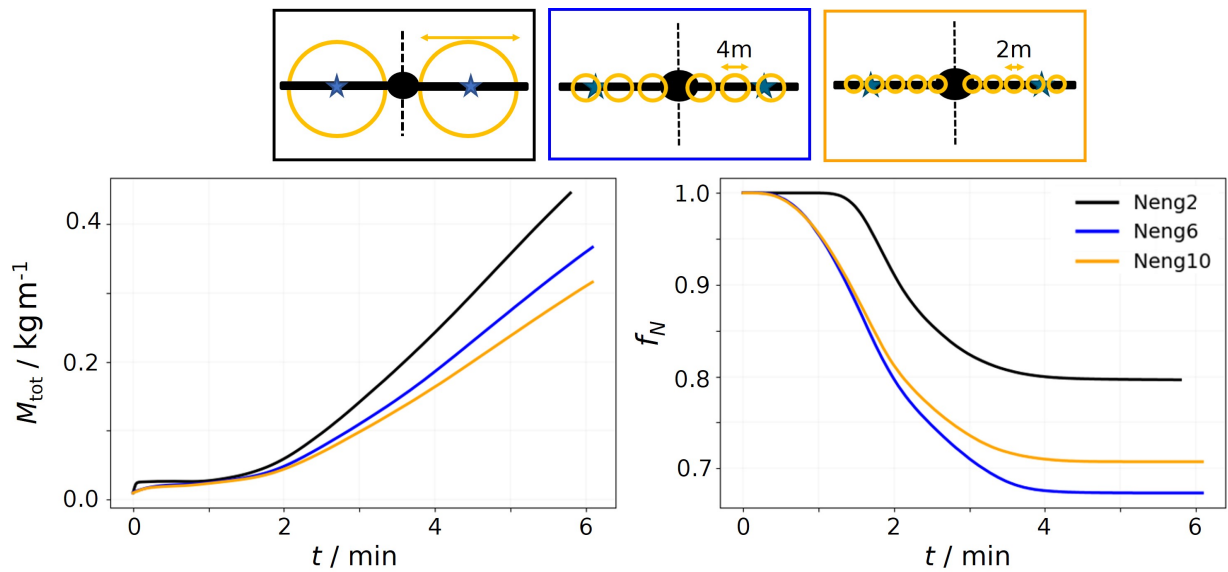


Figure A16: Temporal evolution of total ice mass (left panel) and normalized ice crystal number (right panel) for three different numbers of plumes indicated by color: two (black, default), six (blue), and ten (orange). The sketches on top illustrate the plume initialization.

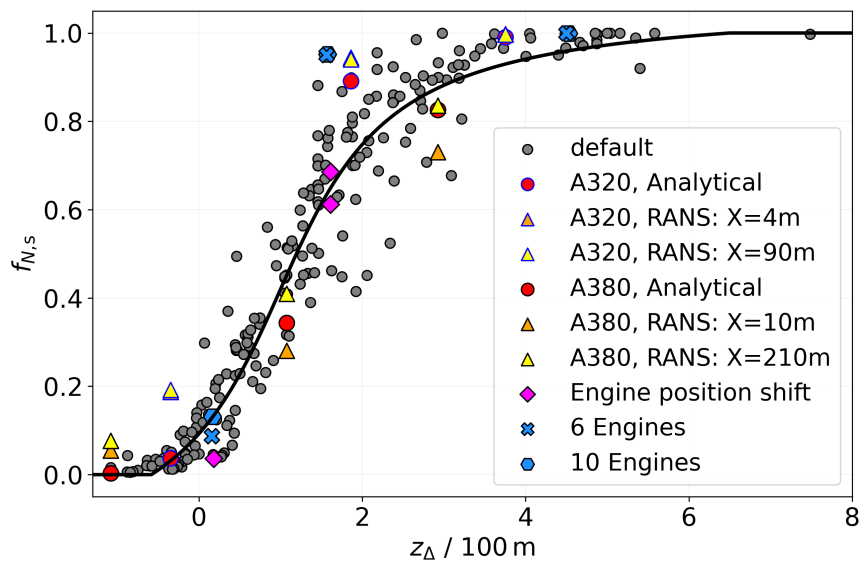


Figure A17: Simulated ice crystal survival fractions of the vortex phase simulations performed during the Bachelor's project and the internship versus the parameter z_{Δ} . The values for the A320 aircraft have a blue frame to differentiate them from the A380-results.

No.	AC	Tca (K)	RH _{amb} (%)	Mpv (10 ⁻² s ⁻¹)	N ₀ #sim	I ₀ (gm ⁻¹)	rSD	\hat{f}_{N_s}	\hat{f}_{N_s}	z _{amb} (m)	z _{mit} (m)	z _{desc} (m)
1,2,3,4,5	A350	217	120	1.15	5	15.0	3.0	0.05, 0.23, 0.65, 0.89, 0.98	0.06, 0.23, 0.6, 0.87, 0.97	164	249	339
6,7,8,9,10	A350	217	110	1.15	5	15.0	3.0	0.02, 0.1, 0.28, 0.46, 0.71	0.0, 0.06, 0.22, 0.58, 0.86	85	249	339
11,12,13,14,15,16	A350	217	120	1.15	6	38.55	3.0	0.02, 0.09, 0.39, 0.85, 0.98, 1.0	0.05, 0.2, 0.57, 0.85, 0.96, 1.0	164	546	339
17,18,19,20,21	A350	217	110	1.15	5	38.55	3.0	0.07, 0.27, 0.63, 0.81, 0.92	0.08, 0.29, 0.68, 0.9, 0.98	85	546	339
22,23,24	A350	217	120	1.15	3	15.0	1.0	0.07, 0.88, 1.0	0.06, 0.6, 0.97	164	249	339
25,26,27	A350	217	120	1.15	3	15.0	4.0	0.05, 0.61, 0.98	0.06, 0.6, 0.97	164	249	339
28,29,30	A350	217	110	1.15	3	15.0	1.0	0.05, 0.49, 0.93	0.0, 0.21, 0.86*	85	249	339
31,32,33	A350	217	110	1.15	3	38.55	4.0	0.02, 0.26, 0.67	0.0, 0.22, 0.86	85	249	339
34,35,36	A350	217	120	1.15	3	38.55	1.0	0.18, 1.0, 1.0	0.2, 0.85, 1.0	164	546	339
37,38,39	A350	217	120	1.15	3	38.55	4.0	0.09, 0.81, 0.99	0.2, 0.85, 1.0	164	546	339
40,41,42	A350	217	110	1.15	3	38.55	1.0	0.18, 0.92, 1.0	0.08, 0.68, 0.98	85	546	339
43,44,45	A350	217	110	1.15	3	38.55	4.0	0.06, 0.58, 0.89	0.08, 0.68, 0.98	85	546	339
46,47,48	A350	217	120	0.5	3	15.0	3.0	0.02, 0.28, 0.66	0.0, 0.26, 0.94	164	249	515
49,50,51	A350	217	110	0.5	3	15.0	3.0	0.01, 0.1, 0.31	0.0, 0.02, 0.73	85	249	515
52,53,54	A350	217	120	0.5	3	38.55	3.0	0.04, 0.46, 0.84	0.02, 0.71, 1.0	164	546	515
55,56,57	A350	217	110	0.5	3	38.55	3.0	0.02, 0.26, 0.53	0.0, 0.36, 0.96	85	546	515
Simulations at higher ambient temperatures												
58,59,60,61,62	A350	225	120	1.15	5	15.0	3.0	0.02, 0.12, 0.45, 0.76, 0.95	0.03, 0.14, 0.44, 0.79, 0.94	177	110	339
63,64,65,66,67	A350	225	110	1.15	5	15.0	3.0	0.01, 0.04, 0.13, 0.25, 0.45	0.0, 0.01, 0.09, 0.3, 0.69	92	110	339
68,69,70,71,72	A350	225	120	1.15	5	38.55	3.0	0.04, 0.21, 0.63, 0.9, 0.99	0.08, 0.28, 0.67, 0.9, 0.98	177	262	339
73,74,75,76,77	A350	225	110	1.15	5	38.55	3.0	0.02, 0.1, 0.29, 0.46, 0.68	0.0, 0.07, 0.27, 0.65, 0.89	92	262	339
78,79,80,81,82	A350	230	120	1.15	5	38.55	3.0	0.03, 0.15, 0.57, 0.86, 0.97	0.05, 0.21, 0.57, 0.86, 0.97	186	163	339
83,84,85,86,87	A350	230	110	1.15	5	38.55	3.0	0.01, 0.05, 0.17, 0.31, 0.52	0.0, 0.03, 0.15, 0.46, 0.81	97	163	339
88,89,90,91,92	A350	233	120	1.15	5	38.55	3.0	0.02, 0.12, 0.45, 0.78, 0.97	0.05, 0.19, 0.53, 0.84, 0.96	191	123	339
93,94,95,96,97	A350	233	110	1.15	5	38.55	3.0	0.01, 0.04, 0.14, 0.26, 0.45	0.0, 0.02, 0.12, 0.38, 0.76	99	123	339
98,99,100	A350	233	120	1.15	3	38.55	1.0	0.03, 0.63, 1.0	0.04, 0.53, 0.96*	191	123	339
101,102,103	A350	233	120	1.15	3	38.55	4.0	0.02, 0.43, 0.96	0.05, 0.53, 0.96	191	123	339
104,105,106	A350	233	110	1.15	3	38.55	1.0	0.01, 0.25, 0.59	0.0, 0.12, 0.76	191	123	339
107,108,109	A350	233	110	1.15	3	38.55	4.0	0.01, 0.12, 0.43	0.0, 0.12, 0.76	99	123	339
110,111,112,113,114	A350	235	120	1.15	5	38.55	3.0	0.02, 0.11, 0.43, 0.75, 0.95	0.04, 0.18, 0.52, 0.83, 0.96	195	102	339
115,116,117,118,119	A350	235	110	1.15	5	38.55	3.0	0.01, 0.03, 0.12, 0.23, 0.42	0.0, 0.01, 0.1, 0.34, 0.73	101	102	339
Simulations with A320/B737-like aircraft												
120	A320	217	120	1.15	1	3.7	3.0	0.89	0.72	164	176	231
121,122,123	A320	225	120	1.15	3	3.7	3.0	0.05, 0.78, 1.0	0.13, 0.64, 0.96	177	76	231
124,125,126	A320	225	110	1.15	3	3.7	3.0	0.01, 0.29, 0.86	0.03, 0.21, 0.78	92	76	231
127,128,129	A320	225	120	1.15	3	9.51	3.0	0.07, 0.85, 1.0	0.2, 0.76, 0.99	177	185	231
130,131,132	A320	225	110	1.15	3	9.51	3.0	0.03, 0.52, 0.96	0.07, 0.39, 0.9	92	185	231
133,134,135	A320	230	120	1.15	3	9.51	3.0	0.05, 0.8, 1.0	0.17, 0.72, 0.98	186	114	231
136,137,138	A320	230	120	1.15	3	9.51	3.0	0.02, 0.35, 0.88	0.04, 0.29, 0.85	186	114	231
139,140,141	A320	233	120	1.15	3	9.51	3.0	0.04, 0.78, 1.0	0.16, 0.71, 0.97	191	85	231
142,143,144	A320	233	110	1.15	3	9.51	3.0	0.01, 0.3, 0.86	0.04, 0.26, 0.82	99	85	231
145,146,147	A320	235	120	1.15	3	9.51	3.0	0.04, 0.76, 1.0	0.16, 0.7, 0.97	195	70	231
148,149,150	A320	235	110	1.15	3	9.51	3.0	0.01, 0.27, 0.84	0.03, 0.24, 0.81	101	70	231

Table A1: Summary of the simulations performed. Columns 3–5 list the meteorological parameters, while columns 6–8 present the microphysical initialization settings. Columns 9 and 10 display both the simulated and parameterized survival fractions. Lastly, columns 11–13 specify the length scales employed in the parameterization. Rows displaying five simulations correspond to sets with N_0 -scaling factors of 100, 10, 1, 0.1, and 0.01. Rows showing three simulations represent sets with scaling factors of 100, 1, and 0.01. In the third row, a total of six simulations is included, with simulation 11 using a scaling factor of 1000. *The slight variation of \hat{f}_{N_s} with rSD is not a direct dependence, but stems from an implicit dependence of \hat{f}_{N_s} on rSD via N_0 due to the numerical discretization in the ice particles' initialization process.

No.	$\hat{f}_{N,s}$	$\hat{f}_{N,s}$	$\hat{f}_{N,s}$	z_{am} / m	$\hat{z}_{\text{am}} / \text{m}$	$z_{\text{emit}} / \text{m}$	$\hat{z}_{\text{emit}} / \text{m}$
1,2,3,4,5	0.06, 0.23, 0.6, 0.87, 0.97	0.05, 0.21, 0.59, 0.87, 0.98	0.05, 0.21, 0.59, 0.87, 0.98	164	163	249	250
6,7,8,9,10	0.0, 0.06, 0.22, 0.58, 0.86	0.0, 0.05, 0.22, 0.59, 0.87	0.0, 0.05, 0.22, 0.59, 0.87	85	87	249	250
11,12,13,14,15,16	0.05, 0.2, 0.57, 0.85, 0.96, 1.0	0.05, 0.19, 0.55, 0.86, 0.97, 1.0	0.05, 0.19, 0.55, 0.86, 0.97, 1.0	164	163	546	541
17,18,19,20,21	0.08, 0.29, 0.68, 0.9, 0.98	0.08, 0.28, 0.68, 0.91, 0.99	0.08, 0.28, 0.68, 0.91, 0.99	85	87	546	541
22,23,24	0.06, 0.6, 0.97	0.05, 0.59, 0.98	0.05, 0.59, 0.98	164	163	249	250
25,26,27	0.06, 0.6, 0.97	0.05, 0.59, 0.98	0.05, 0.59, 0.98	164	163	249	250
28,29,30	0.0, 0.21, 0.86	0.0, 0.21, 0.87	0.0, 0.21, 0.87	85	87	249	250
31,32,33	0.0, 0.22, 0.86	0.0, 0.22, 0.87	0.0, 0.22, 0.87	85	87	249	250
34,35,36	0.2, 0.85, 1.0	0.19, 0.85, 1.0	0.19, 0.85, 1.0	164	163	546	541
37,38,39	0.2, 0.85, 1.0	0.19, 0.86, 1.0	0.19, 0.86, 1.0	164	163	546	541
40,41,42	0.08, 0.68, 0.98	0.08, 0.68, 0.99	0.08, 0.68, 0.99	85	87	546	541
43,44,45	0.08, 0.68, 0.98	0.08, 0.68, 0.99	0.08, 0.68, 0.99	85	87	546	541
46,47,48	0.0, 0.26, 0.94	0.0, 0.25, 0.95	0.0, 0.25, 0.95	164	163	249	250
49,50,51	0.0, 0.02, 0.73	0.0, 0.02, 0.74	0.0, 0.02, 0.74	85	87	249	250
52,53,54	0.02, 0.71, 1.0	0.01, 0.7, 1.0	0.01, 0.7, 1.0	164	163	546	541
55,56,57	0.0, 0.36, 0.96	0.0, 0.35, 0.97	0.0, 0.35, 0.97	85	87	546	541
Simulations at higher ambient temperatures							
58,59,60,61,62	0.03, 0.14, 0.44, 0.79, 0.94	0.02, 0.13, 0.43, 0.8, 0.95	0.02, 0.13, 0.43, 0.8, 0.95	177	176	110	112
63,64,65,66,67	0.0, 0.01, 0.09, 0.3, 0.69	0.0, 0.0, 0.09, 0.31, 0.7	0.0, 0.0, 0.09, 0.31, 0.7	92	95	110	112
68,69,70,71,72	0.08, 0.28, 0.67, 0.9, 0.98	0.07, 0.27, 0.67, 0.9, 0.99	0.07, 0.27, 0.67, 0.9, 0.99	177	176	262	263
73,74,75,76,77	0.0, 0.07, 0.27, 0.65, 0.89	0.0, 0.07, 0.27, 0.66, 0.9	0.0, 0.07, 0.27, 0.66, 0.9	92	95	262	263
78,79,80,81,82	0.05, 0.21, 0.57, 0.86, 0.97	0.05, 0.2, 0.56, 0.86, 0.97	0.05, 0.2, 0.56, 0.86, 0.97	186	185	163	163
83,84,85,86,87	0.0, 0.03, 0.15, 0.46, 0.81	0.0, 0.03, 0.15, 0.47, 0.82	0.0, 0.03, 0.15, 0.47, 0.82	97	99	163	163
88,89,90,91,92	0.05, 0.19, 0.53, 0.84, 0.96	0.04, 0.17, 0.52, 0.84, 0.96	0.04, 0.17, 0.52, 0.84, 0.96	191	191	123	121
93,94,95,96,97	0.0, 0.02, 0.12, 0.38, 0.76	0.0, 0.02, 0.12, 0.39, 0.77	0.0, 0.02, 0.12, 0.39, 0.77	99	102	123	121
98,99,100	0.04, 0.53, 0.96	0.04, 0.52, 0.96	0.04, 0.52, 0.96	191	191	123	121
101,102,103	0.05, 0.53, 0.96	0.04, 0.52, 0.97	0.04, 0.52, 0.97	191	191	123	121
104,105,106	0.0, 0.12, 0.76	0.0, 0.12, 0.77	0.0, 0.12, 0.77	99	102	123	121
107,108,109	0.0, 0.12, 0.76	0.0, 0.12, 0.77	0.0, 0.12, 0.77	99	102	123	121
110,111,112,113,114	0.04, 0.18, 0.52, 0.83, 0.96	0.04, 0.16, 0.5, 0.83, 0.96	0.04, 0.16, 0.5, 0.83, 0.96	195	194	102	99
115,116,117,118,119	0.0, 0.01, 0.1, 0.34, 0.73	0.0, 0.01, 0.1, 0.35, 0.74	0.0, 0.01, 0.1, 0.35, 0.74	101	104	102	99
Simulations with A320/B737-like aircraft							
120	0.72	0.72	0.72	164	163	176	183
121,122,123	0.13, 0.64, 0.96	0.12, 0.64, 0.97	0.12, 0.64, 0.97	177	176	76	79
124,125,126	0.03, 0.21, 0.78	0.03, 0.21, 0.8	0.03, 0.21, 0.8	92	95	76	79
127,128,129	0.2, 0.76, 0.99	0.19, 0.76, 0.99	0.19, 0.76, 0.99	177	176	185	186
130,131,132	0.07, 0.39, 0.9	0.06, 0.4, 0.91	0.06, 0.4, 0.91	92	95	185	186
133,134,135	0.17, 0.72, 0.98	0.16, 0.72, 0.98	0.16, 0.72, 0.98	186	185	114	113
136,137,138	0.04, 0.29, 0.85	0.04, 0.29, 0.86	0.04, 0.29, 0.86	186	185	114	113
139,140,141	0.16, 0.71, 0.97	0.15, 0.7, 0.98	0.15, 0.7, 0.98	191	191	85	83
142,143,144	0.04, 0.26, 0.82	0.03, 0.26, 0.83	0.03, 0.26, 0.83	99	102	85	83
145,146,147	0.16, 0.7, 0.97	0.15, 0.69, 0.98	0.15, 0.69, 0.98	195	194	70	67
148,149,150	0.03, 0.24, 0.81	0.03, 0.24, 0.82	0.03, 0.24, 0.82	101	104	70	67

Table A2: List of parameterized survival fractions derived with length scales that are computed via the numerical (Eqs. 3.15 and 3.16) or the analytical method (Eqs. A9 and A10), denoted with a tilde, and the corresponding length scales. Rows with three, five, or six simulations correspond to sets where the N_0 -scaling factors 100, 1, 0.01; 100, 10, 1, 0.1, 0.01; or 1000, 100, 10, 1, 0.1, 0.01 are applied, respectively.

AC	T_{CA} / K	$RH_{i,amb} / \%$	$I_{00} / (g\ m^{-1})$	$N_0 / (10^{12}\ m^{-1})$	$I_0 / (g\ m^{-1})$
A350	217	110	15.0	0.02, 0.15, 0.95, 3.34, 6.93	4.7, 7.1, 7.5, 7.0, 6.2
			38.6	0.03, 0.27, 2.13, 9.25, 22.08	7.8, 12.0, 13.7, 14.0, 13.2
		120	15.0	0.03, 0.3, 2.18, 7.74, 16.36	12.7, 19.6, 21.4, 21.9, 20.8
			38.6	0.03, 0.33, 2.85, 13.14, 31.84	15.0, 22.3, 24.5, 24.4, 23.7
			15.0	0.02, 0.08, 0.43, 1.19, 2.19	9.7, 11.5, 11.3, 10.2, 9.1
			38.6	0.02, 0.16, 0.98, 3.25, 6.8	14.8, 21.3, 23.7, 21.6, 19.5
	225	110	15.0	0.03, 0.26, 1.51, 4.21, 8.2	34.0, 50.9, 53.2, 50.3, 45.5
			38.6	0.03, 0.3, 2.12, 7.1, 15.03	37.5, 55.4, 59.1, 59.0, 54.6
	230	110	38.6	0.02, 0.11, 0.59, 1.71, 3.35	24.6, 31.0, 29.8, 26.1, 23.2
			38.6	0.03, 0.28, 1.73, 4.91, 9.94	74.7, 105.2, 112.3, 106.8, 98.5
		120	38.6	0.02, 0.09, 0.46, 1.25, 2.37	31.3, 37.5, 35.8, 31.6, 28.2
			38.6	0.03, 0.26, 1.52, 4.14, 8.17	107.0, 149.6, 159.9, 151.3, 138.1
233		110	38.6	0.01, 0.08, 0.4, 1.04, 1.92	37.3, 43.8, 41.9, 36.9, 32.7
			38.6	0.03, 0.25, 1.45, 3.75, 7.41	136.7, 189.0, 200.5, 189.8, 174.0
A320	225	110	3.7	0.01, 0.25, 1.13	5.0, 9.5, 6.9
			9.5	0.01, 0.44, 2.97	5.9, 12.5, 11.5
		120	3.7	0.01, 0.66, 3.86	13.3, 25.8, 23.2
			9.5	0.01, 0.72, 5.71	14.0, 27.0, 24.9
			110	0.01, 0.3, 1.55	8.6, 18.1, 15.5
			120	0.01, 0.68, 4.19	23.2, 44.5, 42.2
	230	110	9.5	0.01, 0.25, 1.2	12.3, 24.3, 19.2
			9.5	0.01, 0.66, 3.78	33.6, 64.6, 60.6
	233	110	9.5	0.01, 0.23, 1.04	15.6, 29.8, 22.6
			120	0.01, 0.65, 3.46	43.4, 81.0, 76.7
	235	110	9.5		
			120		

Table A3: Properties of the initialized contrails. Total ice crystal number N_0 and mass I_0 after vortex phase as functions of the respective aircraft, ambient temperature, ambient relative humidity with respect to ice, and initial amount of emitted water vapor according to Tab. 4.1. For the A350/B777-like aircraft, five values are provided for N_0 and I_0 , which denote the N_{00} -scaling simulations with scaling factors 0.01, 0.1, 1, 10, and 100. For the smaller A320/B737-like aircraft, N_0 and I_0 values are available for scalings of 0.01, 1, and 100.

Danksagung

Kein Weg ist zu weit und keine Herausforderung zu groß, wenn man die richtigen Menschen an seiner Seite hat. Ihnen gilt mein tiefster Dank.

Zunächst möchte ich bei meinem Doktorvater Prof. Dr. Markus Rapp für die Möglichkeit bedanken, am Institut für Physik der Atmosphäre an diesem gesellschaftsrelevanten Thema zu arbeiten. Unsere Gespräche und das Feedback bei den Komiteetreffen waren sehr hilfreich und haben den Fortschritt der Arbeit maßgeblich beeinflusst. Ebenfalls ein großes Dankeschön an meinen Zweitgutachter Prof. Dr. George Craig, der mit ebenso konstruktivem Feedback die Doktorarbeit vorangebracht hat. Darüber hinaus möchte ich mich bei Prof. Dr. Jochen Weller, Prof. Dr. Hartmut Zohm und Prof. Dr. Thomas Preibisch bedanken. Vielen Dank an das gesamte Komitee, sich die Zeit zu nehmen, die Arbeit zu begutachten!

Ein großes Dankeschön geht an die gesamte Abteilung Angewandte Meteorologie. Den Zusammenhalt und die gute Stimmung bei diversen Ausflügen, Kaffeepausen und Klausuren weiß ich sehr zu schätzen. Mein besonderer Dank gilt den Abteilungsleitern Dr. Thomas Gerz und Dr. Norman Wildmann für die Unterstützung und die große Freiheit, den Arbeitsalltag nach eigenen Wünschen und Bedürfnissen zu gestalten. Auch unserer Sekretärin Brigitte Ziegele möchte ich mich bedanken, ohne deren Hilfe und Ratschläge die organisatorischen Belange während des PhDs die dreifache Zeit eingenommen hätten. Danke, liebe Brigitte, dass du mir immer den Rücken freigehalten und zahlreiche Anfragen sofort und pragmatisch beantwortet hast. Vielen Dank an Stephanie Zähle, mit der ich das erste Telefonat im April 2021 geführt habe, um mich nach einer Praktikumsstelle am DLR zu erkundigen. Sie hat letztlich den Kontakt zu Simon vermittelt und mich so ans DLR gebracht (trotz Corona-Zeiten). Herzlichen Dank dafür!

Aus dem Institut möchte ich mich vor allem bei Moritz Spraul, Niklas Wartha, Kianusch Vahid Yousefnia und Cornelius Weiß-Rehm bedanken. Vielen Dank für die großartigen fachlichen Gespräche und die zahlreichen, gleichzeitig lustigen und ernsten, PhD-Therapiestunden während unserer gemeinsamen Bürotage. Danke Moritz, dass ich die frühen Morgenstunden nicht alleine verbringen musste, sondern mich immer auf einen netten Ratsch mit dir freuen konnte, bevor sich das Büro gefüllt hat! Ein großer Dank gilt Simon Braun für die Bereitstellung der Daten der Nephela 2 Kampagne.

Darüber hinaus bedanke ich mich bei den internen Reviewern meiner Publikationen: Dr. Thomas Gerz, Dr. Klaus Gierens und Dr. Ziming Wang. Herzlichen Dank, dass ihr euch die Zeit genommen habt, die Manuskripte durchzuarbeiten und mit konstruktiven und hilfreichen Vorschlägen diese zu verbessern! Darüber hinaus möchte ich mich bei Caleb Akhtar-Martinez bedanken; die wertschätzende Zusammenarbeit und der Austausch über Länder- und Gruppengrenzen hinweg haben mir großen Spaß gemacht. In diesem Sinne möchte ich mich ebenfalls bei Charles Renard für sein Engagement und seinen Input im Zuge des H₂-Projekts bedanken.

Als Nächstes möchte ich ein ganz großes Dankeschön an die "Kondensstreifen-Gruppe" aussprechen: Dr. Simon Unterstraßer, Dr. Wing-Fai Thi, Dr. Francesco Vannini, Josef Zink, Dennis Hillenbrand, Judith Pauen, Benedikt Rabe, Adam Schroeder und Pedro Munoz Jimenez. Die gemeinsame Zeit mit vielen Gesprächen auf fachlicher und privater Ebene hat mich und meine Arbeit maßgeblich geprägt. Danke an Wing-Fai für die Fortführung des RadMod-Projekts und vielen Dank für die zahlreichen Verbesserungsvorschläge zum Coding und wissenschaftlichen Texten. Vielen Dank, Benedikt, dass du mit so viel Motivation und Eifer die Bachelorarbeit angepackt hast. Die Betreuung hat mich fachlich und menschlich sehr vorangebracht. Ein großes Dankeschön möchte ich Josef aussprechen, der mir stets mit Engelsgeduld diverse Zusammenhänge, meist meteorologischer Natur, erläutert hat. Vielen Dank an Dennis für das offene Ohr und das große Herz. Ich bedanke mich bei Judith für den regen Austausch zu EULAG und das große Engagement. Jede Gruppe braucht "eine Judith".

Der Mensch, der am meisten zum Inhalt und schließlich zur Fertigstellung dieser Arbeit beigetragen hat, ist mein Betreuer Simon. Vielen Dank, Simon, für deine Geduld, deinen Humor und deine Hilfsbereitschaft. Es heißt, dass das Gelingen einer Doktorarbeit mit der Betreuung steht oder fällt. Wie gut, dass ich an

dich geraten bin! Danke für dein stets offenes Ohr und die großen Freiheiten, die du mir zugestanden hast. Danke, dass du das Projekt/mich nie aufgegeben hast und bei einer vermeintlich verschlossenen Tür zehn neue geöffnet hast.

Ein großes Dankeschön geht an die A8 und den Münchner Ring für die großartige Bereitschaft, gerade dann Staus und Baustellen bereit zu halten, wenn ich auf der Hin- oder Rückreise zu/von der Arbeit war. Liebe A8, durch dich konnte ich meine Arbeitszeit am Institut auf ein Maximum ausdehnen, um mehrstündigen Staus zu umgehen, was den Fortschritt der Arbeit sehr vorangetrieben hat.

Ich möchte mich bei meinen Freundinnen Katha, Maria, Tina, Sophie und Julia für die stets wunderbare und lustige gemeinsame Zeit bedanken. Danke, dass ihr mich bei allen Up and Downs des PhDs immer ertragen habt und mit aufbauenden Worten immer zur Stelle seid.

Danke an Rosi und Jürgen für die Herzlichkeit, mit der ihr mir immer begegnet, und die Gastfreundschaft in Mudau und in der Allgäu-WG. Vielen Dank an Chris und Becci für die vielen schönen Erlebnisse bei gemeinsamen Reisen in England und Irland.

Ich möchte mich bei meiner Omi Ursula Hoffmann für das unglaubliche Interesse an meinem Leben und beruflichem Werdegang bedanken. Auch wenn sie die Fertigstellung dieser Arbeit nicht mehr erleben konnte, werden mir unsere vielen wunderbaren Gespräche auf ihrem Balkon immer im Gedächtnis bleiben und im Herzen weitergeführt werden. Von ganzem Herzen möchte ich mich bei meinen Eltern Claudia und Werner bedanken. Danke für die selbstlose Unterstützung bei allen großen und kleinen Fragen des Lebens und die Möglichkeit, meine Träume zu verfolgen und auszuleben. Ihr glaubt gerade dann an mich, wenn ich es selbst nicht tue. Danke an meinen Bruder Albrecht, ohne den mein Leben wahrscheinlich in Chaos versinken würde. Danke für die Liebe und Hilfsbereitschaft, die du mir immer zuteil werden lässt. Du bist ein Mensch, auf den ich immer zählen und bauen kann. Ich kann mich so glücklich schätzen, dich als großen Bruder zu haben.

Schließlich möchte ich mich bei meinem Freund Basti herzlich bedanken. Danke für die vielen genialen Abenteuer während unserer Reisen und gemeinsamen Touren, um den nötigen Ausgleich zum PhD-Alltag herzustellen. Danke, dass du mich getragen hast, wenn ich nicht mehr konnte. Danke für deine Liebe, deinen Zuspruch und deine Fürsorge während der letzten vier Jahre.

Curriculum vitae

Education

2002–2006	Primary School, Bad Reichenhall
2006–2014	Karls gymnasium Bad Reichenhall
June 2014	Abitur, final grade: 1.4
February 2015	Internship at Universitätssternwarte Dresden
2015–2018	B.Sc. in Physics, University of Regensburg <i>Bachelor's Thesis: "Evaluation of transition probabilities of photonic Boson sampling beyond the case of two open channels"</i> , final grade: 1.5
2019–2021	M.Sc. in Astrophysics, Ludwig-Maximilians-Universität Munich <i>Master's Thesis: "Dynamical mass constraints of X-ray selected galaxy clusters"</i> , final grade: 1.1
Since 2021	PhD student in Physics, Ludwig-Maximilians-Universität Munich / Institute for Atmospheric Physics, DLR Oberpfaffenhofen

Publications

- A. Bier, S. Unterstrasser, J. Zink, D. Hillenbrand, T. Jurkat-Witschas, and A. Lottermoser. Contrail formation on ambient aerosol particles for aircraft with hydrogen combustion: a box model trajectory study. *Atmos. Chem. and Phys.*, 24(4):2319-2344, 2024. DOI: [10.5194/acp-24-2319-2024](https://doi.org/10.5194/acp-24-2319-2024)
- A. Lottermoser and S. Unterstrasser. Towards intermediate complexity modelling of contrail formation: the new dynamical framework RadMod. *Aeronaut. J.*, 1-29, 2024. DOI: [10.1017/aer.2024.130](https://doi.org/10.1017/aer.2024.130)
- A. Lottermoser and S. Unterstrasser. High-resolution modeling of early contrail evolution from hydrogen-powered aircraft. *Atmos. Chem. Phys.*, 25:7903-7924, 2025. DOI: [10.5194/acp-25-7903-2025](https://doi.org/10.5194/acp-25-7903-2025)
- A. Lottermoser and S. Unterstrasser. Modeling of the impact of alternative fuels and hydrogen propulsion on contrail-cirrus: a parameter study. *in revision for J. Geophys. Res.*